Characterization and performance optimization of the focal plane of the Micro-channel X-ray Telescope on-board the space astronomy mission SVOM

Francesco Ceraudo

université PARIS-SACLAY

NNT : 2019SACLS595

Thèse de doctorat

Caractérisation et optimisation des performances du plan focal du télescope X de la mission d'astronomie spatiale SVOM

Thèse de doctorat de l'Université Paris-Saclay
préparée à l'Université Paris-Sud au sein du
Département d'Astrophysique du CEA de Saclay

École doctorale n°127
Astronomie et Astrophysique d'Île de France (AAIF)
Spécialité de doctorat: Astronomie et Astrophysique

Thèse présentée et soutenue à Saclay, le 18-12-2019, par

FRANCESCO CERAUDO

Composition du Jury :

Bruno Maffei — Président
Professeur des Universités, Université Paris-Sud

Julian Osborne — Rapporteur
Professeur des Universités, University of Leicester

Gianpiero Tagliaferri — Rapporteur
Directeur de recherche, INAF–Osservatorio Astronomico di Brera

Fabienne Orsini — Examinatrice
Directrice de recherche, Synchrotron SOLEIL

Florian Schopper — Examinateur
Ingénieur chercheur, Halbleiterlabor der Max-Planck-Gesellschaft

Hiroshi Tsunemi — Examinateur
Professeur émérite, Osaka University

Bertrand Cordier — Directeur de thèse
Directeur de recherche, CEA-Irfu

Aline Meuris — Encadrante de thèse
Ingénieure chercheuse, CEA-Irfu

Doctoral Thesis of the University of Paris-Saclay
prepared at the University of Paris-Sud at the
Astrophysics Division of CEA in Saclay

Doctoral school n°127
Astronomy and Astrophysics in Île de France (AAIF)
Thesis subject: Astronomy and Astrophysics

Characterization and Performance Optimization of the Focal Plane of the Micro-Channel X-ray Telescope on board the Space Astronomy Mission SVOM

Thesis presented and defended in Saclay, on the 18th of December 2019, by

Francesco Ceraudo

Members of the board:

Bruno Maffei University Professor, Université Paris-Sud	President
Julian Osborne University Professor, University of Leicester	Referee
Gianpiero Tagliaferri Research Director, INAF–Osservatorio Astronomico di Brera	Referee
Fabienne Orsini Research Director, Synchrotron SOLEIL	Examiner
Florian Schopper Research Engineer, Halbleiterlabor der Max-Planck-Gesellschaft	Examiner
Hiroshi Tsunemi Professor Emeritus, Osaka University	Examiner
Bertrand Cordier Research Director, CEA-Irfu	Supervisor
Aline Meuris Research Engineer, CEA-Irfu	Co-supervisor

NNT: 2019SACLS595

université PARIS-SACLAY

ÉCOLE DOCTORALE
Astronomie et Astrophysique d'Île-de-France

Titre : Caractérisation et optimisation des performances du plan focal du télescope X de la mission d'astronomie spatiale SVOM

Mots clés : Astronomie Spatiale, Astronomie en rayons X, Instrumentation Spatiale, SVOM, MXT

Résumé : SVOM est une mission Franco-Chinoise prévue pour fin 2021, pour l'étude des sursauts gamma (GRBs). SVOM sera composée d'un réseau de télescopes au sol, ainsi que d'un satellite. À bord de celui-ci, le Télescope X à Micro-canaux (MXT) étudiera l'émission rémanente des GRBs dans la bande 0.2-10 keV et localisera les sources avec une précision de 2 arcmin. Au plan focal d'optiques à œil de langouste, MXT montera un Charge Coupled Device en silicium complètement déplété et basé sur jonctions pn (pnCCD), hérité de XMM-Newton et eROSITA. Dans ce travail, les premiers essais de laboratoire sur le détecteur de MXT sont présentés. Une attention particulière est portée à l'étalonnage spectral par des méthodes instrumentales et d'analyse permettant une caractérisation rapide et fiable du détecteur, au sol et en vol. L'évolution des performances est critique en raison de l'environnement radiatif sévère de l'orbite terrestre basse auquel le détecteur sera exposé. Ceci fait l'objet de simulations Monte Carlo approfondies, amenant aux prédictions des performances à la fin de la mission, ainsi qu'à la planification d'une campagne d'essais d'irradiation de protons dans un accélérateur de particules pour une validation expérimentale des prédictions.

Université Paris-Saclay
Espace Technologique / Immeuble Discovery
Route de l'Orme aux Merisiers RD 128 / 91190 Saint-Aubin, France

université PARIS-SACLAY

ÉCOLE DOCTORALE
Astronomie et Astrophysique d'Île-de-France

Title: Characterization and performance optimization of the focal plane of the Micro-channel X-ray Telescope on-board the space astronomy mission SVOM

Keywords: Space Astronomy, X-ray Astronomy, Space Instrumentation, SVOM, MXT

Abstract: SVOM is a Chinese-French astronomy mission due to launch at the end of 2021 for the study of Gamma-Ray Bursts (GRBs). SVOM will be composed of a network of ground telescopes along with a satellite. On board, the Micro-channel X-ray Telescope (MXT) will study the afterglow emission of GRBs in the 0.2-10 keV range and provide source localization within a 2 arcmin precision. At the focal plane of lobster-eye optics, MXT will mount a back-illuminated fully-depleted frame-store Charge Coupled Device based on silicon pn-junctions (pnCCD), heritage of XMM-Newton and eROSITA. In this work, the first laboratory tests on the MXT detector are presented. Special attention is dedicated to energy calibration, in terms of algorithms and setups for fast and reliable characterization of the detector, both on ground and in orbit. The evolution of the performance is of critical concern because of the harsh radiation environment of the low Earth orbit to which the detector will be exposed. This is the object of extensive Monte Carlo simulations, leading to predictions of the end-of-life performances as well as the planning of a proton irradiation campaign at a particle accelerator for the experimental validation of the predictions.

Université Paris-Saclay
Espace Technologique / Immeuble Discovery
Route de l'Orme aux Merisiers RD 128 / 91190 Saint-Aubin, France

Contents

Chapter 1

SVOM, a Gamma-Ray Burst mission

This chapter will lay out the general framework of this thesis work, by introducing the context surrounding the SVOM mission. This will provide the background necessary to understand the drivers behind the design and the requirements of the instruments that will be dealt with during the course of this manuscript.

After introducing the Gamma-Ray Bursts (§ 1.1), that constitute the main science case for the entire mission, an overview of the various components of the SVOM mission will be provided (§ 1.2), paying special attention to the Micro-channel X-ray Telescope (§ 1.3), on which this whole thesis is based. The discussion will eventually allow to ask a series of questions that will guide this manuscript until the end (§ 1.4).

1.1 Gamma-Ray Bursts

Gamma-Ray Bursts or GRBs are the most energetic phenomena known in the universe. Appearing randomly and uniformly across the sky, they are thought to originate from the most violent environments in existence, i.e. collapsing stars and colliding compact objects. Having been a puzzle for astronomers since their first detection, they make up the scientific background of the SVOM mission, which represents the context of this entire work.

This section will begin with the general description of the phenomenology of Gamma-Ray Bursts (§ 1.1.1) and then with the presentation of the most

accepted models of their working mechanism (§ 1.1.2). It will then conclude with a list of some of the open questions that scientists are still trying to answer and which the SVOM mission will tackle (§ 1.1.3).

1.1.1 Phenomenology

In the next sections, some of the main features of Gamma-Ray Bursts shall be listed, at first from a rather general point of view (§ 1.1.1.1) and then by paying more attention to the different phases (§ 1.1.1.2 and § 1.1.1.3).

1.1.1.1 Overview

Gamma-Ray Bursts appear as intense and localized light emissions over a wide range of energies, from γ-rays to radio waves. They are composed of two phases:

1. the *prompt* emission, mainly in hard-X and γ-rays ($\sim 100\,\mathrm{keV} - 1\,\mathrm{MeV}$), which lasts from fractions of a second to several hundred seconds and provides the *trigger* that starts the detection process at the instrument level;

2. the *afterglow*, a much broader-band phenomenon (from X-rays to radio waves) occurring over a longer period of time, up to several minutes, hours or even days from the trigger. Thanks to the emission at longer wavelengths, the afterglow can be used by large telescopes capable of very high angular resolutions to accurately localize the GRB and therefore calculate its distance through redshift[1] measurements on its host galaxy.

It is important to point out that sometimes a *precursor* is detected, i.e. a smaller burst before the prompt emission, from which it is separated by several seconds or even minutes with no emission (Hu et al., 2014).

As discussed below, GRBs display very complex *light curves*, i.e. the number of detected counts as a function of time, to the point that it is difficult to precisely define a beginning and end of a burst, especially since the extremities

[1] *Redshift* z is caused by the expansion of the space-time, which stretches the wavelength as light travels between the source and the observer. Redshift is calculated from spectral features as $z = (\lambda_{\mathrm{obs}} - \lambda_{\mathrm{emit}})/\lambda_{\mathrm{emit}}$, where λ_{obs} and λ_{emit} are the observed and emitted wavelengths respectively. Redshift z relates to luminosity distance D_{L} via cosmological equations such as Huble's law $cz = H_0 D_{\mathrm{L}}$, where $H_0 \approx 70\,\mathrm{km\,s^{-1}\,Mpc^{-1}}$ is Hubble constant.

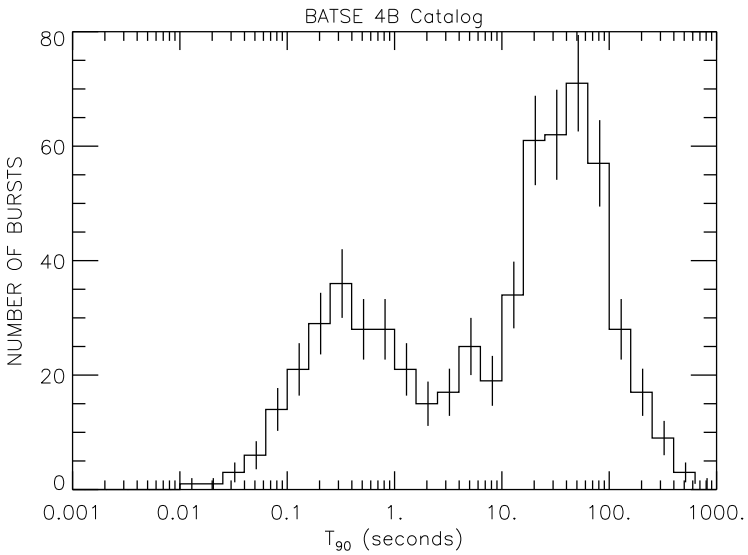

Figure 1.1 – Distribution of GRB time lengths from BATSE 4B catalog. The bimodal nature is clearly visible. (NASA, image available at `https://gammaray.nsstc.nasa.gov/batse/grb/`)

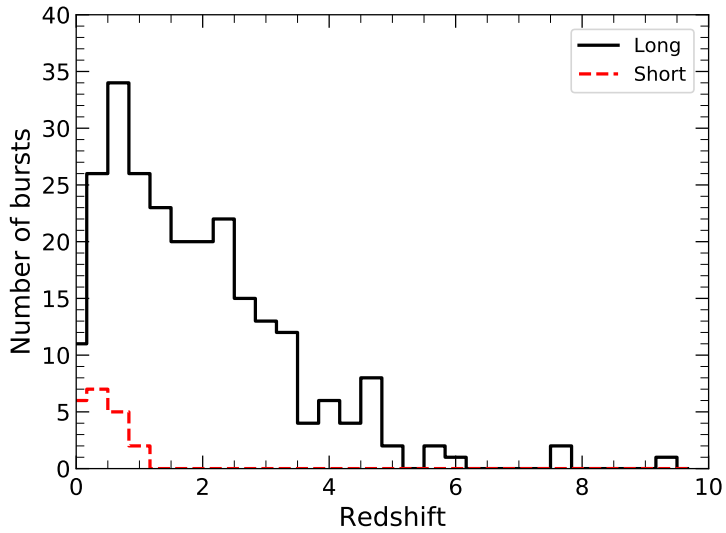

Figure 1.2 – Redshift distribution of long and short Gamma-Ray Bursts. (Data available at `https://swift.gsfc.nasa.gov/archive/grb_table/`)

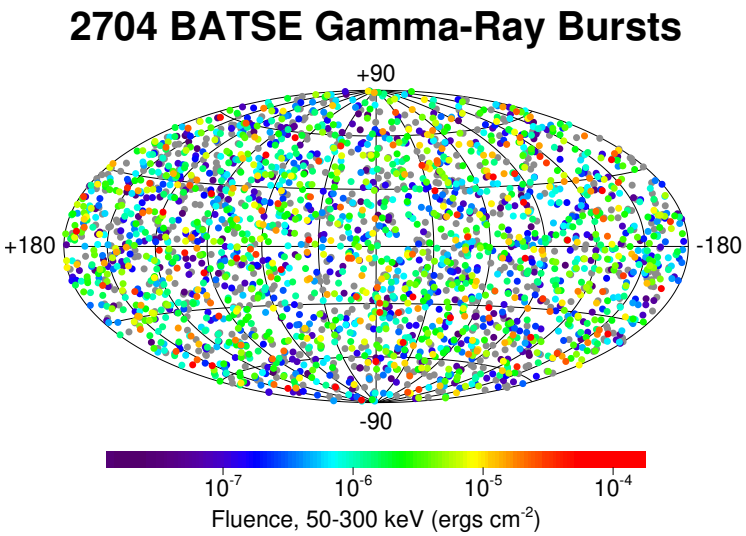

Figure 1.3 – Spatial distribution of BATSE GRBs. Isotropy of the sources in the sky is evident. (NASA, image available at `https://gammaray.nsstc.nasa.gov/batse/grb/`.)

of the light curves are usually buried in the background. Customarily, one defines the burst duration as T_{90} (T_{50}), i.e. the time needed to go from 5 % (25 %) to 95 % (75 %) of the fluence, i.e. the time-integrated flux (or total number of detected counts), in a chosen energy band. With this definition, one finds that the distribution of the burst duration is double-peaked (Kouveliotou et al., 1993), with a separation roughly at 2 s (Fig. 1.1): GRBs lasting less than 2 s ($\langle T_{90}\rangle_{\rm short} \approx 0.3\,{\rm s}$) are called *short*, whereas GRBs emitting for longer than 2 s are classified as *long* ($\langle T_{90}\rangle_{\rm long} \approx 20\,{\rm s}$). Normally, short GRBs have harder spectra and typically occur at $\langle z\rangle \sim 0.5$ (Fig. 1.2), whereas long GRBs appear softer and are distributed across a wide range of redshifts ($0.0085 \lesssim z \lesssim 9.4$) but concentrated around $\langle z\rangle \sim 1-2$ (Berger, 2014). The two classes are thought to have different progenitors, despite developing according to similar physics (§ 1.1.2).

Both types of GRBs appear randomly and are uniformly distributed across the sky (Fig. 1.3). The typical redshift values[2] imply cosmological distances, which translate to enormous amounts of energy, estimated in the order of $E_{\rm iso} \sim 10^{48} - 10^{55}\,{\rm erg}$ (Sun et al., 2015), where the subscript iso implies that the emission is supposed to be isotropic (which is most certainly not the case, as will be explained in § 1.1.2).

[2]One must bear in mind that so far only $\sim 30\,\%$ of long GRBs and a handful of short ones have their redshift measured.

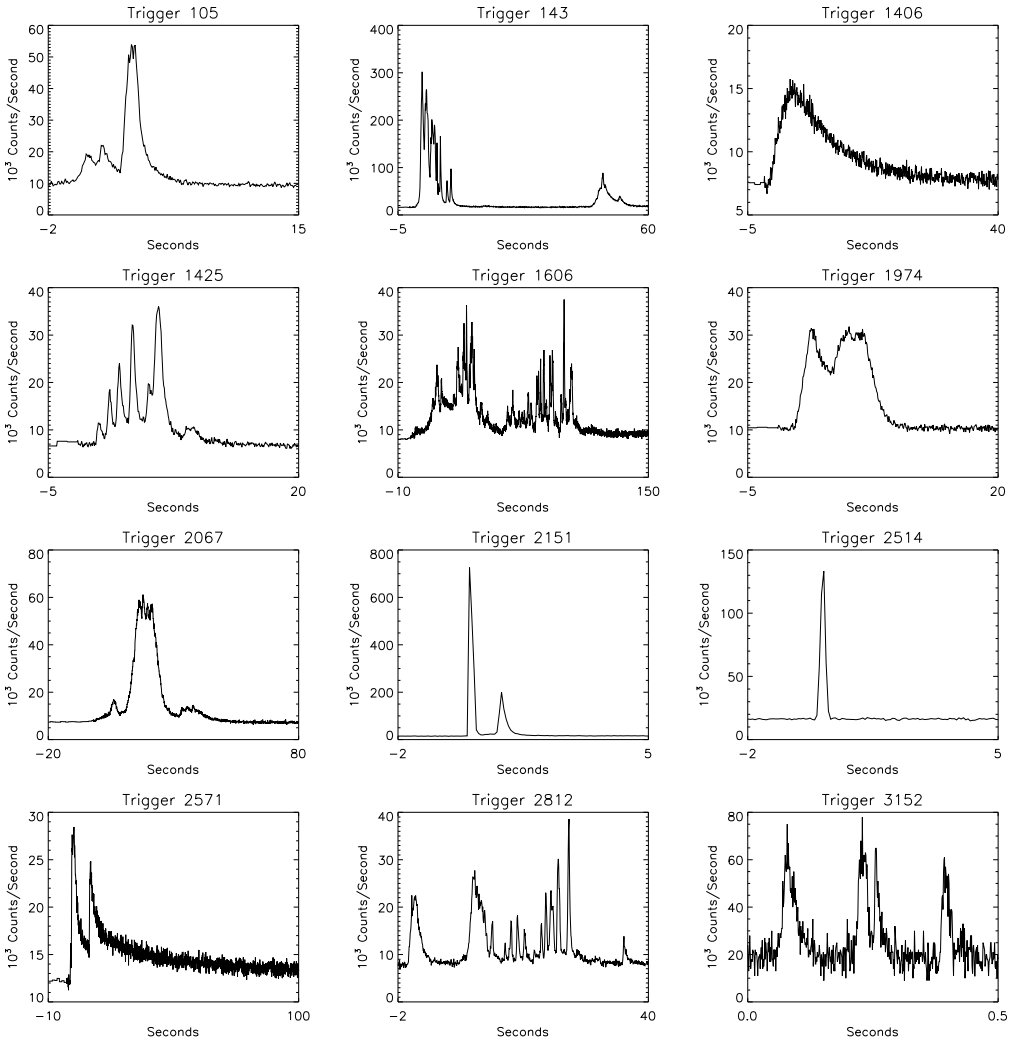

Figure 1.4 – Sample GRB prompt emission light curves. (NASA, image available at `https://gammaray.nsstc.nasa.gov/batse/grb/`)

It is worth noting that short GRBs are less common in catalogs than long ones, with a ratio of about one to three (Fig. 1.1): this may be explained by an intrinsic asymmetry between the two classes, but also by their being more difficult to detect due to their shorter duration and smaller total fluence.

1.1.1.2 Prompt emission

As hinted above, GRB light curves show a large range of shapes in γ-rays, most of them featuring a time variability δT over scales much smaller than the burst duration T. For others, $\delta T \sim T$ and almost no variability is observed during the burst. Examples of such light curves are shown in Fig. 1.4.

The Fermi satellite has extended the energy range of study of the prompt emission up to $\sim 300\,\mathrm{GeV}$, yielding several discoveries such as the detection of $> 100\,\mathrm{MeV}$ photons consistently arriving a few seconds after lower-energy γ-rays and lasting longer than the prompt emission at $\sim 1\,\mathrm{MeV}$, i.e. $\sim 10^3\,\mathrm{s}$ against ~ 1 minute (Abdo et al., 2009).

GRBs display non-thermal spectra in the hard-X-ray and γ-ray bands. From BATSE data, Band et al. (1993) developed the most commonly used expression to fit GRB spectral data. It is a purely empirical formula which does not imply any direct relation to the underlying physics, but it describes well the energy distribution $N(E)$ of the incoming GRB photons:

$$N(E) = N_0 \begin{cases} \left(\frac{E}{E_{\mathrm{ref}}}\right)^{\alpha} \exp\left(-\frac{E}{E_0}\right) & E < (\alpha-\beta)\,E_0 \\ \left[(\alpha-\beta)\,\frac{E_0}{E_{\mathrm{ref}}}\right]^{\alpha-\beta} \left(\frac{E}{E_{\mathrm{ref}}}\right)^{\beta} \exp\left[-(\alpha-\beta)\right] & E > (\alpha-\beta)\,E_0 \end{cases} \tag{1.1}$$

In eq. (1.1), E_{ref} is a reference energy (e.g. $100\,\mathrm{keV}$) and, in most cases, $E_0 = E_{\mathrm{peak}}/(\alpha+2)$, where E_{peak} is the energy at which $E^2\,N(E)$ reaches its maximum (Piran, 1999). Values of $\alpha \sim -1$ and $\beta \sim -2$ give good fit results for most bursts. Eq. (1.1) well explains the smooth decay after the starting peak in γ-ray spectra up to high energies, even though other components must sometimes be taken into account. In general, $100\,\mathrm{keV} < E_{\mathrm{peak}} < 400\,\mathrm{keV}$ with a maximum at $E_{\mathrm{peak}} \sim 200\,\mathrm{keV}$, which, in conjunction with the non-thermal spectra, rules out optically thick scenarios as possible explanations for the GRBs. Indeed, such models require the redistribution of high energy photons towards lower energies, a feature that has never been observed (Piran, 1999).

1.1.1.3 Afterglow emission

The afterglow occurs on much larger timescales than the prompt emission, on the order of thousands or tens of thousands of seconds, during which both the flux and the spectrum vary. It spans a wider frequency interval, ranging from X-rays to visible to radio waves.

Fig. 1.5 shows a schematic depiction of a typical GRB light curve in the X-ray band, in which its evolution is broken down into several phases, each obeying a power law.

1. *Phase 0* represents the prompt emission.

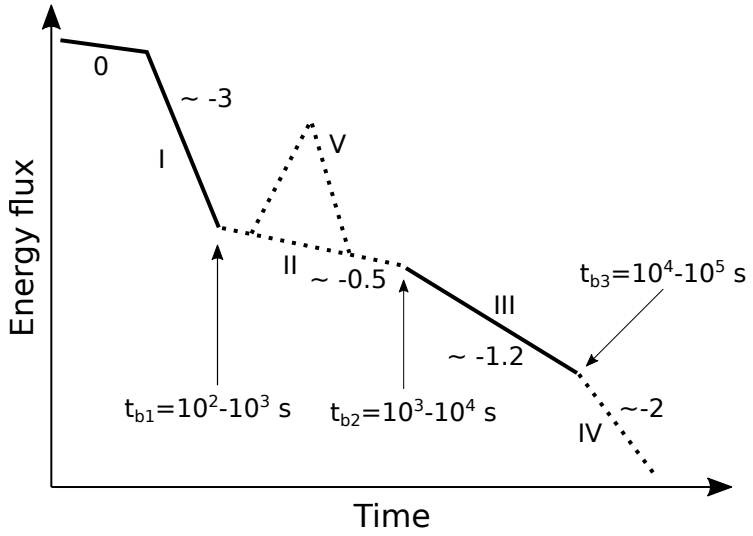

Figure 1.5 – Schematic of a typical afterglow light curve. (Zhang, 2006)

2. *Phase I* is the steep decay with a slope of ~ -3, starting at $t \gg T_{90}$. During this phase, the spectrum evolves from that of the prompt and becomes softer, with an index $\beta_{\rm X} \sim 1 - 1.5$ ($F_{\rm X} \propto E^{-\beta_{\rm X}}$).

3. *Phase II* starts approximately $10^2 - 10^3$ s after the γ-ray trigger and is characterized by the sharp turn to a shallow plateau with a slope of ~ -0.5. The spectrum at this stage is comparable or harder than the previous one ($\beta_{\rm X} \sim 1$). This phase is entirely missing in so-called *non-canonical* GRBs.

4. *Phase III* features a steeper decay (~ -1.2) happening after $10^3 - 10^4$ s, consistent with the interaction between jets and interstellar medium. The associated spectral index is $\beta_{\rm X} \sim 1$. For most bursts, this is the last observable phase due to the rapidly decreasing flux.

5. *Phase IV* may be observed in some cases, with a steep decay (~ -2) starting at $10^4 - 10^5$ s. The typical spectrum is unchanged. This segment is known as *jet break* (§ 1.1.2.3).

6. *Phase V* may be recorded in some cases and it consists of bright X-ray flares with (often also time-dependent) spectra similar to those of Phase I. They can occur between a few hundreds second or even a day after trigger and, due to their variability, they are thought to be caused by the re-activation of the central engine.

Sample afterglow light curves are shown in Fig. 1.6. It is worth noting that the X-ray flux decreases by three or four orders of magnitude already in the first segment of the evolution: this implies the necessity of quick measurements of the afterglow for the purposes of both characterizing its early phases and reliably identifying the position of the GRB.

The afterglow emission appears to be frequency-dependent. No temporal breaks are sometimes visible in the optical band as the X-ray curves moves between phase II and III or III and IV. Radio flares have also been measured (Kulkarni et al., 1999).

1.1.2 Models

The following sections shall provide a very brief review of the models explaining the physics of Gamma-Ray Bursts. The discussion is by no means complete and the reader may refer mainly to Kumar & Zhang (2015) and references therein for a more complete treatment of the subject.

1.1.2.1 Progenitors

As soon as it became clear that two classes of GRBs existed based on their duration, astronomers identified them as manifestations of two intrinsically different kind of progenitors.

Long GRBs are thought to be one of the possible outcomes of core-collapse supernovae (SNe) starting at masses $> 30\,\mathrm{M}_\odot$ (collapsar model). This hypothesis is supported by the prevalence of this type of bursts in star-forming galaxies, as well as the association to SNe Ib and Ic in all but a few instances, provided that the event is close enough ($z \lesssim 1$) that the SN signal does not fade in the afterglow (Cano et al., 2017).

On the other hand, short GRBs are thought to arise from compact object mergers, notably two neutron stars (NS-NS) or a neutron star and a black hole (NS-BH). This idea is supported by the localization of members of this GRB class in elliptical galaxies and, more generally, in regions where stars are not being formed anymore: in those places, enough time has passed for stellar remnants in binary systems to undergo significant orbital decay through the emission of gravitational waves to allow merging. Recently, a strong point in favor of this hypothesis was scored as a kilonova (an optical-IR weaker

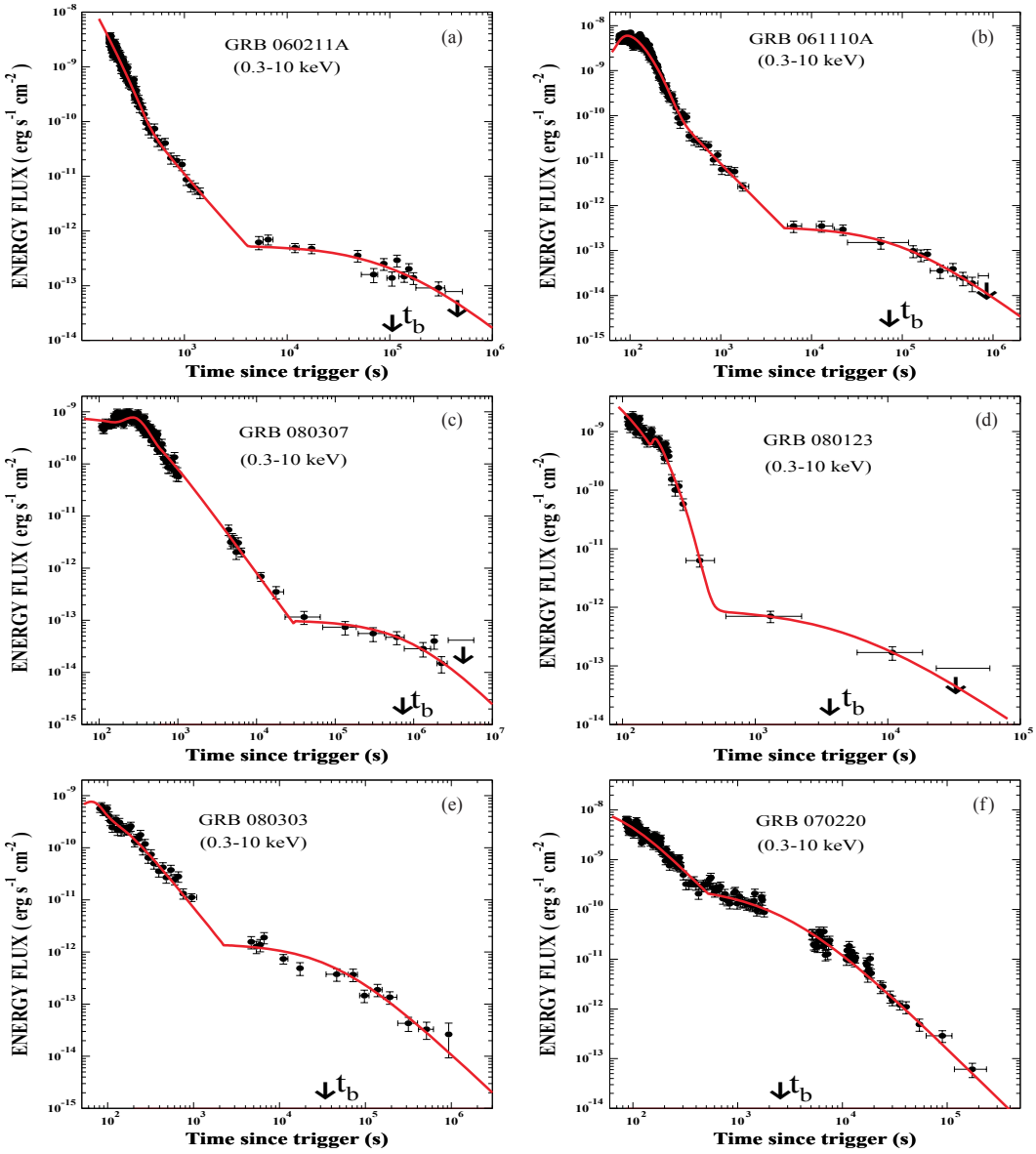

Figure 1.6 – Examples of afterglow light curves measured by Swift/XRT. (Dado et al., 2009)

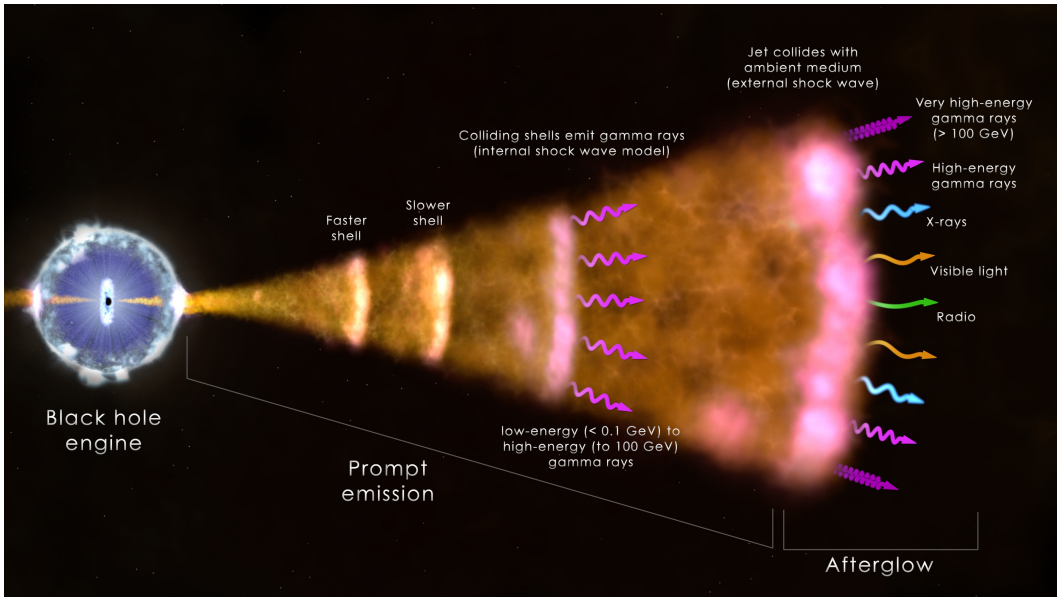

Figure 1.7 – Depiction of the underlying processes of GRBs. (NASA, image available at `https://fermi.gsfc.nasa.gov/science/eteu/grbs/`)

version of a supernova) was undoubtedly associated with a short GRB and a gravitational wave train resulting from a NS-NS merger (Abbott et al., 2017).

The neat classification described so far is open to modifications, because, for example, some long GRBs have been detected without SN counterparts, have displayed clear short-GRB-like characteristics or are difficult to classify due to the presence of a short peak followed by a very long ($10 - 100\,\mathrm{s}$) soft γ-ray emission (Gehrels et al., 2006; Zhang, 2006; Ofek et al., 2007). In addition, other bursts have shown prompt emissions extending above thousands of seconds and have therefore been labeled as *ultra-long GRBs* (Campana et al., 2011; Virgili et al., 2013; Zhang et al., 2014; Gendre et al., 2013), while exceptionally strong bursts from Soft Gamma Repeaters (i.e. highly active magnetars[3]) may also be recorded as short GRBs. Furthermore, it must be remembered that, since the definition of T_{90} is based on a fraction of the measured fluence, the duration of a GRB is detector-dependent, to the point that the class of a GRB may change if it is measured by instruments differing by their sensitivity and energy range. Finally, if one accounts for the time dilation associated with the redshifts, the difference in duration no longer appears distinct (Ghirlanda et al., 2015).

[3]A *magnetar* is a highly magnetized neutron star with a surface magnetic field $\gtrsim 10^{14}$ G.

1.1.2.2 Prompt emission

Regardless of the progenitor, it is well understood that the process responsible for GRBs should stay the same, as long and short GRBs display almost the same features, but on different timescales. Fig. 1.7 schematically depicts the main phases of the phenomenon, which shall be discussed in more detail in the following.

Due to their duration and total emitted energy, both classes of Gamma-Ray Bursts are thought to originate from compact objects interacting with the surrounding material. The most accepted model, the so-called *fireball model* (Piran, 1999), involves the occurrence of an accretion phenomenon on a compact object, e.g. black hole or millisecond magnetar[4], during which the accreting material forms a torus around the central object, with consequent emission of two relativistic jets along the rotation axis[5]. The presence of collimated jets instead of an isotropic sphere is supported by the *jet-break* feature of the afterglow emission, which can be observable from X-rays to radio waves and also provide constraints for the jet aperture in the $2 - 10^\circ$ range, thus reducing by a factor of $\sim 100 - 1000$ the estimated energy from $E_{\rm iso}$.

Jets are thought to be composed of hot ($> 20\,\mathrm{keV}$) magnetized plasma of photons, electron-positron ($e^\pm$) pairs and baryons (protons and neutrons), and are optically thick as long as there is equilibrium between photons and $e^\pm$ pairs. Moreover, jets need to make their way through the outer shells of the star surrounding the compact object, if present. This implies that the first phase cannot be observed from the outside.

As the jets move, they accelerate to relativistic velocities, expand and cool down, until they become transparent to photons. If one of the jets happens to be pointed towards some instruments, the prompt emission of a GRB is detected. Although the mechanism is still not well understood, the most adopted model involves the emission of γ-rays from *internal shocks* arising from the highly variable inner engine creating shock fronts propagating at different speeds and eventually outrunning one another, with consequent energy dissipation. This model is able to accurately reproduce the observed light curves but it fails when it comes to the spectra. Alternative explanations identify inverse Compton or synchrotron with the surrounding medium as the

[4] A *millisecond magnetar* is a fast-rotating magnetar with a period on the order of $10^{-3}\,\mathrm{s}$.

[5] Relativistic effects need to occur in order to explain why the jets are optically thin (*compactness problem*), as shown in § 1.1.1.2.

cause of prompt γ-rays. Broadband studies of the prompt emission, especially at lower energies such as X-rays and visible light, may help constrain the physical models.

It is worth noting that the moment at which the prompt emission evolves into the steep decline at the beginning of the afterglow (Phase I of Fig. 1.5) relates to the opening angle of the jet as well as the position at which the γ-rays are generated within the jet itself due to relativistic beaming effects (Zhang et al., 2006). Furthermore, if the viewing angle of the jet is taken into account, different types of transients, such as long GRB and X-ray flashes, might be traced back to the same underlying class of phenomena being observed from different directions (Dado et al., 2009).

1.1.2.3 Afterglow emission

The interaction between the jet and the circum-burst medium (CBM) is thought to be at the basis of the afterglow emission (Fig. 1.7), supposedly much better understood than the prompt. When the collision between the two occurs, both a forward shock into the CBM and a reverse shock into the jet itself are created with consequent energy dissipation and the production of synchrotron radiation, which explains the observed broadband emission from X-rays to radio waves. Synchrotron is the cause of the ~ -1 slope of the afterglow light curve and fits the spectra well. As the jets decelerate, their relativistic beaming decreases as well, causing the sharp fall at the end of the light curve known as *jet break* (Phase IV of Fig. 1.5). As already mentioned in § 1.1.1.3, X-ray flashes may occur following the reactivation of the central engine during the afterglow phase.

It is interesting to point out that the phenomenon of *orphan afterglows*, in which an afterglow emission is measured alone without any prompt signal, should be observed if highly beamed jets are directed away from the observer: however, no detection has occurred so far, although a strong candidate exists in the radio domain (Law et al., 2019). Finally, although the general underlying mechanism stays the same, one may expect important variations in the afterglows of different GRBs, especially between long and short ones, because of the different density and composition of the CBM, if one takes into account that massive stars near the end of their lives eject their outermost layers in the surrounding space.

1.1.3 Open questions

From the phenomenology and the theory described so far, some questions naturally arise. They are unanswered to this day and shall be addressed by future experiments, especially with the dawn of multi-messenger astrophysics, in which not only photons of any wavelength will be studied but also other carriers such as gravitational waves, cosmic rays and neutrinos. Here, just a few of these open issues related to GRBs are reported, both in terms of their features and physics, and as a tool to probe astrophysics at cosmological scales.

1.1.3.1 GRB progenitors and physics

- How do the properties of the progenitor influence the features observed in GRBs?
- What is the nature of the compact object (magnetar or black hole)?
- What are the processes involved in the jet formation and propagation?
- What is the jet composition?
- How can jets traverse the dense envelope of a massive star and stay collimated?
- How do gravitational waves correlate to GRBs?
- What is the micro-physics behind the prompt emission?
- What determines the huge variety of observed prompt light curves?
- What are the features of prompt emission at lower frequencies (e.g. X-rays and visible)?
- What are the interactions occurring between jets and circum-burst medium?
- What is the cause of the observed time variability of the afterglow?
- How are X-ray flashes generated after the prompt emission?
- What is the redshift distribution of GRBs?

- Should the simple long-short dichotomy be superseded by another classification more rooted in the underlying physics?
- How do the different classes of long GRBs, such as X-ray flashes, underluminous and ultra-long GRBs, relate to each other?
- Can the long-short statistical asymmetry be solved?

1.1.3.2 GRBs as astrophysical probes

- Are GRBs acceleration sites for Ultra-High Energy Cosmic Rays ($\sim 10^{20}$ eV)?
- Do GRBs generate a detectable flux of $\gtrsim$ TeV neutrinos and photons?
- Are population III (primordial metal-free) stars the progenitors of long GRBs at $z \gtrsim 20$?
- Could GRBs be used as *standard candles*[6]?
- Do fundamental constants vary with redshift?

1.2 SVOM

The *Space-based multi-wavelength astronomical Variable Object Monitor* (SVOM) is a French-Chinese mission designed to address all the open questions that arose from the study of Gamma-Ray Bursts, along with many more. To be launched at the end of 2021, it will operate in a thrilling scientific environment, besides new observatories that will be exploring the universe with unprecedented fast responses and sensitivities, in known as well as little known domains, such as the very high energy photons or radio waves, or even neutrinos and gravitational waves.

In this panorama, SVOM will participate with its core feature, which is, as its name suggests, the ability to perform observations over a broad energy range. Indeed, when put together, its different instruments, developed by a truly international collaboration, are sensitive to photons between 200 eV and 5 MeV,

[6] A *standard candle* is an astrophysical object of known intrinsic luminosity which therefore allows to determine the distance once its flux is measured. Examples are SNe Ia and Cepheid and RR Lyrae Variables.

as well as in the optical band and in the very near infrared ($400 - 1000\,\mathrm{nm}$). SVOM will take advantage of its broadband abilities to study GRBs along with a wide variety of other astrophysical targets, mainly in the form of transient phenomena, for which multi-energy investigations are often still limited.

The following sections are going to be dedicated to the scientific program of the mission and its predicted contributions (§ 1.2.1), its array of scientific instruments (§ 1.2.2) and the observation strategy by which the latter will be used to carry out the former (§ 1.2.3). A final summary highlighting the features setting SVOM apart from other experiments will be be given in § 1.2.4.

1.2.1 Scientific program

SVOM's scientific program is divided into three parts, named *Core Program*, *General Program* and *Target of Opportunity Program*. Each part addresses a particular range of topics and questions, and combined they determine the observation strategy of the mission as a whole, that will be described in § 1.2.3.

More details about the contributions SVOM can provide in each case can be found in the white papers of the project, such as Wei et al. (2016).

1.2.1.1 Core program

The central topic of SVOM's science will be Gamma-Ray Bursts, which represent its Core Program. The mission will be able to address all the open questions listed in § 1.1.3 and many more, thanks to its unique combination of multi-wavelength observations and temporal coverage of both prompt and afterglow emissions, combined with a follow-up strategy that will enable the determination of the redshift for $\sim 2/3$ of the detected bursts (§ 1.2.3.1).

Contrary to previous missions, SVOM instruments and strategy will allow *at the same time* the capacity to trigger on all types of GRBs, efficient follow-up observations and determination of the redshift for the majority of detected bursts, and good spectral and temporal coverage of both prompt and afterglow emission. This will allow not only to investigate the topics laid out in § 1.1.3, but also other subjects such as the earliest epochs of the universe and the first stars to appear in it, as well as the properties of GRB host galaxies.

1.2.1.2 General program

Thanks to the sensitivity of its instruments and the very large energy range they globally cover, SVOM will be able to observe a wide variety of astrophysical sources, not limited to Gamma-Ray Bursts. Here is a brief summary of some of the fields of study to which the mission will contribute.

Active Galactic Nuclei *Active Galactic Nuclei* (AGNs) are galaxies containing in their centers a supermassive black hole undergoing accretion. They include nuclear regions whose emission in the form of spectral lines and/or a continuum cannot be explained by simple stellar activity, they may also present jets and are in general variable sources. Observationally, their features depend on many parameters, such viewing angle, obscuration along the line of sight and rate of accretion, which have historically given origin to a rich nomenclature (e.g. Seyfert galaxies, quasars, blazars etc.) before they were understood to all rely on the same physical processes.

AGNs emit light over the entire electromagnetic spectrum, from radio waves to high energy γ-rays and are therefore well suited to be observed by an experiment like SVOM, especially because their emission has been known to vary simultaneously across a wide energy range.

Accreting objects The uninterrupted spectral coverage between 200 eV and 5 MeV provided by SVOM is adapted to follow galactic objects such as *cataclismic variables*, *X-ray binaries*, *black hole binaries* and *micro-quasars*, in which a compact object in the form of a white dwarf, a neutron star or a black hole respectively accretes matter from a companion star. SVOM capabilities are useful not only to study their occasional outbursts, but also their quiet emission, which can shed light on the behavior of matter under extreme conditions of gravity and magnetism.

Flaring objects Bursts from *magnetars*, i.e. young highly magnetized isolated neutron stars, in X- and γ-rays (classified as *Anomalous X-ray Pulsars* and *Soft Gamma Repeater* according to their spectral properties) may be detected by SVOM as short hard bursts and quickly followed up. This will allow to shed light on their working principles especially by exploring the lower energy range, which is still poorly studied in this context.

1.2.1.3 Targets of opportunity

Target of Opportunity (ToO) is the general term used to describe unplanned observations which require rapid follow-ups of alerts. In the astronomical landscape of the near future, populated by new instruments capable of exploring little known portions of the electromagnetic spectrum and beyond with unprecedented sensitivity and fast response, a great number of transient sources will be available for observation and follow-up. SVOM will be able to receive alerts from the wider astrophysical community and put its broadband observational capabilities into action. Its contributions will be manifold:

- localization and follow-up observations of Gamma-Ray Bursts detected by other facilities;
- search for counterparts to supernova events, such as those that will be detected by the Large Synoptic Survey Telescope (Ivezić et al., 2019);
- follow-up of multi-messenger alerts from experiments like LIGO-VIRGO and other gravitational wave detectors (The LIGO Scientific collaboration, 2019), the IceCube (IceCube-Gen2 Collaboration et al., 2014) and KM3NeT (Adrián-Martínez et al., 2016) neutrino detectors, the Cherenkov Telescope Array (Cherenkov Telescope Array Consortium et al., 2019) and the Square Kilometer Array (Braun et al., 2015) and their precursors;
- participation in the discovery of still unknown sources and phenomena that will arise from the widening of the means of astrophysical investigation thanks to the upcoming observatories.

1.2.2 Scientific instruments

The SVOM mission is composed of two portions:

- a satellite, with instruments whose combined sensitivity stretches from 200 eV to 5 MeV in the X-ray and γ-bands and from 400 nm to 1000 nm in the visible;
- a ground segment, with telescopes operating in different ranges from 400 nm to 1800 nm.

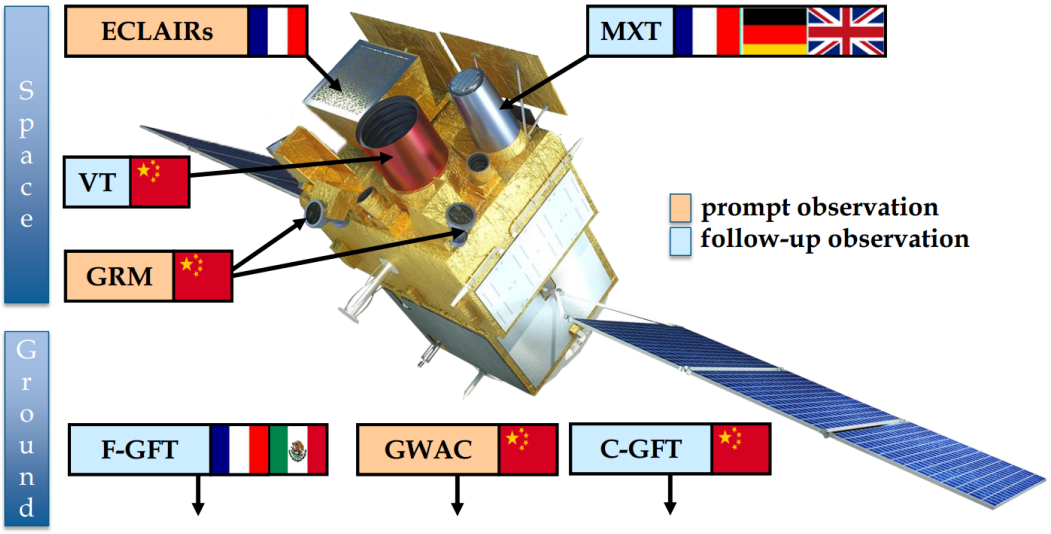

Figure 1.8 – Depiction of the SVOM satellite, with its scientific payload highlighted. The ground telescopes are marked as well. (SVOM collaboration)

Fig. 1.8 shows a depiction of the satellite, with all its on-board instruments marked, as well as the ground telescopes. The mass of the satellite as a whole is $\sim 930\,\mathrm{kg}$, which leaves only $\sim 450\,\mathrm{kg}$ for the scientific payload. The limited mass allowance is defined by the capabilities of the instrument platform and results in a series of constraints on mass, volume and power consumption that drove the design of the instruments, as will be addressed in § 1.3 in the case relevant for this work.

In the following, a basic overview of the various space-borne instruments (ECLAIRs: § 1.2.2.1; GRM: § 1.2.2.2; MXT: § 1.2.2.3; VT: § 1.2.2.4) as well as the ground ones (GWAC: § 1.2.2.5; GFTs: § 1.2.2.6) shall be provided. Further details on each of them can be found in Wei et al. (2016).

1.2.2.1 ECLAIRs

The wide field imager ECLAIRs is one of the French instruments on board the SVOM satellite. Under the scientific responsibility of IRAP Toulouse and developed by CNES and several other French laboratories, its main purpose is the detection and fast localization of hard X-ray transients.

ECLAIRs has a 6400-pixel CdTe detector plane operating in the $4 - 250\,\mathrm{keV}$ and lying 46 cm below a $54\,\mathrm{cm} \times 54\,\mathrm{cm}$ coded-mask aperture (40 % open fraction), which ensures a wide field of view of 2 sr and a *Point-Spread*

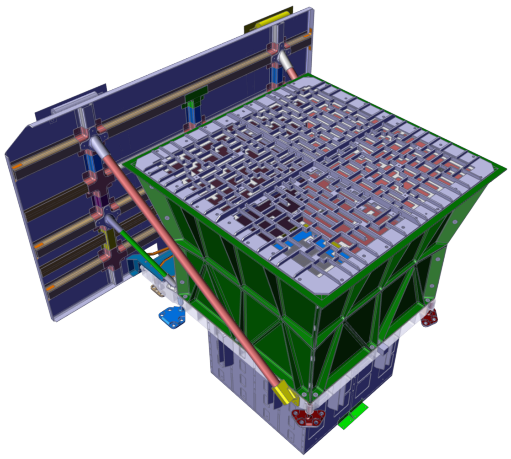

Figure 1.9 – 3D model of the ECLAIRs wide-field camera. (The SVOM collaboration)

Function[7] (PSF) of 52 arcmin (FWHM). As previously demonstrated with INTEGRAL/ISGRI (Lebrun et al., 2003) and Swift/BAT (Barthelmy et al., 2005), coded-mask aperture instruments can achieve a very efficient sky coverage in the hard X-ray domain. Fig. 1.9 shows a model of the instrument.

Thanks to its large effective area ($\approx 400\,\mathrm{cm}^2$ between 10 and 70 keV) and fast response[8], ECLAIRs is predicted to detect ≈ 60 GRBs per year and several other galactic and extra-galactic transient and persistent sources. Furthermore, the 4 keV threshold will enable the study of low-energy phenomena such as X-ray flashes which are still little explored. For 90 % of the sources at detection limit, the localization accuracy will be < 12 arcmin.

1.2.2.2 GRM

The *Gamma-Ray Monitor* (GRM), developed by IHEP Beijing, is a wide-field soft γ-ray detector, which, with its 15 keV − 5 MeV energy range, will operate alongside ECLAIRs to study the prompt emission of GRBs, as well as investigate other phenomena such as Terrestrial Gamma-ray Flashes. The GRM is depicted in Fig. 1.10.

The GRM is divided into three *Gamma-Ray Detectors* (GRDs), each one

[7]The *Point Spread Function* (PSF) is the response of an optical system to a point-like source.

[8]There are two trigger modes: *count rate trigger*, i.e. excess counts on the focal plane over timescales of 10 ms − 20 s; *image trigger*, i.e. excess counts on stacked images over timescales of 20 s − 20 min.

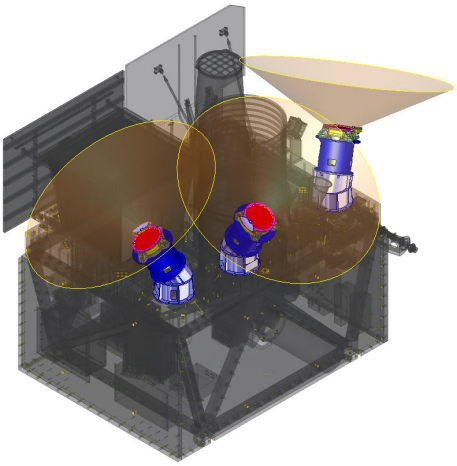

Figure 1.10 – 3D model of the Gamma-Ray Monitor on board the SVOM satellite. The field of view of each module is highlighted. (The SVOM collaboration)

composed of a NaI(Tl) scintillating crystal, its photomultiplier and readout electronics as well as a plastic scintillator on top to distinguish between incoming electrons and γ-rays. Each module is capable of $< 16\,\mu s$ time resolution, along with $> 167\,cm^2$ effective area and 16 % energy resolution at 60 keV. Each GRD has a $\pm 60°$ field of view with respect to its symmetry axis, the three being deployed so that they overlap in correspondence with ECLAIRs for trigger enhancement purposes.

The GRM is also equipped with a *Charged Particle Monitor* to detect entries into the *South Atlantic Anomaly* (§ 1.2.3.1).

1.2.2.3 MXT

The *Micro-channel X-ray Telescope* (MXT) is a narrow-field-of-view instrument ($57\,arcmin \times 57\,arcmin$) operating in the $0.2 - 10\,keV$ range, with an effective area of $23\,cm^2$ at 1 keV. It will perform X-ray observations of the afterglows as well as improve the source localization by ECLAIRs down to 2 arcmin in $< 10\,min$ for > 90 % of detected GRBs. MXT will also provide spectra with a $\sim 80\,eV$ energy resolution at 1.5 keV, especially important for the general program and for the targets of opportunity. The telescope is visible in Fig. 1.11.

MXT is under the responsibility of CNES, which is also in charge of the main structure of the telescope. The optics, based on the *lobster-eye* design, are

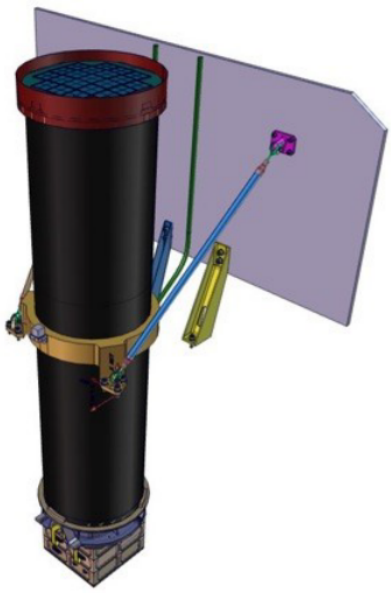

Figure 1.11 – The Micro-channel X-ray Telescope. The tube, the optics, the camera and the radiator are shown. The Data Processing Unit is not present in the image. (CNES)

developed and built by the University of Leicester, using micropore optic plates from Photonis France. CEA Saclay is in charge of the MXT camera, which mounts a pnCCD provided by the Max Planck Institute for Extraterrestrial Physics. The MXT Data Processing Unit is a joint collaboration between CNES and LAL Orsay.

Since it represents the main focus of this manuscript, MXT will be thoroughly described in all its parts in § 1.3.

1.2.2.4 VT

Under responsibility of NAOC Beijing and XIOPM Xian, the *Visible Telescope* (VT) is in charge of the study of GRB afterglows in the visible band, as well as of narrowing the localization already provided by MXT.

The VT (Fig. 1.12) is a 40 cm f/9 Ritchey-Chretien telescope simultaneously observing with a $400 - 650$ nm blue channel and a $650 - 1000$ nm red channel. In both cases, a 2000×2000-CCD is placed at the focal plane. Thanks to its $> 50\,\%$ efficiency at 900 nm, the VT can study GRBs with redshifts up to ≈ 6.5, which will radically increase the amount of available data about high-redshift GRBs, still poorly studied due to the typical delays in the source identification and study, which limit spectral measurements. With a field of

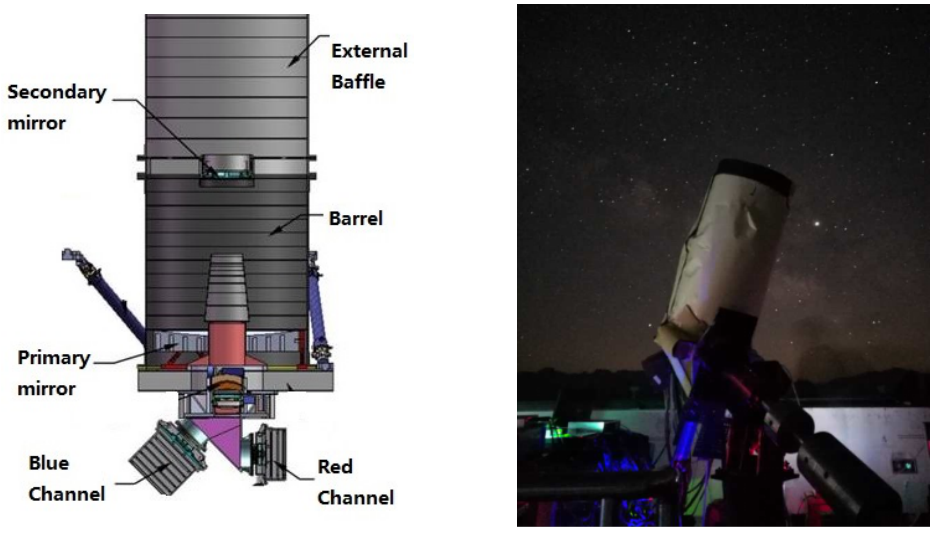

Figure 1.12 – The Visible Telescope. a) Cross-sectional view of the telescope with its main parts indicated. b) Picture of the VT Qualification Model (QM) during tests at the Xinglong observatory, China. (NAOC)

view of $26 \times 26\,\mathrm{arcmin}^2$ and a sensitivity of $m_\mathrm{V} = 23$ after 300 s of exposure, the VT will detect $\approx 80\,\%$ of ECLAIRs GRBs and provide $< 1\,\mathrm{arcsec}$ localization accuracy.

A supplementary feature of the Visible Telescope will be its participation in the guidance and stabilization of the satellite, as its images are fed into the control pipeline, making the instrument effectively acting also as a star tracker (*Fine Guidance System* or FGS).

1.2.2.5 GWAC

The *Ground-based Wide Angle Camera* (GWAC) system is part of the SVOM ground segment. Under the responsibility of NAOC Beijing, its main objective is the study of the GRB prompt emission in the visible band, which, despite being thought to provide an insight on the mechanisms behind jet composition and particle acceleration, is still poorly studied. The GWAC system will operate in three modes to: a) match the ECLAIRs field of view; b) observe targets of opportunity upon request; c) survey even larger patches of the sky by purposely orienting the various cameras. Due to the geographical position of the site, even in the first mode of operation the GWAC will not be able to observe more than $\approx 12\,\%$ of SVOM GRBs from 5 min before to

Figure 1.13 – View of the GWAC site. Some of the mounts are visible, as well as the two 60 cm and the single 30 cm telescopes. (NAOC)

15 min after the trigger. Thanks to its wide field of view, the GWAC will also play an important role in the identification of the visible counterparts of multi-messenger events.

The GWAC system has already been installed at the Xinglong observatory (China). It is composed of 8 mounts, each hosting four 18 cm-cameras, each with a field of view of 150 $\deg^2$ (22 cm-focal length), for a collective coverage of $\approx$ 4800 $\deg^2$. Each camera operates in the $500 - 800$ nm range and is able to achieve a 11 arcsec source localization precision in a 13 s-exposure for magnitudes up to $m_V = 16$. On each mount is another smaller 3.5 cm-camera, useful in case of bright sources, whose field of view coincides with that of the other four cameras. Two supplementary 60 cm- and one 30 cm-telescopes are also deployed to act as cross-checks and follow-ups on the transient sources detected by the rest of the system. Fig. 1.13 shows a view of the GWAC site.

1.2.2.6 GFTs

The *Ground Follow-up Telescopes* (GFTs) will be a network of two robotic ground-based telescopes, under French and Chinese responsibility respectively. The first one, named F-GFT, is located at the National Observatory of San Pedro Mártir in Baja California in Mexico and is a collaboration between French and Mexican institutes (CPPM Marseille, IRAP Toulouse, IRFU/CEA Saclay, LAM Marseille, OHP-OSU Pytheas, UNAM Mexico, UNAM Ensenada). The second one (C-GFT) is located at the Jiling observatory in China, under the responsibility of NAOC Beijing. The two telescopes are visible in Fig. 1.14.

They have similar features in terms of focal length (F-GFT: 1.3 m; C-GFT: 1.2 m) and field of view (F-GFT: 26 arcmin; C-GFT: 21 arcmin), and they will both provide $<$ 1 arcsec localization of SVOM alerts, $\approx$ 20 % of which will

(a) (b)

Figure 1.14 – Views of the two Ground Follow-up Telescopes. a) The French telescope during tests at Astelco Systems (Germany). b) The Chinese telescope at Jilin observatory (China). (The SVOM collaboration)

be immediately observable. The GFTs will operate in the visible and near infrared bands (F-GFT: $400 - 1800$ nm; C-GFT: $400 - 900$ nm), in at least two simultaneous channels to measure the photometric redshift of SVOM GRBs. Thanks to their fast pointing speed and data analysis, the GFTs will keep the delay between the alert reception and the broadcast of the related information as low as 5 min. This will allow fast follow-up by larger facilities (VLT, NTT, ALMA etc.).

1.2.3 Observation strategy

In next sections, a review is given of how the SVOM mission will employ the fast response and wide energy and temporal coverage of its instruments to address the points of its scientific program (§ 1.2.1). After a description of the satellite orbit (§ 1.2.3.1), the allocation of observation time is presented (§ 1.2.3.2), with a particular focus on the sequence of events that follow a GRB trigger.

1.2.3.1 Mission profile

The SVOM satellite is scheduled for launch from Xichang base at the end of 2021, delivered by a Changzheng (Long March) 2C rocket. It will be placed

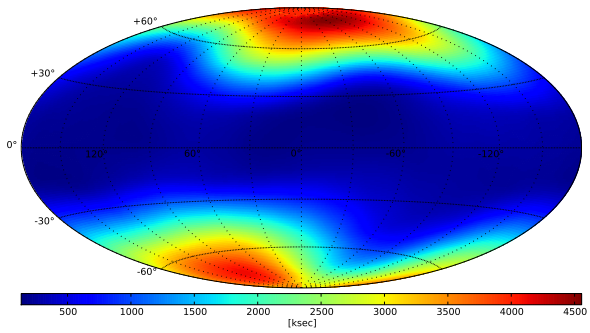

Figure 1.15 – Sky exposure in 10^3 s and galactic coordinates for ECLAIRs after one year of observations. It is clear how the B1 law limits observations of the galactic plane. (The SVOM collaboration)

on a roughly circular orbit, at an altitude of ≈ 625 km and with an inclination of $\approx 30°$ (Low-Earth Orbit or LEO), which will result in an orbital period of ≈ 96 min. The orbit will make the satellite cross the *South Atlantic Anomaly* (SAA, defined in § 4.1.2) several times per day: since each crossing requires a shutdown of the systems, this results in an overall dead time of $\approx 13 - 17\,\%$. More details about the orbit and its environment will be provided in § 4.3.1.

The satellite's attitude (orientation with respect to a inertial reference frame) was optimized to follow a so-called B1 law, by virtue of which:

- the optical axis of SVOM instruments points at about 45° from the anti-solar direction, hence ensuring protection from sunlight, whose effects on the scientific payload range from sensitivity loss to destructive damage;
- bright X-ray sources laying both on the galactic plane and off of it (e.g. X-ray binaries and Scorpius X-1) are kept outside of the field of view of the instruments, thus avoiding the loss of sensitivity towards new sources;
- the most observed regions of the sky are those covered by ground-based 8 m-class telescopes, which are usually located near the Tropics (e.g. Maunea Kea, Cerro Paranal, Roque de lo Muchachos etc.) and whose access to the detected sources is fundamental for fruitful follow-up studies.

Indeed, thanks to the B1 law, all GRBs detected by SVOM will be in the night sky, hence immediately observable by the large facilities mentioned above. This, combined with the fast response to GRB detections, is predicted to enable the determination of the redshift for $\sim 2/3$ of all detected bursts.

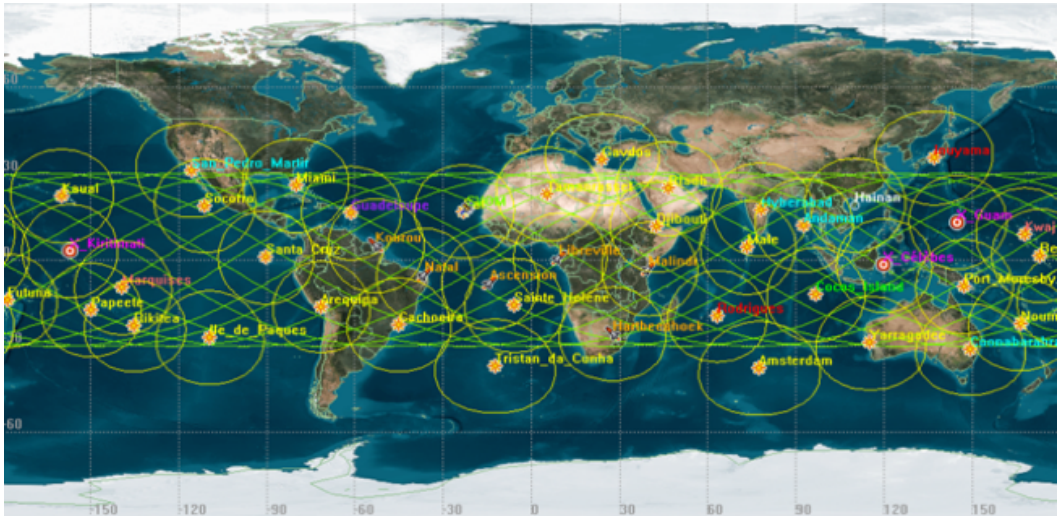

Figure 1.16 – Schematics of the planned distribution of the VHF stations below SVOM's orbit. (The SVOM collaboration)

It should be noted that SVOM's attitude law will cause the Earth to block the field of view of the instruments, reducing their duty cycle to 65 % or even 50 % in case of the narrow-field telescopes.

Commands to the satellite will be uploaded from S-band ground stations in China, South Africa and French Guyana, which will also receive telemetry data. Along with those, X-band stations will be used for science data reception. Finally, a network of 40 VHF antennas distributed in the ±30°-latitude range (Fig. 1.16) will be in place to ensure that GRB alerts are readily transmitted to the ground.

1.2.3.2 Observation time

SVOM's observation time will be split into three parts to resemble its threefold scientific program, i.e. the Core Program, the General Program and the Target of Opportunity Program. The fraction each one will constitute of the total is designed to change after 3 years since launch (extended mission) in order to match the evolving needs of the scientific community during the mission lifetime (Fig. 1.17).

The Core Program of the mission (§ 1.2.1.1) will occupy 25 % of the observation time throughout the mission, with an expected rate of 60-70 GRBs per year.

The General Program (§ 1.2.1.2) will be addressed by observations of targets

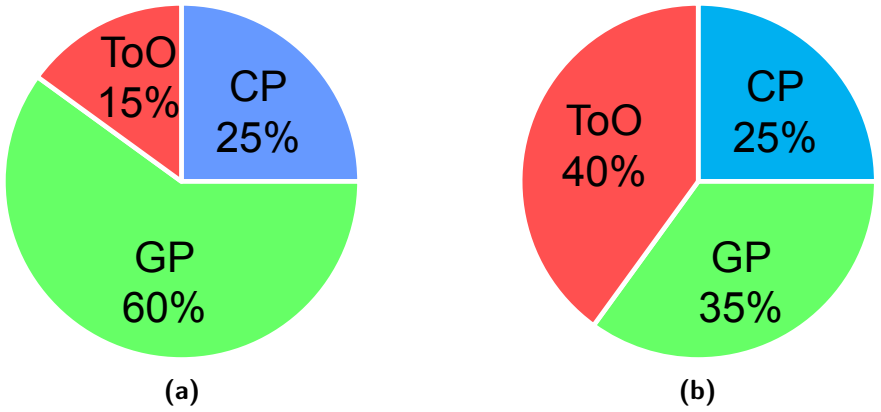

Figure 1.17 – Division of SVOM's observation time according to the nature of the target. a) Nominal mission. b) Program in the extended mission lifetime (starting 3 years after launch).

included in selected proposals, in line with the broader role of SVOM as a space observatory. At the beginning of the mission, as much as 60 % of the observation time can be dedicated to the general program, with this percentage being decreased to 35 % as time passes.

Starting with a single target of opportunity (§ 1.2.1.3) per day (15 % of observation time), this fraction is predicted to increase up to five per day (40 % of observation time) during mission operation, because of the coming on line of new multi-messenger experiments in the near future.

Core program As soon as ECLAIRs triggers on a GRB, possibly thanks to inputs from the GRM, the satellite slews in order to align the two narrow-field instruments (MXT and VT) with ECLAIRs error box around the GRB position. This process is carried out in less than 3 minutes in 80 % of the cases. At the same time, information is sent to the ground via the VHF network in order to begin follow-up observations by ground-based telescopes. When the slew is completed, MXT and VT will observe the afterglow, refine localization and send it down via VHF as well. Once the position uncertainty has been narrowed to sub-arcsec levels or the GRB counterpart has been identified in the catalogs by ground-based follow-ups, very large (8 m-class) telescopes may perform more accurate studies.

Fig. 1.18 summarizes the broadband capabilities of SVOM, which, thanks to the whole array of its instruments, is predicted to be able to study the prompt emission of GRBs over three decades (4 keV – 5 MeV) with ECLAIRs

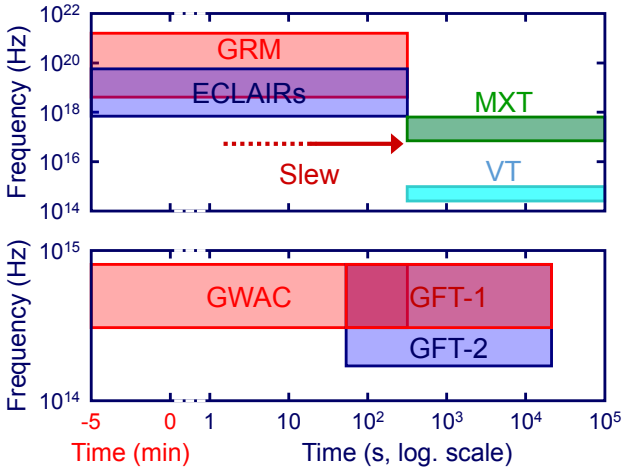

Figure 1.18 – Summary of SVOM's multi-wavelength capabilities. The top plot represents the space-borne instruments, while the ground segment is in the bottom one. The time since the trigger is reported on the x-axis, whereas the y-axis indicates the photon frequency to which each instrument is sensitive. One can see how ECLAIRs, GRM and GWAC are all active even before the trigger. On the contrary, MXT and VT start to play a role after the slew of the satellite is completed.

and GRM, while at the same time providing observations in the optical range with the GWAC in $\approx 12\,\%$ of the cases (§ 1.2.2.5). In addition to that, the on-board narrow-field telescopes MXT and VT together with the fast access to follow-up facilities will allow the accurate study of the afterglow emission, as well as the determination of the redshift, and therefore the distance, for an unprecedented $\sim 2/3$ of the events.

General program The observation of a target within SVOM's General Program requires first the selection of the relative proposal by a dedicated commission according to its scientific merit. Observations are scheduled on a weekly basis and plans are prepared separately for the Chinese and the French payloads. When the mission control uploads the commands, the satellite slews to put the target sources inside the field of view of the concerned instruments and proceeds with the observation for about a single orbit (≈ 45 min of useful time). It is worth noting that at the beginning of the mission, due to the strong sources at low galactic latitudes, only $10\,\%$ of considered targets will be allowed outside of SVOM's attitude law (B1 law), the percentage being increased up to $50\,\%$ during the extended mission.

Table 1.1 – Classification of Targets of Opportunity (ToOs) and their management within SVOM's observation strategy.

ToO	Approval	Delay	Interrupt GRB obs.	Frequency	Duration (orbits)	Tiling
ToO-NOM	ToO scientists	$< 48\,\mathrm{h}$	No	$1 - 5\,\mathrm{day}^{-1}$	1	No
ToO-EX	PIs / ToO sc.	$< 12\,\mathrm{h}$	Yes	$1\,\mathrm{month}^{-1}$	14	No
ToO-MM	PIs / ToO sc.	$< 12\,\mathrm{h}$	Yes	$1\,\mathrm{month}^{-1}$	$7 - 14$	Yes

Target of opportunity program SVOM will distinguish three classes of Targets of Opportunity (ToOs): *ToO-NOM* are the nominal ToOs sent from the ground for follow-up observations of transients, e.g. GRB revisits, flares from known sources etc.; *ToO-EX* include exceptional events which require fast follow-ups; *ToO-MM* are exceptional ToOs arising from multi-messenger alerts (e.g. gravitational wave detection), usually characterized by larger error boxes which normally cannot be observed all at once by SVOM instruments and therefore require a *tiling strategy*, in which the interesting area is progressively scanned in search for the desired source. How the different classes of ToOs are managed within the scope of the observation strategy is summarized in Tab. 1.1.

1.2.4 Unique features and contributions

It is worth spending just a few more words underlining some of SVOM's unique features, what its contributions will be in the framework of GRB studies and how it will compare to previous missions, most notably the Niel Gherels Swift Observatory (Gehrels et al., 2004), which is its direct inspiration.

Thanks to ECLAIRs' 4 keV low-energy threshold, SVOM will be more sensitive than previous missions to X-ray-rich bursts. In addition to that, ECLAIRs' ability to trigger thanks to stacks of images accumulated over long periods of time (up to $\approx 20\,\mathrm{min}$) will enhance the detection capabilities of long-duration GRBs (§ 1.2.2.1).

By sacrificing useful observation time because of the B1 attitude law drastically limiting its duty cycle (§ 1.2.3.1), SVOM will ensure immediate availability

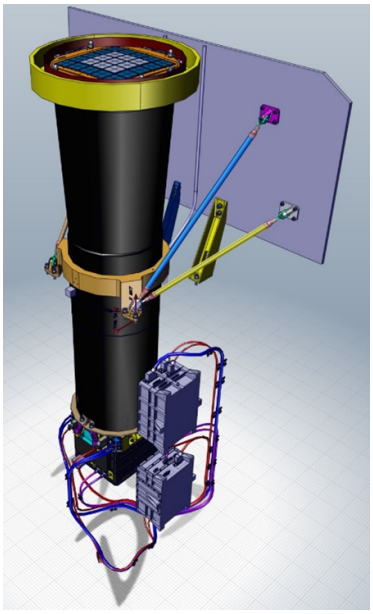

Figure 1.19 – The Micro-channel X-ray Telescope. (CNES)

of the detected GRBs to follow-up studies by on-ground observatories, which will enable very rapid and accurate measurements, as well as the determination of the redshift for $\sim 2/3$ of detected GRBs.

All the above features, along with the broadband coverage from MeV to infrared, will improve the successful detection of high-redshift bursts, a key component in the attempt at answering the questions outlined in § 1.1.3.

Finally, one must not forget that SVOM will operate under the strong mass, volume and power constraints due to the limited size of its scientific payload, which alone sets it apart from missions such as Swift.

1.3 The Micro-channel X-ray Telescope

The following sections contain further details about the *Micro-channel X-ray Telescope* (MXT), already outlined in § 1.2.2.3. After reviewing its specifications and function within the SVOM mission (§ 1.3.1), its three main subsystems will be dealt with: the telescope itself (§ 1.3.2), the camera (§ 1.3.3) and finally its processing unit (§ 1.3.4).

1.3.1 Overview and scientific requirements

MXT is the narrow field-of-view telescope on board SVOM operating in the soft X-ray band ($0.2 - 10\,\mathrm{keV}$). It is under the overall responsibility of CNES and is being developed in collaboration by CNES, CEA Saclay and LAL Orsay, as well as the University of Leicester and the Max Planck Institute for Extraterrestrial Physics.

Its purpose with respect to the core scientific program of the mission (§ 1.2.1.1) is twofold.

As already described in § 1.2.3.2, once the satellite has aligned the the field of view of MXT (and VT) to the error box of the source location provided by ECLAIRs (a process which takes less than 3 min in 80 % of the cases), MXT must quickly refine the source localization and then send it to the VT for sub-image extraction around the position estimated by MXT. The information is finally relayed to the ground in order to initiate follow-up observations by optical telescopes. This is achieved in $< 10\,\mathrm{min}$ to an accuracy better than 2 arcmin for $> 90\,\%$ of GRBs.

MXT is also responsible for recording the photometric (light curve) and spectral evolution of the GRB during the afterglow phase. This will be carried out with a time resolution of 100 ms and down to a sensitivity of $2 \times 10^{-12}\,\mathrm{erg\,cm^{-2}\,s^{-1}} \approx 75\,\mu\mathrm{Crab}$ in 10 ks. The expected energy resolution is 80 eV at 1.5 keV, where the efficiency of the telescope is the highest.

In addition to those functions, MXT will be operated for studies of other transient and non-transient X-ray sources within the scope of the general (§ 1.2.1.2) and target-of-opportunity (§ 1.2.1.3) programs of the mission.

Tab. 1.2 summarizes the features, capabilities and requirements of MXT, some of which will be expanded upon in the next sections and in the rest of the manuscript as well. A feature is worth commenting on, i.e. the limited mass, volume and power budget: those are a consequence of the small dimensions of the SVOM payload and are critical drivers of the design of the whole instrument, from the optics and the main structure to the camera and the operation of the detector. For comparison, the X-Ray Telescope on board Swift (Burrows et al., 2004), which has many similarities to MXT concerning the purpose within the scope of its own mission, has a mass of $\approx 200\,\mathrm{kg}$ and a focal length of 3.5 m.

Table 1.2 – Scientific and technical characteristics of the Micro-channel X-ray Telescope.

Energy range	$0.2 - 10\,\mathrm{keV}$
Detector type	pnCCD
Energy resolution	$80\,\mathrm{eV}$ at $1.5\,\mathrm{keV}$
Optical system	lobster-eye optics
Field of View	$57\,\mathrm{arcmin} \times 57\,\mathrm{arcmin}$
Angular resolution	$6.5\,\mathrm{arcmin}$
Effective area	$23\,\mathrm{cm}^2$ at $1\,\mathrm{keV}$ (central spot), $57\,\mathrm{cm}^2$ at $1\,\mathrm{keV}$ (central spot and cross-arms)
Focal length	$1.15\,\mathrm{m}$
Source location accuracy	$<2\,\mathrm{arcmin}$ in $< 10\,\mathrm{min}$ for $> 90\,\%$ of GRBs
Sensitivity (5σ)	$10^{-10}\,\mathrm{erg\,cm^{-2}\,s^{-1}} \approx 5\,\mathrm{mCrab}$ in $10\,\mathrm{s}$ $2 \times 10^{-12}\,\mathrm{erg\,cm^{-2}\,s^{-1}} \approx 75\,\mu\mathrm{Crab}$ in $10\,\mathrm{ks}$
Time resolution	$100\,\mathrm{ms}$
Total mass	$35\,\mathrm{kg}$
Electrical power	$50\,\mathrm{W}$

1.3.2 Telescope

The telescope is the portion of MXT tasked with

- providing structural integrity to the whole system;
- focusing the X-rays onto the detector;
- ensuring optical alignment between the optics and the detector;
- limiting the amount of undesired light and particles entering the instrument;
- dissipating the heat generated by the cooling system of the focal plane.

In the next sections, an outline is presented of the subsystems making up the telescope: the optics (§ 1.3.2.1), the main mechanical structure (§ 1.3.2.2) and the radiator (§ 1.3.2.3).

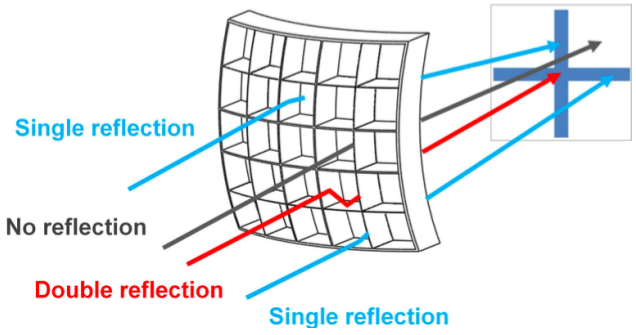

(a)

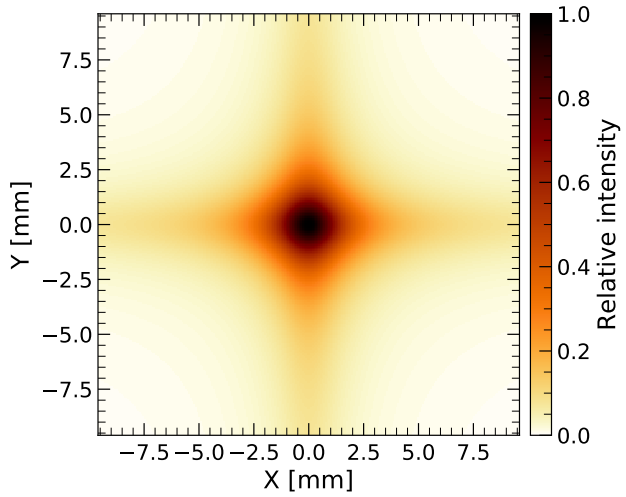

(b)

Figure 1.20 – Working principle of lobster-eye optics. a) Photons undergoing two reflections are focused on the central spot, whereas those reflecting only once end up in the cross-arms. Photons passing straight through make up the diffused background. From `http://ep.bao.ac.cn/?page_id=13`. b) Simulated Point Spread Function of MXT at 1.49 keV.

1.3.2.1 Optics

As a telescope, MXT requires an optical system to focus light on its detector. However, unlike UV, optical and IR bands, in the X-ray domain light collection by usual mirrors and lenses is not possible. Instead, the principle of *grazing reflection* may be used, by virtue of which X-ray photons reflect on surfaces by very small angles thanks to the < 1 refractive index of the latter at high energies. Grazing reflection optics following the design introduced by Wolter (1952) focus X-ray via two reflections on two coaxial surfaces of revolution, such as a hyperboloid and a paraboloid (Wolter I design). Nested mirrors are required to increase the collecting area due to the small geometrical cross-section of the system. Space astronomy experiments such as Swift/XRT, XMM and Chandra mount optical systems of this kind. However, Wolter optics may have very long focal lengths (3.5 m, 7.5 m and 9 m respectively for the three cited telescopes) and their nested mirrors make them bulky. As a consequence of its very limited mass and volume budgets, MXT cannot take advantage of this technology. Instead, it relies on *Mirco-Pore Optics* (MPOs) arranged in a *lobster-eye* configuration.

First developed by Angel (1979), this optical system is based, as the name suggests, on the eyes of lobsters and is made out of a grid of square channels with sides measuring a few tens of micrometers, hence the name Mirco-Pore Optics. Its Point Spread Function (PSF) is composed of a bright central spot, four orthogonal arms and a diffused background: X-ray photons undergoing two grazing reflections on two orthogonal inner walls of the channels are focused in the central spot; photons reflecting only once make up the arms, according to whether the reflection was on the horizontal or vertical wall; photons passing straight through without any reflection are not focused and end up in the diffused background signal (Fig. 1.20).

Lobster-eye optics are divided into modules (MPOs). When arranged on a spherical surface of radius R, they identify a spherical focal plane of radius $R/2$ (Fig. 1.21). Thanks to the lack of a proper optical axis, lobster-eye optics are not affected by spherical aberration or vignetting, respectively arising from the focal length and the collecting area being functions of the distance from the optical axis.

MXT mounts a set of 25 MPOs, designed by the University of Leicester and built by Photonis France. The MPOs are arranged as in Fig. 1.22. Each one

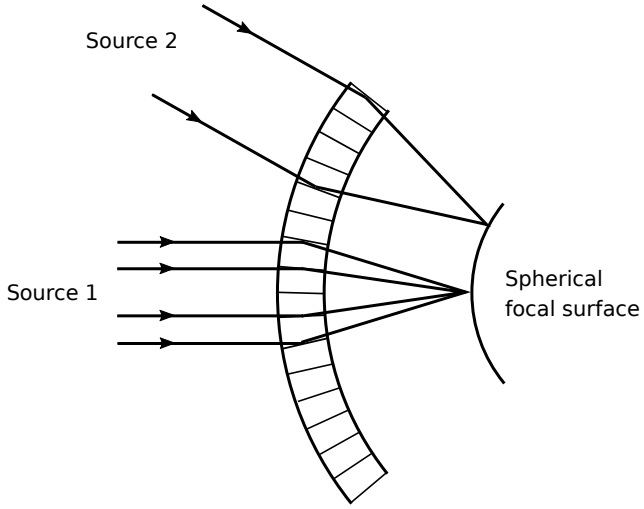

Figure 1.21 – Spherical focal plane identified by lobster-eye optics.

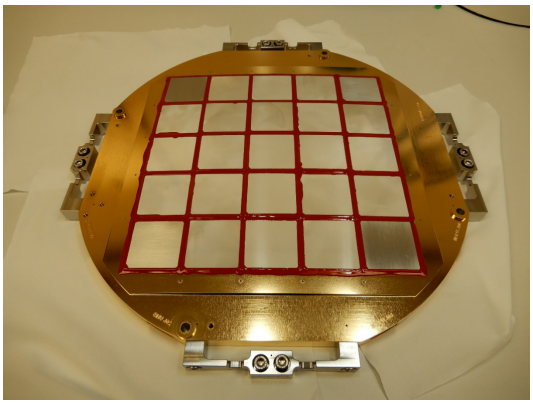

Figure 1.22 – The MXT Micro-Pore Optics, Qualification Model assembly. (University of Leicester)

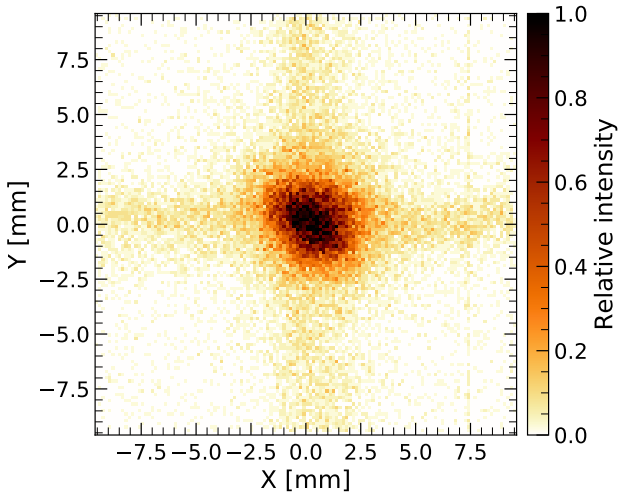

Figure 1.23 – Measured Point-Spread Function of the Qualification Model (QM) of the MXT Micro-Pore Optics at 1.49 keV.

measures 40 mm × 40 mm and presents $\sim 6 \times 10^5$ squared pores with a 40 µm side and a 52 µm pitch. The inner walls of the pores are coated with 25 nm Ir layer to enhance reflectivity. The MPOs are glued to an aluminum frame whose external surface is a 2300 mm-radius sphere. This radius R defines the focal length F of the system, which is then $F = R/2 = 1150$ mm. The thickness of the MPOs varies with the angle from the optical axis, so that the central modules have 2.4 mm-long channels, whereas the outermost ones measure only 1.2 mm. This introduces a slight vignetting, thus enhancing the flux received by the central spot (hence the on-axis effective area) and decreasing that at the arms. The outer surface of the optical system is covered in a 70 nm Al film to block optical light entering the telescope. On the inner side, 36 magnets arranged in a grid make up an electron diverter which decreases the electrons flux at the focal plane the other end of the telescope, thus reducing the background. The optical assembly has a combined mass of 1.8 kg.

Fig. 1.23 shows the measured PSF of the Qualification Model (QM) of the MXT optics. Differences with the theoretical shape arise from imperfections and misalignment issues, especially at a channel-level (fabrication defects). Fig. 1.24 presents the effective area as a function of photon energy, the variations being caused by the different efficiency of grazing incidence with energy, as well as the quantum efficiency of the detector at the focal plane.

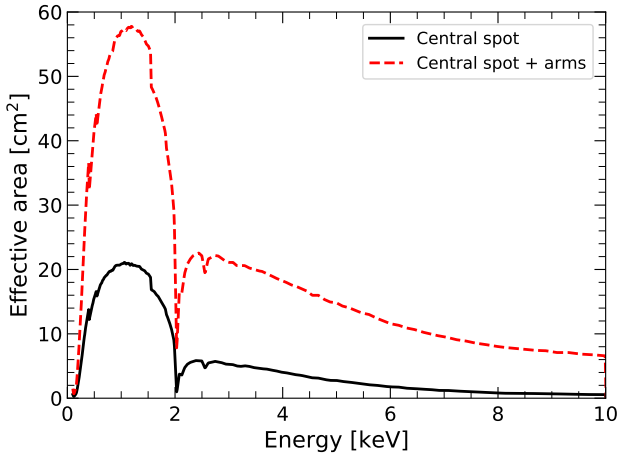

Figure 1.24 – Simulated effective area of the MXT optics. The two curves correspond to the case in which only the central spot is considered or the spot along with the cross-arms.

1.3.2.2 Structure

The structure must ensure the stability of the telescope under the thermo-mechanical stresses it will be subject to during its in-orbit operation, while at the same time being lightweight enough to comply with the mission requirements in terms of mass. The telescope tube has also the pivotal role of maintaining the optical alignment and focal length throughout the lifetime of the instrument.

To achieve this objectives, a design based on a Carbon Fiber Reinforced Polymer (CFRP) has been developed, combined with titanium reinforcements in the form of three legs fixed at 120° between two rings at the optics and the camera. A small baffle at the top protects from stray light from the Sun (Fig. 1.25). This subsystem is under the direction of CNES.

1.3.2.3 Radiator

Due to the lack of atmosphere, the only way left to dissipate the heat produced by the cooling system of the focal plane inside the camera (§ 1.3.3.2) is through radiation. The radiator has therefore the key role of contributing to the definition of the operating temperature of the MXT detector, a task that is made difficult by the limited surface available ($\sim 0.45\,\mathrm{m}^2$) and the highly variable environment of the Low Earth Orbit (Fig. 1.26).

Under the responsibility of CNES, the baseline design of the radiator

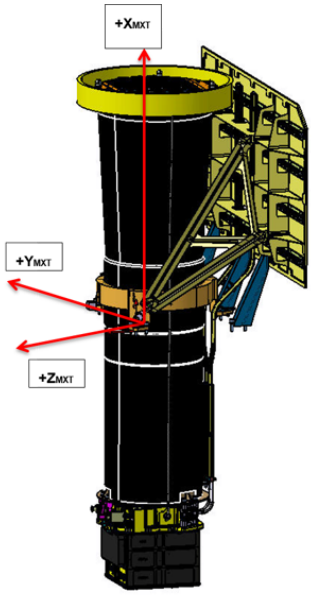

Figure 1.25 – View of the structure of the MXT telescope, along with the coordinate system defined for the instrument. The optics are visible at the top end of the telescope tube and the camera at the bottom. (CNES)

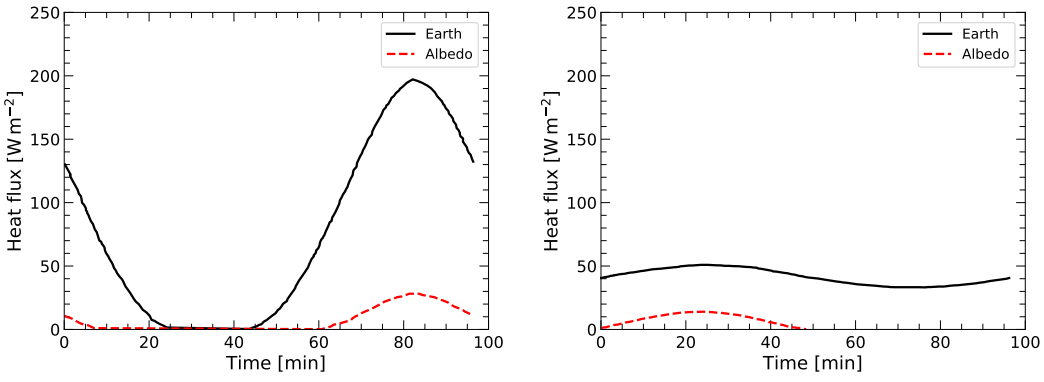

Figure 1.26 – Heat flux at the MXT radiator during a single orbit (passive contributions only). a) Hot-case scenario. b) Cold-case scenario. In both cases, *Earth* refers to the infrared emission by the Earth, whereas *Albedo* is the solar power reflected by the planet.

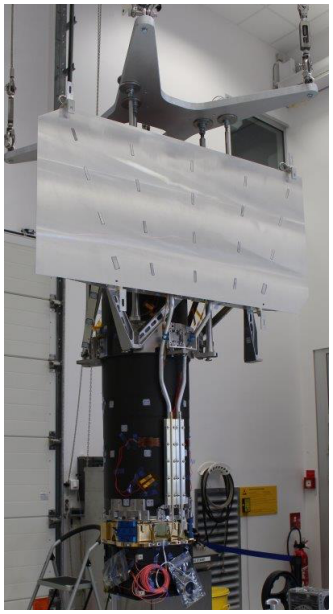

Figure 1.27 – The MXT radiator mounted on the Structural and Thermal Model (STM) of the telescope. The double thermal link to the camera (bottom of the tube) via its heat pipe is visible along the side of the telescope. (CNES)

consists of a six-fold *Constant Conductance Heat Pipe* (CCHP) with propylene fluid, two of the heat pipes being connect directly to those coming out of the camera. Fig. 1.27 shows a view of the Structural and Thermal Model (STM) of the system.

1.3.3 Camera

The MXT camera (MCAM) is the portion of MXT housing the focal plane of the telescope and is therefore in charge of the detection of X-ray photons. The MCAM shall

- detect photons in the $0.2 - 10\,\mathrm{keV}$ range;
- protect the focal plane from space radiation during SAA crossings;
- protect the focal plane from background particles and X-ray photons during observations;
- protect the detector from the light from bright UV and visible sources in the field of view during observations;

Table 1.3 – Scientific and technical requirements of the MXT camera.

Energy range	$0.2 - 10\,\mathrm{keV}$
Energy resolution	$\sim 80\,\mathrm{eV}$ at $1.5\,\mathrm{keV}$ $+100\,\%$ after 3 years $+250\,\%$ after 5 years
Quantum efficiency	$> 95\,\%$ at $1\,\mathrm{keV}$
Focal plane temperature	$-65\,^{\circ}\mathrm{C}$ ($-80\,^{\circ}\mathrm{C}$ to $-60\,^{\circ}\mathrm{C}$)
Non-X-ray background	$\sim 0.02\,\mathrm{cts\,cm^{-2}\,s^{-1}}$ in the MXT band
Total mass	$9\,\mathrm{kg}$
Electrical power	$10\,\mathrm{W}$
Volume	to be included in a $300\,\mathrm{mm}$ tube

- ensure the energy calibration of the detector throughout the mission lifetime;
- ensure the correct operation of the detector, from both a thermal and electrical point of view;
- preprocess scientific data (selection of hit pixels);
- monitor critical systems;
- output scientific and housekeeping data;
- provide the mechanical interface with the rest of the telescope.

CEA Saclay has the overall charge of the camera design and integration of its various assemblies, whereas the Max Planck Institute for Extraterrestrial Physics (MPE) is the provider of the detector and its ASIC.

The MCAM is shown in Fig. 1.28. In the SVOM spacecraft, it is placed below the tube of the telescope, inside the *Platform Interface Module* (PIM) cavity, along with the other scientific instrumentation. Tab. 1.3 summarizes its scientific and technical requirements, which will be further addressed in § 1.4.

The following sections shall describe the subsystems constituting the MXT camera: the *Mechanical Support Assembly* or MSA (§ 1.3.3.1), the *Focal Plane Assembly* or FPA (§ 1.3.3.2), the *Calibration Wheel Assembly* or CWA (§ 1.3.3.3) and the *Front-End Electronics Assembly* or FEE (§ 1.3.3.4). The discussion will remain on general terms at this stage, while more details, such

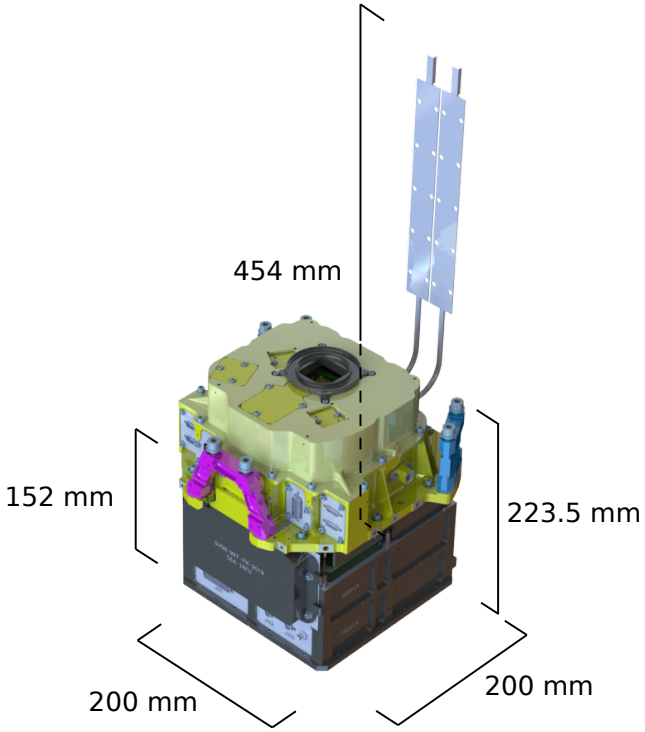

Figure 1.28 – View of the MXT camera with its principal dimensions.

as the working principles of the detector and its electronics, will be given in future chapters.

1.3.3.1 Mechanical Support Assembly

The *Mechanical Support Assembly* or MSA is the mechanical reference of the camera. It is made out of a monolithic aluminum structure (divided into two halves for integration purposes) housing the Focal Plane Assembly (FPA) and the Calibration Wheel Assembly (CWA). It also includes three titanium supports on which the tube of the telescope is mounted (only two of them are visible in Fig. 1.28, in magenta and blue). Those elements ensure the general optical alignment of the instrument. Part of the MSA is also the set of connectors for the electrical interface of both the Thermo-Electric Coolers (§ 1.3.3.2) on the FPA and the calibration wheel to the MXT Data Processing Unit (§ 1.3.4). To resist the stresses during launch, the MSA was designed to have its eigenmodes at frequencies above 350 Hz.

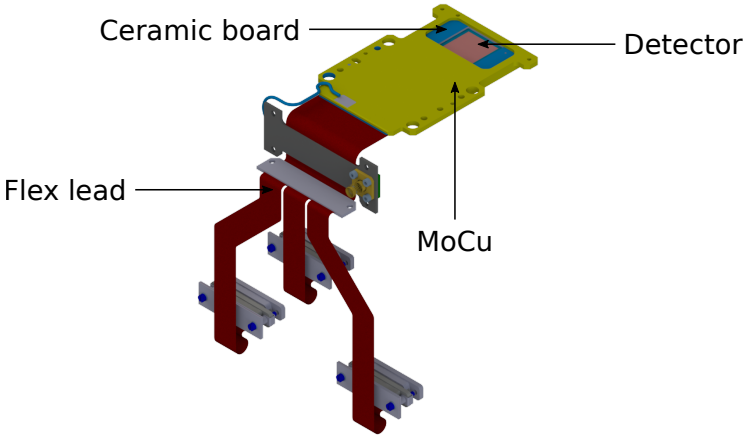

Figure 1.29 – View of the MXT Detector Assembly. The three connectors at the end of the flex lead are the interface to the FEE.

1.3.3.2 Focal Plane Assembly

The *Focal Plane Assembly* or FPA is made out of three sub-units: the Detector Assembly, the active cooling system and the shielding.

Detector Assembly The *Detector Assembly* or DA (Fig. 1.29) consists of the light sensitive device (pnCCD) and its two *Application-Specific Integrated Circuits* (ASICs), named CAMEX, constituting its cold readout electronics. Both the pnCCD and the CAMEX will be described in great detail in § 2.4. The silicon die constituting the pnCCD measures 25 mm × 39 mm and is connected to the ASICs by 25 µm Al wire bonding. Both the pnCCD and the CAMEX ASIC are provided by the MPE.

Detector and ASIC are mounted on a ceramic (alumina, Al_2O_3) board, on which all the bias voltages for the pnCCD and the ASICs and all connections for communication are routed; passive components for bias filtering and impedance adaptation are present as well. The ceramic board is glued to a copper-molybdenum (MoCu) substrate, whose thermal expansion coefficient is close to the one of alumina ($7.5 - 6.7 \times 10^{-6}\,K^{-1}$). The purpose of the substrate is to provide the mechanical interface and enable the proper functioning of the detector (§ 2.4.1.1).

Finally, a flex lead is bonded to one extremity of the ceramic board through 25 µm gold wires. The cable consists of a rigid Printed Circuit Board (PCB) from which three sub-cables allow the connection to the three boards of the FEE (§ 1.3.3.4). The cable carrying the CCD high voltage generated by the

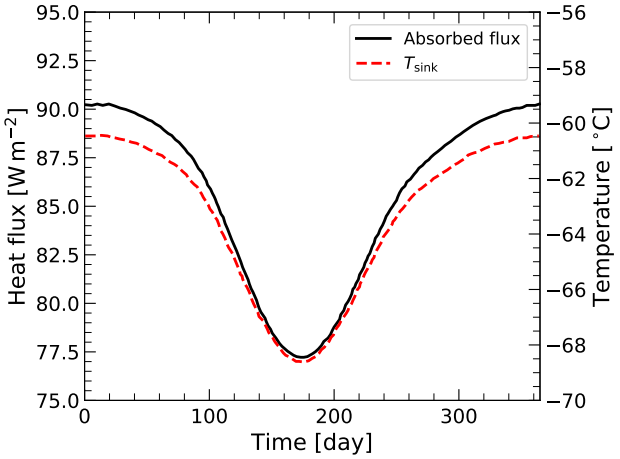

Figure 1.30 – Average orbital heat flux and sink temperature at the MXT radiator as a function of the day of the year for a cold-case scenario (passive contributions only). If no external power is applied, the temperature varies between −60 °C and −68 °C with an average of −65 °C, meaning that in order to operate the MXT detector always below −60 °C it is necessary to employ an active cooling system.

Table 1.4 – Average heat flux and sink temperature at the MXT radiator (passive contributions only). To operate the MXT detector at temperatures $\lesssim -60\,°C$ even in the hot-case scenario, an active cooling system is required.

	Heat flux W m^{-2}	Temperature °C
Hot case	83	−64.9
Cold case	45	−93.4

FEE is connected to the flex PCB.

It is important to point out that the DA is a monolithic structure, therefore portions such as the MoCu substrate and the ceramic carrier board cannot be separated after integration.

Active cooling In order for the MXT detector to achieve the best possible performances, it requires an operating temperature $\lesssim -60\,°C$ (Meidinger et al., 2006a). Furthermore, thermal stability is necessary during each observation by the telescope. To counteract the strong radiative environment of the Low Earth Orbit (Fig. 1.30 and Tab. 1.4), an active cooling system is required. The MXT focal plane relies on three *Thermo-Electric Coolers* or TEC (Peltier-effect

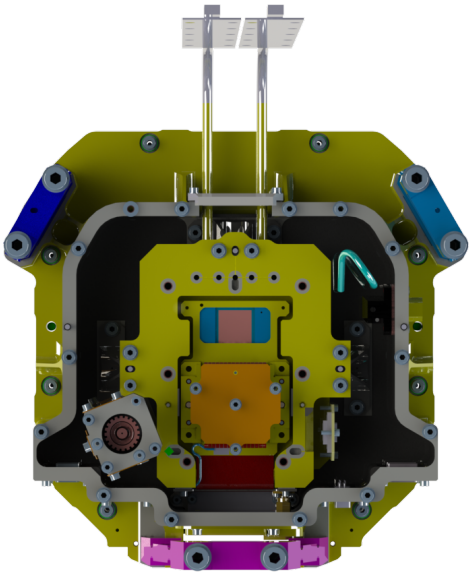

Figure 1.31 – Cross-sectional view of the MXT camera. The copper plate of the TEC system is visible (orange) on the MoCu of the DA, surrounded by the bottom half of the aluminum shielding. The heat pipe can be seen exiting the shielding and going across the outer camera case at the top of the picture.

modules). The TECs are glued between two copper plates, the cold side placed in contact with the Detector Assembly and the warm side in contact with the shielding (Fig. 1.31). The cold interface of the TEC is equipped with main and redundant PT1000 temperature probes for the thermal regulation, while a heat pipe thermally connects the shielding to the MXT radiator (§ 1.3.2.3) to remove the heat. The heat pipe is composed of two 6 mm-diameter *Constant Conductance Heat Pipes* (CCHP) with propylene fluid, linked to the MXT radiator. The system is expected to keep the detector around −65 °C with < 1 °C accuracy during observations. The goal is to have a single temperature throughout the mission. However, due to the large heat flux variations, especially those occurring during satellite slews, the resulting operating point cannot be easily calculated beforehand. On the contrary, a range can be identified between −80 °C and −60 °C.

Shielding As anticipated in § 1.2.3.1 and as will be thoroughly discussed in § 4, the orbit of the SVOM satellite will cross the South Atlantic Anomaly (SAA) several times per day, thus exposing the MXT detector to harmful space

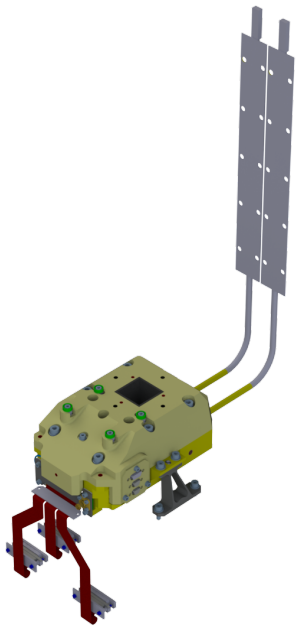

Figure 1.32 – View of the MXT Focal Plane Assembly. The shielding and the heat pipes are visible, along with the triple connector between DA and FEE.

radiation with potential consequences on its performances. To alleviate the consequences, a shielding is in place around the DA and the TEC assembly (Fig. 1.32), with the double purpose of protecting them from the particles trapped in the SAA and decreasing the amount of secondary X-rays originated by cosmic protons as a consequence of their interaction with the surrounding mechanical structure. The shielding, divided into an upper and lower half for ease of integration, has a thickness of 30 mm of aluminum, which ensures compliance with the mass and volume requirements and also a low level of activation and secondary neutron generation thanks to its low mass number. Such a solution produces however an undesired Al fluorescence line at 1.5 keV, i.e. in the region of highest sensitivity of the telescope (§ 1.24). In order to mitigate the issue and also further reduce the amount of secondary particles, the interior of the shielding is covered with metallic layers made of (from the farthest from the detector to the closest one) copper (10 µm), nickel (2 µm) and gold (2 µm), which collectively transmit only 10^{-24} 1.5 keV photons. While the copper and nickel layers are primarily present because they are required by the coating process employed by the subcontractor, gold also grants low emissivity, necessary for the thermal performances of the camera, especially if one takes

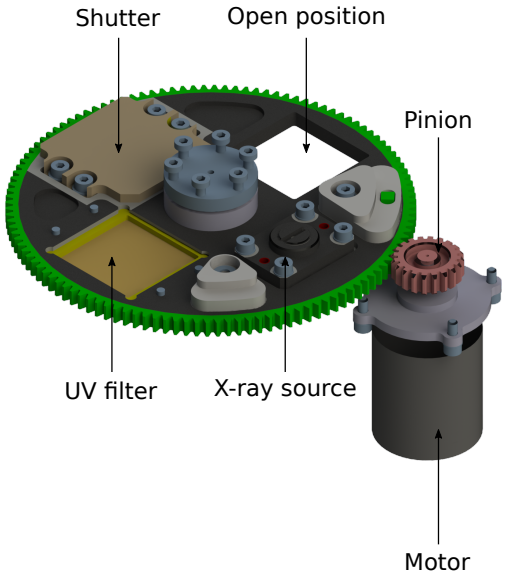

Figure 1.33 – MXT calibration wheel and its motor.

into account that the shielding temperature may get as high as $-30\,°C$, very warm when compared to the required $< 60\,°C$ at which the detector should be operated. Thermal considerations indeed forced to abandon the adoption of a conventional graded-Z shielding configuration, which might have attained a comparable level of background suppression at the expense of having the detector directly surrounded by a high-emissivity black carbon layer.

1.3.3.3 Calibration Wheel Assembly

To account for different in-orbit operating scenarios, the camera is equipped with a calibration wheel. To be compliant with the volume and mass availability, the chosen design relies on a 126 mm aluminum wheel, moved by a pinion-and-cog mechanism (Fig. 1.33). It is worth noting that the wheel motor being placed outside the focal plane shielding allows an efficient protection of the detector to both radiation and potential electromagnetic perturbations.

Four positions are available on the wheel:

1. open position for direct sky observations;

2. UV and visible light filter made of a 160 nm layer of polyimide ($C_{22}H_{10}N_2O_5$) for a $>$ 1000-fold attenuation (up to $\sim 10^{-6}$) of the flux in the $40-100$ nm range (Fig. 1.34), which prevents detector saturation due to brilliant stars in the field of view of the instrument, while at the same time limiting the

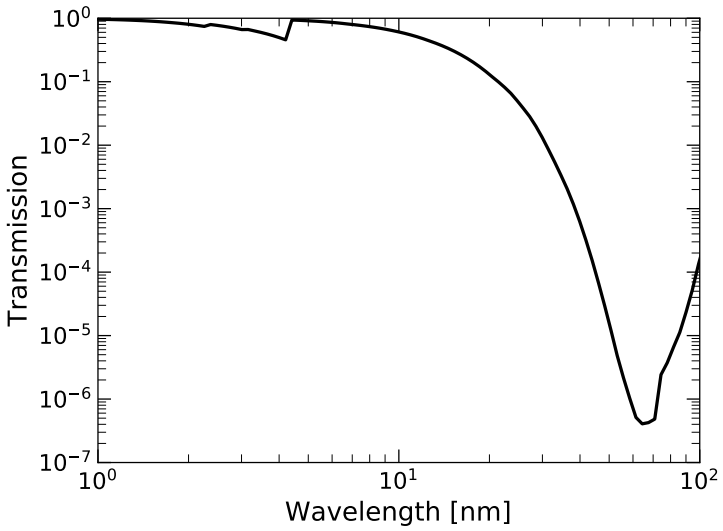

Figure 1.34 – Transmission of the wheel UV filter as a function of wavelength. Data available at `http://henke.lbl.gov/optical_constants/filter2.html`.

impact on X-ray detection ($> 94\,\%$ transmission for energies $> 1\,\mathrm{keV}$);

3. 10 mm-thick copper shutter to protect the focal plane from space particles during SAA crossings and ensure a 30 mm-Al equivalent thickness over the whole solid angle in combination with the FPA shielding;

4. radioactive ^{55}Fe source to be operated for calibration purposes in order to periodically assess the detector performances and monitor their evolution during the mission lifetime (to be addressed in § 5).

1.3.3.4 Front-end electronics Assembly

The Front-End Electronics (FEE) is composed of three printed-circuit boards, each placed inside an aluminum module. The three modules are mechanically independent to facilitate tests and integration. Two additional panels (top and bottom) complete the case. The space between the boards was optimized after the thermal analysis of the assembly to maximize both radiative and conductive heat transfer, always in compliance with mass and volume availability. Fig. 1.35 shows a schematic drawing of the FEE assembly.

The features and the operation of each FEE board will be addressed in § 2.4.3.4, after more details about the working principles of the detector and a description of the acquisition chain are given.

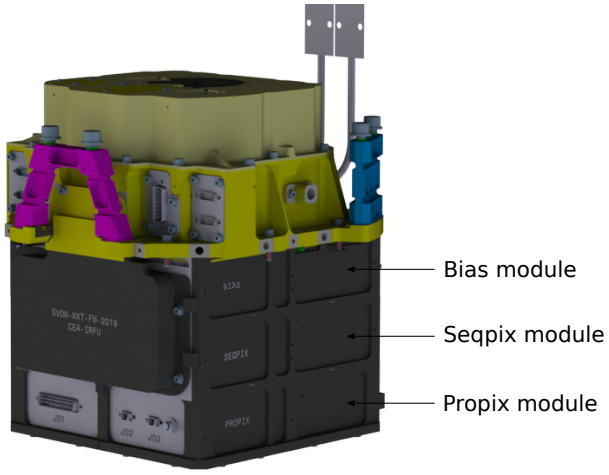

Figure 1.35 – Schematic drawing of the Front-End Electronics in the MXT camera.

1.3.4 Data Processing Unit

The *MXT Data Processing Unit* (MDPU) is the on-board computer which drives the instrument and acts as the interface between MXT and the rest of the satellite. It is composed of a hardware and a software component, whose development is under the direction of CNES (hardware development and control) and LAL (scientific software, i.e. source localization and data telemetry).

The MDPU is designed to

- interface with the *Payload Data Processing Unit* (PDPU), the on-board computer of the satellite;
- distribute power to MXT's subsystems, thanks to its connection to the satellite power distribution box;
- manage the switching on and off of secondary power supplies; drive the MCAM calibration wheel;
- measure and actively control the temperature of the various components of MXT (MCAM and optics);
- interface with the MXT FEE, to direct acquisition sequences, and receive housekeeping and scientific data;
- run the scientific software, including the source localization algorithms.

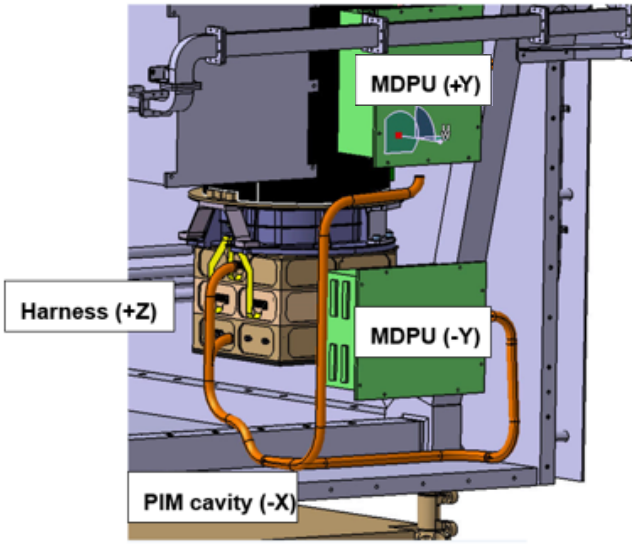

Figure 1.36 – Schematic drawing of the MXT Data Processing Unit next to the MXT camera in the spacecraft.

Two MDPU boxes are present on the spacecraft to ensure cold redundancy. They are placed inside the *Platform Interface Module* (PIM) cavity, next to the MXT camera (Fig. 1.36).

1.4 Science-related issues for the camera design

The camera has the crucial tasks of operating the detector in compliance with the scientific requirements of MXT within the larger scope of the SVOM mission. In particular, it must ensure that the specifications both the energy resolution and the low-level threshold are respected throughout the lifetime of the instrument, since those play a pivotal role in defining the capabilities of the instrument to quickly localize transients and continuously study variable sources (§ 1.3.1).

In the next section, an overview is given of how the scientific specifications translate into a set of constraints to the design and operation of the camera, in particular as far as the detector is concerned. The chapter will finally end with a summary of the main questions originating from the comparison between the requirements and the design, which will guide the rest of the manuscript.

1.4.1 Remarks on the requirements

Several times so far it has been hinted that the Low Earth Orbit poses some challenges to the SVOM mission in general and to the MXT experiment in particular, mainly in the form of high thermal variability and harsh radiation environment of the South Atlantic Anomaly, both of which drove the design of the Focal Plane Assembly of the MXT camera (§ 1.3.3.2).

As later chapters will highlight, temperature control is a crucial parameter on which performances such as energy resolution and low-level threshold (to be formally defined in § 2.3.3) depend. In order to comply with the scientific requirements of § 1.3.1, temperature must be kept stable (especially important for long-duration observations) and below $-60\,°C$, a challenging feat given the variability of the environment and the limited power budget available to the cooling system.

In addition to that, interactions between space radiation and the MXT detector (to be thoroughly addressed in § 4) are expected to degrade the performances of the latter as the mission goes on, which makes it more difficult to fulfill the scientific requirements of the instrument, hence the necessity to protect the detector though a permanent shield around the focal plane as well as a movable shutter. Radiation effects are also temperature dependent, a fact that stresses once again the importance of thermal regulation.

For all those reasons, the worsening of the response of the MXT detector is taken into account in the specifications: starting from the requirement of a 80 eV energy resolution at 1.5 keV, it can be tolerated to experience a +100 % degradation (i.e. 160 eV) after 3 years in orbit and a +250 % degradation (i.e. 280 eV) after 5 years[9]. However, due to the necessity of fast localizing transient sources, whose emission is usually more intense at lower energies in the X-ray band (e.g. the power-law spectra of GRBs), the low-level threshold of the detector should not exceed 200 eV throughout the mission operation.

1.4.2 Questions

Assessing the compliance of the system with the scientific requirements is the main theme of this manuscript. The following chapters shall expand on

[9] Although no requirement is specified, the degradation at higher energies is expected to be less severe than at 1.5 keV.

the theory behind the science-related design and operational issues described above, as well as investigate them through simulations and experiments.

Here are summarized some of the main points that will be discussed in the rest of this manuscript.

- What are the working principles of the detection chain and how are they affected by operational and environmental parameters? § 2
- How are the performances of the detector defined? § 2
- What will the performances of the MXT detector be at the beginning of the mission? How strongly are they affected in practice by operational parameters such as temperature and voltages? § 3
- How much space radiation is the MXT detector going to be exposed to during the mission lifetime? How much will that affect its response? How will the performances evolve? Will the detector comply with the end-of-life requirements? § 4
- How precisely can the response of the detector be evaluated and the degradation be compensated for during in-orbit operation, especially without affecting the schedule of the scientific program? § 5

Chapter 2

The MXT detector

This chapter will lay down the basis for the understanding of the physics and the working principles of the MXT detector, around which this whole thesis is centered. It will also define some quantities which are necessary to measure the performances of the detector and which will guide the investigation throughout the manuscript.

The introduction of the physics of semiconductors (§ 2.1), i.e. the materials the detector is made out of, will be followed by the description of Charge-Coupled Devices or CCDs (§ 2.2), the class of devices the MXT detector is a part of. The topic of X-ray spectroscopy with CCDs will be addressed next (§ 2.3) and the chapter will end with a description of all the components and operations involved in the full acquisition chain of MXT (§ 2.4).

It is worth pointing out that § 2.1 to § 2.3 essentially contain a review of well-known concepts found in literature, with the exception of the model described in § 2.3.2.3 which is completely original. On the other hand, § 2.4 arises from an effort to summarize published papers of various subsystems and internal documents of the MXT collaboration (e.g. reports, meeting notes, discussions etc.), effectively acting as the only complete documentation of the detector that is available at the time of writing.

2.1 Semiconductor physics

In this section, a review is presented of the physics of semiconductors, the class of materials making up the MXT detector. Although there exist many types of semiconductors, the scope of the discussion will be limited to silicon,

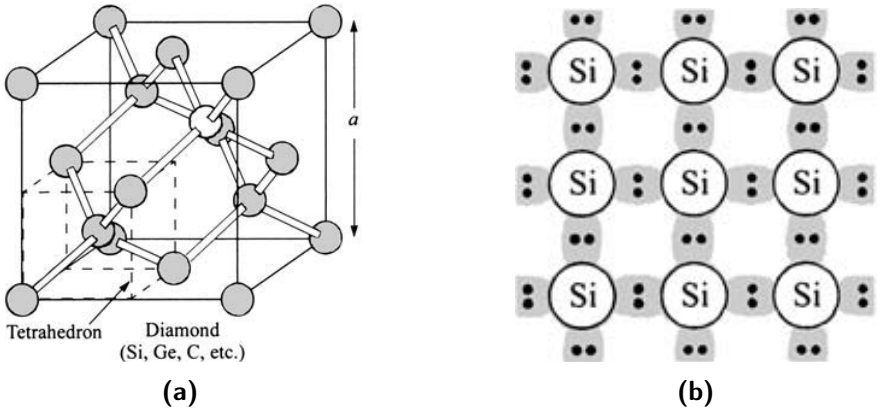

Figure 2.1 – Crystal structure of silicon. a) Three-dimensional representation. b) Two-dimensional representation. Adapted from Sze & Ng (2006)

which is the most commonly used one in modern technology, in addition to being the one actually used in the fabrication of the device under study.

After the definition of the general properties of semiconductors (§ 2.1.1), the physics behind the generation and recombination of charge carriers will be laid out (§ 2.1.2), finishing with a review of the most important structures that make up the MXT detector (§ 2.1.3).

2.1.1 Introduction to semiconductors

Here an overview is provided of basic semiconductor physics, along with a list of all the properties defining the operation of the devices described later in the manuscript. Starting from fundamental properties such as crystalline structure (§ 2.1.1.1) and energy bands (§ 2.1.1.2), a review of the properties of charge carriers (§ 2.1.1.3 and § 2.1.1.4) follows, ending with the definition of intrinsic semiconductors (§ 2.1.1.5).

2.1.1.1 Crystalline structure

Most common semiconductors present a *crystalline structure*, i.e. its atoms are arranged in a periodic configuration, with the repetition of an elementary structure called the *primitive cell*. The period a is called *lattice constant*[1]. In silicon, each atom can be considered at the center of a *tetrahedron*, whose vertexes are made of its nearest neighbors. They all share their own four

[1]Lattices in three dimensions generally have three lattice constants, except in case of special shapes such as cubes or hexagons.

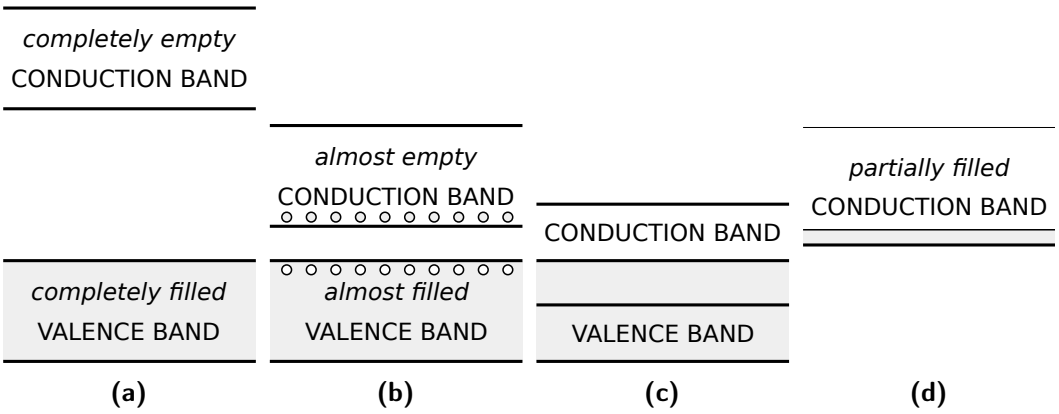

Figure 2.2 – Schematic representation of the energy bands. a) Insulators. b) Semiconductors. c, d) Metals. Adapted from Lutz (2007).

outermost (valence) electrons with each other, thus creating covalent bonds. A schematic view of this arrangement is depicted in Fig. 2.1.

2.1.1.2 Energy bands

Let us consider N atoms, originally very far apart from each other, which are slowly brought together. At the beginning, the electron configuration of each one would be that of an isolated atom. However, as their separation decreases, orbitals would start to interact and, since each one is N-fold degenerate, they would start to split into N closely separated levels due to Pauli's exclusion principle, eventually forming *energy bands* if $N \to +\infty$ ($N \sim 10^{20}$ in a solid). By solving the Schrödinger equation, one can show (Sze & Ng, 2006) that actually two bands form, called *valence* and *conduction* band, lying respectively below and above a region of forbidden energy levels, the *band gap* E_G, which is therefore the difference between the energy of the bottom of the conduction band E_C and that of the top of the valence band E_V.

$$E_\mathrm{G} = E_\mathrm{C} - E_\mathrm{V}. \tag{2.1}$$

Electrons in the valence band remain tied to their respective atoms in covalent bonds, whereas in the conduction band they behave almost as free particles (§ 2.1.1.3), and thus can contribute to conduction.

The extent of the band gap is what differentiates insulators, metals and semiconductors (Fig. 2.2): in an insulator, the gap is so large ($E_\mathrm{G} \approx 5\,\mathrm{eV}$) that electrons can almost never be excited into the conduction band, hence those

materials lack conductive properties; on the other hand, in semiconductors, the separation is small enough ($E_G \approx 1\,eV$) that this excitation can sometimes occur; finally, in metals, either the conduction band is always partially filled or valence and conduction bands overlap. Having $E_G = 1.12\,eV$ under standard temperature and pressure conditions, silicon classifies as a semiconductor.

2.1.1.3 Charge carriers

At $T = 0\,K$, all electrons in a semiconductor are bound in covalent bonds and hence are confined to the valence band. If temperature is above absolute zero, thermal agitation may be sufficient to ionize some of the atoms ($kT \approx 0.0259\,eV$ at $300\,K$), so that some electrons are promoted into the conduction band, where they can move almost as free particles, not being tied to any atoms anymore and thus being available for conduction. The electron's original position in the valence band, called *hole*, may be filled by a neighboring electron still in a covalent bond, which in turn leaves another hole that may be filled by another electron. In this way, while (negative) electrons are free to move in the conduction band, (positive) holes move in the valence band and therefore they both are available for conduction[2]. Conventionally, electron energy is positive when measured from E_C *upwards*, whereas hole energy is positive when measured from E_V *downwards*.

Several things are worth noting:

- the mass of the charge carriers depends on the direction, hence it is a tensor m^* and it is different from the free electron mass;
- the bottom of the conduction band and the top of the valence band can be approximated by quadratic relations

$$E = \frac{p^2}{2m^*}, \tag{2.2}$$

  corresponding to the energy of a free particle, with p being the momentum of the electron/hole;
- the maximum of the valence band lies at zero momentum, unlike the conduction band, which also has multiple minima. A semiconductor

[2]Although technically holes are just lack of electrons, which are the ones moving even in the valence band, they can be modeled as particles with mass, momentum and energy different from those of an electron.

sharing this characteristic (e.g silicon) is called *indirect semiconductor*, whereas a material in which the momentum of both the top of the valence and the bottom of the conduction bands is zero is known as a *direct semiconductor* (e.g. GaAs). This peculiarity is important as both energy and momentum must be conserved during electron-hole generation, as well as during its reverse process *recombination*: due to the mismatch in momentum, generation and recombination are more difficult in indirect semiconductors. This has two consequences.

- On average, more energy is needed to promote an electron from the valence to the conduction band than simply E_{G}: in silicon, where $E_{\mathrm{G}} = 1.12\,\mathrm{eV}$, the electron-hole pair creation energy is $\epsilon_{\mathrm{eh}} = 3.63\,\mathrm{eV}$. This surplus goes into making a band-to-band transition without change in momentum (thus requiring more energy than E_{G}) or into supplying the momentum difference.
- Carrier generation and recombination depend on impurities or crystal defects having energy and momentum states within the band gap, making those processes far more likely.

2.1.1.4 Carrier concentration

Being *fermions*, electrons in silicon obey the Fermi-Dirac distribution law:

$$F_n(E) = \frac{1}{1 + e^{(E - E_{\mathrm{F}})/kT}}, \tag{2.3a}$$

where E is the electron energy, k is the Boltzmann constant, T the absolute temperature and E_{F} is the *chemical potential*, also known as the *Fermi level*, which corresponds to the energy for which the probability is 1/2. Since holes are electron vacancies, their distribution law is complementary to eq. (2.3a):

$$F_p(E) = 1 - F_e(E) = \frac{1}{1 + e^{(E_{\mathrm{F}} - E)/kT}}. \tag{2.3b}$$

The charge carrier concentration for electron and holes can then be calculated as

$$n = \int_{E_{\mathrm{C}}}^{+\infty} \mathcal{N}_n(E)\, F_n(E)\, \mathrm{d}E \qquad p = \int_{-\infty}^{E_{\mathrm{V}}} \mathcal{N}_p(E)\, F_p(E)\, \mathrm{d}E, \tag{2.4a}$$

where $\mathcal{N}_{n,p}(E)$ is the *density of states* for electrons in the conduction band and holes in the valence band respectively. If $E_C - E_F \gtrsim 3kT$ and $E_F - E_V \gtrsim 3kT$, which is satisfied for non-degenerate semiconductors (semiconductors with low doping concentrations – see below), eq. (2.3) can be approximated by exponential functions and thus eq. (2.4) can be written as

$$n = N_C e^{-(E_C - E_F)/kT} \qquad p = N_V e^{-(E_F - E_V)/kT}, \tag{2.5}$$

where the *effective density of states* N_C and N_V are defined as

$$N_C = 2\left(\frac{2\pi m_n^* kT}{h^2}\right)^{\frac{3}{2}} \qquad N_V = 2\left(\frac{2\pi m_p^* kT}{h^2}\right)^{\frac{3}{2}}, \tag{2.6}$$

with m_n^* and m_p^* being the electron and hole effective masses. Experimentally, their values are (Jackson & Schröter, 2000)

$$m_n^* = 1.18 m_e \qquad m_p^* = 0.81 m_e, \tag{2.7}$$

$m_e = 9.109\,383\,56 \times 10^{-28}$ g being the free electron mass.

2.1.1.5 Intrinsic semiconductors

In an *intrinsic* semiconductor (i.e. with negligible amount of impurities), in steady state, the concentration of free electrons n and holes p must be the same. This common value is called *intrinsic carrier concentration* n_i, which, thanks to eq. (2.5), can be written as

$$n = p = n_i \tag{2.8a}$$

$$n_i = \sqrt{N_C N_V} e^{-E_G/2kT}, \tag{2.8b}$$

where one recognizes the energy gap E_G.

The Fermi level E_F of an intrinsic semiconductor is called the *intrinsic level* E_i, and, from eq. (2.8a) and eq. (2.5), it can be expressed as

$$E_i \equiv E_F = \frac{E_V + E_C}{2} + \frac{3}{4} kT \log\left(\frac{m_p^*}{m_n^*}\right). \tag{2.9}$$

In intrinsic semiconductors, the Fermi level is near the middle of the band gap.

In general, for any *non-degenerate* semiconductor, i.e. a semiconductor

in which the concentration of impurities is much less than $N_{\mathrm{C,V}}$, in thermal equilibrium, the following relations are defined

$$np = n_{\mathrm{i}}^2 \tag{2.10}$$

$$n = n_{\mathrm{i}} e^{(E_{\mathrm{F}} - E_{\mathrm{i}})/kT} \qquad p = n_{\mathrm{i}} e^{(E_{\mathrm{i}} - E_{\mathrm{F}})/kT}. \tag{2.11}$$

Eq. (2.10) is known as the *mass-action law*. Of course, eq. (2.11) coincides with eq. (2.8a) in case of an intrinsic semiconductor, as $E_{\mathrm{i}} = E_{\mathrm{F}}$.

2.1.2 Generation, recombination and transport

The next two sections shall review the phenomena thanks to which electrons and holes may be exchanged between the energy bands of a semiconductor, known as generation and recombination (§ 2.1.2.1), and move through the lattice itself (§ 2.1.2.2). It must be pointed out that, as far as generation and recombination are concerned, the discussion will be limited to thermal effects, leaving charge production by photons and other particles to other sections (§ 2.3.1 and § 4.2.2.1 respectively).

2.1.2.1 Thermal generation and recombination

At thermal equilibrium, the concentration of electrons and holes fluctuates around an equilibrium value expressed by the mass-action law of eq. (2.10). This is possible because two competing processes are at play, one that lifts electrons from the valence to the conduction band thanks to thermal energy fluctuations (*thermal generation*) and one according to which low-energy electrons from the conduction band occupy vacancies in the valence band (*recombination*). When out of equilibrium, the mass-action law does not hold any more, and therefore one of the two processes takes advantage over the other.

As mentioned in § 2.1.1.3, generation and recombination of charge carriers in indirect semiconductors relies on the presence of impurities and crystal defects providing energy levels in the forbidden energy gap between the top of the valence band and the bottom of the conduction band, as direct transitions between the bands are very unlikely due to the conservation of momentum. Those processes shall now be treated more quantitatively in the framework of the Schockley-Read-Hall statistics (Shockley & Read, 1952; Hall, 1952), with reference to textbooks such as Lutz (2007) and Sze & Ng (2006) for further

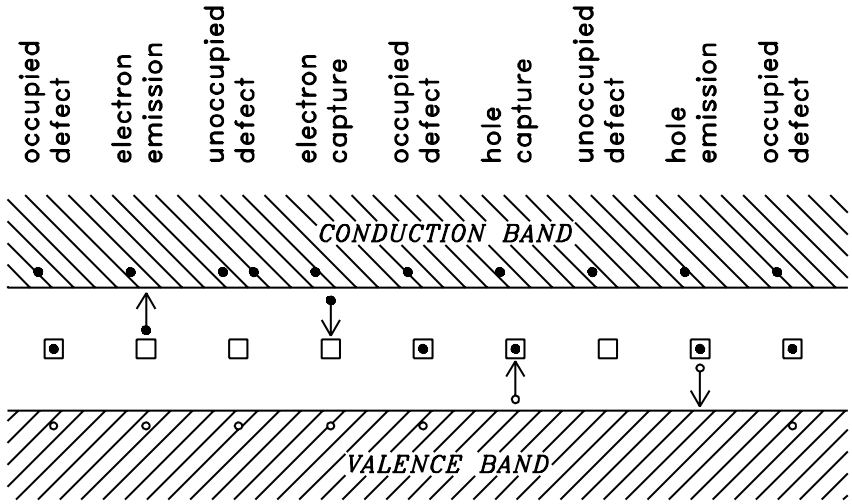

Figure 2.3 – Evolution of a single energy level as it capture and emits electrons and holes. Time goes from left to right in the figure. (Lutz, 2007)

details.

Let us consider for simplicity single energy level defects, i.e. defects that can only assume one of two states at a time (neutral or charged), depending on whether they are empty or occupied by a positive or negative carrier (Fig. 2.3). Defects are labeled as *donors* and *acceptors* according to the same conventions already expressed in § 2.1.3.1. Let N_t be the concentration of those defects.

The concentration of charge carriers is defined by four competing processes, each occurring at a specific rate:

- electron emission

$$R_\mathrm{en} = e_\mathrm{n} N_\mathrm{t} f_t \tag{2.12a}$$

- electron capture

$$R_\mathrm{cn} = c_\mathrm{n} n N_\mathrm{t} \left(1 - f_t\right) \tag{2.12b}$$

- hole emission

$$R_\mathrm{ep} = e_\mathrm{p} N_\mathrm{t} \left(1 - f_t\right) \tag{2.12c}$$

- hole capture

$$R_\mathrm{cp} = c_\mathrm{p} p N_\mathrm{t} f_t \tag{2.12d}$$

where f_t is the probability that a defect of energy level E_t is occupied, n and p are the concentrations of free electrons and holes, e and c are the specific

capture and emission rates respectively (for electrons and holes, according to the subscript).

In thermal equilibrium, emission and capture processes equal each other for electrons and holes separately ($R_{\mathrm{en}} = R_{\mathrm{cn}}$, $R_{\mathrm{ep}} = R_{\mathrm{cp}}$). Moreover, the occupational probability of a defect is given by eq. (2.3a), with $E = E_{\mathrm{t}}$. If one also rewrites n and p according to eq. (2.5), the following relations can be obtained:

$$e_{\mathrm{n}} = c_{\mathrm{n}} N_{\mathrm{C}} e^{-(E_{\mathrm{C}} - E_{\mathrm{t}})/kT} \qquad e_{\mathrm{p}} = c_{\mathrm{p}} N_{\mathrm{V}} e^{-(E_{\mathrm{t}} - E_{\mathrm{V}})/kT}. \tag{2.13}$$

Alternatively, one can rely on eq. (2.11) to arrive to a similar result:

$$e_{\mathrm{n}} = c_{\mathrm{n}} n_{\mathrm{i}} e^{-(E_{\mathrm{i}} - E_{\mathrm{t}})/kT} \qquad e_{\mathrm{p}} = c_{\mathrm{p}} n_{\mathrm{i}} e^{-(E_{\mathrm{i}} - E_{\mathrm{t}})/kT}. \tag{2.14}$$

Customarily, the specific capture rates c_{n} and c_{p} are written in terms of the *capture cross section* σ and the thermal velocity $v_{\mathrm{th}} = \sqrt{\frac{3kT}{m^*}}$ of the charge carriers. With this notation, eq. (2.13) becomes

$$c_{\mathrm{n}} = \sigma_n v_{\mathrm{th},n} \qquad e_{\mathrm{n}} = \sigma_n v_{\mathrm{th},n} N_{\mathrm{C}} e^{-(E_{\mathrm{C}} - E_{\mathrm{t}})/kT} \tag{2.15a}$$

$$c_{\mathrm{p}} = \sigma_p v_{\mathrm{th},p} \qquad e_{\mathrm{p}} = \sigma_p v_{\mathrm{th},p} N_{\mathrm{V}} e^{-(E_{\mathrm{t}} - E_{\mathrm{V}})/kT}. \tag{2.15b}$$

It is important to note that the previous relations do not depend on the Fermi level E_{F} and thus are valid not only in thermal equilibrium, but also in the general case.

Let us now turn to the non-equilibrium case, in which $R_{\mathrm{en}} \neq R_{\mathrm{cn}}$ ($R_{\mathrm{ep}} \neq R_{\mathrm{cp}}$) and f_t is not expressed by eq. (2.3a). One defines the *net electron emission rate* as $R_{\mathrm{n}} = R_{\mathrm{en}} - R_{\mathrm{cn}}$, an equivalent definition holding for holes. The following analysis shall be restricted to the stationary state, in which

$$\frac{\mathrm{d}n_{\mathrm{t}}}{\mathrm{d}t} = R_{\mathrm{cn}} + R_{\mathrm{ep}} - R_{\mathrm{en}} - R_{\mathrm{cp}} = R_{\mathrm{p}} - R_{\mathrm{n}} = 0, \tag{2.16}$$

as the average concentration n_{t} of carriers in the defects must be constant. By equating R_{n} and R_{p}, f_t can be isolated, which eventually leads to

$$R_{\mathrm{n}} = \frac{c_{\mathrm{n}} c_{\mathrm{p}} N_{\mathrm{t}} \left(n_{\mathrm{i}}^2 - np\right)}{c_{\mathrm{n}} \left[n + N_{\mathrm{C}} \exp\left(-\frac{E_{\mathrm{C}} - E_{\mathrm{t}}}{kT}\right)\right] + c_{\mathrm{p}} \left[p + N_{\mathrm{V}} \exp\left(-\frac{E_{\mathrm{t}} - E_{\mathrm{V}}}{kT}\right)\right]}, \tag{2.17}$$

with the expressions for c_n and c_p being contained in eq. (2.15).

The dependence on $(n_\mathrm{i}^2 - np)$, where n_i is the intrinsic carrier concentration given by eq. (2.11), means that the predominance of carrier generation or recombination depends on the concentration of free carriers with respect to their intrinsic values: in case of an excess, recombination is favored, whereas emission dominates when the concentration of free carriers is low.

Eq. (2.17) can be used to calculate an expression for the *leakage current*, i.e. the current arising from the thermal generation of charge carriers in a depleted region, where free carriers are constantly removed thanks to an electric field (§ 2.1.3.2). By assuming a uniform generation rate across the depleted volume of thickness W, the leakage current density (expressed in units of current per surface) is given by

$$J = qWR_\mathrm{n} = \frac{qn_\mathrm{i}W}{\tau_\mathrm{g}}, \tag{2.18}$$

where the *generation lifetime* τ_g has been introduced.

Once charges are created in a depleted region, they are immediately swept aside by the electric field: as a result, the concentration of free carriers is negligible ($n \approx p \approx 0$). With this in mind and by using eq. (2.13) to (2.15), eq. (2.17) becomes

$$R_\mathrm{n} = N_\mathrm{t}\frac{e_\mathrm{n}e_\mathrm{p}}{e_\mathrm{n} + e_\mathrm{p}}, \tag{2.19}$$

and, by inverting eq. (2.18), τ_g writes

$$\tau_\mathrm{g} = \frac{1}{N_\mathrm{t}}\left[\frac{1}{v_{\mathrm{th,n}}\sigma_\mathrm{n}}\exp\left(\frac{E_\mathrm{i} - E_\mathrm{t}}{kT}\right) + \frac{1}{v_{\mathrm{th,p}}\sigma_\mathrm{p}}\exp\left(\frac{E_\mathrm{t} - E_\mathrm{i}}{kT}\right)\right]. \tag{2.20}$$

In order to evaluate eq. (2.20), one supposes that the capture cross section and the thermal velocity of the holes are equal to those of the electrons ($\sigma_n = \sigma_p$, $v_{\mathrm{th},n} = v_{\mathrm{th},p}$), which allows to simplify the expression to

$$\tau_\mathrm{g} = \frac{2}{\sigma N_\mathrm{t}}\sqrt{\frac{m_\mathrm{n}^*}{3kT}}\cosh\left(\frac{E_\mathrm{t} - E_\mathrm{i}}{kT}\right), \tag{2.21}$$

where cosh is the hyperbolic cosine. The minimum of τ_g, which provides the maximum of J, is reached when cosh = 1, i.e. $E_\mathrm{t} = E_\mathrm{i}$. This implies that the defects most efficiently contributing to the leakage current are those whose energy levels are close to the middle of the band gap. This is intuitively correct, as they have to lift electrons from the valence to the conduction band.

By putting eq. (2.21) with cosh = 1 into eq. (2.18) and by explicitly writing the temperature dependence of n_i with the help of eq. (2.8b), one obtains for the leakage current density

$$J = qW\sigma N_\mathrm{t} \left(\frac{18\pi}{h^2}\right)^{\frac{3}{2}} k^2 \left(m_\mathrm{n}^*\right)^{\frac{1}{4}} \left(m_\mathrm{p}^*\right)^{\frac{3}{4}} T^2 e^{-\frac{E_\mathrm{G}}{2kT}}. \tag{2.22}$$

It is finally worth mentioning that in case of a population of defects, energy-distributed according to a density of states $\mathcal{N}_\mathrm{t}$, eq. (2.17) becomes

$$R_\mathrm{n} = \int \frac{c_\mathrm{n} c_\mathrm{p} \mathcal{N}_\mathrm{t} \left(n_\mathrm{i}^2 - np\right)}{c_\mathrm{n}\left[n + N_\mathrm{C} \exp -\frac{E_\mathrm{C}-E}{kT}\right] + c_\mathrm{p}\left[p + N_\mathrm{V} \exp -\frac{E-E_\mathrm{V}}{kT}\right]} \,\mathrm{d}E. \tag{2.23}$$

2.1.2.2 Charge transport

In the following, an outline is given of the two main processes that regulate the transport of electrons and holes in semiconductors in the presence of low electric fields and concentration gradients, i.e. drift and diffusion respectively. Topics such as the behavior under strong electric fields or in the presence of magnetic fields shall be left out of the discussion.

Drift In normal conditions, charge carriers move randomly inside a semiconductor, with a consequently zero mean velocity. When subject to an electric field $\vec{\mathcal{E}}$, charge carriers are accelerated between their random collisions with the crystal lattice and therefore develop a net velocity parallel to the electric field itself, known as *drift velocity* $\vec{v}_\mathrm{drift}$. If $\mathcal{E}$ is weak enough that the velocity change is small compared to the thermal velocity $v_\mathrm{th} = \sqrt{\frac{3kT}{m^*}}$, $\vec{v}_\mathrm{drift}$ is directly proportional to $\vec{\mathcal{E}}$ via the *mobility* μ:

$$\vec{v}_\mathrm{drift,n} = -\mu_\mathrm{n}\vec{\mathcal{E}} \qquad\qquad \vec{v}_\mathrm{drift,p} = \mu_\mathrm{p}\vec{\mathcal{E}}. \tag{2.24}$$

In silicon, $\mu_\mathrm{n} \approx 1500\,\mathrm{cm^2\,V^{-1}\,s^{-1}}$ and $\mu_\mathrm{p} \approx 500\,\mathrm{cm^2\,V^{-1}\,s^{-1}}$.

Diffusion Charge carriers may also move under the influence of concentration gradients. Starting from an non-homogeneous distribution, which may arise from, e.g., charge injection at a junction or non-uniform illumination in case of light-sensitive devices, carriers move randomly in the absence of external fields. Since it is more likely that carriers move from high-concentration regions to

low-concentration regions than the reverse, differences are smoothed out until uniformity is reached. The flux $\vec{\mathcal{F}}$ of this diffusion process is described by Fick's law, from which the *diffusion current density* can be derived:

$$\vec{J}_{\mathrm{diff,n}} = -q\vec{\mathcal{F}} = qD_{\mathrm{n}}\vec{\nabla}n \tag{2.25a}$$

$$\vec{J}_{\mathrm{diff,p}} = q\vec{\mathcal{F}} = -qD_{\mathrm{p}}\vec{\nabla}p. \tag{2.25b}$$

The diffusion constant $D_{\mathrm{n,p}}$ is related to mobility through Einstein's relation

$$D_{\mathrm{n,p}} = \frac{kT}{q}\mu_{\mathrm{n,p}}. \tag{2.26}$$

2.1.3 Basic semiconductor structures

In § 2.1.1.5, intrinsic semiconductors were described. In practice, they are almost never used in any application due to the difficulty of obtaining a sufficiently high-purity material. On the contrary, it is more useful to purposely add specific impurities during crystal growth or later on selected regions. This procedure called *doping* has the result of altering the properties of a semiconductor. Materials which have undergone different doping processes, may then be put together in *junctions*, in order to take advantage of their joint properties.

The following sections shall examine first the general properties of a doped semiconductor (§ 2.1.3.1) and then the two structures at the basis of every future discussion about detectors: the *pn*-junction (§ 2.1.3.2) and the MOS capacitor (§ 2.1.3.3).

2.1.3.1 Doped semiconductors

In *doped* or *extrinsic* semiconductors, impurities (*doping*) are purposely added to break the electron-hole equality of eq. (2.8a), resulting in a modification of the electrical properties of the material.

Let us consider a tetravalent semiconductor such as silicon or germanium, in which an atom of the lattice has been switched for a pentavalent atom, such as phosphorus, antimony or arsenic. As shown in Fig. 2.4a, four of the electrons of the impurity would be in covalent bonds with the surrounding silicon atoms. The fifth electron however would be available for ionization, having an energy level E_{D} just below E_{C} ($E_{\mathrm{C}} - E_{\mathrm{D}} \approx 0.05\,\mathrm{eV}$, Fig. 2.4b): at room temperature,

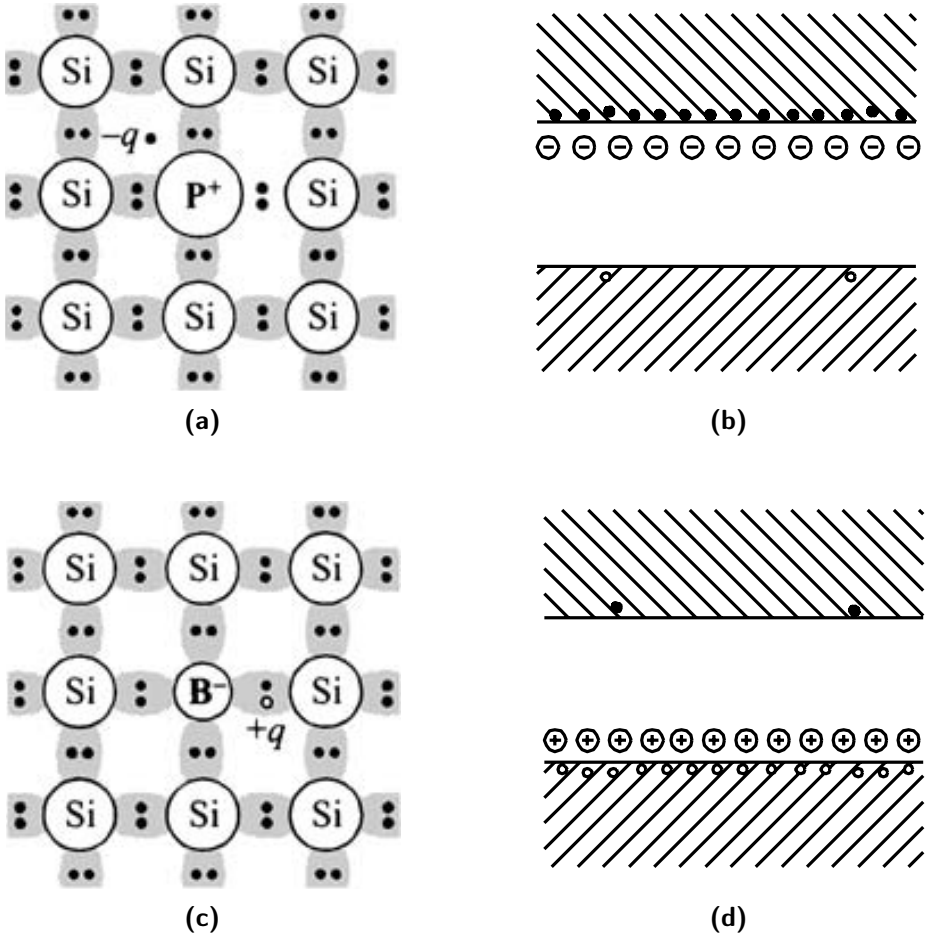

Figure 2.4 – Doped silicon. a) Two-dimensional bond structure of n-type silicon with a phosphorus impurity. b) Energy band structure of n-type silicon. c) Two-dimensional bond structure of p-type silicon with a boron impurity. d) Energy band structure of p-type silicon. Adapted from Lutz (2007)

essentially all such impurities would be ionized, thus increasing the number of free electrons, which are in this case known as *majority carriers*, whereas holes are *minority carriers*. Due to their property of giving away electrons, this kind of impurities are defined *donors*, and more generally one says that an impurity has a *donor level* if it is neutral when occupied by an electron and positive when empty. A donor level is ionized when it is empty. A semiconductor doped with donors is a *n-type semiconductor*.

Let us now consider a trivalent impurity, e.g. boron, indium or gallium (Fig. 2.4c). Unlike the previous case, here all three valence electrons of the dopant are in covalent bonds and an extra empty state is left. Such an impurity is called *acceptor* and it has *acceptor levels* if they are neutral when empty and negative when occupied by an electron, in which case they are considered to be ionized. Acceptor levels are generally very close to the valence band ($E_\mathrm{A} - E_\mathrm{V} \approx 0.05\,\mathrm{eV}$, Fig. 2.4d) and therefore can be easily filled by electrons from the valence band, leaving behind holes, which become the majority carriers, while electrons are the minority carriers. A semiconductor doped with acceptors is called a *p-type semiconductor*.

It is worth noting that in case of both non-degenerate n and p semiconductors, the concentration of impurities is nonetheless far below that of silicon ($10^{13} - 10^{20}\,\mathrm{cm}^{-3}$ against $10^{22}\,\mathrm{cm}^{-3}$). A + or − sign can be added to n and p depending on whether the semiconductor is heavily or lightly doped.

In extrinsic semiconductors, the mass-action law of eq. (2.10) still holds, along with the conservation of electrical charge

$$n + N_\mathrm{A}^- = p + N_\mathrm{D}^+, \tag{2.27}$$

where N_A^- and N_D^+ are the concentration of ionized acceptors and donors respectively. Within a wide range of temperatures ($100 - 500\,\mathrm{K}$, Sze & Ng (2006)), all of the dopants are ionized, so that $N_\mathrm{A}^- \approx N_\mathrm{A}$ and $N_\mathrm{D}^+ \approx N_\mathrm{D}$. For a n-type semiconductor, for which acceptors are negligible, one then obtains from eq. (2.5), (2.11), (2.10) and (2.27)

$$n \approx N_\mathrm{D} \qquad\qquad p \approx \frac{n_\mathrm{i}^2}{N_\mathrm{D}} \tag{2.28a}$$

$$E_\mathrm{F} - E_\mathrm{i} = kT \log\left(\frac{N_\mathrm{D}}{n_\mathrm{i}}\right) \qquad\qquad E_\mathrm{C} - E_\mathrm{F} = kT \log\left(\frac{N_\mathrm{C}}{N_\mathrm{D}}\right). \tag{2.28b}$$

Equivalently for a p-type semiconductor

$$p \approx N_\mathrm{A} \qquad n \approx \frac{n_\mathrm{i}^2}{N_\mathrm{A}} \tag{2.29a}$$

$$E_\mathrm{i} - E_\mathrm{F} = kT \log\left(\frac{N_\mathrm{A}}{n_\mathrm{i}}\right) \qquad E_\mathrm{F} - E_\mathrm{V} = kT \log\left(\frac{N_\mathrm{V}}{N_\mathrm{A}}\right). \tag{2.29b}$$

2.1.3.2 The pn-junction

Let us consider a semiconductor where the concentration of dopants changes abruptly from acceptors of concentration N_A to donors of concentration N_D. Such a structure is called (abrupt) *pn*-junction. If $N_\mathrm{A} \gg N_\mathrm{D}$ or $N_\mathrm{D} \gg N_\mathrm{A}$, one talks about one-sided abrupt p^+n- or n^+p-junction respectively.

In thermal equilibrium, because of the difference in carrier concentrations, electrons flow from the n to the p side, while holes do the reverse. As more carriers leave their respective side of the junction, more impurities are ionized, so that the n side features an increasing positive charge, while negative charges accumulate in p side. As a consequence, a voltage difference, called *built-in potential* V_bi, is established across the junction contrasting the diffusion of electrons and holes, and a region almost empty of free carriers (*depletion* or *space-charge* region) is formed at the boundary between the n and p side.

Let us consider a simplified model like the one shown in Fig. 2.5, in which the charge density is constant on each side of the depletion region. Due to the conservation of electrical charge

$$W_\mathrm{D,p} N_\mathrm{A} = W_\mathrm{D,n} N_\mathrm{D}, \tag{2.30}$$

with $-W_\mathrm{D,p}$ and $W_\mathrm{D,n}$ being the limits of the depletion region on the p and n side of the junction respectively. By successively integrating Poisson's equation in one dimension, one obtains the following expression for the built-in voltage (Leo, 1994)

$$V_\mathrm{bi} = \frac{qN_\mathrm{A}}{2\varepsilon} W_\mathrm{D,p}^2 + \frac{qN_\mathrm{D}}{2\varepsilon} W_\mathrm{D,n}^2, \tag{2.31}$$

where ε is the permittivity in silicon. By use of eq. (2.30) and eq. (2.31), the

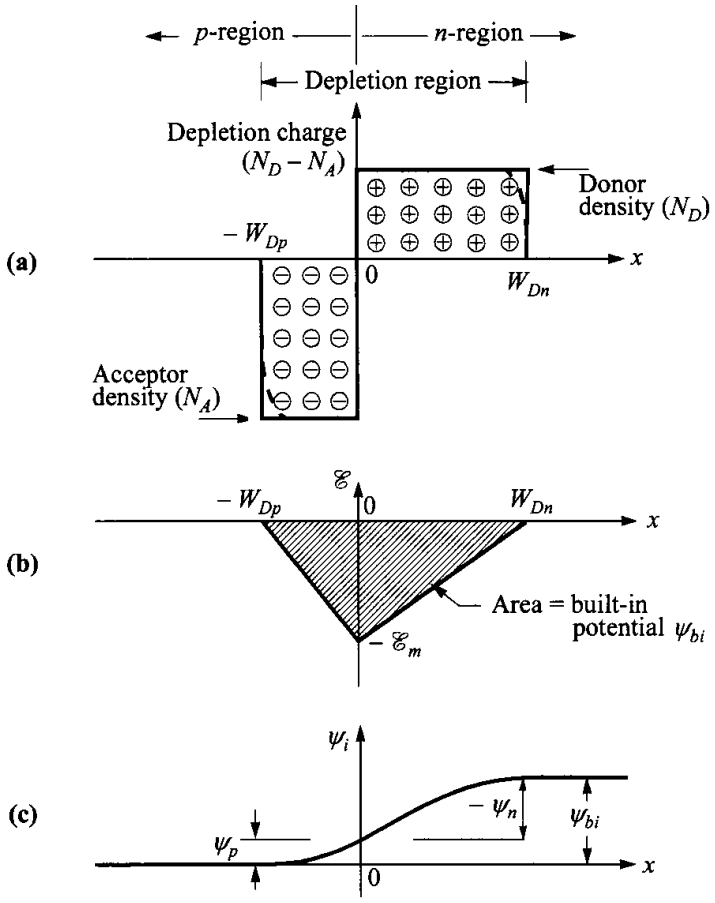

Figure 2.5 – Abrupt *pn*-junction. a) Charge distribution. b) Electric field. c) Electric potential. Adapted from Sze & Ng (2006)

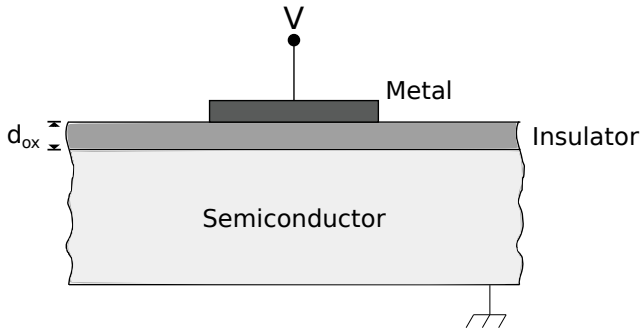

Figure 2.6 – Schematic representation of a Metal-Insulator-Semiconductor capacitor.

full width W_{D} of the depletion region writes

$$W_{\mathrm{D}} = W_{\mathrm{D,n}} + W_{\mathrm{D,p}} = \sqrt{\frac{2\varepsilon V_{\mathrm{bi}}}{q}\frac{N_{\mathrm{A}} + N_{\mathrm{D}}}{N_{\mathrm{A}} N_{\mathrm{D}}}}. \tag{2.32}$$

If an external voltage V is applied to the junction, then $V_{\mathrm{bi}} \longrightarrow V_{\mathrm{bi}} \pm V$, the $+$ corresponding to *reverse bias* (p-side at lower potential than n-side) and $-$ to *forward bias* (opposite voltage configuration). In particular, since in a reverse-biased junction usually one applies $V \gg V_{\mathrm{bi}}$, eq. (2.32) becomes

$$W_{\mathrm{D}} = \sqrt{\frac{2\varepsilon V}{q}\frac{N_{\mathrm{A}} + N_{\mathrm{D}}}{N_{\mathrm{A}} N_{\mathrm{D}}}}. \tag{2.33}$$

Finally, in case of a one-sided abrupt junction, eq. (2.30) and eq. (2.31) tell that the depletion region extends almost entirely in the less doped region.

2.1.3.3 The MOS capacitor

A capacitor in which one of the plates is swapped for a doped semiconductor, as shown in Fig. 2.6, is known as a *Metal-Insulator-Semiconductor* (MIS) capacitor. Commonly, the insulator consists of silicon oxide SiO_2 and one talks about *Metal-Oxide-Semiconductor* (MOS) structures.

Here follows a brief survey of the different operating regimes of a MOS capacitor.

Flat-band condition Let us consider a perfect insulator that completely prevents carriers from moving between the metal and a n-type semiconductor (the reasoning may be applied to a p-type structure as well by reversing all

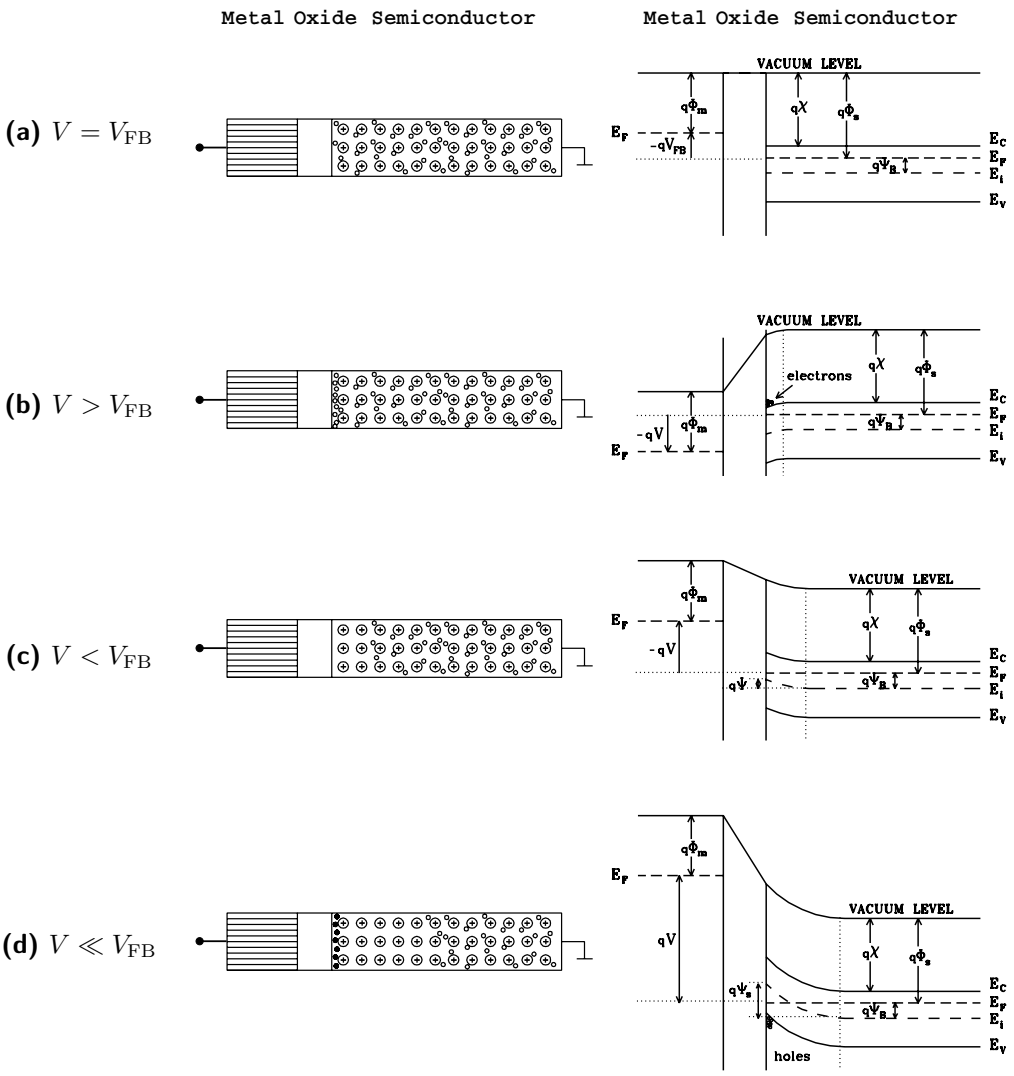

Figure 2.7 – Schematic view of the different operating regimes of a Metal-Insulator-Semiconductor capacitor. a) Flat-band condition. b) Accumulation. c) Depletion. d) Inversion. Adapted from Lutz (2007).

polarities), and let us further suppose that no charges are present on the insulator itself.

A configuration in which the electron density is uniform in the semiconductor is called *flat-band* condition (Fig. 2.7a) and can be achieved by applying a voltage V so that

$$V_{\mathrm{FB}} = \Phi_{\mathrm{m}} - \Phi_{\mathrm{s}}, \tag{2.34}$$

with $q\Phi_{\mathrm{m}}$ and $q\Phi_{\mathrm{s}}$ being the *work functions* of the metal and semiconductor respectively, i.e. the energy necessary to move an electron from the Fermi level to the vacuum just outside the material. Eq. (2.34) derives from the fact that the vacuum level must be the same for the whole device in absence of charges on the insulator (Lutz, 2007).

Accumulation If one applies a voltage difference larger than the flat-band voltage, i.e. $V > V_{\mathrm{FB}}$, than electrons will accumulate at the insulator-semiconductor interface, in a configuration called therefore *accumulation* (Fig. 2.7b). In this scenario, an equivalent positive charge will be induced on the metal contact, so that the structure can be modeled as a capacitor with a capacitance per unit area given by

$$C = \frac{\varepsilon_{\mathrm{ox}}\varepsilon_0}{d_{\mathrm{ox}}} = C_{\mathrm{ox}}, \tag{2.35}$$

where ε_0 is the permittivity of the vacuum, and C_{ox}, $\varepsilon_{\mathrm{ox}}$ and d_{ox} are the capacitance, permittivity and thickness of the insulator.

Depletion If the applied voltage is $V < V_{\mathrm{FB}}$, *depletion* takes place and the electrons are driven away from a narrow region next to the insulator (Fig. 2.7c). The capacitance can be calculated for this configuration as well (Kim, 1979):

$$C = C_{\mathrm{ox}} / \sqrt{1 + \frac{2\varepsilon_{\mathrm{ox}}^2\varepsilon_0}{qN_{\mathrm{D}}d_{\mathrm{ox}}^2}\,(V_{\mathrm{FB}} - V)}. \tag{2.36}$$

It is worth pointing out that as $V_{\mathrm{FB}} - V$ increases and the depletion region expands, *deep depletion* or *overdepletion* occurs. If however $V \ll V_{\mathrm{FB}}$, thermally-generated holes start to accumulate near the semiconductor-insulator interface: this regime is called *inversion* (Fig. 2.7d).

In case the insulator contains a charge distribution ρ within its volume and some charges are also trapped at the semiconductor-insulator interface with density σ, eq. (2.34) becomes

$$V_{\mathrm{FB}} = \Phi_{\mathrm{m}} - \Phi_{\mathrm{s}} - \frac{1}{\varepsilon_{\mathrm{ox}}\varepsilon_0}\left[\sigma d_{\mathrm{ox}} + \int_0^{d_{\mathrm{ox}}} \rho\,(x)\, x\ \mathrm{d}x\right], \tag{2.37}$$

and all the previous results are still valid.

2.2 Charge-Coupled Devices

The following text shall analyze the features of *Charge-Coupled Devices* (CCDs), among the most common imaging detectors in Astronomy. For the sake of brevity, the discussion shall be limited to their applications for the study of X-rays, which is the focus of this work. Starting with the description of the well-established technology of MOS CCDs (§ 2.2.1), the underlying working principles are introduced, along with the advantages and issues of this kind of device. Afterwards, the improvements embodied by pnCCDs (§ 2.2.2), on which the MXT detector is based, are discussed.

2.2.1 MOS CCDs

Charge-Coupled Devices were invented in their early form by Boyle & Smith (1970), who shared a Nobel prize in 2009 for the achievement. In the following, *three-phase buried-channel* CCDs are described, which are based on the improvements made by Walden et al. (1972) and Esser (1974) on the original design: the difference lies in the fact that, in order to limit the effects of charge trapping caused by surface impurities, charges are moved towards the interior of the detector, hence the original type of CCDs are referred to as *surface-channel* CCDs. Buried-channel CCDs have been used on most X-ray Astronomy missions, such as ESA's XMM (Turner et al., 2001), and NASA's Chandra (Garmire et al., 2003) and Swift (Burrows et al., 2004).

2.2.1.1 Working principle

A traditional CCD is a semiconductor (silicon) device whose surface is divided into pixels by means of a matrix of MOS structures. To be more

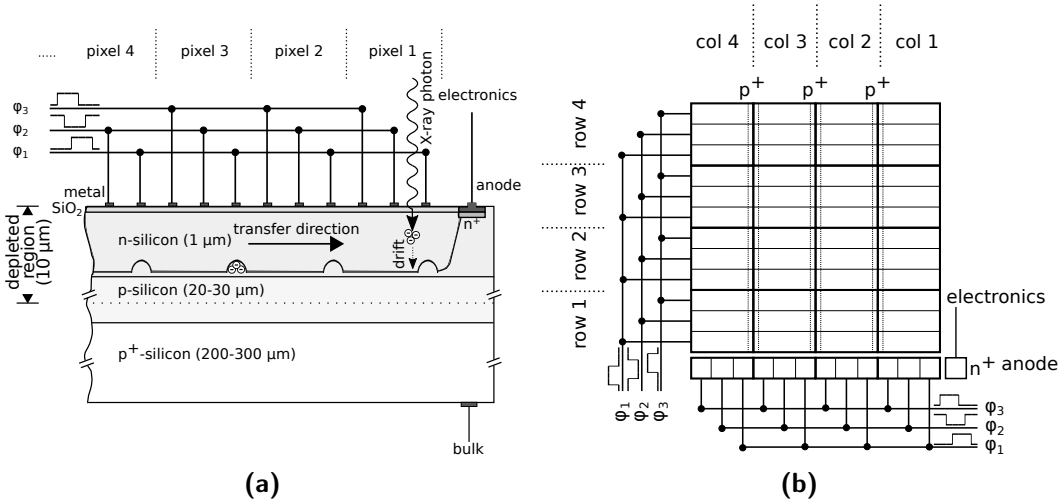

Figure 2.8 – Schematic views of a buried-channel MOS CCD. a) Cross-section along the transfer direction. b) Top view.

specific, optically-transparent polysilicon gates (in substitution of classic metal) are placed on an insulating SiO_2 sheet which in turn sits on top of a diode structure, composed of a 1 µm n-layer, a $20 - 30$ µm p-type epitaxial layer and a $200 - 300$ µm p^+-substrate. In a *three-phase* CCD, each pixel is divided into three electrodes, called *phases* or *shift registers*, which are at a higher potential than the bulk. This depletes the volume of the semiconductor down to few micrometers below its surface, thanks to the combination of depletion of the p-MOS capacitor (§ 2.1.3.3) and reverse biasing of the junction created by the n-layer and the p-epitaxial layer (§ 2.1.3.2). Furthermore, one of the phases is kept at $+V_{\text{bias}}$ with respect to the other two, creating local potential minima for electrons (Fig. 2.8).

If an ionizing particle or a photon hits the device, it creates a charge cloud of electrons and holes (§ 2.3.1.2 and 2.3.1.3). While the holes move to and are eventually absorbed by the undepleted bulk and other p^+-structures (to be discussed below), the electrons generated in the depletion zone drift under the influence of the electric field and are collected in the minima. Once this integration phase ends, the *charge transfer* begins (Fig. 2.9). Starting from a configuration in which ϕ_1 is the one at $+V_{\text{bias}}$, ϕ_2 is raised to the same potential widening the local minimum and allowing the charge cloud to spread under ϕ_2 as well as ϕ_1. Then, ϕ_1 is lowered so that the whole electron packet now is below ϕ_2. In a similar manner, ϕ_3 is raised to $+V_{\text{bias}}$, followed by the decrease of the potential applied to ϕ_2, which shifts the charges again under the next

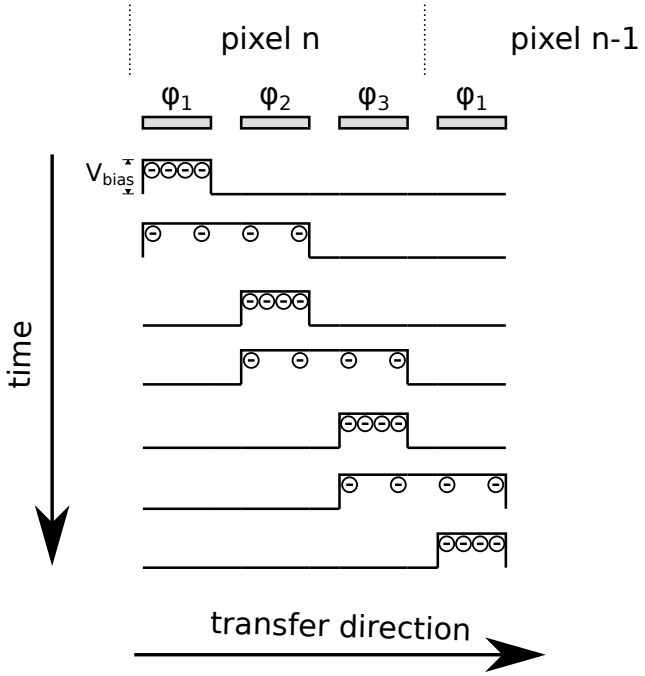

Figure 2.9 – Clock scheme enabling charge transfer between pixels in a CCD.

electrode. By repeating the procedure, this time with ϕ_3 and ϕ_1 of the *next pixel*, the electron cloud is moved to the adjacent pixel, i.e. the next row, as the shifts occur on all columns in parallel. By means of this mechanism, the charges may be transported all the way to the bottom of the matrix. When they reach it, an analogous horizontal shift is performed (*serialization*), i.e. the packets are moved to the next column, until they reach the readout anode. By counting the number of vertical and horizontal transfers, a two-dimensional position can be associated with each packet.

To prevent charges from spreading horizontally during integration and vertical transfer, *channel stops* in the form of p^+-implantations are inserted between neighboring columns, their negative charge acting as a potential barrier for the electrons.

2.2.1.2 Limitations

This kind of detector presents several issues for X-ray imaging and spectroscopy.

- Electrons may be collected only if the radiation interacts with the depleted region. Since the latter is so thin with respect to the whole detector

thickness (10 µm at most[3] against ≈ 300 µm), this implies that the device is not sensitive to higher energies (§ 2.3.3.1).

- Ionizing radiation that interacts with the oxide of the MOS structures may generate unmovable holes which build up over time (§ 4.2.2) and modify the shape of the electric potential creating an accumulation layer at the Si–SiO_2 interface, thus affecting the quality of the charge transfer: this implies a high sensitivity to radiation damage.

- Channel stops may inject thermally-generated holes into the bulk, which can then recombine with the electrons of the charge packets, degrading the signal.

- Readout is slow, as the electric field gets weaker the farther from the surface, and as each charge packet has to be transferred all the way to the bottom row and then horizontally towards the only readout anode.

- Being a front-illuminated device, it offers a $< 100\,\%$ fill factor, due to the gates of the electrodes, i.e. photons interacting with the electronic parts are lost and do not produce a signal inside the detector.

- The undepleted layer is a strong source of thermal charges (leakage current), which requires an operation at very low temperatures ($< -100\,°C$).

It is worth noting that some of the issues may be solved by thinning the silicon wafer so much that the undepleted region disappears. This allows the detector to be back-illuminated, allowing a 100 % fill factor and better sensitivity to lower energies. Moreover, leakage current is greatly reduced. The downside is the loss of structural integrity. Furthermore, the depleted thickness is still the same, therefore the high-energy response does not improve.

2.2.2 pnCCDs

In order to solve the issues with MOS CCDs, pnCCDs were invented (Gatti & Rehak, 1984; Strüder et al., 1987a,b). Their first use on board of a space astronomy mission was on one of the European Photon Imaging Cameras (EPIC) on board ESA's X-ray Multi-Mirror (XMM) mission (Strüder et al.,

[3]The depletion thickness varies with technology and was improved over time: it measures $35 - 40\,\mu m$ in XMM/EPIC-MOS, 65 µm in Suzaku/XIS and 70 µm in Chandra/ACIS.

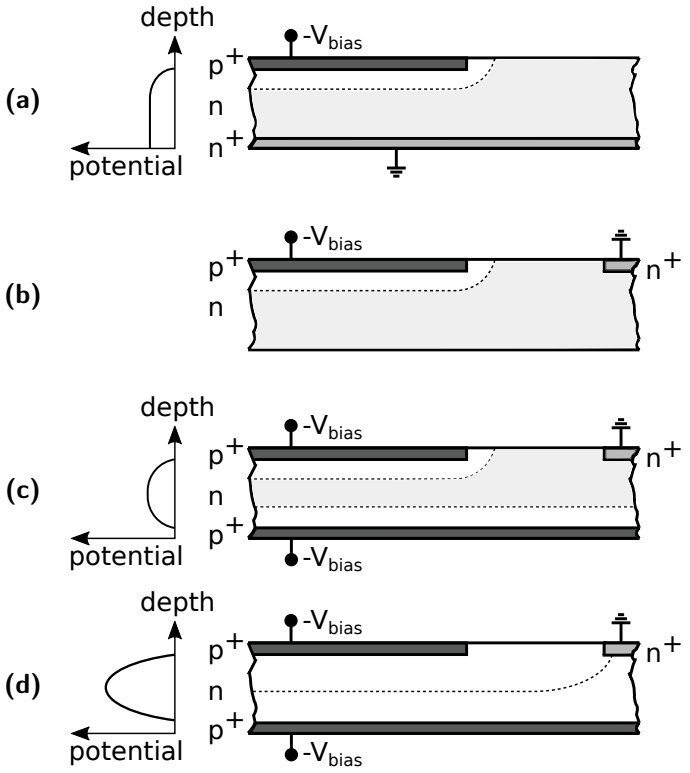

Figure 2.10 – Principle of the sidewards depletion. A detailed description of the figure is provided in § 2.2.2. Adapted from Lutz (2007).

2001). In the future, both SVOM/MXT (Mercier et al., 2018) and eROSITA (Meidinger et al., 2010a,b) will mount this kind of detector at their focal planes.

2.2.2.1 Working principle

The basis of pnCCDs is the principle of *sidewards depletion*, first introduced by Gatti & Rehak (1984). Let us consider a reverse-biased p^+nn^+ structure, as shown in Fig. 2.10a. As the applied voltage is increased, electrons fill the acceptor states on the p^+-side (cathode) to counterbalance the positive charge of the ionized donors on the n-side of junction, in which the depletion region mostly extends (compare to eq. (2.33)). Notably, the n^+n-contact only provides the conduction necessary to evacuate the electrons lost by the donors. This implies that it is not necessary for the n^+n-junction to extend across the whole diode or lie opposite to the p^+-side: it may thus be limited to a small contact anywhere on the device (anode), as in Fig. 2.10b. By doubling the p^+n-junction (Fig. 2.10c) and applying a negative voltage to the cathodes with respect to the n^+-anode, the result would be equivalent to depleting

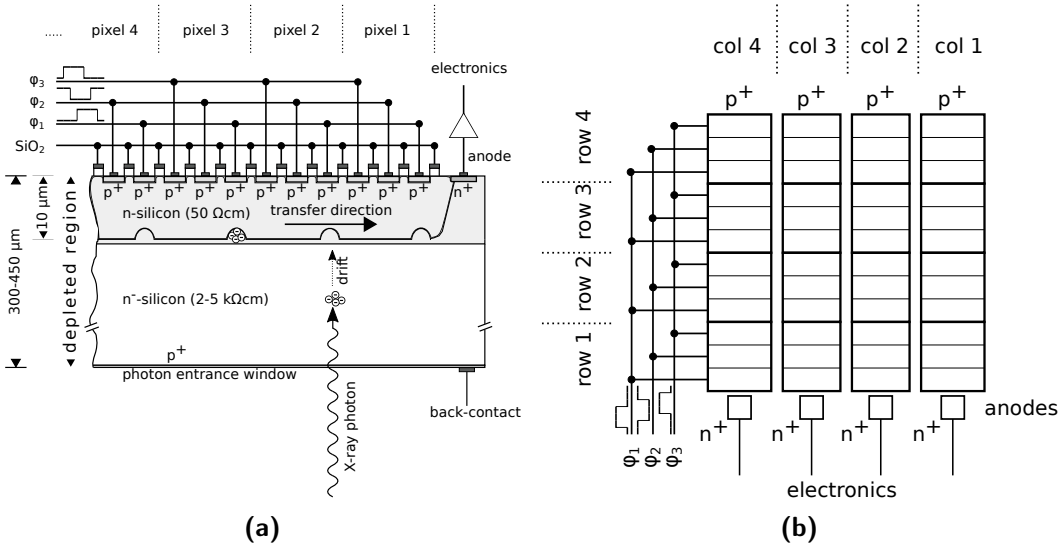

Figure 2.11 – Schematic views of a pnCCD. a) Cross-section along the transfer direction. b) Top view.

two side-by-side diodes at the same time. As long as an undepleted region stands between the two depleted layers, a conductive link to the n^+-electrode ensures the removal of the electrons and thus the widening of the depletion regions. When the two finally touch (Fig. 2.10d), the bulk is fully depleted and a potential minimum for electrons forms in the middle, where electrons (created by thermal agitation or ionization) can accumulate. The voltages on the two cathodes may be adjusted to move the potential minimum inside the bulk and one of the sides may also be segmented into pixels which are in turn subdivided into electrodes that create local minima for the electrons to be collected, exactly like in a conventional CCD.

2.2.2.2 Physical realization

In order to work properly, the internal structure of a pnCCD must be slightly modified from the simple description given above, as shown in Fig. 2.11. The top p^+-segmented cathodes, i.e. the shift registers which extend across the whole width of the detector, are isolated from each other by SiO_2 structures. Just below the front side lies a low-resistivity ($\sim 50\,\Omega\,\mathrm{cm}$) deep n-implantation[4], which sits on top of the high-resistivity ($2 - 5\,\mathrm{k}\Omega\,\mathrm{cm}$) n^--bulk. A p^+-back contact completes the scheme.

[4]An epitaxial layer in earlier devices, after XMM-Newton the fabrication was replaced by the high-energy implantation of phosphorous atoms (Schmidt et al., 2014).

The deep n-implantation is segmented into strips parallel to the direction of transfer which act like *guiding* (or *transfer*) *channels* for the charge packets, because the n^--interruptions between them create an effective potential barrier that prevents the charges from spreading into neighboring columns, essentially playing the role of channel stops. Furthermore, the positive charge of the n-channels counteracts the injection of thermally generated (positive) holes from the p^+-shift registers into the bulk, which may recombine with the signal electrons.

2.2.2.3 Advantages

A pnCCD has many clear advantages over a conventional CCD.

- The whole thickness of the detector is depleted, therefore able to detect ionization. This implies a much higher sensitivity to high energy particles and photons (§ 2.3.3.1), as well as higher collection efficiency, since no holes are injected from an undepleted region to recombine with the signal electrons.

- The voltages can be adjusted to put the potential minima well inside the silicon lattice and thus far from the impurities lying near the surface. This increases the transfer efficiency (§ 2.3.2.3).

- The depletion region and the drift field extending throughout the bulk also mean that particles may come from the back contact (also known as *entrance window* for this reason) instead of the front side, where the shift registers are located: the device is *back-illuminated*. This allows a 100 % fill factor, because the window may be built as a single piece and thus be made thin and homogeneous. This increases the quantum efficiency at lower energy, which is now only limited by the p^+ doping profile, creating an insensitive layer.

- Charged particles energetic enough to cross the whole detector may still deposit some (positive) charges on the insulating layer between the registers. In the case of a pnCCD however, the build-up of holes on the SiO_2 enhances the potential barrier preventing the spreading of electrons between the electrodes: the positive charges cause an accumulation layer of thermally-generated electrons below the gates, which works alongside

the positive space-charge regions of the depleted deep n-implantation to further insulate the shift registers from each other. Therefore, a pnCCD is more resistant to ionization damage than MOS CCDs (§ 4.2.2): no effects were observed after exposures up to $1-5\,\mathrm{Mrad}$ on some prototypes (Strüder et al., 1990).

- As particles enter the device far from the transfer region, most of those normally causing lattice defects which may disrupt the transfer (§ 2.3.2.3 and § 4.2.3.3) will be blocked by the thickness of the CCD itself, i.e. the device is *self-shielding* against low-energy particles. A pnCCD is then more resistant to bulk damage (§ 4.2.3).

- Having no conductive undepleted regions, the dark current is a smaller problem and the detector may be operated at temperatures as high as $-25\,^{\circ}\mathrm{C}$ (against $T \lesssim -100\,^{\circ}\mathrm{C}$ of MOS CDDs), the value obviously depending on the dimensions of the detector, the quality of the silicon and the desired performances.

- The electric field inside a pnCCD is stronger than the equivalent inside an ordinary CCD. This allows for higher drift velocities, i.e. faster transfer, which may require even less than $400\,\mathrm{ns\,row^{-1}}$. At this speed, the readout time is limited by the electronics.

2.2.2.4 Limitations

Despite all those advantages, two main drawbacks remain.

- The detector is always sensitive to ionizing radiation, even during transfer. Charges created during this phase, called *out-of-time* (OoT) events, will appear on the final image as blurred traces along the direction of transfer. The fraction of these OoT depends on the ratio between exposure and readout time of each frame.

- The extension of the sensitivity to the low-energy end of the spectrum implies that the device is sensitive to optical/UV photons.

While the latter can be easily solved with an optical/UV filter, the former may be tackled from different angles.

A first possible solution is to increase the readout speed. To achieve this, the columns of a pnCCD may be each equipped with an anode and independently

connected to an ASIC channel: they are thus read out in parallel, lowering the necessary time down to a few tens of milliseconds, depending on the dimensions of the matrix and the performances of the surrounding electronics (Fig. 2.11b). This was indeed the strategy adopted in the case of EPIC-pn on board ESA's XMM.

Another way might be to quickly transfer the charges accumulated during the frame exposure to a *shielded frame-store region*, where they can be read out without the possibility of new packets being created, as out-of-time events can be produced only in the unshielded pixels. Since, for the reasons previously mentioned, the quick transfer can be as short as 100 µs for a whole frame, depending on its dimensions, while the integration time is usually a few tens of milliseconds, the fraction of OoTs can get well below 1 %. This is the rationale behind a *frame-store* pnCCD, such as the ones at the focal planes of MXT and eROSITA. It is worth noting that the concept of frame-store CCD has been implemented with MOS design as well, such as in XMM's EPIC-MOS.

2.3 X-ray spectroscopy with CCDs

The principal concern of this thesis is with the characterization and evolution of the spectroscopic performances of the pnCCD at the focal plane of the Microchannel X-ray Telescope on board the SVOM mission. This means that it is necessary to be able to quantify the ability of the device to detect incoming X-ray photons and determine their energy.

The next sections are dedicated to the physics that makes the process of photon detection possible (§ 2.3.1), but also perturbs its reliability (§ 2.3.2). At the end is a series of figures of merit that allow to measure the spectral response of a detector from an experimental point of view (§ 2.3.3).

2.3.1 Charge generation by X-rays

The following discussion will be limited to ionizing electromagnetic radiation, mostly X-rays, since they represent the primary information carrier for the MXT detector. This is in spite of the fact that radiation detectors such as CCDs are able to detect all kinds of ionizing particles (§ 2.3.1.3), as long as the amount of charge they deposit is above the noise.

A phenomenological description of light-matter interactions will be outlined

in § 2.3.1.1 and then described from the point of view of its physics in § 2.3.1.2. Finally, § 2.3.1.3 will describe the phenomena allowing to link the measured signal to the energy of the incoming X-ray.

2.3.1.1 Absorption coefficient

Let us consider a mono-energetic photon beam of intensity I passing through a medium of thickness $\mathrm{d}x$. Due to the nature of light-matter interactions (to be discussed in the next section), photons either stay unaffectedor are removed from the beam, because they get absorbed or scattered (hence they change direction). This implies that even though the energy of the beam does not change as it propagates through $\mathrm{d}x$, its intensity (i.e. the number of photons) does. The variation $\mathrm{d}I$ of the beam intensity after $\mathrm{d}x$ can be described by

$$\mathrm{d}I = -\alpha I \,\mathrm{d}x \tag{2.38a}$$

$$I(x) = I_0 e^{-\alpha x}, \tag{2.38b}$$

where I_0 is the beam intensity at $x = 0$. The proportionality constant α of eq. (2.38a) is called *linear attenuation* (or *absorption*) *coefficient* and represents the strength of the light-matter interaction. It is linked to the total *cross section* σ, i.e. the probability per atom and per unit area that a photon will interact with the medium, by

$$\alpha = \frac{\rho N_\mathrm{A}}{A}\sigma, \tag{2.39}$$

where ρ is the density of the medium, A its molar weight and N_A Avogadro's number. The cross section is to be intended as summed over all possible interactions. In practice, the *mass attenuation* (or *absorption*) *coefficient* μ is preferred to α, the two being related by

$$\alpha = \rho\mu. \tag{2.40}$$

With this in mind, eq. (2.38b) becomes

$$I(x) = I_0 e^{-\rho\mu x}. \tag{2.41}$$

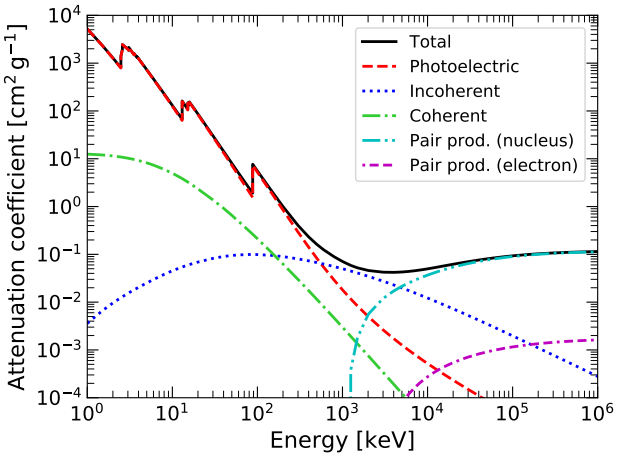

Figure 2.12 – Mass attenuation coefficient μ of lead (Pb) as a function of energy, broken down into its components, described in § 2.3.1.2. Data available at `https://physics.nist.gov/PhysRefData/Xcom/html/xcom1.html`.

An example of μ as a function of energy is given in Fig. 2.12. It is worth pointing out that, due to the low cross section of photon interactions with respect to charged ionizing radiation, photons can penetrate deeply into matter before interacting.

In case of a mixture, the total absorption coefficient is calculated as

$$\frac{\mu_{\text{tot}}}{\rho_{\text{tot}}} = \sum_j w_j \frac{\mu_j}{\rho_j}, \tag{2.42}$$

where the sum goes over all the elements in the mixture and w_j is the mass fraction of each one.

From eq. (2.41), one can define the *transmission* $\mathcal{T}$ and the *absorption* $\mathcal{A}$, defined by

$$\mathcal{T} = \frac{I(x)}{I_0} = e^{-\rho\mu x} \tag{2.43a}$$

$$\mathcal{A} = 1 - \mathcal{T} = 1 - e^{-\rho\mu x}, \tag{2.43b}$$

which respectively quantify how much radiation passes through or is absorbed after a path x.

2.3.1.2 Light-matter interactions

The following paragraphs give a summary of the principal interactions between X-ray photons and matter. The reader should refer to textbooks such as Als-Nielsen & McMorrow (2011), Leo (1994) and Siegbahn (2012) for a more complete physical and mathematical treatment of the subject, as here it will be mostly limited to a phenomenological approach.

It is worth noting that, of the following interactions, only the photoelectric effect has a real importance in the energy range of operation of the MXT detector ($0.2 - 10\,\mathrm{keV}$), as all other phenomena occur at either higher or lower energies.

Photoelectric effect The *photoelectric effect* concerns the interaction of a photon and an electron bound to an atom, with consequent ionization of the latter and emission of the former with a kinetic energy equal to

$$E_\mathrm{e} = E_\gamma - E_\mathrm{B}, \tag{2.44}$$

where E_B is the *binding energy* of the electron in the atomic shell. In the process, the photon is lost. It is worth noting that, even though the interaction is apparently only between a photon and an electron, the reaction

$$\gamma + e^- \longrightarrow e^- \tag{2.45}$$

does not conserve the invariant mass (energy and momentum) of the system. The presence of the nucleus is therefore mandatory for the photoelectric effect to take place, as it absorbs the recoil momentum without absorbing energy. On the basis of this reasoning, one may also infer that the photoelectric cross section should decrease as photon energy increases, because the momentum transfer becomes more and more important. Likewise, it should increase for heavier nuclei, because they are more efficient at absorbing the recoil momentum. Experimentally, one finds

$$\sigma_\mathrm{pe} \propto \frac{Z^4}{E^3}, \tag{2.46}$$

with Z being the atomic number of the target atom.

It is interesting to comment on the variation of the absorption coefficient μ

(or cross section σ) of the photoelectric effect as a function of energy, which is shown again in Fig. 2.12 for Pb. As the energy of the incoming photon decreases, μ increases until $E = 88\,\mathrm{keV}$ is reached, corresponding to the binding energy of the K shell. Below this point, photons do not have enough energy to ionize this shell and therefore absorption drops. The same reasoning is valid for the L and M shells at $\approx 14\,\mathrm{keV}$ and $3.85\,\mathrm{keV}$ respectively. The structure around $\approx 14\,\mathrm{keV}$ is due to the orbital split of the L shell.

Scattering *Compton scattering* is the scattering of photons onto free electrons. It is *incoherent*, as no phase relation exists between the scattered photons, and *inelastic* as photons and electrons exchange energy in the interaction. The energy transfer decreases with lower energy and the Compton cross section approaches the Thomson one (i.e. it becomes *elastic*). The kinematics of this scattering can be completely resolved and its cross section (Klein-Nishina cross section) can be derived by use of quantum electrodynamics (Fig. 2.12).

Photons interacting with bound electrons may be subject to *Rayleigh scattering*, a form of *coherent* scattering, in which all the electrons participate in the interaction (Fig. 2.12).

Pair production Photons with an energy $> 2m_\mathrm{e}c^2 = 1.022\,\mathrm{MeV}$ have enough energy to create electron-positron pairs. As with the photoelectric effect, a reaction of the form

$$\gamma \longrightarrow e^- + e^+ \tag{2.47}$$

does not conserve the invariant mass and thus must occur in the field of another particle, which has to absorb the excess momentum. This particle may be a nucleus or even another electron (Fig. 2.12).

2.3.1.3 Electron-hole pair creation

Let us consider an X-ray photon with energy $E_\gamma \geq 1.839\,\mathrm{keV}$, i.e. the ionization energy for electrons in the K shell ($n = 1$ orbital) for a silicon atom, and suppose it actually ionizes a silicon atom inside a silicon detector.

The expelled electron is ejected into the conduction band with an energy $E_\mathrm{e} = E_\gamma - 1.839\,\mathrm{keV}$ that might be high enough to lift other electrons from the valence band, in a multiplication process that will be described below

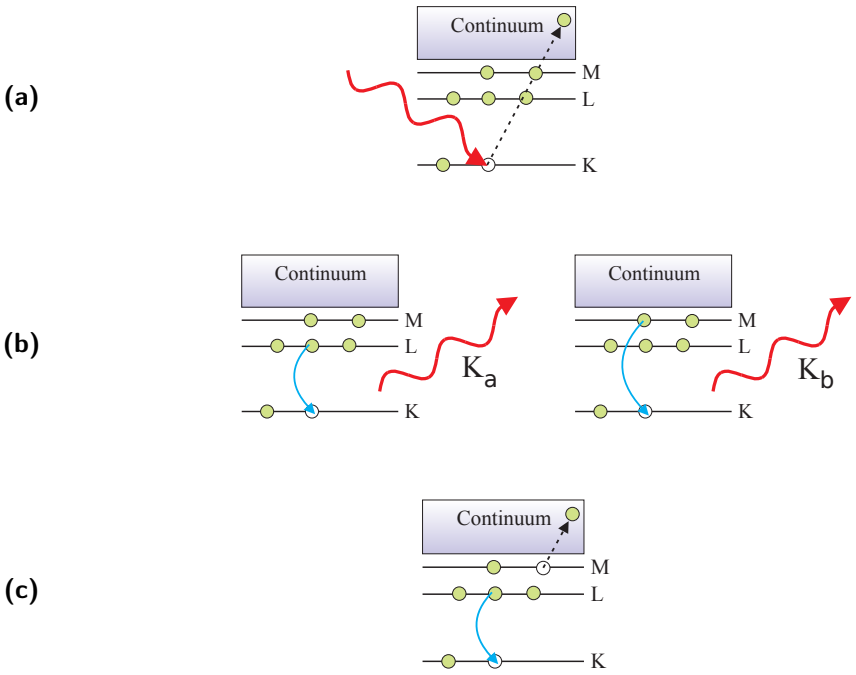

Figure 2.13 – Scheme of the rearrangement of the electronic configuration after a photoelectric absorption. a) Photoelectric absorption. b) Fluorescent X-ray emission (K_α and K_β). c) Auger electron emission. (Als-Nielsen & McMorrow, 2011)

(Fig. 2.13a). The ionized atom now presents a vacancy in the K shell, which corresponds to an unstable situation that can be resolved in one of two ways:

- the transition of an electron from the L shell ($n = 2$ orbital) or M shell ($n = 3$ orbital) to the K shell, with the consequent emission of a *fluorescence* photon with energy equal to the difference between the shells involved, known as K_α or K_β respectively (Fig. 2.13b);

- the transition of an electron from the L shell to the K shell, with the consequent emission of an *Auger electron* from the outermost orbitals (Fig. 2.13c), whose energy equals the difference between the $L - K$ electronic transition and the binding energy of the orbital from which the Auger electron was ejected (M in this case).

If, as a consequence of this new arrangement, a vacancy forms in another orbital, the reasoning may be iterated until the atom finally reaches a stable configuration. Of course, the same description holds true if the primary interaction is not with the K but with another shell, or even if the primary

particle is not a photon but another kind of ionizing radiation, which by definition is able to generate electrons as it passes through matter.

Auger electrons ejected while the atom tries to get back to a stable configuration may undergo the same multiplication processes of the first emitted electron, if their energy allows it. Likewise, the fluorescence photons generated at the same time may start the process all over again if they interact with the surrounding atoms. Whenever an electron is promoted to the conduction band, obviously holes are also formed accordingly in the valence band.

Experiments showed (Klein, 1967) that the quantum yield N, i.e. the number of electron-hole pairs produced per incoming particle, is directly proportional to the energy E it deposits in the detector. The following relation therefore holds true

$$N = \frac{E}{\epsilon}, \tag{2.48}$$

where ϵ is the *average energy* that goes into the creation of an electron-hole pair. It is important to point out that this does not correspond to the energy required to generate a single electron-hole pair, as this latter is linked to the ionization energy of the material.

The production of charges inside a detector comprises of three phases:

- the ionizing particle generates some *hot* primary electron-hole pairs;
- primary pairs produce *hot* secondaries through impact ionizations in a generation-multiplication cascade;
- electrons and holes progressively lose energy to interactions with the lattice (phonons) until they become unable to continue the cascading process and thus they reach *thermal equilibrium*.

Due to the energy E_{R} lost to low-frequency phonons, ϵ is larger than the band gap E_{G}. This is particularly true for indirect semiconductors, if one factors in the fact that momentum must be conserved even though the crystal wave vectors of the bottom of the conduction band and of the top of the valence band do not coincide (§ 2.1.1.3).

From the above discussion, several observations can be made.

- Radiation detectors are in principle sensitive to all types of ionizing particles.

- The quantum yield being proportional to the kinetic energy lost by the incoming particle implies that by measuring the number of carriers, i.e. the charge generated inside the detector, one can derive the energy deposited into the device and therefore can make *spectroscopy*.

- Spectroscopy with low-energy (e.g. visible or infra-red) light cannot be performed on the basis of the same principles, as the energy given to carriers is so low (just above E_G) that no cascading process takes place, and in general a single electron-hole pair is created, which rapidly thermalizes by dissipating its excess energy to phonons. This however does not mean that radiation detectors are not sensitive to light, because, even though only about one pair is created per interacting photon, the number of photons (and therefore charge) can be high enough to saturate or even damage the device, especially its readout electronics.

Experimental results and simulations show that ϵ is a function of both the temperature of the detector and the energy of the primary particle.

While in Fraser et al. (1994), the temperature dependence of phonon emission and absorption coefficients influence the result, Klein (1968) and Alig et al. (1980) estimated their contribution to be negligible, implying that $\epsilon\,(T)$ is determined by the variation of the energy band gap E_G, which may be parametrized via the Varshni formula (Varshni, 1967)

$$E_\mathrm{G}\,(T) = 1.170\,\mathrm{eV} - \frac{4.73 \times 10^{-4}\,\mathrm{eV\,K^{-1}} \cdot T^2}{T + 636\,\mathrm{K}}. \tag{2.49}$$

In general, the temperature dependence is on the order of $-0.01\,\%\,\mathrm{K}^{-1}$ (Fraser et al., 1994; Lowe & Sareen, 2007), i.e. $5 \times 10^{-4}\,\mathrm{eV\,K^{-1}}$ (Mazziotta, 2008). The commonly used value for average electron-hole pair creation energy in silicon at room temperature is $\epsilon = 3.63\,\mathrm{eV}$ (Alig et al., 1980).

For primary photon energies $E_\gamma \gtrsim 1\,\mathrm{keV}$, ϵ reaches an asymptotic value, well attained by both theoretical calculations and experiments (Alig et al., 1980; Fraser et al., 1994; Lechner et al., 1996; Scholze et al., 1998). For lower energies, however, measurements become difficult as the entrance window effects of the detectors gain importance at very low energies (e.g. doping profiles and surface defects) and an incorrect model of the low-energy efficiency of the device may affect the results (Lechner et al., 1996). Moreover, simulations may start to diverge according to whether the contribution of holes is taken into account

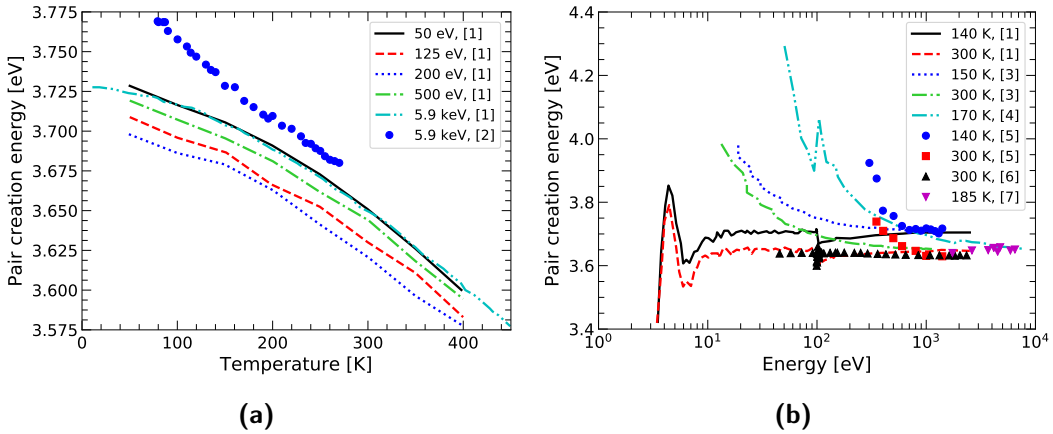

Figure 2.14 – Average electron-hole pair creation energy ϵ as a function of temperature (a) and primary photon energy (b). [1] Mazziotta (2008), [2] Lowe & Sareen (2007), [3] Alig et al. (1980), [4] Fraser et al. (1994), [5] Lechner et al. (1996), [6] Scholze et al. (1998), [7] Kotov et al. (2018). Datasets [1], [3] and [4] are simulations, [2] and [7] are experimental points and [5] is a calculation based on experiments. [3] is based on the ionization by secondary electrons, hence no dependence on the silicon edges is visible, [4] does not take into account hole contribution, which explains the low energy divergence. [2] and [5] might be influenced by hypotheses and entrance window effects respectively.

(Scholze et al., 1998). In general, the average pair creation energy is expected to correlate with the K and L edges of silicon through discontinuities (Fraser et al., 1994; Scholze et al., 1998; Mazziotta, 2008). Some experimental and theoretical results are shown in Fig. 2.14.

One may fit a relation of the form

$$\epsilon\left(T\right) = aE_{\mathrm{G}}\left(T\right) + b \tag{2.50}$$

to the 5.9 keV dataset of Mazziotta (2008), which seems to best agree with the experiments of Lechner et al. (1996) and Scholze et al. (1998), at least in the asymptotic regime (Fig. 2.14b). To better refine the estimation, the dataset can be rescaled so that $\epsilon\left(E_\gamma \gtrsim 1\,\mathrm{keV}, 300\,\mathrm{K}\right) = 3.63\,\mathrm{eV}$, which has been confirmed by may experiments. If E_{G} is expressed through eq. (2.49), this operation leads to $a = 1.7016 \pm 0.0026$ and $b = (1.7173 \pm 0.0031)\,\mathrm{eV}$, which will be used henceforth.

2.3.2 Phenomena limiting the spectral response

Let us consider a beam of mono-energetic photons impinging on a detector. According to eq. (2.48), each absorbed photon will generate an average amount of electrons directly proportional to its energy, the actual amount fluctuating around that value due to *noise*.

Various phenomena that influence the actual charge that is measured at the end of a readout chain will be discussed next. After describing two contributions to the noise common to every semiconductor detector system, i.e. statistical or Fano noise (§ 2.3.2.1) and readout noise (§ 2.3.2.2), the attention will be focused on two more noise sources that apply more specifically to CCDs, i.e. charge transfer inefficiency (§ 2.3.2.3) and charge sharing (§ 2.3.2.4). Finally, the problem of pile-up will be outlined (§ 2.3.2.5).

2.3.2.1 Fano noise

From the discussion in § 2.3.1.3, one gets that an X-ray photon of energy E that is completely absorbed in a detector generates a number of electron-hole pairs N (quantum yield) equal to eq. (2.48): $N = E/\epsilon$. One might assume that N fluctuates according to Poisson statistics, i.e. its uncertainty corresponds to its square root. However, a systematically lower value was experimentally found. Starting from considerations by Fano (1946, 1947) originally regarding gas detectors, one defines the *Fano factor* F as the ratio between the mean square deviation of the number of generated pairs and its average N:

$$F = \frac{\langle (Q - N)^2 \rangle}{N}, \tag{2.51}$$

where Q is the measured quantum yield. If one considers that the denominator of eq. (2.51) is equal to the variance in Poisson statistics, it is clear that eq. (2.51) represents the deviation from that regime.

In order to explain this phenomenon, one must consider the process leading to the generation of electron-hole pairs in the detector. In Poisson regime, it is supposed that all the events occur *independently* of one another. In case under examination, however, this is not true, as the total deposited energy E_γ is fixed and therefore must be conserved by all the processes taking place, such as ionization and phonon excitation. A *correlation* arises between the events and the total fluctuation is smaller than the Poisson case.

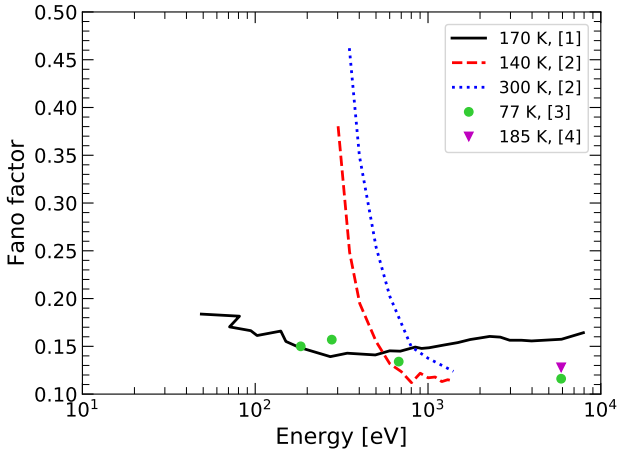

Figure 2.15 – Fano factor as a function of energy and temperature. [1] Fraser et al. (1994), [2] Lechner et al. (1996), [3] Lowe (1997) and [4] Kotov et al. (2018). [1] is a simulation, whereas [2] to [4] are experimental data. [1] does not take into account hole contribution. [2] might be influenced by entrance window effects.

Experimentally, the Fano factor is measured from the energy-dependent irreducible component of the noise that is still present when all other components are accounted for. For silicon, this leads to a value of $F = 0.115$ (Alig et al., 1980). From simple considerations of energy conservation, it can be shown (Spieler, 2005) that the Fano factor depends on $\epsilon\,(E_\gamma, T)$, and therefore it its a function of primary energy and temperature as well. However, experiments and simulations suggest that its dependence is very weak, and therefore the hypothesis of a constant value for F is reasonable (Fig. 2.15).

It is worth noting that Fano noise is intrinsic to semiconductor detectors: even a perfectly noiseless system cannot enjoy infinitely sharp spectral lines because of the very processes responsible for generating the signal in the detector. For this reason, a device may be considered (nearly) *Fano-limited*, when this noise component is dominant.

2.3.2.2 Readout noise

Electronic or *readout noise* is the noise associated with the measuring process itself. Let us consider a simplified schematic of the detector and readout circuit, as the one depicted in Fig. 2.16, in which the detector is reduced to a pulse current generator $Q\delta\,(t)$ injecting a the charge Q deposited on the detector onto the total capacitance $C_{\text{tot}} = C_{\text{detector}} + C_{\text{parasitic}}$. Noise

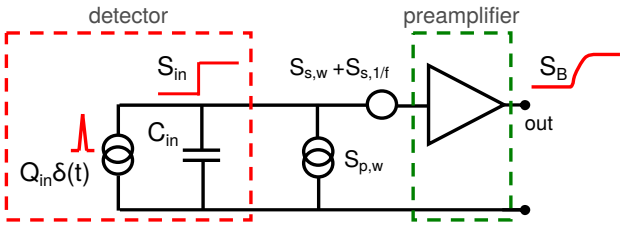

Figure 2.16 – Schematic of the detector and preamplifier system. The detector is a pulse current generator while noise sources are regrouped into a voltage and a current generator, respectively in series and parallel. All capacitance is in C_{tot}.

sources may be then represented as voltage or current generators, respectively placed in series or in parallel with the line over which the detector signal travels. According to this distinction, contributions are classified as being in *series* or *parallel*.

The readout noise is usually expressed in terms of the *Equivalent Noise Charge* or ENC (measured in electrons), which is the charge needed at the input in order to measure a unitary signal-to-noise ratio at the output:

$$\mathrm{ENC}^2 \cdot h^2\left(t_{\mathrm{M}}\right) = \langle i^2 \rangle, \tag{2.52}$$

where $\langle i^2 \rangle$ is the total noise current variance, t_{M} is the measure time and $h\left(t\right)$ is the *impulse response* of the readout circuit, i.e. its response to a δ-like input signal. Strictly speaking, the impulse response is defined only for *time-invariant* circuits, in which the response depends on time solely through the input and not explicitly. This implies that the circuit is always sensitive to an incoming signal, whenever it arrives. On the other hand, the output of *time-varying* circuits does depend on the time of arrival of the input. For them, a *weighting function* is defined instead, although mathematically it can be used in the same way as an impulse response.

2.3.2.3 Charge transfer inefficiency

As it was hinted many times throughout § 2.2, when a charge packet is transferred from a pixel to the next in a CCD (no matter the type), a fraction of it is lost, due to reasons that will be explained in detail below. This fractional loss is named *Charge Transfer Inefficiency* or CTI. Equivalently, one may talk

about *Charge Transfer Efficiency* or CTE, simply defined as

$$\mathrm{CTE} = 1 - \mathrm{CTI}. \tag{2.53}$$

Let us consider a flat field in which every pixel contains a number of electrons N at the beginning of the transfer phase and let us focus on a packet that needs n transfers to reach the anode. When the charges are moved to the next pixel, $\mathrm{CTI} \cdot N$ electrons will be left behind and only $\mathrm{CTE} \cdot N$ electrons will be successfully transferred. At the next shift $\mathrm{CTE}^2 \cdot N + \mathrm{CTE} \cdot \mathrm{CTI} \cdot N$ electrons will be moved, i.e. $\mathrm{CTE} \cdot (\mathrm{CTE} \cdot N)$ originally in position n and $\mathrm{CTE} \cdot \mathrm{CTI} \cdot N$ leftover from the previous transfer from position $n-1$. If the argument is iterated and the charge is allowed to vary from pixel to pixel, the amount of electrons read out after n shifts will be

$$N_n = \sum_{k=1}^{n} \binom{n}{k-1} \mathrm{CTI}^{n-k}\, \mathrm{CTE}^k N_k. \tag{2.54}$$

Eq. (2.54) can be simplified in case of X-ray observations, because the flux is usually so low that only very few pixels are hit by photons in each frame. Furthermore, the transfer efficiency is usually so high that most of the electrons are moved away at each shift ($\mathrm{CTI} < 10^{-3}$ in most cases). As a consequence, one may take $N_k \approx 0$ for $k \neq n$. If one then considers that, as seen in § 2.3.1.3, the number of electrons N is proportional to the energy of the interacting photon E_γ, eq. (2.54) can be written as

$$E = \mathrm{CTE}^n E_\gamma, \tag{2.55}$$

where E is the energy measured at the node. Even though it has been considered constant so far, the CTE may vary across the detector if the conditions that determine the charge loss are not uniform. However, in most cases, eq. (2.55) well describes the data and, due to the usually small value of the CTI, can even be approximated by a straight line.

The transfer inefficiency does not only contribute to an underestimation of the photon energy according to eq. (2.55), but it also increases its uncertainty. If one measures $N = \mathrm{CTE}^n N_\gamma$ electrons from the original $N_\gamma = E_\gamma/\epsilon$, the

associated variance can be written as

$$N^2_{\text{transf,n}} = N_\gamma - N = N_\gamma \left(1 - \text{CTE}^n\right). \tag{2.56}$$

Theoretical model In the following, I shall derive an analytic formula for the *Charge Transfer Inefficiency* or CTI, i.e. the fraction of a charge packet that is lost after it is moved through a pixel in a CCD.

Let us consider a uniform distribution of single energy level defects of concentration N_t, and let us suppose the their energy level E_t is just below the bottom of the conduction band E_C. If one rewrites eq. (2.15) by using eq. (2.5) and eq. (2.11), the ratio between the electron and hole emission rate becomes

$$\frac{e_\text{n}}{e_\text{p}} = \frac{\sigma_\text{n} \upsilon_{\text{th,n}}}{\sigma_\text{p} \upsilon_{\text{th,p}}} e^{2(E_\text{t} - E_\text{i})/kT}. \tag{2.57}$$

If $E_\text{t} \lesssim E_\text{C}$, then electron emission in the conduction band is far more likely than hole emission in the valence band (E_i is near the middle of the band gap), implying that charge generation and recombination (i.e. the moving of electrons between the two bands) is discouraged in favor of *electron trapping*, in which electrons are captured from and then re-emitted to the conduction band. This conclusion is consistent with the that of § 2.1.2.1, where it was shown that the defects with an energy level near the middle of the band gap are those most contributing to leakage current.

According to the above reasoning, one may henceforth use the term *traps* to refer to the defects with $E_\text{t} \lesssim E_\text{C}$. Furthermore, hole capture and emission can be neglected and thus the subscript n can be dropped, so that the concentration of occupied traps n_t can be written as (compare to eq. (2.16))

$$\frac{\text{d}n_\text{t}}{\text{d}t} = -n_\text{t} \sigma \upsilon_\text{th} N_\text{C} e^{-(E_\text{C} - E_\text{t})/kT} + \left(N_\text{t} - n_\text{t}\right) \sigma \upsilon_\text{th} n_\text{e}. \tag{2.58}$$

Here n_e is the free carrier concentration, which, if the volume of the sensitive part of the detector is depleted, can either be made of electrons generated by the leakage current J over a period t or be a sum of those and the charges created by a photon of energy E:

$$n_\text{J} = \frac{JAt}{qV} \tag{2.59a}$$

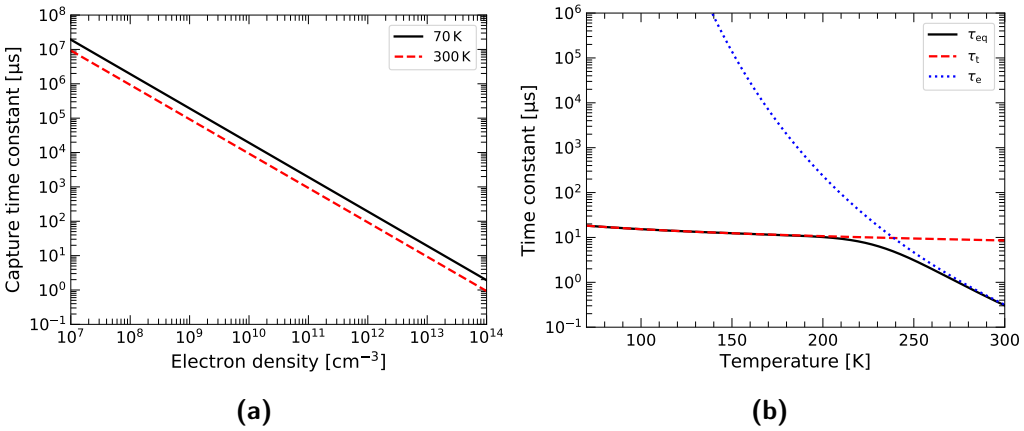

Figure 2.17 – Time constants as functions of temperature and electron density. The following parameters were used: $\Delta H = 0.3\,\mathrm{eV}$, $X_\mathrm{n} = 1$ and $\sigma = 10^{-15}\,\mathrm{cm}^2$. a) Capture time constant as a function of electron density for two temperatures. b) Emission, capture and equilibrium time constants versus temperature for an electron cloud generated by 5.9 keV-photons.

$$n_\gamma = n_\mathrm{J} + \frac{E}{\epsilon V}, \tag{2.59b}$$

where J is expressed by eq. (2.22), A is the cross section of the depleted volume over which the current has been accumulating (i.e. the pixel area), ϵ is given by eq. (2.48) and (2.50) and V is the volume occupied by the charges.

The *emission time* τ_e and the *capture time* τ_t, as well as an *equilibrium time* τ_eq, can now be defined respectively as

$$\tau_\mathrm{e} = \frac{e^{(E_\mathrm{C}-E_\mathrm{t})/kT}}{\sigma v_\mathrm{th} N_\mathrm{C}} \tag{2.60a}$$

$$\tau_\mathrm{t} = \frac{1}{\sigma v_\mathrm{th} n_\mathrm{e}}, \tag{2.60b}$$

$$\frac{1}{\tau_\mathrm{eq}} = \frac{1}{\tau_\mathrm{e}} + \frac{1}{\tau_\mathrm{t}}. \tag{2.60c}$$

In eq. (2.60a), as well as in any previous semiconductor equation, the *energy* E is to be intended as *Gibbs free energy* $E = H - TS$, where H is the *enthalpy* and S the *entropy*. This allows the substitution

$$e^{(E_\mathrm{C}-E_\mathrm{t})/kT} = e^{-\Delta S/k} e^{\Delta H/kT} = \frac{1}{X} e^{(\Delta H)/kT}, \tag{2.61}$$

where $X = e^{\Delta S/k}$ is the *entropy factor* for electron emission. This change of notation is useful because some experimental methods, such as *Deep Level Transient Spectroscopy* and *Thermally Stimulated Current*, allow the measurement of ΔH and ΔS, and thus bibliographic sources about defect physics usually cite those parameters when describing traps. Fig. 2.17 shows the three time constants for a set of parameters relevant within the framework of this manuscript.

With the definitions in eq. (2.60), eq. (2.58) can be written as

$$\frac{\mathrm{d}n_\mathrm{t}}{\mathrm{d}t} = -\frac{n_\mathrm{t}}{\tau_\mathrm{eq}} + \frac{N_\mathrm{t}}{\tau_\mathrm{t}}. \tag{2.62}$$

If at time $t = 0$ the concentration of occupied traps is $n_{\mathrm{t},0}$, then the solution to eq. (2.62) is

$$n_\mathrm{t}(t) = \frac{\tau_\mathrm{eq}}{\tau_\mathrm{t}} N_\mathrm{t} + \left(n_{\mathrm{t},0} - \frac{\tau_\mathrm{eq}}{\tau_\mathrm{t}} N_\mathrm{t} \right) e^{-t/\tau_\mathrm{eq}}. \tag{2.63}$$

It is interesting to notice that for very low charge concentrations $\tau_\mathrm{t} \gg \tau_\mathrm{e}$ and $\tau_\mathrm{eq} \approx \tau_\mathrm{e}$, reducing eq. (2.63) to

$$n_\mathrm{t}(t) = n_{\mathrm{t},0} e^{-t/\tau_\mathrm{e}}, \tag{2.64}$$

which corresponds to simple charge emission from the filled traps.

From eq. (2.63), it is clear that traps are responsible for CTI, as they absorb (and release) electrons when a charge packet moves through a pixel. Since pnCCDs are the primary focus of the discussion, the presence of surface defects can be neglected. Indeed, they play a role only when the transfer occurs near the surface of the detector, which is not the case for pnCCDs, for which only bulk defects are relevant. Hereafter, variables that depend on the nature of the charge packet shall have a superscript J (*leakage charge packets*) or γ (*photon charge packets*) in line with eq. (2.59a) and (2.59b) respectively.

Let us consider a pixel hit by a photon during integration and use values relevant for the case of MXT for the parameters when needed (Tab. 2.1). Since $\tau_\mathrm{eq}^\gamma \approx 10\,\mu\mathrm{s}$ whereas $t_\mathrm{int} \approx 100\,\mathrm{ms}$, $n_\mathrm{t}^\gamma(t)$ does not depend on time and it reaches an asymptotic value of

$$n_{\mathrm{t},\infty}^\gamma = \frac{\tau_\mathrm{eq}^\gamma}{\tau_\mathrm{t}^\gamma} N_\mathrm{t}. \tag{2.65}$$

Furthermore, due to the fact that the integration time is much longer than the time to transfer the whole frame ($t_{\rm int} \gg t_{\rm transfer}$), the amount charge accumulated by leakage current during transfer shall be neglected compared to that generated during integration. In this way, $n_{\rm J}$ of eq. (2.59) is calculated with $t = t_{\rm int}$.

Let us now consider that after integration the photon charge packet is transferred away and a leakage charge packet is moved in. From eq. (2.63) with $n_{\rm t,0} = n^{\gamma}_{\rm t,\infty}$, one gets

$$n^{\rm J}_{\rm t}(t) = \frac{\tau^{\rm J}_{\rm eq}}{\tau^{\rm J}_{\rm t}} N_{\rm t} + N_{\rm t}\left(\frac{\tau^{\gamma}_{\rm eq}}{\tau^{\gamma}_{\rm t}} - \frac{\tau^{\rm J}_{\rm eq}}{\tau^{\rm J}_{\rm t}}\right) e^{-t/\tau^{\rm J}_{\rm eq}}. \tag{2.66}$$

Due to the difference in the electron densities of the two charge packets, which affects the time constants, the effect is a net charge emission such as in eq. (2.64).

If a photon charge packet is brought in the same pixel where a previous photon packet used to be, the two being separated by a time t_{γ}, then the concentration of electrons stored in traps is described by eq. (2.63) with initial condition described by eq. (2.66) with $t = t_{\gamma}$:

$$n^{\gamma}_{\rm t}(t) = \frac{\tau^{\gamma}_{\rm eq}}{\tau^{\gamma}_{\rm t}} N_{\rm t} - N_{\rm t}\left[\left(\frac{\tau^{\gamma}_{\rm eq}}{\tau^{\gamma}_{\rm t}} - \frac{\tau^{\rm J}_{\rm eq}}{\tau^{\rm J}_{\rm t}}\right) - \left(\frac{\tau^{\gamma'}_{\rm eq}}{\tau^{\gamma'}_{\rm t}} - \frac{\tau^{\rm J}_{\rm eq}}{\tau^{\rm J}_{\rm t}}\right) e^{-t_{\gamma}/\tau^{\rm J}_{\rm eq}}\right] e^{-t/\tau^{\gamma}_{\rm eq}}, \tag{2.67}$$

where γ' and γ indicate the *old* and *new* photon respectively.

Finally, if the transfer from one electrode to the next inside a pixel takes a finite amount $t_{\rm transf}$, it is possible for some electrons to be re-emitted from the traps, in virtue of the drop in free electron density, as in eq. (2.64). After taking this effect into account as well as considering a permanence time $t_{\rm pix}$ for the photon charge packet in the pixel, the concentration of occupied traps becomes

$$n^{\gamma}_{\rm t} = N_{\rm t}\left[\frac{\tau^{\gamma}_{\rm eq}}{\tau^{\gamma}_{\rm t}} - \left[\left(\frac{\tau^{\gamma}_{\rm eq}}{\tau^{\gamma}_{\rm t}} - \frac{\tau^{\rm J}_{\rm eq}}{\tau^{\rm J}_{\rm t}}\right) - \left(\frac{\tau^{\gamma'}_{\rm eq}}{\tau^{\gamma'}_{\rm t}} - \frac{\tau^{\rm J}_{\rm eq}}{\tau^{\rm J}_{\rm t}}\right) e^{-t_{\gamma}/\tau^{\rm J}_{\rm eq}}\right] e^{-t_{\rm pix}/\tau^{\gamma}_{\rm eq}}\right] e^{-t_{\rm transf}/\tau_{\rm e}}. \tag{2.68}$$

By definition, the Charge Transfer Inefficiency is the fractional amount of

charge that *does not* leave a pixel after a packet is brought in, and therefore gets trapped in the defects. This corresponds to

$$\mathrm{CTI} = \frac{n_\mathrm{t}^\gamma - n_{\mathrm{t},0}^\gamma}{n_\gamma}, \tag{2.69}$$

which, by combining eq. (2.68), eq. (2.66) with $t = t_\gamma$ and eq. (2.59b), becomes

$$\begin{aligned}\mathrm{CTI} = \frac{N_\mathrm{t}}{n_\gamma}\Bigg[&\frac{\tau_\mathrm{eq}^\gamma}{\tau_\mathrm{t}^\gamma}\left(1 - e^{-t_\mathrm{pix}/\tau_\mathrm{eq}^\gamma}\right) e^{-t_\mathrm{transf}/\tau_\mathrm{e}} \\ &- \left[\frac{\tau_\mathrm{eq}^\mathrm{J}}{\tau_\mathrm{t}^\mathrm{J}} + \left(\frac{\tau_\mathrm{eq}^{\gamma'}}{\tau_\mathrm{t}^{\gamma'}} - \frac{\tau_\mathrm{eq}^\mathrm{J}}{\tau_\mathrm{t}^\mathrm{J}}\right) e^{-t_\gamma/\tau_\mathrm{eq}^\mathrm{J}}\right] \cdot \\ &\cdot \left(1 - e^{-t_\mathrm{pix}/\tau_\mathrm{eq}^\gamma - t_\mathrm{transf}/\tau_\mathrm{e}^\gamma}\right)\Bigg]. \end{aligned} \tag{2.70}$$

It is worth commenting on this result. If one considers the definitions of all the variables that appear in eq. (2.70), it is clear that the CTI depends on several parameters:

- defect properties:
  - defect type, characterized by trap cross section σ, energy depth $E_\mathrm{t} - E_\mathrm{C}$ and concentration N_t; defects also depend on the material of the detector, its fabrication process, and the amount, energy and kind of radiation it is exposed to;
- detector features:
  - thickness of the depleted region and pixel dimensions, which affect the contribution of the leakage current;
  - doping structure, which influences the volume V occupied by the charges and hence their interactions with the (uniformly distributed) traps;
- operating conditions:
  - temperature, due to the temperature dependence of τ_e and τ_t, and the leakage current J;
  - integration time t_int;

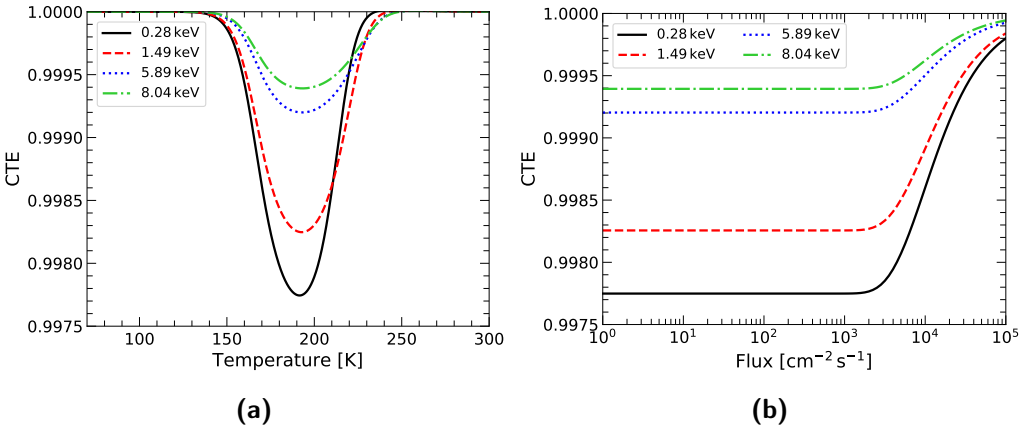

Figure 2.18 – Charge Transfer Efficiency for an MXT-like detector for four energies corresponding to spectral lines of common use in X-ray spectroscopy: 277 eV (C-K), 1486 eV (Al-K$_\alpha$), 5898 eV (Mn-K$_\alpha$), 8040 eV (Cu-K$_\alpha$). Other parameters used are: $N_\mathrm{t} = 10^{10}\,\mathrm{cm}^{-3}$, $\sigma = 10^{-15}\,\mathrm{cm}^2$, $\Delta H = 0.3\,\mathrm{eV}$ and $X = 1$, which represent typical values of radiation-induced defects (§ 4.4.1). a) CTE as a function of temperature for $F = 300\,\mathrm{ph\,cm}^{-2}$. b) CTE as a function of flux for $T = 190\,\mathrm{K}$. The flux is always considered monochromatic.

  - clock scheme, i.e. t_pix and t_transf
  - operating voltage, which may influence the volume V;

- characteristics of the photon source:
  - energy E of the photons under study, through n_γ and therefore τ_t;
  - mean photon energy, because of the dependence on γ';
  - mean photon flux F, because the average interval between two photon charge packets passing through the same pixel can be calculated as

$$t_\gamma = \frac{t_\mathrm{pix}}{F A_\mathrm{pix} t_\mathrm{int}}, \tag{2.71}$$

    with A_pix being the area of a pixel.

Fig. 2.18a shows the Charge Transfer Efficiency as a function of temperature T for different photon energies. For very low temperatures, the emission time constant τ_e (Fig. 2.17b) is so large that filled traps essentially never emit their charges. Since occupied traps cannot store more electrons, charge packets pass unaffected: as a consequence, the CTE is high. On the other side of the temperature range, τ_e is so small that electrons that are trapped are released

soon after, before the packet exits the pixel. The total charge then stays unaffected and the CTE is high again. For an intermediate temperature range, however, τ_e and τ_t are such that electrons are likely to be trapped when the packet is moved in, but released when it has already left the pixel. As a result, CTE is low. The fact that $\tau_e \propto e^{(E_C - E_t)/kT}$ implies that the CTE minimum depends on the energy level of the trap.

The dependence of the CTI on the energy is clearly understandable, since a lower-energy photon generates fewer charges, and therefore is more susceptible to losses than a larger packet by a higher-energy photon (Fig. 2.18a). Less intuitive is the dependence on the source flux and mean energy, even though it derives naturally from what was observed above. If the flux is high, a large number of traps will be filled at every moment, preventing those from taking in more electrons: this improves the CTE (Fig. 2.18b). The same is true if the spectrum is harder, as a larger number of electrons will be available in each packet to fill in empty traps.

2.3.2.4 Charge sharing

Let us consider an X-ray photon interacting within a CCD through photoelectric effect. According to § 2.3.1.2, a primary electron is ejected, whose range depends on its kinetic energy $E_{e^-} = E_\gamma - E_B$. As was discussed in § 2.3.1.3, a charge cloud of secondary electrons is formed. If one supposes that the dimension of this cloud is mainly defined by the range of the primary electron, which is the most energetic particle emitted by the silicon atom during the relaxation process (Grum-Grzhimailo et al., 2017), the cloud radius can be calculated as (Valkealahti et al., 1989)

$$R = \frac{A}{\rho N_A} \alpha \left(E_\gamma - E_B\right)^{1.70}, \tag{2.72}$$

where R is measured in cm, the energy is in keV, $\alpha = 5.5 \times 10^{16}\,\mathrm{cm}^{-2}$, ρ and A are the silicon density and atomic weight respectively, and N_A is Avogadro's number. For the photon energies of interest ($E_\gamma \leq 10\,\mathrm{keV}$), $R \lesssim 0.4\,\mu\mathrm{m}$, so the cloud can be considered point-like.

Under the influence of the electric field of the CCD, the electrons drift towards the electron potential minimum under the storage electrode. During the drift, the cloud expands due to diffusion and electrostatic repulsion. If one

considers the first phenomenon alone, as time t passes, the charge assumes a Gaussian profile[5]. The radius of the spherical surface containing approximately 99 % of the distribution, i.e. the 3σ radius of a three-dimensional Gaussian distribution, will therefore evolve according to

$$R_{\text{diff}} = 3\sqrt{2D_{\text{n}}t}, \tag{2.73}$$

where D_{n} is the diffusion coefficient described in § 2.1.2.2. By considering the electrostatic repulsion inside a spherically-symmetric electron cloud[6], one instead obtains

$$R_{\text{rep}} = \left(\frac{3q\mu_{\text{n}}}{4\pi\varepsilon}\frac{E_\gamma}{\epsilon}\right)^{\frac{1}{3}}, \tag{2.74}$$

with μ_{n} being the electron mobility and ε the permittivity of silicon. In the energy range of concern, $R_{\text{rep}} \ll R_{\text{diff}}$, hence the electrostatic repulsion is negligible. From this fact follows the important fact that the volume of the charge cloud does not depend on the photon energy.

The diameter of the cloud when it reaches the storage position can be estimated if the drift time t is expressed as a function of the detector thickness d and the voltage difference V applied to the two sides of the detector:

$$D = 2R_{\text{diff}} = 6\sqrt{2D_{\text{n}}\frac{d^2}{\mu_{\text{n}}V}} = 6d\sqrt{\frac{2kT}{qV}}. \tag{2.75}$$

If relevant values are plugged in (see § 2.4.1 for a physical description of the MXT detector), one finds $D \lesssim 40\,\mu\text{m}$, which is smaller than a pixel ($75\,\mu\text{m} \times 75\,\mu\text{m}$ for MXT).

If a photon creates an electron cloud that drifts approximately towards the center of a pixel, the charge will be stored in that pixel alone. If it is off center, the charge will be accumulated in two or more pixels. This is called *split event*. Due to the geometry of the problem and the above consideration about the cloud dimensions, a photon cannot induce a signal in more than four adjacent pixels arranged in a square-like shape. A straightforward consequence is that only some of the triple and quadruple events can be accepted. This fact is

[5]To this conclusion, one arrives by solving the diffusion equation via Fourier transforms with a δ-density profile as initial condition.

[6]This can be achieved by solving the continuity equation for s spherically-symmetric electric charge distribution.

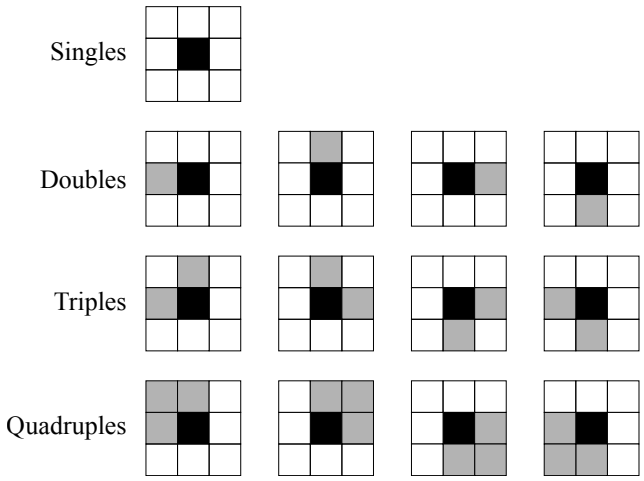

Figure 2.19 – Allowed patterns for a split event. The darkest pixel in each figure is the one holding the largest charge. Grey pixels hold the rest of the electrons. White pixels are below the threshold.

illustrated in Fig. 2.19.

The incoming position of the photon is not the only factor defining the *multiplicity* of an event. Indeed, if a pixel holds a charge that is below or compatible with the low-level threshold E_{thr} (§ 2.3.3.3), it is discarded during the analysis and not recognized as part of a split event: as a result, the measured multiplicity will be smaller (Fig. 2.20 and 2.21). This effect also depends on the photon energy E_γ, which defines the total number of electrons that are divided among the pixels. Dennerl et al. (2012) experimentally found that the true dependence is actually on the *relative threshold*, i.e. the ratio $E_{\mathrm{thr}}/E_\gamma$. Since the photon energy is estimated as the sum of the energies deposited in the pixels being part of the same split event, this phenomenon increases the uncertainty on E_γ.

2.3.2.5 Pile-up

CCDs *integrate* the image over a certain period of time t_{int}, i.e. they accumulate charges for t_{int} before readout. Since X-rays deposit a charge proportional to their energy in the detector (§ 2.3.1.3), it is important to be able to keep track of their energy, in order to carry out spectroscopic studies.

If two (or more) photons hit the same pixel during integration, the energy associated to the deposited charge will equal the sum of the two photon energies. This phenomenon is called *pile-up*. Although in case of a purely

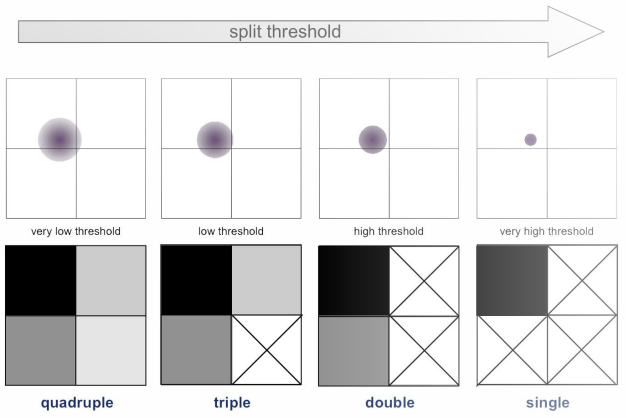

Figure 2.20 – Effect of the low-energy threshold on the measured event multiplicity. The upper row shows the shrinking of the apparent extension of the charge cloud as the energy threshold increases, as illustrated in Fig. 2.21b. The lower row presents the corresponding change in measured event multiplicity. (Dennerl et al., 2012)

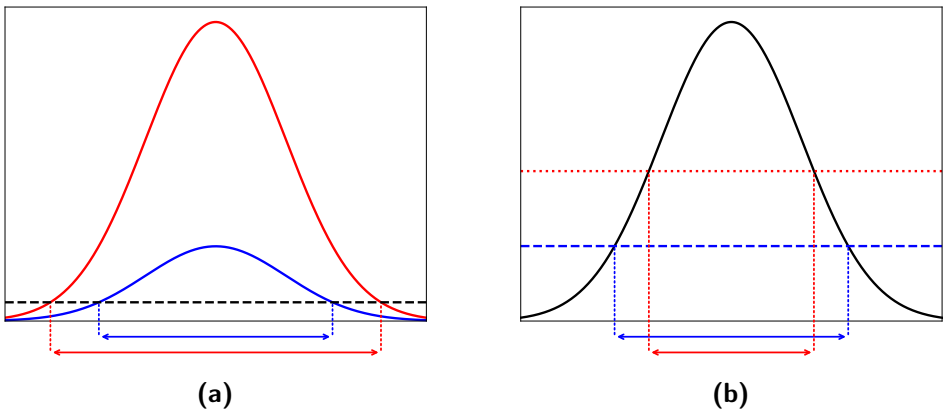

Figure 2.21 – Effect of the low-energy threshold on the perceived extension of a charge cloud. a) The same threshold applied to two Gaussian profiles with different normalization but same σ makes the two have different apparent dimensions. b) A higher threshold makes a Gaussian profile look smaller. In both cases, the effect has been exaggerated for illustration purposes.

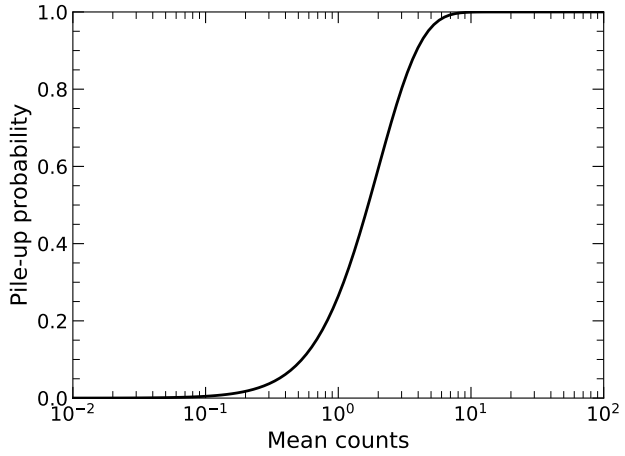

Figure 2.22 – Probability of pile-up as a function of the mean number of counts per pixel.

monochromatic source this is hardly a problem, in the general scenario of a more complex source spectrum disentangling the contributions of every photon or distinguishing between superposing events from single more energetic ones may be very difficult or even impossible. Pile-up is therefore undesirable.

Let us consider a source of photon flux $F(E)$ for simplicity. The average number of counts (no charge splitting is being considered here) per pixel of area A_{pixel} in a frame is

$$\lambda = t_{\text{int}} A_{\text{pixel}} \int F(E)\, \mathrm{d}E, \tag{2.76}$$

where the integral is performed over the energy range in which the detector is sensitive. The probability of observing k counts in a pixel follows a Poisson distribution

$$P(k;\lambda) = \frac{\lambda^k}{k!} e^{-\lambda} \tag{2.77}$$

The probability of two or more photons hitting the same pixel during integration is therefore equal to

$$P_{\text{pile-up}}(\lambda) = \sum_{k=2}^{\infty} \frac{\lambda^k}{k!} e^{-\lambda} = 1 - (1+\lambda)\, e^{-\lambda}. \tag{2.78}$$

Fig. 2.22 shows a plot of eq. (2.78). In it, three regions are identifiable.

- *Single-photon counting* ($\lambda < 0.1$). It is the preferred regime for spectroscopic studies, since the energy of each photon can be reconstructed;

- *Integration* ($\lambda > 0.1$). Pile-up becomes dominant very fast and the detector is integrating the flux, essentially acting as a photometric device, with almost no information left about the energy content of the photons;

- *Saturation.* The charge per pixel becomes so large that it may start to overflow to the neighboring pixels. The onset of saturation depends on the specifics of the detector under consideration and is defined by its *charge handling capacity.*

In order to limit the operation to the first scenario, one can take advantage of the terms in eq. (2.76).

- Bright sources should be avoided. During laboratory activity, one may be able to tune the photon flux, which in turn is probably not a viable option during astrophysical observation. The installation of filters absorbing the light to which the detector is sensitive but which is of no interest for the particular observation may be considered.

- In case exposure to high fluxes is not avoidable, decreasing the integration time is an effective way to reduce pile-up.

- Smaller pixels are also a very effective way to limit pile-up, although the choice of the dimension of the pixels is influenced by other parameters, such as technology or the angular resolution of the optical system at the focal plane of which the detector is installed.

2.3.3 Detector performances

In the following sections, some figures of merit that allow to quantify the spectral performances of a detector are reviewed, with special regard to pnCCDs, that will be the main topic of this study: quantum efficiency (§ 2.3.3.1), energy resolution (§ 2.3.3.2), low-level threshold (§ 2.3.3.3) and spectral gain (§ 2.3.3.4).

2.3.3.1 Quantum efficiency

In order to be measured, photons have to be absorbed by the sensitive silicon bulk of the pnCCD. Before that, they have to reach the detector in the first place, i.e. survive through layers of materials that may absorb them

and therefore remove them from the beam. By making use of eq. (2.43), one defines the *quantum efficiency* QE as

$$\mathrm{QE} = \underbrace{\left(1 - e^{-\rho_{\mathrm{Si}}\mu_{\mathrm{Si}}d}\right)}_{\text{Si absorption}} \underbrace{\prod_i e^{-\rho_i\mu_i x_i}}_{\text{filter transmission}} , \tag{2.79}$$

where the product goes over all the layers of thickness x_i, density ρ_i and attenuation μ_i the photons pass through before reaching the CCD. Usually, *filters* are purposely placed in front of the detector in order to absorb light that might be harmful for the device, such as in § 1.3.3.3 and § 2.4.1.2.

2.3.3.2 Energy resolution

As was seen in § 2.3.1.3, once a photon is absorbed in a detector, it generates a number of electrons whose average value is given by eq. (2.48). The distribution of the measured charge packets will be therefore peaked around a mean value and have a certain width. Such a feature is known as a spectral line.

Due to the discrete nature of the charge carriers and their production, one can reasonably expect their distribution to follow a Poisson statistics. Furthermore, since the number of electrons generated at each interaction is large (> 270 at 1 keV), the line profile will be well described by a Gaussian curve:

$$G\left(E; E_\gamma, \sigma, A\right) = Ae^{-\frac{(E-E_\gamma)^2}{2\sigma^2}}, \tag{2.80}$$

where E is the photon energy that can be calculated from the deposited charge and E_γ is the center of the distribution (i.e. the real photon energy). It is customary to express the line width in terms of the *Full Width at Half Maximum* ($\mathrm{FWHM} = 2\sqrt{2\ln 2}\sigma \approx 2.35\sigma$) instead of the Gaussian standard deviation, because it is more easily visible and practical to use in an experimental environment.

In X-ray physics, the *energy resolution* is defined as the ratio between the line width FWHM and its center E_γ, measured in percents. In practice, the two values of FWHM and E_γ are just given separately, as energy resolution is normally a function of the energy itself. Equivalently, one may consider the inverse of the aforementioned ratio, in order to have a higher value the sharper the spectral line: this convention is mostly used in other branches of

spectroscopy, such as infrared.

Each of the noise sources described in § 2.3.2 contributes to the width of a spectral line. Since they are considered uncorrelated, they combine in quadrature as

$$\mathrm{FWHM}^2 = \mathrm{FWHM}^2_{\mathrm{Fano}} + \mathrm{FWHM}^2_{\mathrm{transf}} + \mathrm{FWHM}^2_{\mathrm{readout}} \tag{2.81}$$

The following paragraphs contain a brief review of the phenomena already discussed in § 2.3.2 , this time from the point of view of energy resolution.

Fano noise Following directly from eq. (2.51), the contribution of Fano noise to the width of a spectral line of central energy E_γ is

$$\mathrm{FWHM}_{\mathrm{Fano}} = 2.35\sqrt{\epsilon E_\gamma F}. \tag{2.82}$$

Transfer noise By averaging over the total number of transfers N_{transf} in eq. (2.56), the charge transfer inefficiency adds to a spectral line of center E_γ a width of

$$\mathrm{FWHM}_{\mathrm{transf}} = 2.35\sqrt{\epsilon E_\gamma \left(1 - \frac{1}{N_{\mathrm{transf}}} \sum_{n=1}^{N_{\mathrm{transf}}} \mathrm{CTE}^n\right)}. \tag{2.83}$$

If the CTI is so low that the approximation $\mathrm{CTE}^n \approx 1 - n\mathrm{CTI}$ holds true (which is usually the case), then eq. (2.83) can be approximated to

$$\mathrm{FWHM}_{\mathrm{transf}} = 2.35\sqrt{\frac{N_{\mathrm{transf}} + 1}{2}\epsilon E_\gamma \mathrm{CTI}}. \tag{2.84}$$

Readout noise Since the ENC is measured in electrons, the FWHM associated to the electronic or readout noise is simply

$$\mathrm{FWHM}_{\mathrm{readout}} = 2.35\epsilon\mathrm{ENC}; \tag{2.85}$$

Charge sharing noise If a photon charge is split among N_{split} pixels, the signals will be read out separately and later recombined into a single event, whose energy will be the sum of the energies in each pixel. In addition to not being able to correctly estimate the photon energy E_γ if some of the charge is lost below the noise level, as discussed in § 2.3.2.4, each pixel in a split event

will contribute with a term such as eq. (2.85) to the overall noise, for a total of N_{split} in the squared sum, so that, if charge sharing is taken into account, the readout noise becomes

$$\text{FWHM}_{\text{readout}} = 2.35\epsilon\text{ENC}\sqrt{N_{\text{split}}}. \tag{2.86}$$

2.3.3.3 Low-level threshold

As previously seen with eq. (2.59a), during the integration time t_{int}, the leakage current J given by eq. (2.22) will accumulate in each CCD pixel of area A_{pix} a number of electrons equal to

$$N_{\text{J}} = \frac{J}{q} A_{\text{pix}} t_{\text{int}}. \tag{2.87}$$

The presence of those electrons has a double effect on the determination of the charge deposited by incoming photons:

- it adds an offset;
- it affects the uncertainty with a term $\sqrt{N_{\text{J}}}$.

Although the offset can be removed fairly easily from a measured frame, the impact of the noise contribution is more subtle. On the one hand, it raises the overall ENC of the system, contributing to the widening of the spectral lines. On the other, it influences the minimum energy a detector is sensitive to, according to a process already hinted in § 2.3.2.4, and that will now be examined in more detail.

Since the goal of an observation is the study of a light source, one must be able to distinguish between the pixels that have been hit by incoming photons and those containing a charge generated by leakage current. Since every pixel contains at least $N_{\text{J}} \pm \sqrt{N_{\text{J}}}$ electrons, by considering a signal that is a few times, say k, $\sqrt{N_{\text{J}}}$ in an *offset-subtracted* frame, one can isolate the pixels which contain a photon charge from those which do not. Obviously, to this value one must also add the contribution of the total electronic noise ENC of the readout chain. In this way, a *low-energy threshold* is established:

$$E_{\text{thr}} = k\epsilon\sqrt{\frac{J}{q} A_{\text{pix}} t_{\text{int}} + \text{ENC}^2}. \tag{2.88}$$

It is worth noting that the leakage current of eq. (2.87) and (2.88) is not necessarily only described by eq. (2.22), because if, say, a residual infrared/visible/UV light is present and not properly accounted for, its macroscopic effect will be that of a temperature-independent current.

The application of a low-energy threshold has a major drawback, because, if a photon deposits a charge smaller than E_{thr}, it is misidentified as noise. This is particularly relevant in case of split events (§ 2.3.2.4).

2.3.3.4 Spectral gain

At the anode at the base of a CCD column, charge packets are converted to voltage steps and then passed on to the readout chain, where they are amplified and filtered. Eventually, an Analog-to-Digital Converter (ADC) translates the measurements into *Analog-to-Digital Units* (ADU) or *Pulse Height Amplitudes* (PHA) in order to store them in a computer memory. This implies that spectral data are available not as keV or electrons but as ADU, to be converted back to energies. The *spectral gain*, measured in $\mathrm{eV\,ADU^{-1}}$, is the factor that enables this conversion.

Ideally, the spectral gain is the only thing one needs to *calibrate* a spectrum, i.e. to allow the correspondence between ADU and eV. However, this is usually not the case and an offset must be taken into account as well, sometimes along with one or more parameters $\theta_{\mathrm{n.l.}}$ combined in a function f representing the non-linearity of the readout system

$$E = \mathrm{gain} \times \mathrm{ADU} + \mathrm{offset} + f\left(\mathrm{ADU}; \theta_{\mathrm{n.l.}}\right). \tag{2.89}$$

It is worth noting that, since the conversion from energy to ADU is affected by the complete readout chain, the gain depends on the input channel of the electronics. This is particularly relevant in case of a pnCCD, in which each column has its own anode and is connected to a separate ASIC input, in order for the signals to be processed in parallel. As a consequence, the content of each pixel must be corrected for the column-dependent gain before any combination, which is especially important for split events.

2.4 The MXT Detector Assembly

After discussing the underlying physics, working principles and figures of merit that define its performances, a detailed description of the MXT Detector Assembly is provided. An overview of its components was already presented in § 1.3.3.2. The rest of the chapter shall now be dedicated to the analysis of the properties of both the MXT detector itself (§ 2.4.1) and its ASIC (§ 2.4.2). Finally, the various steps of the complete detection chain of the system will be laid out (§ 2.4.3).

2.4.1 The MXT detector

Heritage of the European Photon Imaging pn-Camera (EPIC-pn) on board ESA's X-ray Multi Mirror (XMM) mission (Strüder et al., 2001), the MXT detector was provided by the Max-Planck-Institut für extraterrestrische Physik (MPE) and originally developed within the scope of the DUO and ROSITA missions (Meidinger et al., 2004, 2006a,b), and further improved for the eROSITA mission (Meidinger et al., 2010a,b).

2.4.1.1 Physical characteristics

The MXT detector is a 450 µm-thick fully-depleted back-illuminated frame-store silicon pnCCD. A schematic is shown in Fig. 2.23, while Tab. 2.1 summarizes its most relevant features. As a pnCCD, the basic design and working principles described in § 2.2.2 still hold true, despite a few notable differences.

- The SiO_2 insulating the shift registers from each other was replaced with Metal-Insulator-Semiconductor structures, consisting of a 3000 Å-thick SiO_2 layer, a 1450 Å-thick Si_3N_4 layer above that and a 10 000 Å-thick Al layer on top, the silicon of the pnCCD itself completing the MIS capacitor at the bottom. Similar structures allow to isolate the anodes as well. Normally operated at 0 V, their voltage can be manually lowered to mitigate the effects of ionizing radiation damage (§ 4.2.2), in case the accumulation layer of electrons underneath the MIS gates, which normally helps insulate the electrodes from each other, becomes so important that it interferes with the transfer.

- The detector is surrounded by reverse-biased shallow p-implantations

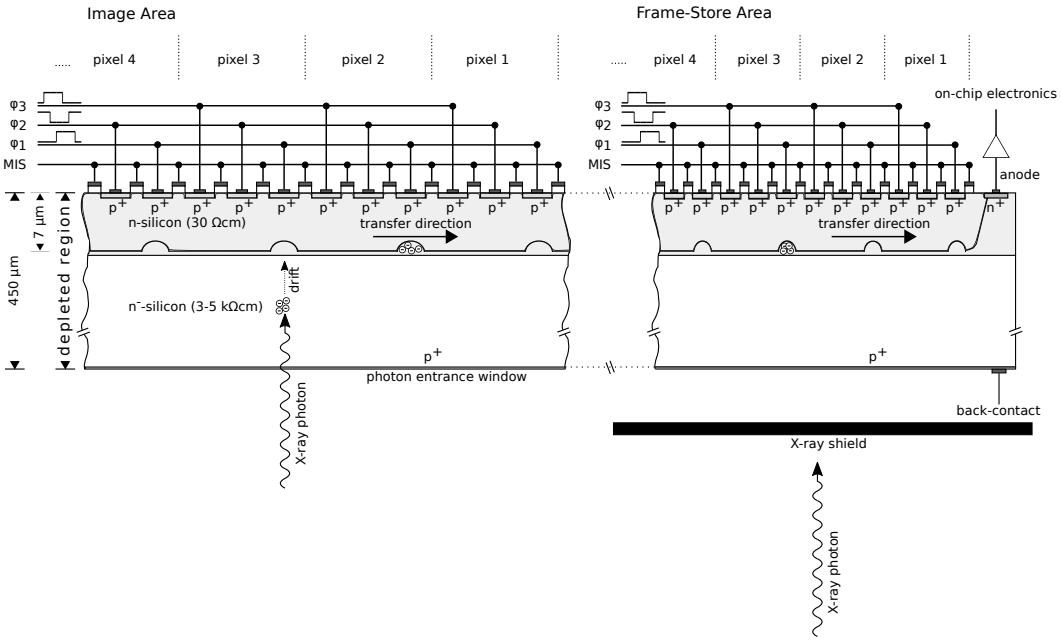

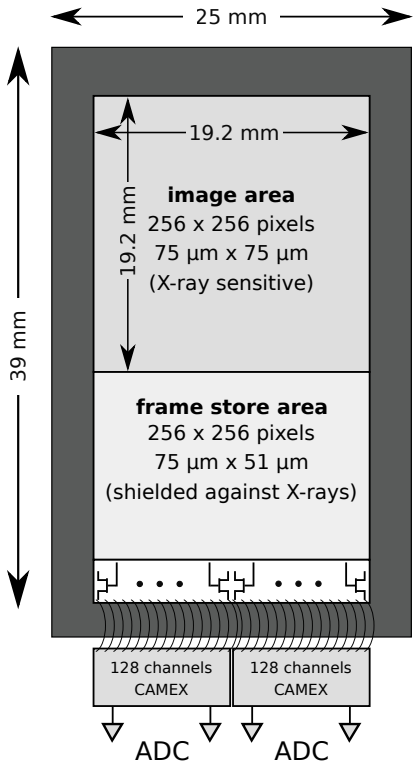

Figure 2.23 – Schematic of the MXT pnCCD detector. a) Cross-section along the transfer direction. b) Top view. Adapted from Meidinger et al. (2004).

Table 2.1 – Details of the MXT detector system, according to the baseline of the instrument.

Detector type	Frame-store pnCCD
Total surface	$6\,\mathrm{cm}^2$ ($19.2\,\mathrm{mm} \times 32.3\,\mathrm{mm}$)
Active area	$4\,\mathrm{cm}^2$ ($19.2\,\mathrm{mm} \times 19.2\,\mathrm{mm}$)
Pixels	256×256 (image), 256×256 (frame-store)
Pixel size	$75\,\mu\mathrm{m} \times 75\,\mu\mathrm{m}$ (image) $75\,\mu\mathrm{m} \times 51\,\mu\mathrm{m}$ (frame-store)
Charge handling capacity	10^5 electrons per pixel
Thickness	$450\,\mu\mathrm{m}$
Sensitive thickness	$450\,\mu\mathrm{m}$
Quantum efficiency	$\geq 90\,\%$ in $1 - 10\,\mathrm{keV}$
Energy resolution	FWHM $(1.5\,\mathrm{keV}) = 80\,\mathrm{eV}$
CTI	10^{-5} at $6\,\mathrm{keV}$
Readout	2×CAMEX 128MJD (128 channels each)
Integration time	$100\,\mathrm{ms}$ per frame
Fast-transfer time	$100\,\mu\mathrm{s}/4\,\mathrm{cm}^2$
Readout time	$10\,\mathrm{ms}/4\,\mathrm{cm}^2$
Frame rate	$10\,\mathrm{frame\,s}^{-1}$
Out-of-Time events	$0.2\,\%$
Operating temperature	$-65\,^\circ\mathrm{C}$ ($-80\,^\circ\mathrm{C}$ to $-60\,^\circ\mathrm{C}$)
Power dissipation	$200\,\mathrm{mW}$

performing the role of *guard rings* (*outer guard rings* or `OGR`), which prevent charges from the undepleted exterior of the die from entering the detector. A similar structure is placed around the anodes for the same reason (*guard rings of the anodes* or `GRA`).

- CTI was reduced thanks to a narrowing of the transfer channel through a second deep phosphorous implantation which limits the lateral spread of charges.

- Deep p^+-implants are present between the channels (channel stops).

In line with the frame-store design already anticipated in § 2.2.2.4, the MXT detector is divided into two regions, an *image area*, which is exposed to X-rays during integration, and a *frame-store area*, which is on the contrary shielded against X-rays by the MoCu (§ 1.3.3.2). Both regions are divided into 256 × 256 pixels, measuring 75 µm × 75 µm and 75 µm × 51 µm in the image and frame-store regions respectively. This translates into an active area of 19.2 mm × 19.2 mm and a total detector surface of 19.2 mm × 32.3 mm. Combined with the 1.15 m focal length of the telescope, each pixel of the image area covers 13 arcsec × 13 arcsec, resulting in a total field of view of 57 arcmin × 57 arcmin.

A high voltage $V_{\mathrm{HV}} = -220\,\mathrm{V}$ is applied to the entrance window, whereas the phases are operated between $-17\,\mathrm{V}$ and $-23\,\mathrm{V}$ ($-16\,\mathrm{V}$ and $-22\,\mathrm{V}$ in the frames-store): this ensures full depletion of the detector and an internal drift field of the most effective shape for charge transfer, with a minimum at about 7 µm below the front side, corresponding to the projected range of the phosphorous ions used in the fabrication of the guiding channels.

2.4.1.2 On-chip optical filter

In accordance to what has been previously stated about the properties of pnCCDs, the detector is sensitive to visible and UV light as well as to X-rays. To protect it from saturation, an optical *on-chip filter* is deposited directly on the entrance window of the detector. Composed of three layers (100 nm of Al, 30 nm of SiO_2 and 40 nm of Si_3N_4), it has a transmission below $\sim 10^{-8}$ for $100\,\mathrm{nm} < \lambda < 800\,\mathrm{nm}$, and therefore it efficiently blocks visible light (Fig. 2.24). It may be operated jointly with the filter housed in the calibration wheel for protection against UV light as well (§ 2.4.2.2).

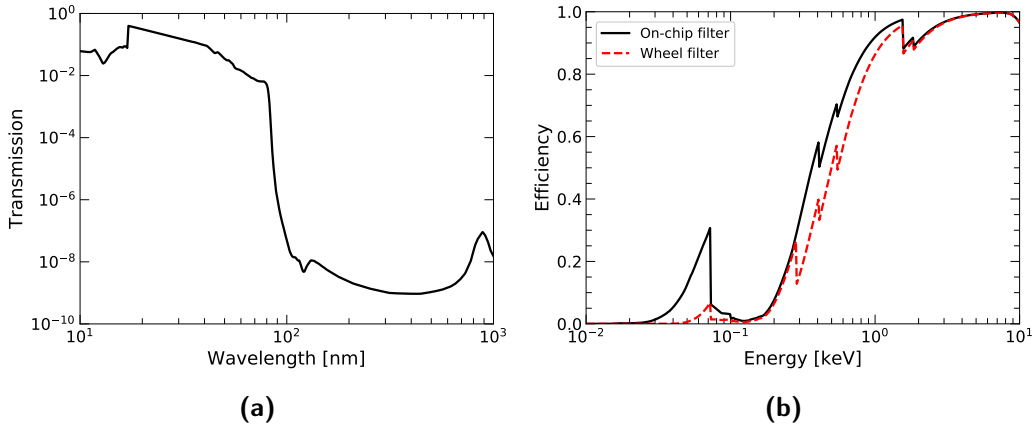

Figure 2.24 – Performances of the optical light filter placed on the chip of the MXT detector. a) Transmission of the on-chip filter as a function of wavelength in the UV/visible band. b) Quantum efficiency of the MXT detector when the on-chip filter is taken into account; the two curves also show the effect of the use of the UV filter of the calibration wheel (§ 2.4.2.2). Data available at `https://refractiveindex.info/` and `http://henke.lbl.gov/optical_constants/filter2.html`.

2.4.1.3 The first FET

As was the case for XMM/EPIC-pn, each of the columns of the MXT detector is equipped with its own anode. In addition, implanted directly on the silicon die is a *n*-channel JFET per column, which provides the first amplification stage, as well as a continuous reset of the anode itself. The *n*-channel JFET, also called *first FET* (Fig. 2.25) is operated in *source follower* mode, its drain voltage and current being supplied externally by the CAMEX ASIC. It is worth noting that the absence of wire-bonds between the anode and the first amplification stage ensures a low parasitic capacitance and by extension a low noise. Furthermore, being entirely made out of *pn*-junctions makes this first amplification stage resistant to ionizing radiation, just like the rest of the detector.

Fiorini & Lechner (1999) showed that the peculiar architecture of the transistor generates a gate leakage current I_{G} which is dependent on both drain-source current I_{DS} and voltage V_{DS} in a way explainable only through a *weak avalanche multiplication* mechanism. In this phenomenon, I_{DS} electrons flowing in the JFET channel are accelerated by V_{DS} and impact against the the atoms of the depleted region ionizing them: this creates holes that can flow to the gate, hence contributing to the gate current I_{G}.

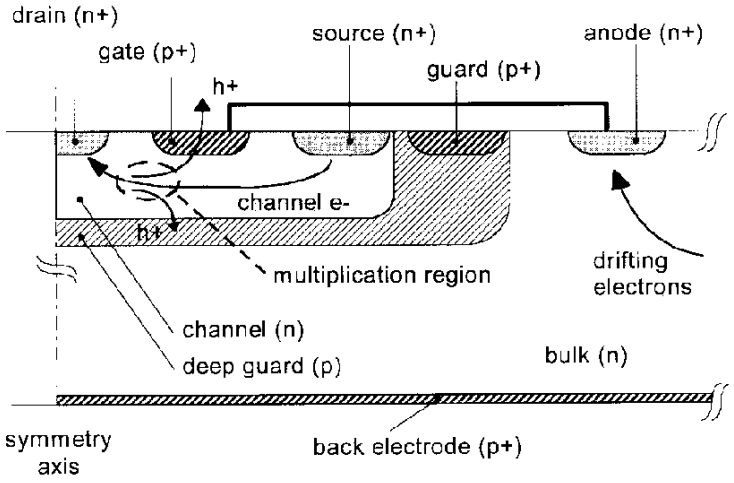

Figure 2.25 – Cross section and reset mechanism of the integrated n-JFET (first FET). (Fiorini & Lechner, 1999)

The source follower configuration in which the transistor is operated ensures the self-regulation of this process. Whenever a charge packet is transferred to the anode, it makes the electrical potential V_{DG} of the gate, to which the anode is routed, drop with respect to the drain. As usual in a source follower, the source voltage drops as well, because the increased drain-gate voltage difference makes the depletion region expand and the conductive channel contract, which in turn increases V_{DS} given that I_{DS} and V_{drain} are forced to be constant by the ASIC: this allows the amplification (principle of the charge-regulated resistor). At the same time, under a stronger V_{DS}, the electrons of I_{DS} are more accelerated and thus the effect of the impact ionization events is enhanced, resulting in a larger positive hole current to the gate, also aided by an increased V_{DG}. The positive charges flowing to the gate of the transistor, and by extension to the anode of the CCD column, recombine with the electrons and raise the gate potential. The above reasoning can be repeated in reverse, the net effect being a continuous reset applied to the anode, occurring on a timescale that nevertheless allows the readout by the ASIC. By taking advantage of this phenomenon, the capacitance arising from the circuitry of an explicit reset mechanism can be saved, improving the overall noise performances.

2.4.2 The CAMEX

The *CMOS Amplifier and MultiplEXer* or *CAMEX* is the Application Specific Integrated Circuit (ASIC) used for the readout of the pnCCD of MXT

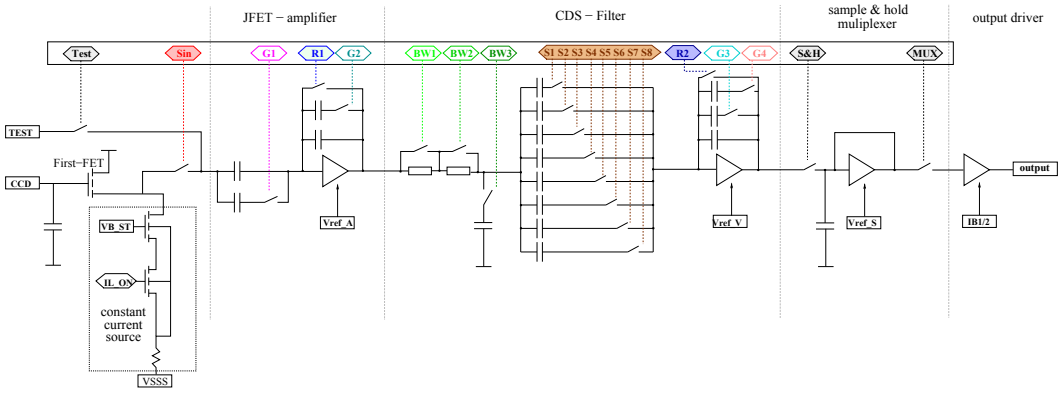

Figure 2.26 – Schematic outline of a single CAMEX channel. (Schanz, 2017)

and bias of its first FETs. Originally developed for the focal plane of XMM's EPIC-pn (Strüder et al., 1990, 2001), it was greatly improved in preparation for the eROSITA mission (Herrmann et al., 2007, 2008). The CAMEX is fabricated with standard 0.35 µm CMOS technology in a 5 V process.

Two 128-channel CAMEX (CAMEX 128MJD) are required for the parallel readout of all the 256 columns of the pnCCD. Each channel, whose schematic is shown in Fig. 2.26, is composed of a JFET amplifier with programmable gain, a filtering stage based on a Correlated Double Sampling (CDS) filter, and a sample-and-hold stage. Signals exiting the channels are eventually multiplexed to a single differential output buffer. In the following, the various components shall be analyzed in more detail, with constant reference to Fig. 2.26 for the names of the ASIC registers.

2.4.2.1 First FET biasing

As previously mentioned, the CAMEX biases the first FET directly implanted on the CCD die, and this in turn provides the first amplification stage and the continuous reset of the anode. To do this, the CAMEX fixes the drain voltage and regulates the current through the gate voltage of another transistor (`VB_ST`), which can be manually fine-tuned to maximize the amplification. Another transistor (`IL_ON`) allows to switch off the first FET, when the system goes into power-safe mode (§ 2.4.2.5).

2.4.2.2 The filtering stage

Every CAMEX channel is equipped with a gain-selectable n-JFET preamplifier (`G1`, `G2`) as well as a passive low-pass filter (`BW1` to `BW3`). However, the main filtering and amplifying stage is represented by the *eight-fold Correlated Double Sampling* (8×CDS) filter, whose working principle is described below.

- At the beginning, both reset switches `R1` and `R2` are closed, so that no charge is present on the CDS capacitors. Then `R1` is opened to allow the accumulation of new charges.
- Before the charges are transferred to the anode of the CCD column and by extension to the input of the CAMEX, the *baseline* is sampled by alternatively closing (and immediately after opening) the `S1` to `S8` switches, while maintaining the reset switch `R2` closed. This way, a charge $C_{\mathrm{CDS}}V_{\mathrm{b}}$ is accumulated on each of the eight capacitors (which are assumed to be equal).
- As soon as the charge packets are shifted to the input, `R2` is opened.
- When the signal-plus-baseline potential $V_{\mathrm{b+s}}$ is applied at the beginning of the CDS, the eight-fold sampling takes place again. However, this time the capacitors are already partially charged with $C_{\mathrm{CDS}}V_{\mathrm{b}}$, thus they only gain a charge corresponding to $C_{\mathrm{CDS}}\left(V_{\mathrm{b+s}} - V_{\mathrm{b}}\right)$. Since `R2` is now opened, the current responsible for that charge must flow through the feedback capacitors C_{f} of the CDS op-amp, which get charged, so that at the output of the CDS the voltage equals $8 \times \frac{C_{\mathrm{CDS}}}{C_{\mathrm{f}}}\left(V_{\mathrm{b+s}} - V_{\mathrm{b}}\right)$.

The procedure has the effect of removing the baseline from the signal, as well as amplifying the measurement as many times as the number of taken samples.

The CDS decreases the bandwidth by integrating (low-pass) and differentiating (high-pass), hence attenuating the contribution of white noise (§ 2.3.2.2). More quantitatively, given a signal $x\left(t\right)$ sampled $N = 8$ times at a frequency $1/T$ from which $N = 8$ samples previously taken are subtracted

$$x\left(t\right) \approx \frac{1}{N}\sum_{n=0}^{N-1}\left[x\left(\left(n+N\right)T\right)\delta\left(t-\left(n+N\right)T\right) - x\left(nT\right)\delta\left(t-nT\right)\right], \quad (2.90)$$

the complex transfer function of the CDS then writes (Buttler et al., 1990;

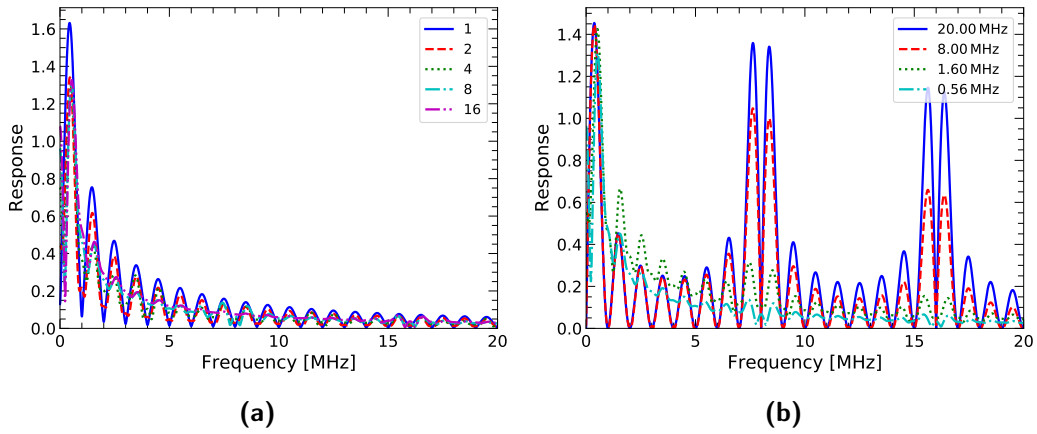

Figure 2.27 – Transfer function of a system composed of a low-pass and a CDS filter. a) Transfer function for varying number of samples taken by the CDS filter. b) Transfer function for different bandwidths of the low-pass filter.

Porro et al., 2007)

$$H_{\mathrm{CDS}}(s) = \frac{1}{N}\sum_{n=0}^{N-1}\left[e^{-(n+N)Ts} - e^{-nTs}\right], \tag{2.91}$$

where s is the complex frequency of the Laplace transform. In both eq. 2.90 and 2.91, the sum was divided by the number of samples N for normalization purposes. The full transfer function of a single CAMEX channel in frequency domain must also take into account the bandwidth limitation of the low-pass filter:

$$H_{\mathrm{BW}}(s) = \frac{1}{1+\frac{s}{\mathrm{BW}}}. \tag{2.92}$$

Therefore, one obtains

$$H_{\mathrm{tot}} = H_{\mathrm{CDS}} H_{\mathrm{BW}}. \tag{2.93}$$

Fig. 2.27 shows an example of eq. (2.93).

From the description of the CDS filter, it is obvious that the switches inside each CAMEX channel change status during operation, hence its response changes as well: the CAMEX is a *time-variant circuit*. Signals arriving at different times are not necessarily processed in the same way and will not have the same effect on the final measurement: in particular, they will affect the result according to the time difference between their arrival and the measurement time, which, for the case under study, corresponds to the moment

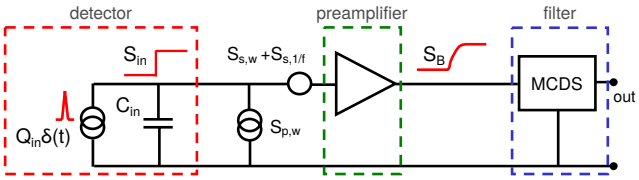

Figure 2.28 – Schematic of a detector circuit containing a CDS filter. This is equivalent to Fig. 2.16, used in the noise calculations.

the *sample-and-hold* stage opens. For this reason, for time-variant circuits, it is customary to define the *weighting function* as the function of time which gives the output at a specific measurement time T_{m} for an input arrived at time t (Gatti & Manfredi, 1986; Porro et al., 2007). The weighting function is for time-variant circuits the equivalent of the impulse response in case of time-invariant circuits (§ 2.3.2.2).

To calculate the weighting function of the CAMEX, let us simplify the circuit as in Fig. 2.28, with the detector reduced to a δ-current source in parallel to the input capacitance C_{in}: each $Q\delta\left(t\right)$ will produce a voltage step $S_{\mathrm{in}} = Q_{\mathrm{in}}/C_{\mathrm{in}}$ at the input of the circuit. It is worth noting that this is valid for both the *scientific signal* and the *noise*. Due to the passive low-pass filter, the bandwidth of each incoming signal will be limited by an exponential rise of time constant 1/BW

$$S_{\mathrm{B}} = S_{\mathrm{in}}\left(1 - e^{-\mathrm{BW}t}\right). \tag{2.94}$$

Moreover, the presence of the reset `R1` means that every input before the time T_{r} in which `R1` is released, will be identically zero.[7]

The weighting function of the circuit can be written as (Porro et al., 2007)

$$W_p\left(t\right) = W_p^*\left(t\right) h\left(t + T_{\mathrm{CDS}}\right), \tag{2.95}$$

where T_{CDS} is when the CDS filter is activated, $h\left(t\right)$ is the Heaviside function

$$h\left(t\right) = \begin{cases} 0 & t < 0 \\ 1 & t \geq 0 \end{cases} \tag{2.96}$$

[7] In reality, it will be damped with a very short time constant τ_{R}.

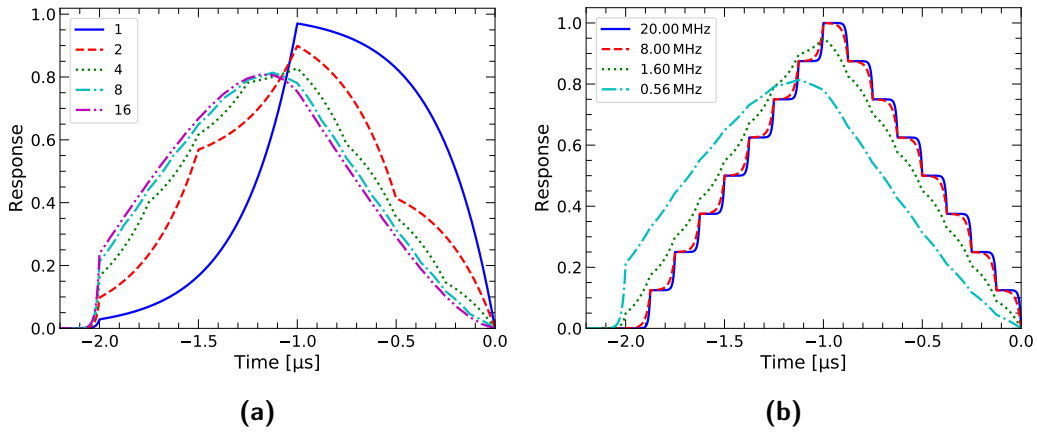

Figure 2.29 – Weighting function of a system composed of a low-pass and a CDS filter. a) Weighting function for different samples taken by the CDS filter. b) Weighting function for different low-pass filter bandwidths.

and $W_p^*(t)$ is the weighting function of the low-pass and CDS system

$$W_p^*(t, T_\mathrm{m}) = \frac{1}{N}\sum_{n=0}^{N-1}\Big[h\big(T_\mathrm{m} - (t+nT)\big)\Big(1 - e^{-(T_\mathrm{m}-(t+nT))\mathrm{BW}}\Big) - h\big(T_\mathrm{m} - (t+(n+N)\,T)\big)\Big(1 - e^{-(T_\mathrm{m}-(t+(n+N)T))\mathrm{BW}}\Big)\Big], \quad (2.97)$$

with T being the sampling time of the CDS filter and T_m the measurement time. Example are shown in Fig. 2.29.

The subscript p in eq. (2.95) and (2.97) stands for *parallel*, because the function has been calculated for a source in parallel with the input. Like the pulse response of time-invariant circuits, different functions can be calculated according to the specific (noise) source considered (e.g. white series voltage noise, white parallel current noise, $1/f$ series voltage noise etc.), all eventually related to W_p through operations such as derivation and convolution (Pullia, 1998). Indeed, exactly like the pulse response, the weighting function can be used to calculate the contribution of the different sources on the final noise (§ 2.3.2.2).

As it is clear from Fig. 2.27b and 2.29b, the choice of BW is crucial because the lower the bandwidth, the smaller the noise contribution (Porro et al., 2007). However, at the same time, the lower the bandwidth, the wider the weighting function: at a certain point the maximum value is not reached before readout and the weighting function may even stretch outside the operating time window

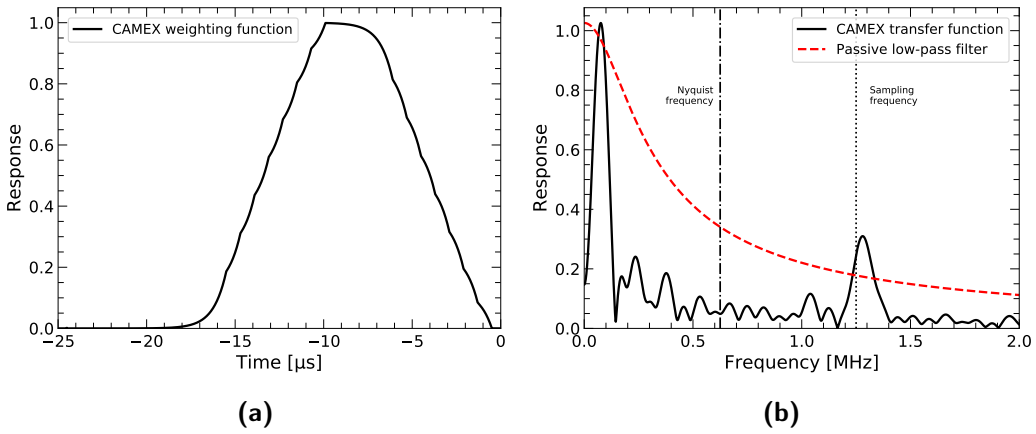

Figure 2.30 – Response of the CAMEX ASIC with sampling time $T = 800\,\text{ns}$, bandwidth $\text{BW} = 220\,\text{kHz}$ and a $3\,\mu\text{s}$ flat top. a) Weighting function. b) Transfer function.

of the CDS filter T_{CDS} and be truncated by the preamplifier reset. Once the proper timing (to be discussed in § 2.4.3.2) and $\text{BW} = 220\,\text{kHz}$ are taken into account, the final forms of eq. (2.93) and (2.95) for MXT become those plotted in Fig. 2.30. It is worth noting that Fig. 2.30a features a $3\,\mu\text{s}$ flat top in the middle of the operating window: this corresponds to the shift of the CCD line to the anodes and the delay for the input JFET to settle. From the shape of the weighting function, it is clear that the highest sensitivity is to signals arriving at the input at that very moment, as it is expected since eq. (2.95) is valid for parallel sources, just like the CCD itself was schematized in Fig. 2.28.

2.4.2.3 The test input

Each CAMEX channel is provided with a test input on which a charge may be deposited without the necessity of a working detector connected to the ASIC input. The ASIC can be programmed to inject the charge on every $1+3n$, $2+3n$ or $3+3n$ channel, hence potentially on all the 128 channels. This may simulate the readout of a CCD or be used for inspection purposes. This functionality is useful for functional tests before mounting the actual detector.

2.4.2.4 The internal registers

As pointed out on a few occasions in § 2.4.2.2, the status of many switches in each CAMEX channel varies during readout. This process is controlled by an *internal sequencer* (iSEQ), which acts on all the 128 channels of the

ASIC at the same time and is driven by a *sequencer clock*, or SCLK. The internal sequencer has a static and a dynamic register, both of which must be reprogrammed every time the CAMEX is powered up. A switch is closed when its corresponding bit is high.

The static register is made out of 54 bits. The first 14 set the gain and bandwidth (`G1`–`G4` and `BW1`–`BW3`), the multiplexing mode, the output current and polarity, and the configuration of the test injection (§ 2.4.2.3). The other 40 define the power supply of the various amplifiers (`Vref_A`, `Vref_V` and `Vref_S`) and for the differential output buffer (`IB_1`, `IB_2`), thanks to the presence of a programmable bias master reference inside the CAMEX.

The dynamic register is made out of 64 lines, each one composed of 16 bits and regulating the status of

- the connection to the CCD `Sin` (1 bit);
- the preamplifier reset `R1` (1 bit);
- the CDS capacitor switches `S1-S8` (8 bits);
- the CDS reset `R2` (2 bits);
- the connection to the sample-and-hold stage `S&H` (2 bits);
- the connection to the output driver `MUX` (1 bit);
- a parity bit `P` (1 bit).

The role of the parity bit is fundamental from an housekeeping perspective. Since the iSEQ registers are not accessible from the outside during the detector readout, an additional (visible) bit called `TG` is introduced to monitor the operation. Since at every instant `TG` is calculated as the exclusive OR of the line being executed as well as the static register, the parity bit `P` is chosen to make `TG` have a known value at each time: by comparing `TG` to the predefined pattern, one can check the occurrence of radiation-induced random changes in the status of each line (§ 4.2.2.3).

2.4.2.5 Power-safe mode

One disadvantage of the CAMEX is its relatively high power consumption of 660 mW per ASIC, which implies a high heat dissipation. This may cause

issues when trying to cool down a detector system, if the available cooling power is limited (like in MXT). For this reason, the main (analog) stages of the CAMEX are switched off during integration, by means of the `VR_ON` signal, and turned on just for the readout phase for a time $t_{\mathrm{CMX,on}}$. This smaller duty cycle reduces heat dissipation to a factor $t_{\mathrm{CMX,on}}/t_{\mathrm{int}}$ and therefore allows to reach lower temperatures. It is worth noting that the power supply for the digital stages stays up, implying that it is not necessary to reprogram the CAMEX each time, as its registers are not wiped out.

A final remark is that the same reduced duty cycle to limit power consumption is applied to the first FET through the CAMEX-controlled `IL_ON` switch, as already anticipated in § 2.4.2.1.

2.4.3 The MXT detection chain

The following sections describe in detail the complete MXT detection chain, from the integration and fast transfer to the frame-store region (§ 2.4.3.1), to the readout (§ 2.4.3.2) and multiplexing (§ 2.4.3.3) phases. Afterwards, the features of the Front-End Electronics (§ 2.4.3.4) shall be expanded upon and finally the data pre-processing (§ 2.4.3.5) and analysis (§ 2.4.3.6) shall be quickly outlined.

2.4.3.1 The integration and fast transfer

During the $t_{\mathrm{int}} = 100\,\mathrm{ms}$ frame integration, X-ray photons enter from the back side and generate electron-hole pairs inside the depleted volume of the detector. Under the action of the internal drift field, holes move towards the cathodes where they are eventually absorbed, while electrons drift towards the potential minima under the shift electrodes, where they are accumulated along with thermally-generated electrons (leakage current).

As soon as the integration is over, the voltages applied to the transfer registers are changed as in Fig. 2.9 in order to quickly transport the charge packets to the frame-store region (Fig. 2.31). This operation is accomplished within $t_{\mathrm{transfer}} = 230\,\mu\mathrm{s}$, i.e. with a phase period of 900 ns. The central electrodes, i.e. ϕ_2 and ϕ_5, are chosen as the most positive ones when transfer is not occurring.

Since during the fast transfer 256 shifts are performed by all the phases $\phi_1 - \phi_6$, as the charge packets are moved from the image to the frame-store

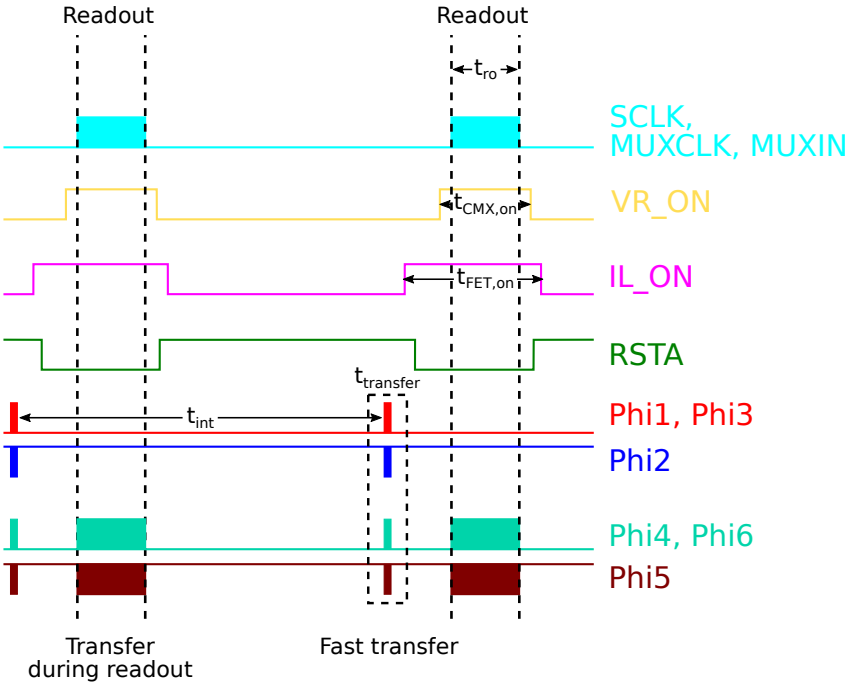

Figure 2.31 – Scheme of the acquisition of frames. Filled rectangles represent fast signals that cannot be resolved at this timescale.

region, those previously present in the latter are transferred to the anodes. Those electrons must therefore be evacuated in order not to damage or saturate the anodes. This is achievable thanks to n-type implants acting as anode reset contacts (`RSTA`, Fig. 2.32). Held at an adjustable non-negative voltage throughout integration up to after this stage (Fig. 2.31), they allow the reset of even massive charges, such as those accumulated by ionizing particles.

Once in the frame-store region, no more photoelectrons can be produced, thanks to the X-ray shield. This means that Out-of-Time (OoT) events, i.e. charges generated by incoming photons outside the integration time window, may occur only during the quick transfer, which effectively reduces their fraction out of the total number of signal events to $t_{\text{transfer}}/t_{\text{int}} = 0.2\,\%$. Since it is an area where charges are simply waiting for readout, the frame-store region's pixels can be smaller than the image area's ones in the direction of transfer, as they do not influence the angular resolution of the instrument.

2.4.3.2 The readout process

The complete readout phase starts by lowering to zero the voltage of the reset anode `RSTA` and powering up the first FET amplifier through `IL_ON`. After

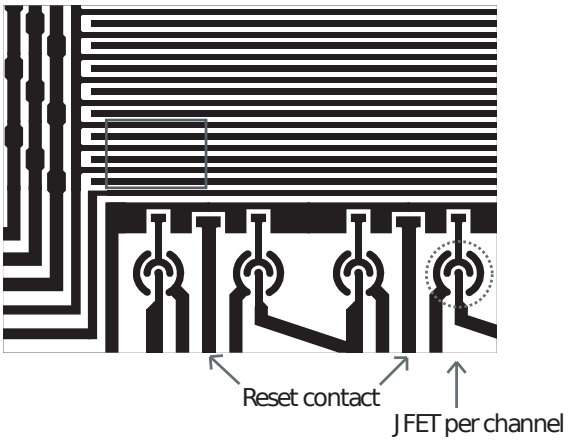

Figure 2.32 – Close-up of the aluminium layer of the frame-store and anode regions of the pnCCD of MXT. On the left, the lines supplying the phases ϕ are visible, while at the bottom of the picture, the n-JFETs and the reset contacts are highlighted. (Meidinger et al., 2004)

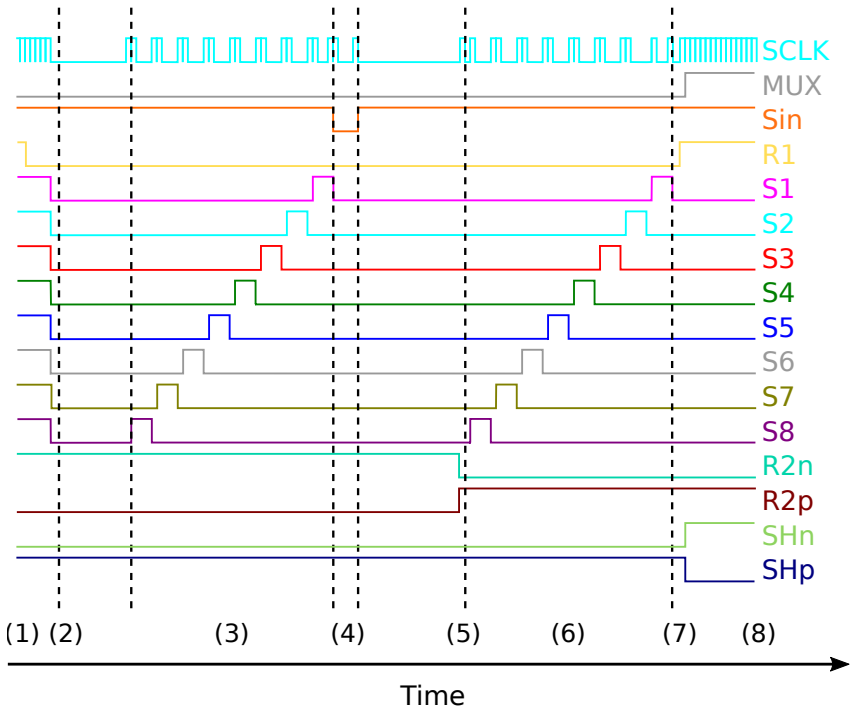

Figure 2.33 – Scheme of the readout of a line. 1) Reset of JFET amplifier and CDS filter. 2) Amplifier reset released. 3) Baseline sampling. 4) Charge shift to the channel input. 5) CDS filter reset released. 6) Signal sampling. 7) Sample-and-hold connected. 8) Waiting for multiplexing.

that, both ASICs are switched on thanks to `VR_ON`. As previously mentioned in § 2.4.2.5, this procedure allows to limit the power consumption of both the first FET and CAMEX to a manageable $P_{\mathrm{FET,on}} = 20\,\mathrm{mW}$ ($t_{\mathrm{FET,on}} = 12\,\mathrm{ms}$, $t_{\mathrm{FET,on}}/t_{\mathrm{int}} = 12\,\%$, $P_{\mathrm{FET}} = 0.65\,\mathrm{mW\,ch^{-1}}$) and $P_{\mathrm{CMX,on}} = 132\,\mathrm{mW}$ ($t_{\mathrm{CMX,on}} = 10\,\mathrm{ms}$, $t_{\mathrm{CMX,on}}/t_{\mathrm{int}} = 10\,\%$, $P_{\mathrm{CMX}} = 5.16\,\mathrm{mW\,ch^{-1}}$) respectively. This is illustrated in Fig. 2.31.

At this point, the actual line-by-line readout may begin for all the 256 CAMEX channels at the same time. This process was already discussed in § 2.4.2.2 when describing the working principle of the CDS filter, and can now be summarized again with reference to Fig. 2.33 and § 2.4.2.4.

1. The connection `Sin` between CAMEX and first FET is closed, as well as the resets of the JFET preamplifier (`R1`) and the CDS op-amp (`R2p` and `R2n`) and capacitors switches (`S1`–`S8`), ensuring the complete discharge of all capacitors.

2. With `R2` still closed, all the other resets are released, ready for sampling.

3. The baseline is sampled by successively closing and opening the CDS capacitor switches `S1`–`S8`.

4. `Sin` is opened and later closed again, the frame-store phases $\phi_4 - \phi_6$ shifting the bottom line to the anodes in the meantime.

5. The CDS reset `R2` is released.

6. The signal is sampled.

7. The sample-and-hold switch `S&H` is closed to charge the corresponding capacitance.

8. `S&H` is opened again and `MUX` connection is established to allow the multiplexing of the measurement.

In the case of MXT, the sampling time T_{CDS} is defined by the CAMEX switch-on time, which is $t_{\mathrm{CMX,on}} = 10\,\mathrm{ms}$ and includes the warm-up time and the parallel processing of a whole frame. Under those considerations, a sampling time of 800 ns was chosen (`SCLK`), implying a pixel processing time of 32 µs, meaning that the readout of a whole frame lasts for about $t_{\mathrm{ro}} = 8\,\mathrm{ms}$.

2.4.3.3 Multiplexing

As soon as the last line of the dynamic register is clocked, i.e. when the analog processing is complete (after bit 63 of the dynamic register), multiplexing of the output buffers begins, driven by a dedicated clock signal known as `MUXCLK`. A single 1 (`MUXIN`) is clocked into the multiplexer register and shifted by one bit at every `MUXCLK`. After two `MUXCLK` hits, the first analog signal of the first channel arrives at the output. According to the position of the 1 in the register, the multiplexer switches close on the rising and falling edge of `MUXCLK`, so that 64 periods are needed to multiplex 128 pixels. After 66 clock cycles, the 1 is shifted to the output signal `MUXOUT`, marking the complete multiplexing of a row.

With a `MUXCLK` frequency of 2.5 MHz (400 ns-period), pixel data can be output every 200 ns, resulting in an output rate of 5 MHz per ASIC or 10 Mpixel s^{-1}. An Analog-to-Digital Converter (ADC) with a period of 100 ns is also implemented per ASIC to ensure an oversampling with a factor of 2.

It is important to notice that the process described so far implies that when the line n of the CCD is being multiplexed, the line $n + 1$ is being processed in the analog channel. This is possible because a full line is output in 25.6 µs (the two CAMEX are multiplexed at the same time), which is shorter than the 32 µs required for the analog processing. This also implies that, although there are 256 rows in a frame, 257 lines have to be multiplexed, the first one being ignored as it is empty because it starts with the analog processing of the first line, and, as was just pointed out, it corresponds to line -1.

2.4.3.4 The Front-End Electronics

After the CAMEX, the readout chain continues with the Front-End Electronics (FEE), whose structure was outlined in § 1.3.3.4. Here, the functions of its three modules, which are outlined in Fig. 2.34, are more closely described.

1. The *Bias* board (`B_BIAS`) is the closest to the focal plane for better noise performances and includes most analog functions:

    - all bias supplies of the focal plane except the high voltage, some being tunable by digital-to-analog converters (DAC): examples are the voltages needed by the first FET and the bias master reference of

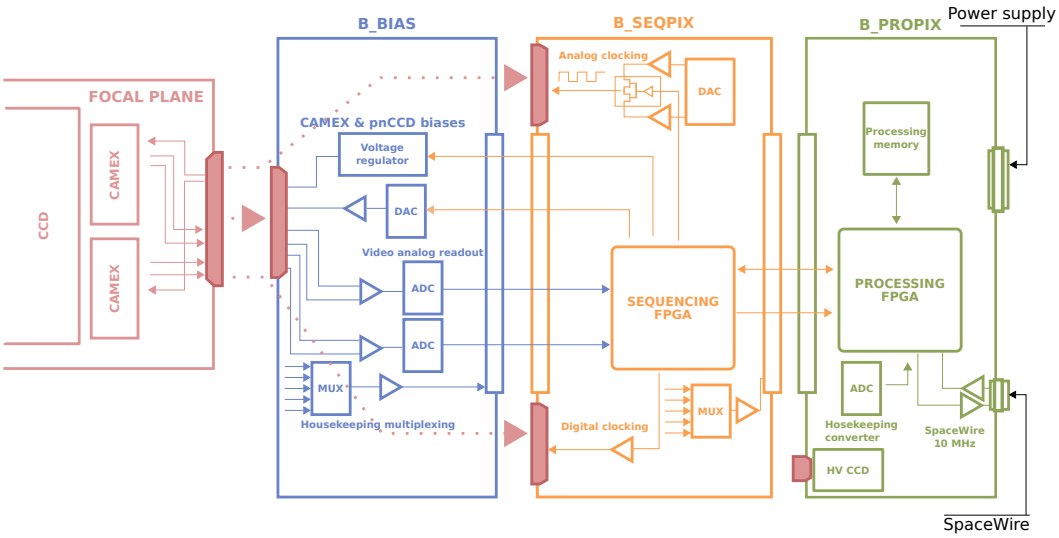

Figure 2.34 – Schematic view of the functions of each FEE board.

the CAMEX, as well as constant voltages for correct CCD operation (e.g. guard rings and MIS gates);

- CAMEX signal adaptation and digitization with two ADCs operating at 10 mega samples per second;
- housekeeping measurements, such as the readout of applied voltages and currents.

2. The *SeqPix* board (`B_SEQPIX`) mainly deals with the readout of the focal plane, providing:
   - CCD and CAMEX clocking ($\phi_1 - \phi_6$, `SCLK`, `MUXCLK`, `MUXIN`);
   - iSEQ programming;
   - the memory storing the output of the two ADCs on `B_BIAS`;
   - the memory for the sequence configurations (internal RAM of the FPGA);
   - housekeeping measurements (e.g. temperature and power supply).
3. The *ProPix* board (`B_PROPIX`) mainly includes the functions for the data processing and the communication interface:
   - a 16 Mbit-SRAM for raw data and correction tables (§ 2.4.3.6);
   - a FPGA to correct, read and write the processing memory and format data containers with full frame or event data (§ 2.4.3.6);

this FPGA is also in charge of the communication with the MDPU (§ 1.3.4);

- a SpaceWire interface for command/control and data transmission;
- the generation of the CCD high voltage via a flyback converter fed by a 50 kHz PWM and followed by a series voltage multiplier;
- housekeeping measurement (e.g. temperature and power supply) and encoding.

It is worth noting that, due to exportation issues, the FEE assembly obeys a completely US-free design. This also explains the presence of two FPGAs on the SeqPix and ProPix boards respectively instead of a single one ensuring the functionalities of both of them. Indeed, measurements and simulations conclude that the operating frequency of the chosen FPGA (model Atmel ATF280) drops as the occupancy in terms of RAM and IOs increases, rapidly bringing it below the 20 MHz required for the 10 ms CAMEX readout. This therefore prevents the merging of the two FPGAs.

2.4.3.5 On-line data pre-processing

The ProPix board has the pivotal role of extracting photon events from the acquired frames and send them to the MXT Data Processing Unit (MDPU, § 1.3.4). To accomplish this task, two steps are necessary, all performed by the board itself: frame correction and event extraction.

The following paragraphs will quickly go through the on-line analysis performed by the FEE, leaving a more detailed discussion to § 3, where the off-line algorithms used in this work are presented.

Frame correction Various components of the analog channels (Fig. 2.26) add different constant values to the signals being processed. At the moment of digitization the resulting effect is the presence of an *offset* superimposed to the output. Furthermore, leakage current is always responsible for a few uniformly-distributed counts per pixel, even in the absence of X-rays. This overall offset must be subtracted from the acquired frames. For this purpose, the FEE accepts an *offset map* O_{ij}, i.e. a value of the offset in ADU for every pixel of row i and column j. The offset map, which is not calculated by the FEE but loaded into its memory by the MDPU, may be taken, for example,

as the pixel-by-pixel average of a stack of N *dark frames*, i.e. images in which no X-ray source is present. Frames must be of course cleaned from outliers before calculations.

After the offset subtraction, the *common-mode noise* must be corrected as well. The common-mode noise arises from the fact that an image is read out in parallel one line after the other. Time-dependent power supply fluctuations of the analog components and cross-talk therefore affect each line in a different way, creating a row-dependent noise. The common-mode map CM_{ik} is calculated as the row-by-row median for each offset-subtracted frame of index k. Since each frame is read out by two CAMEX, the median must be calculated separately for the left- and right-hand side of a frame (so that 512 values per image are computed).[8]

When images are corrected for both offset and common-mode noise, each pixel of the resulting frame F is obtained from the original frame S as

$$F_{ijk} = S_{ijk} - O_{ij} - \mathrm{CM}_{ik}. \tag{2.98}$$

It is worth noting that the offset is temperature-dependent and therefore must be calculated in the same thermal environment as the observation, usually a few moments prior. On the contrary, the common-mode map must be calculated anew for each frame.

Event extraction In order to extract pixels containing charges deposited by photons, one must be able to distinguish signals from noise. In order to do that, the FEE compares the corrected frames F_{ijk} with a *threshold map* T_{ij} (in ADU), so that every pixel for which

$$F_{ijk} > T_{ij} \tag{2.99}$$

is considered part of a photon event and therefore sent to the next analysis steps. As in the case of the offset, the threshold map is not computed by the ProPix board, but loaded into it by the MDPU. For example, it may be taken as K times the pixel-by-pixel standard deviation of N outlier-removed dark frames.

[8]Since the median is computing intensive, a *pseudo-median* is taken instead, as the center of the middle bin of the histogram of the values of each half row.

2.4.3.6 Data processing

As soon as the photon event pixels are extracted from the frames, they are sent to the Data Processing Unit, which formats them into X-band telemetry packets to be sent to the ground. The MDPU also performs on-line source identification, and creates VHF packets for transmission to the Payload Data Processing Unit, i.e. the on-board computer of the satellite. Data processing, which also takes place on ground, consists of pattern recognition and classification (§ 2.3.2.4), ADU-to-energy conversion (§ 2.3.3.4), CTI-correction (§ 2.3.2.3) and split event reconstruction.

It is important to note that the calculation of offset and noise maps require all the pixels of several frames in whihc no X-ray photons are present. Therefore, the FEE provides a second mode of operation, alongside the *event mode* described above, called *full-frame mode*, in which complete images are sent to the MDPU, not only pixels satisfying eq. (2.99). Due to limitations of the Spacewire link between FEE and MDPU, however, full frames are output at half the rate of event-mode frames ($5\,\mathrm{frame\,s^{-1}}$ instead of $10\,\mathrm{frame\,s^{-1}}$), which is achieved by doubling the integration time from $100\,\mathrm{ms\,frame^{-1}}$ to $200\,\mathrm{ms\,frame^{-1}}$.

Finally it must be pointed out that working in event mode prevents the access to pixels that did not survive the cut of eq. (2.99), whose information is lost as they are not part of the output of the FEE. For this reason, the lowest possible threshold map is uploaded to the FEE, with the possibility of imposing additional higher discriminating levels during subsequent data manipulations.

Chapter 3

Operation and data analysis of the MXT detector

In this chapter are presented the first laboratory tests carried out on the first models of the MXT Detector Assembly available for experimental characterization. At the end of it, the answers to some of the main questions on which this thesis is based will be provided, i.e. what the performances of the MXT detector will likely be at the beginning of the SVOM mission and how strongly they will be influenced by operational parameters such as temperature.

After a description of the algorithms used for the analysis of the experimental data (§ 3.1), the tests and results of the two models of the MXT DA studied in this work are presented, i.e. the Engineering Model (§ 3.2) and the Performance Model (§ 3.3). The chapter will end with a summary and discussion of the findings (§ 3.4).

3.1 Data analysis algorithms

In the following are detailed the algorithms used for the analysis of the data gathered during the on-ground laboratory tests performed over the first models of the MXT detector assembly. All the codes are written in Python 3.6 and 3.7 and are inspired to Andritschke et al. (2008), where the equivalent routines employed by the MPE team for the development of the pnCCDs are described.

To enhance processing speed, operations are implemented in multi-threading

mode whenever possible, enabling the exploitation of as many cores as available (or provided) on the machine to process several data files (§ 3.1.1) or spectra (§ 3.1.2) at the same time.

3.1.1 Frame reduction

As previously outlined at the end of the description of the MXT detection chain in § 2.4.3.5, frames acquired by a pnCCD detector must be processed before the information regarding photons becomes accessible. This treatment shall be referred to as *image* or *frame reduction*.

In the next sections, the various steps pf this part of the analysis are to be discussed in a manner similar to what was previously done in § 2.4.3.5.

3.1.1.1 Offset map

During image integration, leakage current[1] accumulates in every pixel of the detector, creating an baseline over which the photons deposit their charges. In addition to that, every analog channel of the ASIC (Fig. 2.26) adds a different constant value to their signals. The two effects combine in an overall *offset* superimposed to the data, which must be appropriately subtracted.

The offset can be easily calculated as a pixel-by-pixel average of several *dark frames*, i.e. images in which no light source has been placed in front of the detector. The use of dark frames is required because charge packets by photons would appear as spikes above the baseline, thus altering the average value, which is, as stated above, independent of the presence of a source. However the same problem occurs if an unintended charge is deposited on some pixels of a dark frame by, say, a passing cosmic ray. Solutions to this issue are discussed in Andritschke et al. (2008) but are not applied in this work, where I opted for a more straightforward approach. Given a *cube of dark frames*, i.e. a succession of images S_k labeled by the subscript k, I define the *offset map* O as the pixel-by-pixel median taken along the temporal direction:

$$O_{ij} = [S_{ijk}]_k^{50\,\%}, \tag{3.1}$$

[1] Although filters are in place to prevent optical light from reaching the detector (§ 2.4.1.2), if visible/UV photons do interact with the device, due to their shear number, they generate so many electron-hole pairs that they are detected as leakage current rather than isolated events.

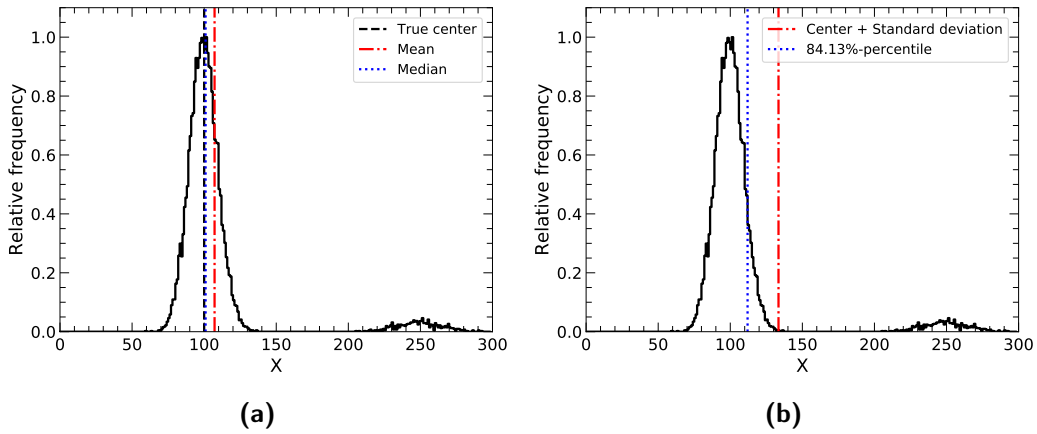

Figure 3.1 – Robustness of the implemented methods to outliers. The assessment is carried out on a main Gaussian distribution (on the left-hand side of each plot) to which a distribution of outliers is added (on the right-hand side of each plot). The mean of the main Gaussian curve is considered to be the *true center* of the event distribution. a) The median of the total distribution is essentially indistinguishable from the true center, whereas the average suffers from the presence of the outliers. b) The 84.13 %-percentile is clearly a better estimator of the 1-σ width of the distribution than the standard deviation.

where $[\cdot]_k^{50\,\%}$ represents the median along the time axis, whereas i and j indicate the line and column of each pixel.

The advantage of the median over a simple (although corrected) mean is its robustness to outliers, i.e. data points that stray significantly from the rest of the distribution (Fig. 3.1). If a large enough number of dark frames is acquired, than the pixel-by-pixel count distribution is sufficiently well defined that outliers such as passing cosmic rays do not influence its median. In practice, approximately one or two hundred dark frames are recorded.

It is worth noting that if the median is used, even photons count as outliers and therefore do not affect the result of the calculation if their flux is sufficiently small. This potentially allows to use photon frames for this step of the analysis without the need for dark images.

3.1.1.2 Noise map

From each of dark frames, the offset map is subtracted, after which the *common-mode noise* is corrected. Due to the way the CCD is read out (one line at a time), short-period time-dependent variations in the references of the analog channels affect equally all the pixels of the same row, while at the same

time their influence changes from one row to the next. This line-dependent noise is calculated as the median along each row of a offset-subtracted frame:

$$\mathrm{CM}_{ik} = [S_{ijk} - O_{ij}]_j^{50\,\%} \tag{3.2}$$

It is important to point out that CM_{ki} must be determined separately for each CAMEX. After the correction of both offset and common mode, a frame is referred to as a *flat frame* F:

$$F_{ijk} = S_{ijk} - O_{ij} - \mathrm{CM}_{ik}. \tag{3.3}$$

The simplest way to estimate the noise is at this point to calculate the pixel-by-pixel standard deviation of the flat dark frames. However, in this case one runs into the same issue with outliers as above. Instead of the method used in Andritschke et al. (2008), I define the *noise map* N as the pixel-by-pixel difference between the 84.13 %-percentile and the median (which should be zero after all the corrections) of the distribution of counts along the time axis:

$$N_{ij} = [F_{ijk}]_k^{84.13\,\%-50\,\%}. \tag{3.4}$$

This approach retains the same robustness to outliers as discussed above while at the same time coinciding with a 1-σ interval in case the distribution is symmetric and Gaussian[2]. Moreover, eq. (3.4) is well defined even in case of an arbitrary asymmetric distribution, which is not the case for the standard deviation.

3.1.1.3 Event extraction

Photon frames S, i.e. images acquired when the detector is exposed to an X-ray source, are corrected according to eq. (3.3), by subtracting offset and common-mode, the former being derived from the dark frames and the latter being calculated on each image under processing:

$$F_{ijk} = S_{ijk} - O_{ij} - [S_{ijk} - O_{ij}]_j^{50\,\%}. \tag{3.5}$$

As already hinted at the end of § 3.1.1.1, photon signals appear as spikes

[2]Given a Gaussian distribution of mean μ and standard deviation σ, the integral from $-\infty$ and $\mu + \sigma$ equals 0.8413.

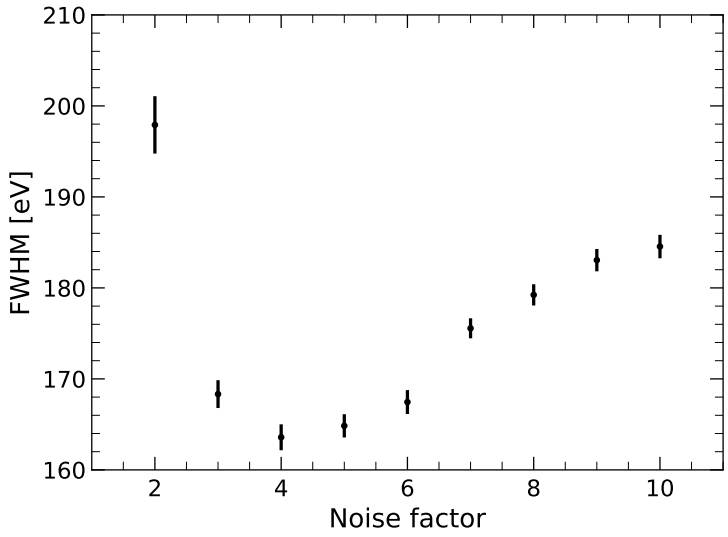

Figure 3.2 – Evolution of the spectral resolution at the Mn-K$_\alpha$ line (5898 eV) as a function of the factor multiplying the noise level defining the threshold for event extraction in eq. (3.6).

which must be separated from genuine noise fluctuations. This is achieved by a pixel-by-pixel comparison with a *threshold map* T, defined as either a fixed value or a multiple of the noise map, so that every pixel having

$$F_{ijk} > T_{ij} \tag{3.6}$$

can be considered as potentially containing a photon charge. Customarily, $T_{ij} = kN_{ij}$ with $k = 4$, in order to reduce the number of spurious noise counts that survive the cut, while at the same time maximize the number of surviving pixels containing a fraction of the charge deposited by a photon. Indeed, if one supposes that the dark counts follow a Gaussian distribution, then the probability of having a fluctuation $> 3\sigma$ is $\approx 0.13\,\%$, which may translate to an important amount of counts if several (thousands in a laboratory environment) 256×256-pixel frames are considered together.

The evidence that the value $k = 4$ serves the aforementioned purpose is contained in Fig. 3.2, where the evolution of the spectral resolution at 5898 eV is plotted as a function of the threshold, expressed in terms of multiples of the noise level. One can see that the sharpest line is achieved around $k = 4$ or $k = 5$. It was chosen to keep the threshold as low as possible near the minimum of the curve (i.e. $k = 4$) in order to be close to the in-orbit operational scenario

Figure 3.3 – Criterion for pattern identification and extraction: pixels must share at least one border to be considered part of the same pattern. a) Two single events. b) One double event. c) Two double events. d) One multiple event. Different colors indicate different events.

of MXT. Indeed, as anticipated in § 2.4.3.6, a first low threshold is applied by the FEE on the data for on-line pixel extraction (event mode), while a higher threshold may be applied later for subsequent data manipulation (e.g. source localization algorithm): this approach allows to retain the information of a larger number of potentially interesting pixels, which would otherwise be lost in a scenario in which only simply a higher threshold is used.

Pixels identified as interesting by the previous step are either isolated or part of more complex structures (*patterns*), the identification of which is based on Python routines included in the `scipy.ndimage` package. All pixels that share at least one border with each other are grouped in the same cluster (Fig. 3.3) and all clusters are univocally numbered with an ID.

Pixels in the same structure may come from a particularly noisy region of the detector (in which case they are flagged as such for future selection) or be part of the same charge deposit, due to a photon or a passing charged particle. In order to separate those arising from photon interactions from all the rest, patterns are classified according to their shape and the number of pixels which compose them, i.e. their *multiplicity*. As discussed in § 2.3.2.4, due to the physics behind charge splits, not all patterns are allowed, but only those made out of 2×2 pixels at most, with the configurations shown in Fig. 3.4a. A `TYPE` keyword, sometimes referred to as *grade* later in the text, is used to classify the shapes according to the convention used by XMM/EPIC, which is widespread in the field of X-ray CCDs and similar to the event classification adopted in missions such as Chandra and ASCA. Non-X-ray events Fig. 3.4b are also included in the classification, representing an important tool to assess the performances of the instrument. Patterns that do not fall into any of those categories, most notably traces by cosmic rays, are assigned a `TYPE` of -1 along with their multiplicity for future selection purposes. It is worth noting that not all the non-X-ray events of the original list are included in the routine,

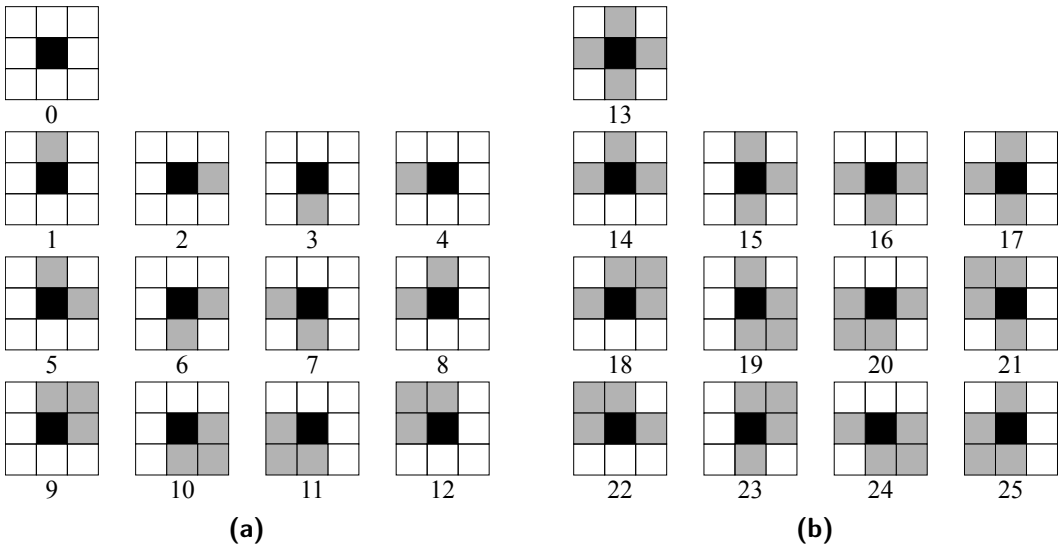

Figure 3.4 – Patterns considered by the event extraction algorithm, each one figuring along with its own code according to the XMM/EPIC convention. a) Allowed patterns (X-ray events). b) Not-allowed pattern (non-X-ray events). The black pixel in each pattern indicates the pixel containing the highest charge; grey pixels are above the threshold but contain less signal; white pixels are below the threshold.

since some of them are not easily identifiable by the algorithm.

At the end of the image reduction pipeline, the list of pixels is saved to a FITS file, each entry presenting its *Pulse Height Amplitude* (`PHA`) in ADU, its column (`X`), row (`Y`) and frame (`FRAME`) position in the data cube, along with its pattern ID (`PATTERN`), multiplicity (`MULTIPLICITY`) and classification (`TYPE`). In additions, pixels are flagged if they correspond or are close to a noisy spot[3] on the matrix (`NOISY` and `NEXTTONOISY`) or if they occur at the border of the CCD (`ATBORDER`), in which case their pattern type may be wrong due to charge split between the sensitive part of the detector and the surrounding guard rings.

3.1.2 Spectral analysis

The information gathered so far is enough for imaging purposes, where the main interest is the spatial distribution of the counts on the matrix. On the other hand, to retrieve the energy distribution of the incoming photons a *calibration* step is necessary, by which parameters linked to the CCD's own

[3]Noisy pixels are identified as those being farther than four times the width (defined in terms of percentiles as in § 3.1.1.2) of the distribution of the pixel values of the noise map.

working principles (e.g. gain and charge transfer efficiency) are determined.

Experimentally, calibration requires photons to be uniformly distributed across the matrix, which may be achieved by shining a defocused X-ray source (e.g. radioactive isotope or X-ray tube) to the detector. Moreover, the photon energy must be known beforehand, as it is used as a reference in the calculations.

3.1.2.1 Gain estimation and correction

The first step in the calibration process is the determination of the spectral gain of the acquisition chain, in order to allow the conversion between the *Analog-to-Digital Units* (ADU), in which the data are recorded, back to energy, in units such as keV.

As already anticipated in § 2.3.3.4, due to the parallel readout of the pnCCD (§ 2.4), the gain is a function of the column number. The first step is therefore the selection of those patterns which lay completely in a single column, i.e. singles (`TYPE` $= 0$) and vertically-arranged doubles (`TYPE` $= 1, 3$), with the latter being used only in case of very low statistics where an analysis based entirely on singles cannot be performed[4]. In case of doubles, they are combined into a single equivalent pixel at the same column (`X`) and containing an ADU signal equal to the sum of the values in the two original pixels.

Column-by-column histograms are then calculated and calibrated. For this task, I implemented and tested several alternative methods of different degrees of complexity, precision and efficiency.

1. The routine may automatically identify the spectral lines by comparison with a reference spectrum, after which rough estimations of the line centers, height and widths are provided. The algorithm then fits the whole spectrum with as many Gaussians as the identified lines, no background added. Fitted line centers (in ADU) and reference line energies (in keV) are then used in a linear calibration to derive a spectral gain and offset. The main disadvantage of this technique is that centers may be misidentified in case of asymmetric spectral lines, since the fit is performed over the entirety of the spectrum.

2. The user may provide a list of ADU intervals from which to extract the maxima, each one supposedly associated with a reference energy.

[4]One must remember that the electronic noise is multiplied by the square root of the pattern multiplicity (eq. (2.86)), so that doubles are noisier than single counts.

Each spectral line is then fitted separately from the others, allowing for asymmetric fits (i.e. only over a portion of the spectral lines, say, the $-1\sigma/+2\sigma$-interval). As in the previous case, a spectral gain and offset are calculated from the fitted line centers and reference energies. The principal drawback of this approach is that in case of close spectral lines and a fairly varying gain distribution, some peaks may fall partially or completely outside the input ADU intervals, resulting in poor calibration.

3. A mix of the two previous approaches is also implemented, in which the ADU intervals of the latter are tweaked on the basis of a rough gain estimation performed by the former, which allows for a better line identification while at the same time enabling asymmetric fits for more precise results.

4. A final approach is the use of the *Energy Calibration via Correlation* (ECC) method, in which spectral lines are not fitted, but gain and offset are determined as those minimizing the deviation between the observed spectrum and a reference one. This code is an evolution of the one presented in Maier & Limousin (2016) and it is not part of the routine itself, but is called as an external existing program.

Unless otherwise stated, when dealing with the data analysis of the tests performed on the models of the MXT Detector Assembly, the third algorithm will be used, as it is better integrated within the complete analysis pipeline.

As a precaution not to prevent the following steps of the analysis, if a column does not get calibrated for some reason, it is assigned a gain and offset calculated as the median of all the other channels where the fit has been successful.

Once every column has its own gain g and offset o, the ADU content of each pixel in position ij may be converted to energy E according to

$$E_{ij} = g_j \mathrm{ADU}_{ij} + o_j. \tag{3.7}$$

3.1.2.2 CTE estimation and correction

The Charge Transfer Efficiency (CTE) of the detector can be estimated from energy-calibrated data. Since the CTE affects a charge packet according to the number of transfers it undergoes before reaching the anode, it follows

that charges deposited on the same row of the matrix are affected to the same degree and can be grouped together to enhance statistics. Row-wise spectra are therefore calculated from calibrated data, their reference lines being fitted by Gaussian functions in the same manner as described above in § 3.1.2.1, with the exception that no calibration is performed, as the values are already in keV. For this step, only singles (`TYPE` $= 0$) and horizontally-arranged doubles (`TYPE` $= 2, 4$) are considered, as they are the only ones extending over a single row. As before, doubles are only employed if the statistics is too low to use only single events: they are combined in the same manner described in the previous section, resulting in a single equivalent pixel placed on the same row `Y` and containing the summed keV values of the two original pixels. Furthermore, the last and first rows as well as all the other border pixels are not considered in the calculations, since their content is altered by charge splitting with the guard rings surrounding the detector.

In § 2.3.2.3, an extensive discussion took place of how the transfer inefficiency causes some charges to be lost as they are shifted towards the anodes. From a spectral point of view, this phenomenon translates into the center of the lines moving towards lower energies as the number of transfers increases, since less and less electrons manage to reach the bottom of the detector:

$$E = \mathrm{CTE}^n E_\gamma, \tag{3.8}$$

which is the same as eq. (2.55).

The case of a frame-store pnCCD is however somewhat different from the general one. The two pixel sizes (one for the image and the other for the frame-store region) and the two transfer speeds (fast transfer to the frame-store area and slow transfer during readout), cause the the CTE to assume different values as a pixel charge moves towards the anode, as quantified by eq. (2.70). If one considers a charge generated by a photon of energy E_γ and separated by n shifts from the bottom of the image region, which comprises of N rows in total (the same number being in the frame-store area, of course), then, with reference to Fig. 3.5, one can say that the measured energy is

$$E_n = E_\gamma \mathrm{CTE}_{\mathrm{fs,fast}}^N \left(\frac{\mathrm{CTE}_{\mathrm{im,fast}} \mathrm{CTE}_{\mathrm{fs,slow}}}{\mathrm{CTE}_{\mathrm{fs,fast}}} \right)^n, \tag{3.9}$$

where the subscripts im and fs indicate the image and the frame-store areas

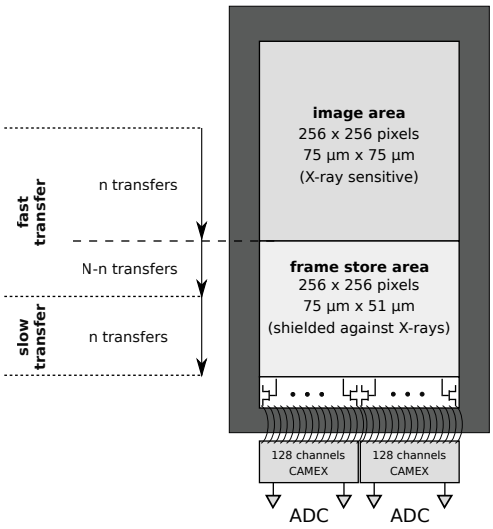

Figure 3.5 – Schematic of the three components of the CTI in the case of a frame-store pnCCD.

respectively, whereas fast and slow stand for fast and slow transfer.

Based on eq. (3.9), I decided to fit a law of the form

$$E_n = E_0 \mathrm{CTE}^n \tag{3.10}$$

to the row-by-row spectral line centers E_n. The amplitude E_0 is left free to vary but it is supposed to be $< E_\gamma$ due to the transfer inefficiency of the frame-store region during fast transfer. It is important to point out that it is not possible to disentangle the three contributions in our system, because the X-ray shielding above the frame-store area cannot be removed and therefore a direct measurements of its CTE is not possible. As a consequence, the CTE one gets from eq. (3.10) is in reality a combination of three different values.

After the CTE has been estimated, the pixel amplitude A_{ij} in ADU or keV may be corrected for this effect too, by simply putting

$$A'_{ij} = \frac{A_{ij}}{\frac{E_0}{E_\gamma}\mathrm{CTE}\,(E_\gamma)^{n_i}}, \tag{3.11}$$

where n_i is the number of transfers corresponding to the i-th row, which depends on the actual row numbering. In the absence of a usable formula capable of providing the CTE at different energies given some measurements, since many of the parameters of eq. (2.70) such as the energy levels and

densities of the defects are yet to be constrained, I decided to correct all the pixels with the same CTE value, in case only a single energy was available, or with the CTE at the E_γ closest to the total amplitude of the pattern the pixel belongs to, in case CTEs at different lines could be calculated. In this way, for example, in case of exposure to a radioactive ^{55}Fe source, all the pixels in a double event generated by a 6.49 keV would be corrected using CTE (5.9 keV), if the corresponding CTE (6.49 keV) could not be estimated. Otherwise, the more correct value of CTE at 6.49 keV would be used.

It it worth noting that this algorithm works properly only in case of the absence of *deep traps*, i.e. defects able to remove a substantial portion of a charge packet, so that step-like structures appear when the measured photon energy is considered as a function of the number of transfers in the CCD. Although they are a common feature of MOS CCDs, especially after radiation damage, such structures have never been observed in pnCCDs, even after particle irradiation up to $\approx 10^9\,\mathrm{cm}^{-2}$ 10 MeV protons (radiation damage will be addressed in § 4).

3.1.2.3 The correction loop

From the discussion done so far, it is clear that during the energy-calibration and gain-correction phase of the analysis (§ 3.1.2.1), the influence of the CTE was neglected as it was practically considered so limited not to significantly influence the results of the calibration. However, this causes the spectral lines to be slightly elongated towards the lower energies even in case gain dispersion and transfer inefficiency are the only occurring phenomena, since in a column-wise spectrum pixels that underwent different amounts of transfers are grouped together. As a consequence, the calibration is affected by an error which in turn undermines the estimation of the CTE (§ 3.1.2.2).

The situation may be solved with an iterative approach.

- Gain and offset are calculated for each column from the ADU data, which are then calibrated.
- The CTE is estimated from the row-wise spectra of the calibrated data.
- Gain and offset are again estimated, this time from the CTE-corrected ADU data, which are calibrated.

- The Charge Transfer Efficiency is assessed from the *already CTE-corrected* (and calibrated) data of the previous step.

- The last two points are repeated until a decided number of iterations has passed or a certain tolerance on gain and/or CTE variation has been reached.

It is important to keep in mind that the data are corrected for the CTE at every iteration, meaning that all the CTE estimates after the very first one are *relative values*: to get the *absolute* CTE at some iteration, the product of all the evaluations up to that point must be multiplied together. This approach does not influence the gain calculation, which is always in keV ADU^{-1}. Experimentally, one or two iterations are enough to attain stability in the results.

Once the process is concluded and every pixel in position ij is given a gain g_j, offset o_j and charge loss CTE^{n_i}, the whole matrix is calibrated and all the pixels can be considered together, without any distinction of column or row, for example, to make a detector-wide spectrum. In case of multiple events, after the calibration with gain and offset derived from single counts[5], the content of the various pixels can be summed together. If the information about the position is important, several approaches with different degrees of complexity may be adopted: examples are to simply round to the closest pixel an average of the coordinates weighted with the value of each pixel; alternatevely there is the more sofisticated algorithm described in Dennerl et al. (2012).

3.2 Engineering Model

The Engineering Model (EM) of the MXT Detector Assembly had the purpose of validating the design of the ceramic carrier board as well as the entire acquisition chain. It was the first prototype available for characterization to the MXT team. The Engineering Model (EM) is visible in Fig. 3.6.

The following sections shall cover the first laboratory tests performed on this model, from the experimental setup (§ 3.2.1) to the results (§ 3.2.2).

[5]Further details about the calibration in case of split events are given in § 5.4.2.3.

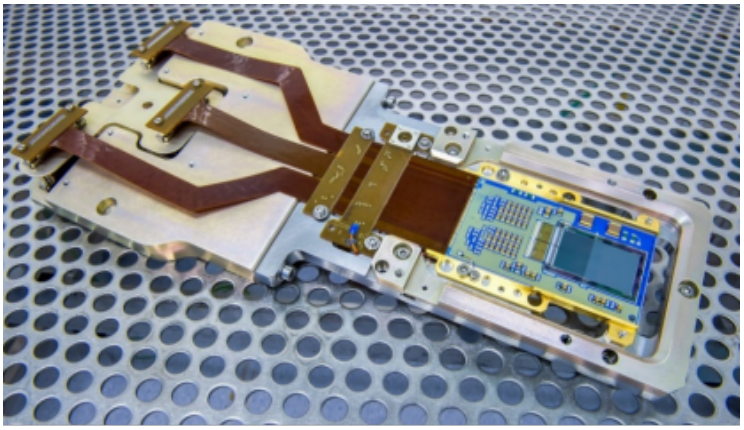

Figure 3.6 – Picture of the MXT Engineering Model taken from the front side. The pnCCD with the image and frame-store areas are visible, as well as the two CAMEX ASICs.

3.2.1 Experimental setup

Fig. 3.7a shows the laboratory setup for the tests on the Engineering Model (EM) of the MXT Detector Assembly. The detector is placed inside a vacuum chamber inherited from a previous project, which was provided with some mechanical adaptations to house the assembly. The main limitations of this setup are the pressure limit of 2×10^{-5} mbar and the temperature limit of $-75\,°\mathrm{C}$ on the DA. For both mechanical stability and to ensure thermal conduction, the focal plane is encased in a copper structure, designed for this purpose and visible in Fig. 3.7b.

The system is driven by a Front-End Electronics prototype (proto-FEE), whose components do not obey the US-free policy of the final design to achieve maximum performances and reliability. The functionalities of the proto-FEE are almost the same as of its future Flight Model, except for the data preprocessing part, which is completely done off line. As a consequence, the proto-FEE only operates in *full-frame mode*, i.e. no event selection takes place on the data, the output consisting of full 256×256-pixel images, which are registered into binary files. A desktop PC allows the users to survey the temperature, control the electronics, perform housekeeping measurements (currents and voltages) and acquire the data, thanks to multiple application-specific pieces of software, which also provide real-time visualization of the images being taken, although, as previously said, all analysis is carried out off line. Critically, due to data transfer rate limitations between the proto-FEE and the PC, only one image

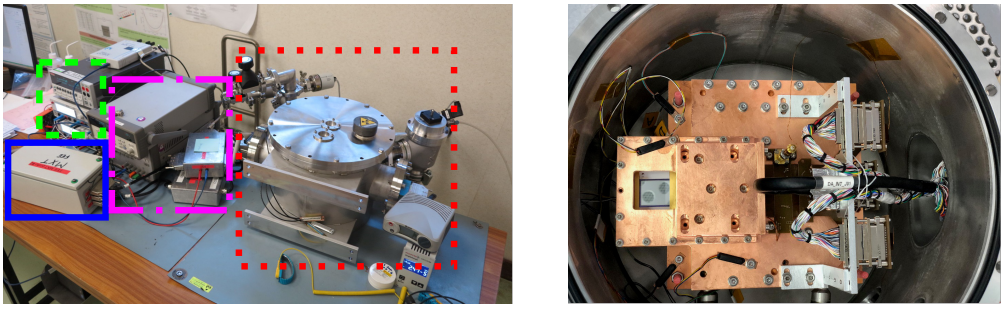

(a) (b)

Figure 3.7 – Experimental setup for the laboratory tests on the Engineering Model of the MXT Focal Plane Assembly. a) Overview of the setup: vacuum chamber (dotted red line), FEE (solid blue line), FEE and detector power supplies (dashed green line), and interface for housekeeping (HK) measurements (dash-dotted magenta line). b) Picture of the MXT Engineering Model inside the vacuum chamber, encased in its copper structure, conceived and realized specifically for the tests.

per second can be recorded, even though the detector operates at its nominal frequency of ten frames per second: this means that 9/10 acquired frames are lost, with clear implications on the duration of the laboratory tests.

A final notable difference between proto-FEE and final design is that housekeeping measurements, i.e. voltage and current values recorded cyclically on CAMEX and detector, are not implemented on the prototype and instead require an external apparatus.

3.2.2 Results

The EM was delivered to CEA in summer 2018 and the first light was achieved shortly thereafter. Its spectral capabilities were tested through exposure to a ^{57}Co radionuclide, which was at the time the only available X-ray source active in the operating range of MXT, with lines at 6400 eV (Fe-K$_\alpha$), 7100 eV (Fe-K$_\beta$) and 14 413 eV (γ-ray) and a high enough activity (300 kBq) to carry out laboratory tests.

3.2.2.1 Guard ring

Operating voltages and currents were nominal, except for the guard ring contact (`GRA-OGR`, § 2.4.1.1), which showed a current exceeding the specifications by several orders of magnitude, indication of an undesired electrical

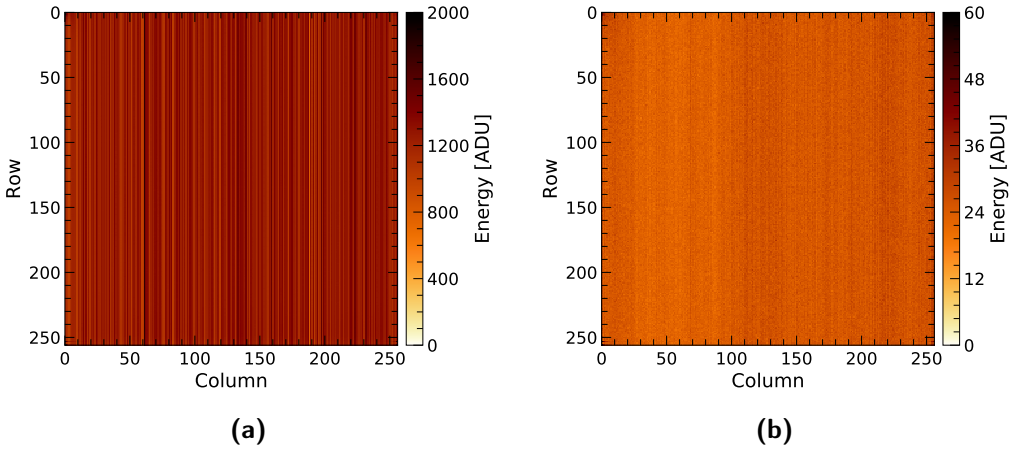

Figure 3.8 – Examples of measured offset (a) and noise (b) maps of the EM measured at $-65\,°C$.

connection, either somewhere along the detector's power supply line or on the die itself. The fact that no short circuit was detected despite thorough searches in the setup and on the ceramic carrier board leaves only the hypothesis that some kind of defect occurred on the detector itself, either during fabrication/mounting or as a consequence of the operation. Indeed, according to other teams working with the same kind of device, the destructive breakdown of some junctions in the detector may be yield results as the ones observed. Too much residual pressure, due to the 2×10^{-5} mbar limitation of the setup, was hypothesized as a possible cause, as it may result in the presence of polar molecules in air, with harmful effects on the device in combination with the strong electric fields of the CCD.

3.2.2.2 Noise and offset

Fig. 3.8 shows its offset and noise maps at $-65\,°C$. No unresponsive columns or bright pixel are visible. Given the $1.8\,\mathrm{eV\,ADU^{-1}}$ gain of the acquisition chain (to be discussed below), the noise level of 25 ADU translates to 45 eV or $12\,\mathrm{e^-_{rms}}$, i.e. more than 8 times the noise of the system without the detector ($\approx 2-3$ ADU), an increase revealing the presence of a large leakage current.

3.2.2.3 Charge trailing

The first visible feature of the photon frames was the the presence of long trails along the transfer direction. This suggested some issues with the transfer

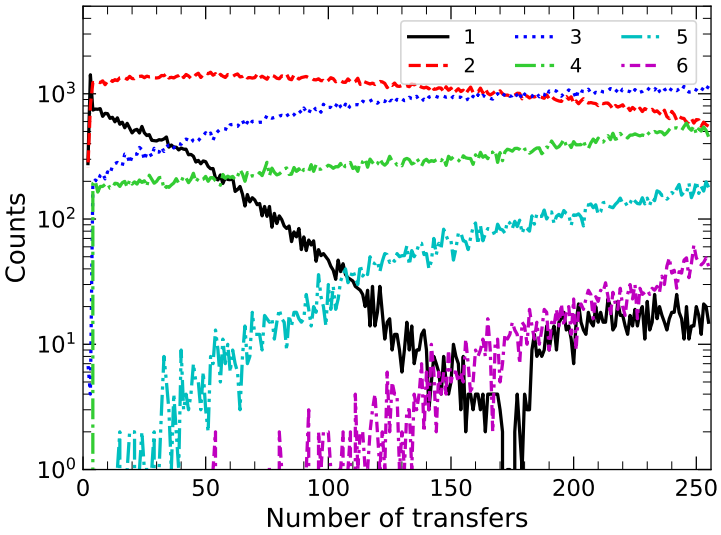

Figure 3.9 – Pattern distribution as a function of the number of transfers in the matrix and the multiplicity. The increase in pattern multiplicity with the number of transfers is a sign of strong charge trailing. The patterns were energy-selected corresponding to the two Fe fluorescence lines.

process. The phenomenon is quantified in Fig. 3.9 where the number of events (reconstructed patterns) is plotted as a function of the number of transfers needed to reach the anode and the multiplicity. The farther a charge packet from the readout electrodes, the higher its multiplicity, implying that not all the electrons are being transferred at each shift, with some being left behind and picked up by the following phase edge. This phenomenon appears to occur several times per packet, resulting in the non-uniform distribution of valid patterns across the detector (Fig. 3.10), as well as the alteration of the expected pattern shapes. Indeed, due to the trailing effect, the number and disposition of pixels inside a cluster may vary for a given multiplicity, causing for example the maximum in a genuine triple event (code 5 to 8, Fig. 3.4) to shift from the corner to one of the extremities, which makes the pattern invalid under normal circumstances.

3.2.2.4 Spectral response

Due to the transfer and pattern shape issues, the usual event selection based on the codes of Fig. 3.4 could not be implemented in case of the spectral tests on the MXT EM, as the number of valid clusters was too small for any meaningful analysis. Simple multiplicity cuts were instead implemented,

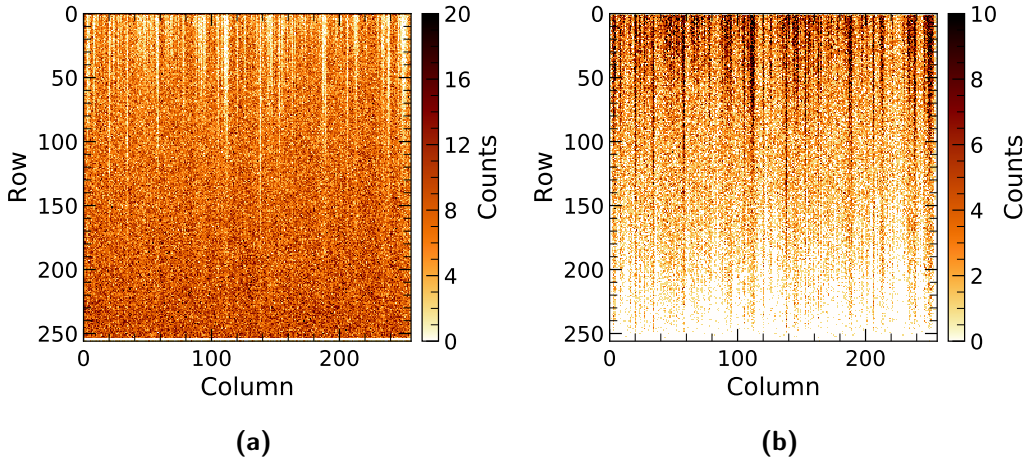

Figure 3.10 – Cumulative map of the (reconstructed) ^{57}Co photon events that hit the detector. a) Valid patterns are less common the farther from the anodes. b) On the contrary, invalid patterns increase in number as the charge packets are transferred.

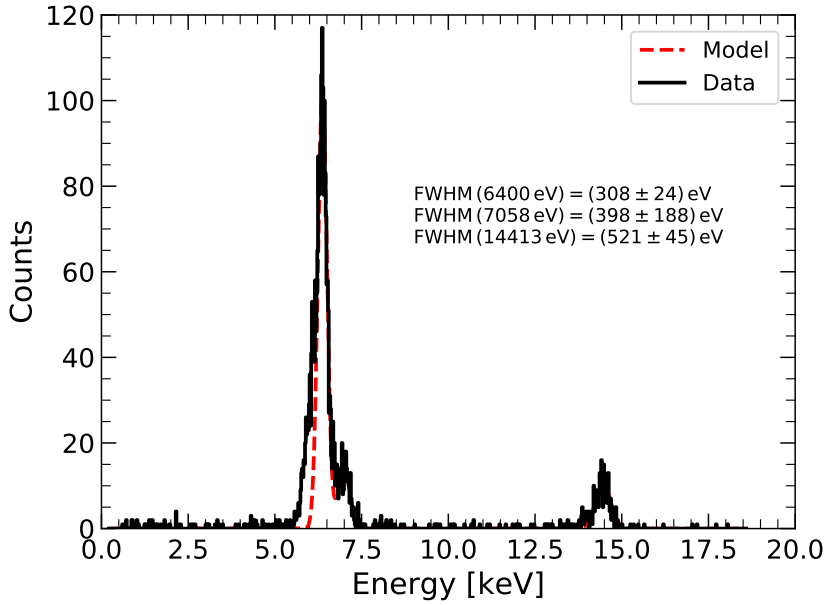

Figure 3.11 – Single-column spectrum of a ^{57}Co source acquired with the EM. The fit was performed according to the third algorithm described in § 3.1.2.1.

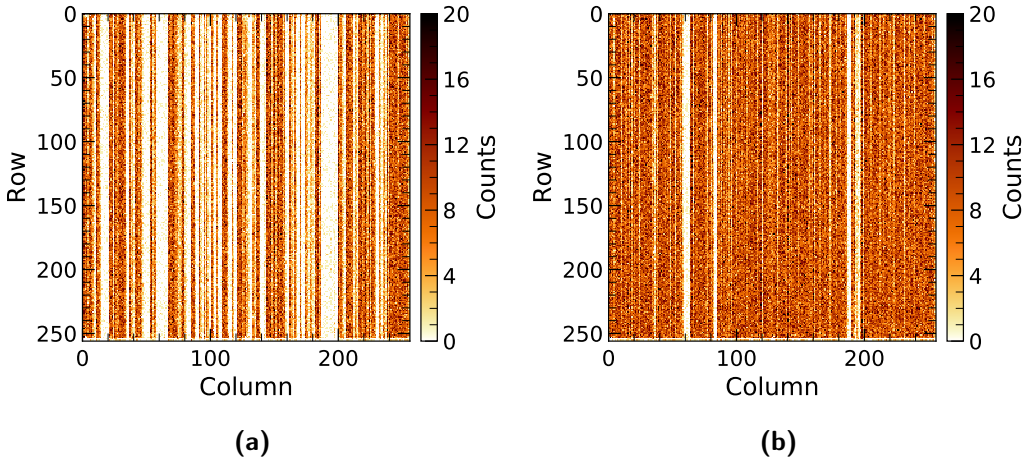

Figure 3.12 – Cumulative map of the (reconstructed) ^{57}Co photon events that hit the detector. a) Large portions of the matrix appear to not register photons, or do that with a much lower efficiency than the other columns. b) The unresponsiveness is not permanent but unpredictable and not easily recoverable.

with a limitation to `MULTIPLICITY` ≤ 6. Patterns were recombined before the gain estimation, without regard for the fact that some events spanned across two neighboring CCD columns, as statistics would otherwise be too limited. Fig. 3.11 shows a ^{57}Co spectrum obtained in this way. Its asymmetric shape and energy resolution are affected by the (high) leakage current of the detector, the transfer inefficiency (not corrected at this stage), the charge sharing noise (due to the multiple pixels in each used patterns) and the gain fluctuation between neighboring columns. The energy resolution at 6.4 keV is ≈ 300 eV, far from the MXT requirements (FWHM (6.4 keV) = 132 eV) and from the nominal capabilities of this kind of detector (Meidinger et al., 2006a).

The spectrum of Fig. 3.11 was obtained by taking the data of a single column, according to the procedure described above. No sum spectrum could be calculated because of the variability of the responses of the readout channels. Some of them were effectively unresponsive or extremely noisy (to the point that energy thresholds up to a few keV had to be put in place), but this behavior showed no consistency with the affected columns or the operational parameters. The channel unresponsiveness may be explained if one considers that the guard ring around the detector (`OGR`) and the one around the anodes (`GRA`) share their potential and that the buildup of electrons at the anode may cause the corresponding column to stop detecting photons: the huge current

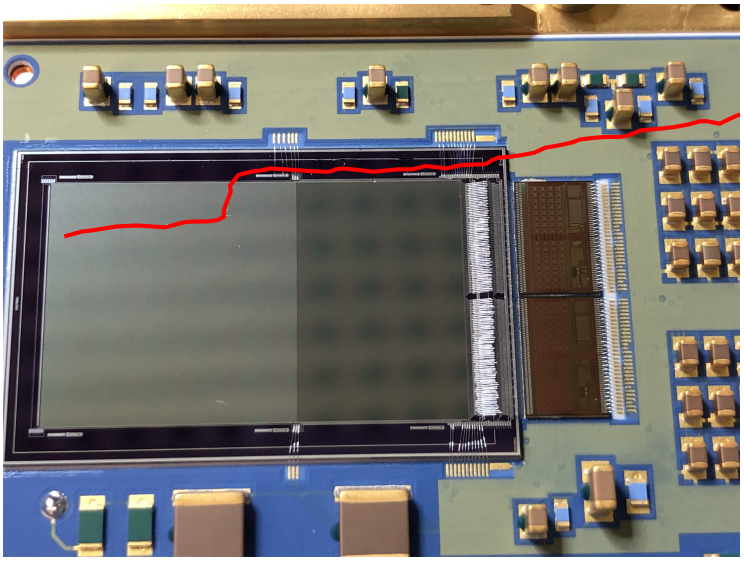

Figure 3.13 – Picture of the MXT Engineering Model after the rupture. The crack has been highlighted to improve visibility. The structures visible on the surface of the CCD are just the reflection of the surrounding environment.

measured through the GRA-OGR contact in combination with its impedance may result in a voltage drop implying an incomplete isolation of the anodes from the charges of the outer substrate. Due to the inability to discriminate between the outer and anode guard rings from an electrical point of view, this hypothesis remained untested.

3.2.3 Aftermath

Several functionality tests were carried out on setup, carrier board and detector to address the issues with the Engineering Model. However, during one of those manipulations, the Detector Assembly cracked (Fig. 3.13) because of accidental mishandling. After this incident, a number of actions were set up by CEA and CNES to secure fabrication, handling and operation of the next detector models. In particular, thorough investigations and upgrades of the ground support equipment were performed. Finally, the Engineering Model underwent physically destructive analyses to qualify different aspects of the assembly process.

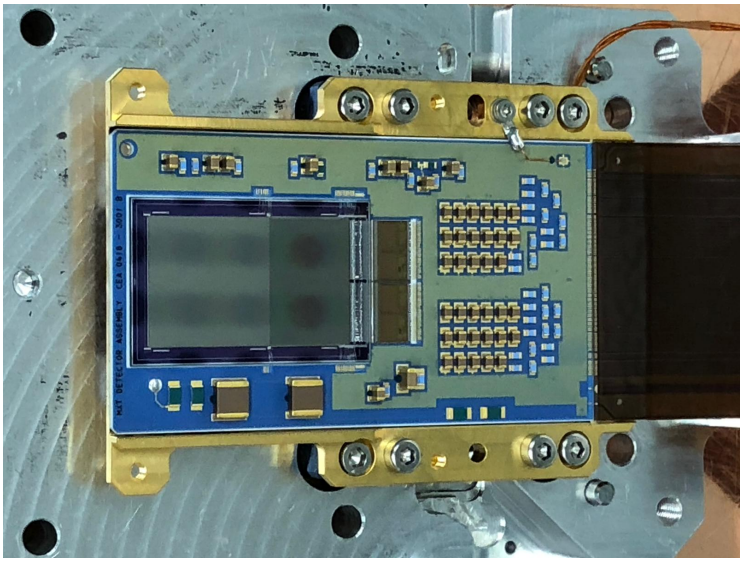

Figure 3.14 – Picture of the MXT Performance Model taken from the front side. The pnCCD with the image and frame-store areas are visible, as well as the two CAMEX ASICs. The structures visible on the surface of the CCD are just the reflection of the surrounding environment.

3.3 Performance Model

The goal of the Engineering Model was to validate the design of the full custom Detector Assembly and the Front-End Electronics. However, it was not possible to reach this objective. As a consequence, it was decided to demote one of the three detectors originally dedicated to the selection of the Fight Model to be a so-called Performance Model, visible in Fig. 3.14. This model was received at CEA at the end of June 2019.

A description of the experimental work of characterization carried out on the PM shall be described, from the experimental setup (§ 3.3.1) to the results (§ 3.3.2).

3.3.1 Experimental setup

The experimental setup, shown in Fig. 3.15, follows similar lines to the one described in § 3.2.1 for the EM, although with major improvements.

A cryostat (Fig. 3.16) replaces the smaller vacuum chamber used previously, allowing to attain both lower pressures (7×10^{-7} mbar) and lower temperatures (down to $-100\,°C$). The cooling system is based on a liquid nitrogen tank thermally linked to the FPA, the connection being regulated via heaters. Two

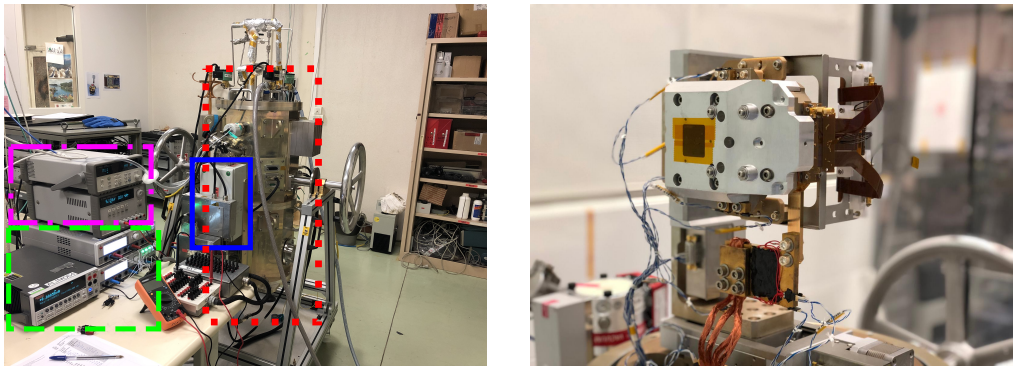

(a) (b)

Figure 3.15 – Experimental setup for the laboratory tests on the Performance Model of the MXT Focal Plane Assembly. a) Overview of the setup: cryostat (dotted red line), proto-FEE (solid blue line), power supply (dashed green line) and interface for housekeeping (dash-dotted magenta line). b) Picture of the aluminum shielding of the MXT focal plane during the preparation of the setup: the detector is mounted inside, as evidenced by the flex coming out of the case.

inlets enable positioning of radioactive X-ray sources very close to the back or front of the detector without the need to operate in vacuum as beryllium windows separate the interior of the cryostat from the outside. The same apertures can be used to mount X-ray tubes. The focal plane is housed inside an aluminum case based on the same design as the shielding of the MXT camera, the only differences being the absence of the coating layers and the presence of an additional aperture on the front side of the detector to match the corresponding cryostat inlet. The shielding is in turn attached to two orthogonal micrometric sliding tables, allowing accurate alignment as well as precision studies of the point-by-point response of the device in calibration facilities. Due to failure of the thermometer mounted on the carrier board on this model of the Detector Assembly, the only available temperature information is on the aluminum shielding, which is used to control the cooling. Calculations show that the temperature difference with the focal plane is about 5 °C.

Power supply and control are ensured by the same setup as § 3.2.1, although the proto-FEE underwent an important change with respect to the configuration used on the EM. During the investigation mentioned in § 3.2.3, it came under attention that the test harness and the detector assembly itself (flex lead and ceramic carrier board) suffer from important impedance and cross-line

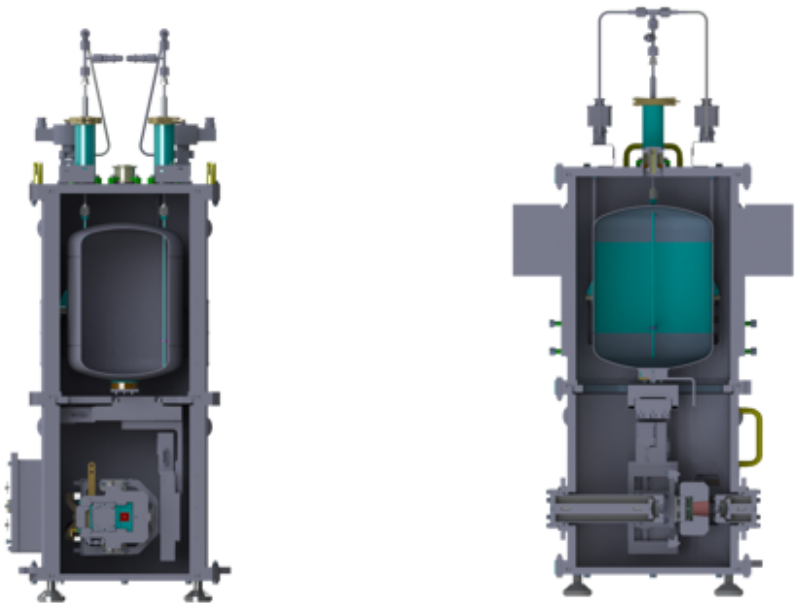

(a) **(b)**

Figure 3.16 – The cryostat for the MXT Performance Model. a) Cross-sectional view from the back of the detector (entrance window). b) Cross-sectional view along the side. In both pictures, the FPA is visible at the bottom of the structure, with the liquid nitrogen tank in the upper half. The case around the FPA is also visible, mounted on the two sliding tables. Furthermore, Fig. b shows how close the radioactive sources can be placed to the detector.

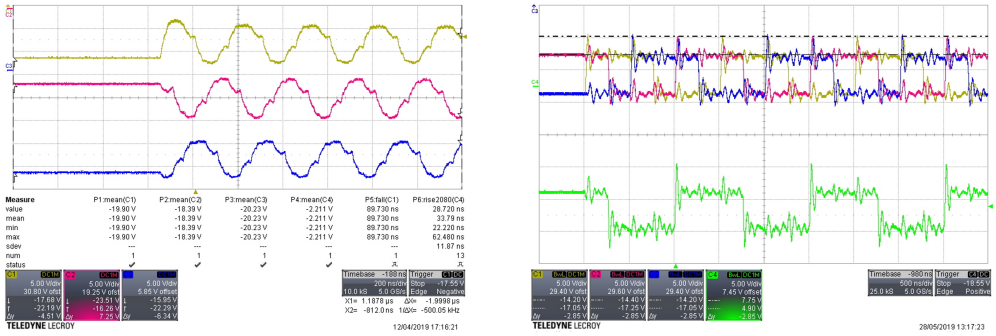

(a) (b)

Figure 3.17 – Measured clocks for the transfer phases at detector level. a) Same configuration used for the tests on the EM (300 ns-period). b) Configuration obtained by slowing down to a period of 1500 ns.

capacitance, causing the distortion of the voltages ensuring the charge shifts towards the anodes in the CCD. The problem was solved by slowing down the period of the phases from 300 ns, i.e. 50 ns per clock state (see Fig. 2.9 for the definition of the states) to 1500 ns, i.e. 250 ns per clock state (Fig. 3.17). This value was not optimized and was only aimed at demonstrating the charge transfer capabilities of a configuration with intermediate harness between FEE and DA.

The housekeeping measurement system was also upgraded to enable precision monitoring of the currents through the guard rings (`GRA-OGR`) and the back contact or photon entrance window (`VRK`, from *Rückkontakt*, the German for *back contact*). The only remaining inconvenience of this setup is the limited transfer rate of the link between proto-FEE and PC, which still leads to a loss of 9/10 recorded frames.

3.3.2 Results

The first light of Performance Model was achieved on the 2nd of July 2019. Unlike the case of the EM, a much stronger (≈ 1 MBq) ^{55}Fe source was available for spectroscopic tests, with lines at 5898 eV (Mn-K$_\alpha$) and 6490 eV (Mn-K$_\beta$).

3.3.2.1 Overview

All currents and voltages were nominal from the start, with no abnormalities being detected. The `GRA-OGR` current was as low as expected. Fig. 3.18 shows

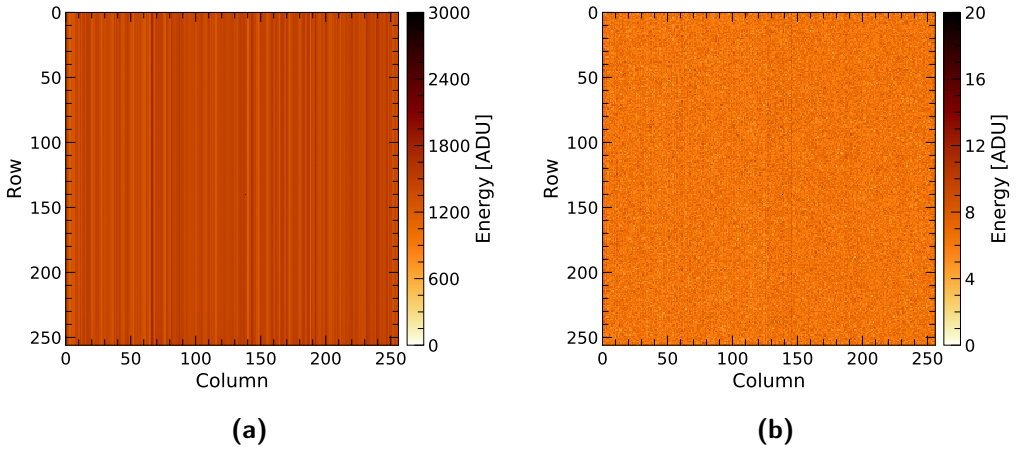

Figure 3.18 – Examples of measured offset (a) and noise (b) maps of the PM. A single noisy pixel near the center of the maps is hardly seen due to its small dimensions in the plots (literally a single pixel of the images).

examples of measured offset and noise maps, both of which appear to be uniform all across their extent. No clear distinction between left and right ASIC is visible. Only the offset map presents some column-wise fluctuations that can be traced back to the gain differences of the CAMEX channels. In combination with the $1.46\,\mathrm{eV\,ADU^{-1}}$ spectral gain (to be discussed below), the noise map corresponds to a level of $\approx 10\,\mathrm{eV}$ ($\approx 3\,\mathrm{e^-_{rms}}$), much lower than in the EM.

A single pixel with a noise level more than four times that of the surrounding pixels is present near the center of the matrix (position $(138, 140)$). Other than that, all channels appears to be responsive. Illumination by a ^{55}Fe radioactive source has evidenced that a few columns (around 145 and 200) have the tendency to stop registering incoming photons. Although this is a reversible state, since normal operation can be resumed by quickly increasing and then decreasing the voltage applied to the guard rings (`GRA-OGR` *toggle*), which flushes away the charges stuck at the anodes, this is a feature worth monitoring during acquisitions, especially given the fact that it is not easily identifiable on the available on-line tools, but instead becomes clear during data processing.

Another peculiarity is that row number 254, i.e. the second to last towards the frame-store region and the anodes, appears to respond very poorly, presenting a very limited number of hits in comparison with the rest of the matrix. Moreover, this row tends not to show the same spectral features than the

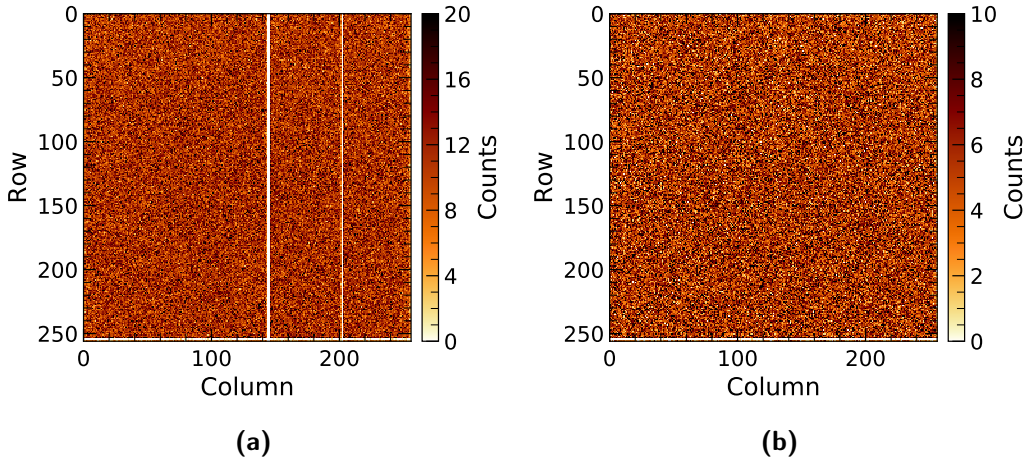

Figure 3.19 – Cumulative map of the (reconstructed) ^{55}Fe photon events that hit the detector. a) A few columns may sometimes stop responding, especially around channel 145 and 200. b) The loss of columns is not permanent and can be recovered through a `GRA-OGR` *toggle*.

others, with lines being barely visible or having apparently inverted relative heights (e.g. the Mn-K$_\beta$ appearing more intense than the Mn-K$_\alpha$). The cause of this behavior is yet to be explained, however it does not seem to influence the charge transfer across the row itself, as the rest of the detector does not share this issue.

3.3.2.2 Multiplexing trailing

The analysis of the pattern shapes after the exposure to ^{55}Fe photons highlighted the presence of an unexpectedly high number of non-X-ray events, i.e. codes 13 to 25 of Fig. 3.4, especially those presenting three pixels on the same row: on the contrary, few clusters were detected extending over more than two rows, clue that the transfer was working properly.

Since no charge cloud from an X-ray photon can be shared by more than 2×2 pixels (§ 2.3.2.4), inter-channel cross-talk was investigated as a possible explanation to the phenomenon. Fig. 3.20 shows two *correlation maps*, in which the content of each pixel above a certain threshold (x-axis) is plotted against the value of the pixel at its immediate right (y-axis): all sub-threshold pixels are forced to zero. The correlation map of the PM data is plotted next to another one obtained from the measurements taken at the Institute for Astronomy and Astrophysics of the University of Tübingen (IAAT), where a pnCCD of the same design was operated under similar conditions (but of

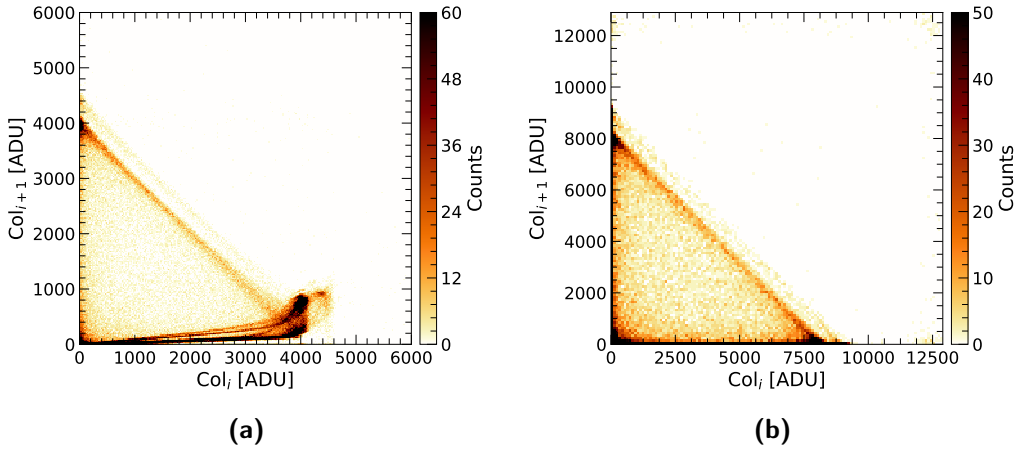

Figure 3.20 – Maps of the correlation between the content of each pixel and the one on its right. a) Correlation map for the PM. b) Correlation map of the IAAT detector, where no cross-talk is detectable. The difference in the ADU ranges covered by the points depends on the different gain of the two acquisition systems.

course with a different setup). Both maps show two main straight lines with slope of about -1 corresponding to the charge sharing between pixels: their sum is constant and equal to the photon energy for every spectral line (two in the case of ^{55}Fe). However, the map for the MXT PM also reveals the presence of a strong correlation effect between the content of each pixel and the one to its right, proving that the charge in a pixel is therefore partly mirrored into the one on its right, with an efficiency that proceeds almost linearly with the energy and then rapidly increases in correspondence to the Mn-K$_\alpha$-line in an almost exponential fashion up to $\approx 20\,\%$. Since proper cross-talk phenomena require proximity and capacitive coupling and should therefore link pixels on both directions on the matrix (which is not the case), it was decided to refer to the observed feature as *multiplexing trailing*, because it follows the multiplexing sequence, which goes from left to right on each row. It is worth noting that the effect described here normally take place in other models of this version of detector and ASIC, although with a much lower efficiency of $\approx 0.8\,\%$.

To ensure that the observed behavior did not depend on some defect on the detector, e.g. on the First FETs, some charges were injected directly at the input of the CAMEX, disabling the connection to the detector. This was possible by taking advantage of the test contact placed at the beginning of each analog channel of the ASIC (§ 2.4.2.3). By deposing a charge equivalent to that of a $\approx 6\,$keV X-ray photon on every third column, a signal was induced

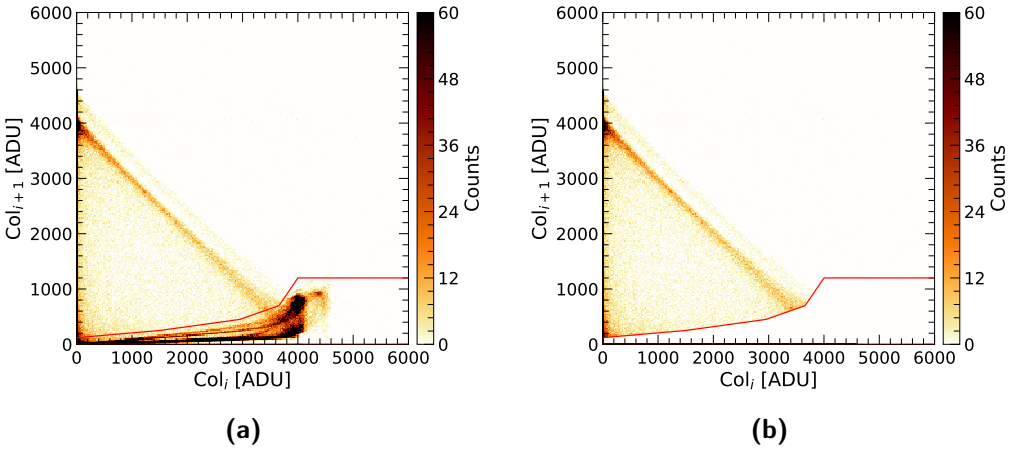

Figure 3.21 – Correlation maps in case of the basic correction algorithm. a) A region of interest is identified on the original map. b) The rightmost pixel of each pair in the region of interest is forced to zero.

on the columns to the immediate right of those where the injection took place, the mirrored amplitude being $\approx 18\,\%$ of the injected value.

Although further investigations and improvements are needed to solve the multiplexing trailing issue from a hardware point of view, useful information may still be extracted from the data if the necessary corrections are applied.

The approach chosen to process data in this work is to identify the region of the correlation map in which multiplexing trailing events are distributed and then force to zero the pixel on the right in every pair of pixels in that region (Fig. 3.21). The desired effect is a modification of the pattern distribution to approach the nominal values (Fig. 3.22). The unfortunate consequence of this method is the introduction of an artificial charge-loss effect, as legitimate charge splits may be misidentified as multiplexing trailing thereby losing part of their charge. This is visible in the pattern statistics (Fig. 3.22), where events such as doubles on the same row (code 2, and to a smaller extent 4) become underrepresented with respect to those on the same column (codes 1 and 3).

After the pattern correction is applied and statistics are restored to a level close to nominal[6], looking at the abundances of events as a function of multiplicity and number of transfer reveals the presence of a small degree of charge trailing (Fig. 3.23), most likely caused again by the bandwidth limitations imposed by the connections in the setup, which are at least as long

[6]Nominal statistics are provided by the analysis of the IAAT data as well as publications such as Dennerl et al. (2012).

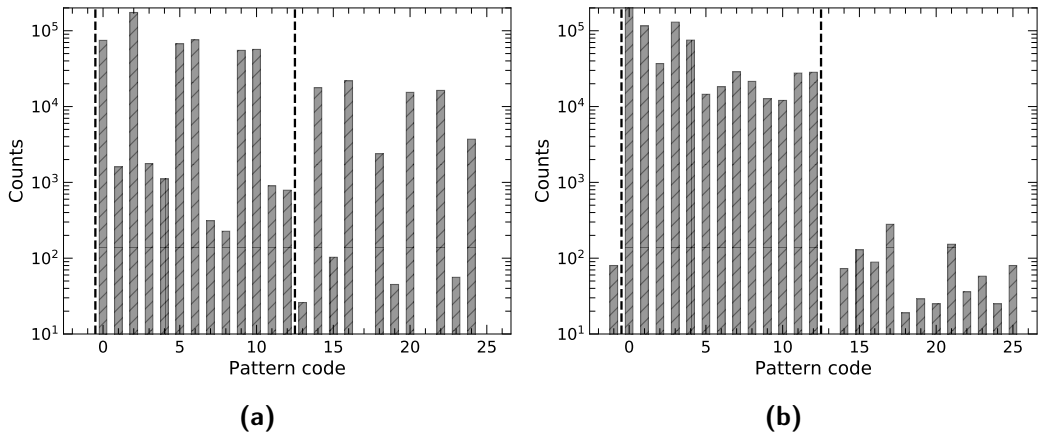

Figure 3.22 – Pattern distributions according to the codes of Fig. 3.4. a) Distribution before the correction. b) Distribution after the correction. In both cases, the dashed vertical lines regroup the codes of the allowed patterns.

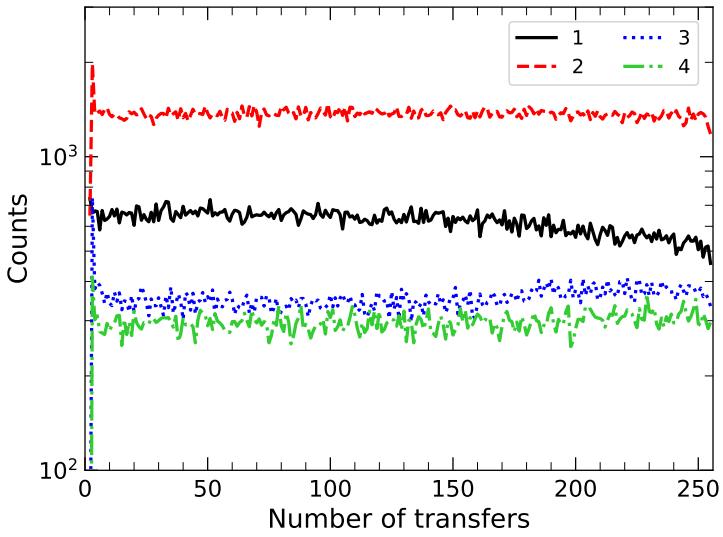

Figure 3.23 – Pattern distribution as a function of the number of transfers in the matrix and the multiplicity. The small decrease of single events the farther from the anodes implies the presence if a residual weak charge trailing. The patterns were energy-selected corresponding to the two ^{55}Fe lines.

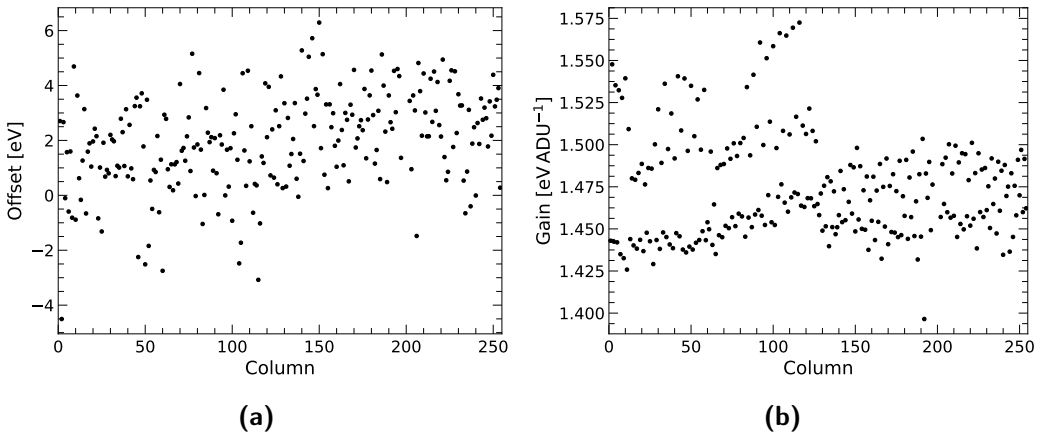

Figure 3.24 – Spectral offset (a) and gain (b) distributions at −80 °C.

as in the case of the EM.

3.3.2.3 Spectral performances

The algorithms described in § 3.1.2 were applied to the cross-talk-corrected ^{55}Fe data to assess the spectral properties of the detector. Results of the parametric studies are discussed in § 3.3.2.4. The statistics was always high enough to restrict the analysis to single events only, which allowed a better determination of gain, CTI and energy resolution. It is worth noting that whenever temperatures are given, they are referred to the detector support (where the thermometer is placed), implying that to obtain the temperature on the detector one must add $\approx +5\,^{\circ}$C.

Calibration The spectral analysis was carried out according to the methods described in § 3.1.2. In particular, gain determination relied on method 3 (and occasionally 2) of the list presented in § 3.1.2.1. Due to the lack of spectral lines available for the linear energy calibration, I decided to add a third point in position $(0, 0)$, with an uncertainty corresponding to the largest of the other two. This allows for a more meaningful fit (straight line through three points) and at the same time takes into account the possibility that a small residual offset persists in the data.

Fig. 3.24 shows the offset and gain at −80 °C as a function of the CCD column. The non-zero mean of the first plot reveals indeed the presence of a small residual offset, that also appears to have a small trend as a function of the channel number, possibly due to the multiplexing sequence, which goes

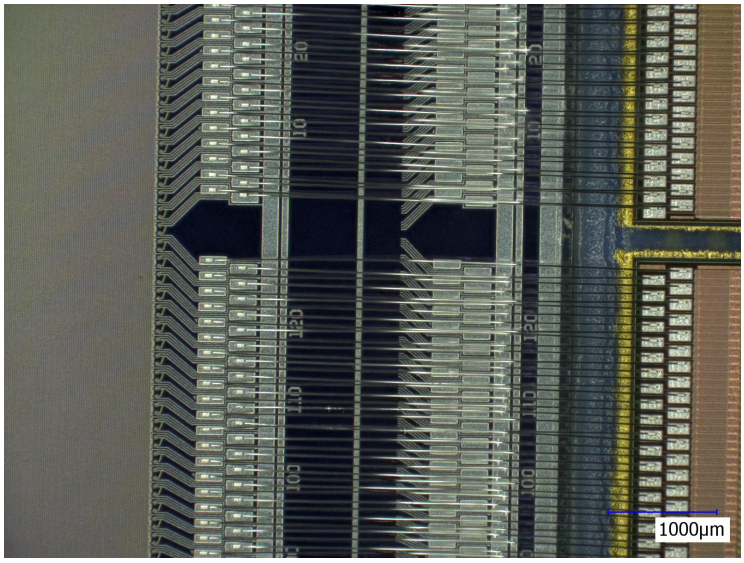

Figure 3.25 – Picture of the bonding configuration between the pnCCD (left) and the ASICs (right) in the PM DA.

in the same direction. In comparison, the gain plot presents more striking features. First of all, there is a clear left-right divide, meaning that the two ASICs have different sets of gains. Furthermore, several levels are visible, with two main cluster which become three in case of the left CAMEX, even though the third uppermost group is less populated than the other two.

One might intuitively explain this phenomenon by means of the peculiar bonding configuration of the CCD to the ASICs, shown in Fig. 3.25: both the output pads of the CCD and the input pads of the CAMEX are arranged along two rows, implying that connections between the two are ensured by wires with roughly two alternating lengths, each of which corresponds to a capacitance value. As the capacitance is involved in the charge-to-voltage conversion at the anodes, one may suspect that the varying length of the bonds may affect the gain of the columns. However, thanks to the JFET being implanted directly on the silicon die (§ 2.4.1.3), the charge-to-voltage conversion takes place *before* the signal leaves the pnCCD, making it impossible for the wire-bond capacitance to affect the gain. This is incidentally also visible in the channel-by-channel spectral resolution, which does not show the two-level behavior of the gain plot (Fig. 3.26), although the same feature would be expected if the wire-bond capacitance played a role, as it would also influence the noise[7].

[7]The capacitance behind the JFET does affect the signal rise time. However, this does not have a visible consequence on the results discussed here.

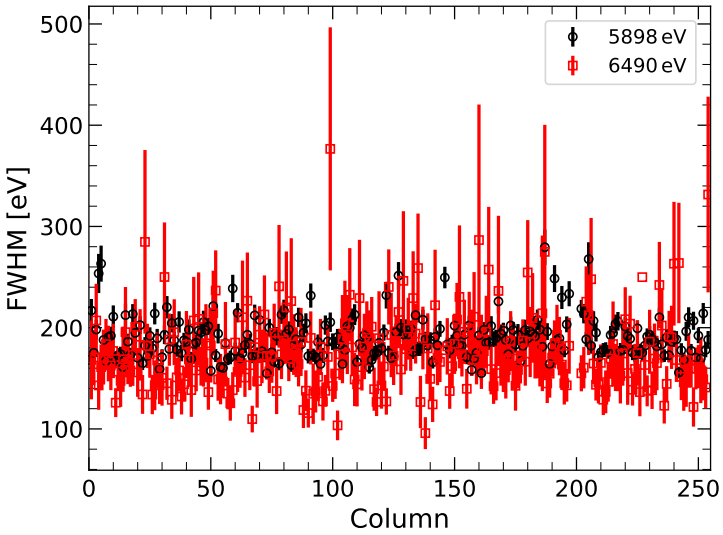

Figure 3.26 – Energy resolution at −80 °C at the two ^{55}Fe lines as a function of CCD column. No alternating behavior such as in the case of the gain (Fig. 3.24b) is visible.

The solution came after the preliminary measurements performed on Engineering Model (EM) of the FEE, which shares the design of the proto-FEE used in the acquisition of the data discussed here, even though it employs different US-free electrical components. Indeed, the new FEE originally suffered from an amplified version of the same two-level gain issue, which was understood to be a consequence of voltage oscillations at the input of both ADCs. After the substitution of a few electrical components, the oscillations were damped and the gain became uniform across the columns.

Unexpectedly, the hardware intervention also resulted in the almost complete elimination of the multiplexing trailing, which appeared to be correlated to the aforementioned signal oscillations. In the new data, the phenomenon is still present, although much reduced, implying that the correction method discussed § 3.3.2.2 is still valid.

It is worth noting that the understanding and solution of both gain dispersion and multiplexing trailing were achieved only *after* the data for this manuscript were acquired, and that the modifications were not implemented on the proto-FEE.

Global spectrum Fig. 3.27 shows an example of a spectrum acquired at −80°, which yields FWHM (5898 eV) ≈ 146 eV. Single events from all over the

detector are used, after both calibration and CTI correction.

Both spectral lines appear clearly asymmetric, especially the Mn-K_α due to its higher number of counts. The cause of this phenomenon is the artificial charge loss introduced by the correction algorithm (§ 3.3.2.2). For this reason, Gaussian fits were always performed asymmetrically as well, i.e. over the $[-1\sigma, +2\sigma]$ interval of each line: this allowed to stay clear of the low-energy tail while at the same time retaining enough points for a meaningful estimation of the line width.

To the left of the two main spectral lines are two other minor lines, better visible in logarithmic scale: those are the Al-K_α (1486 eV), originating from the fluorescence of the aluminum shielding[8] (Fig. 3.15b), and the Mn-K_α silicon escape line (4158 eV). If the statistics allows it and the charge loss is limited enough, even the Mn-K_β silicon escape line (4750 eV) can be seen. If their line centers are compared with the positions they are supposed to be at (highlighted in the plot as well), one can deduce that the response of the device is slightly non linear. Since a linear calibration was imposed on the data, mainly weighted by the two Mn fluorescence lines, a small non-linearity causes the minor lines to be misplaced by a few electronvolts (0.5 % shifts), even though they retain a rather correct position. From the plot it can be further said that this effect is more pronounced at lower energies, whereas for higher values the trend is essentially linear and that it either affects only a few channels or all the channels in the same way, because, if that was not the case, would be probably much wider. Nevertheless, an X-ray source displaying more spectral features is needed to correctly address this aspect of the response. This topic will be discussed in more detail in § 5.4.2.1.

Although a more in-depth discussion, especially in the framework of the mission specifications of MXT, will be provided in § 3.4 after the description of the parametric studies contained in § 3.3.2.4, the main figures of merit derived from the calculations above can already be briefly listed to see how they relate to the mission requirements for MXT.

The measured FWHM at $\approx -80\,^\circ$C at the Mn-K_α line is ≈ 146 eV, corresponding to an ENC of $10\,e^-_{rms}$. This value is not compatible with the one previously calculated from the noise map (§ 3.3.2.1), which implies that elec-

[8] In the final configuration, the shielding will be coated (§ 1.3.3.2) to prevent the Al-K_α fluorescence line to be excited, as it lays near the peak of sensitivity of the telescope and can therefore interfere with observations.

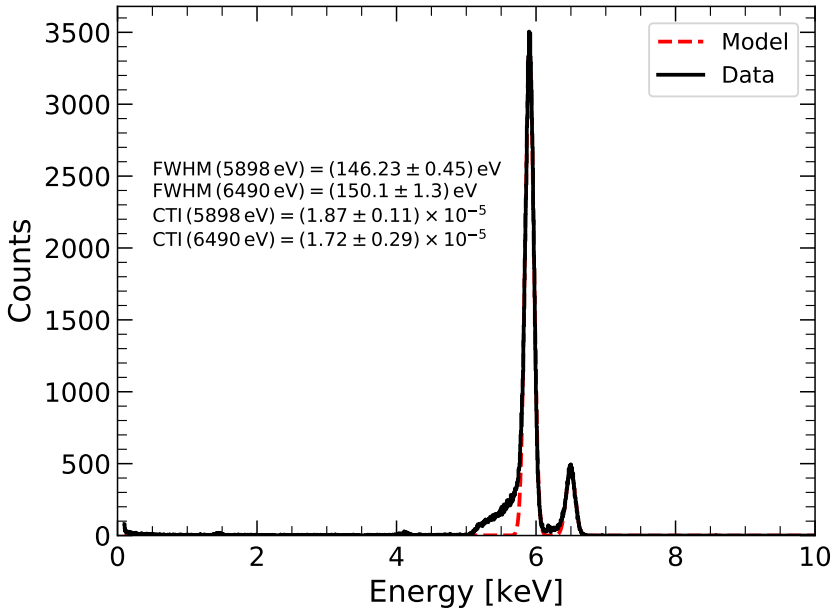

(a)

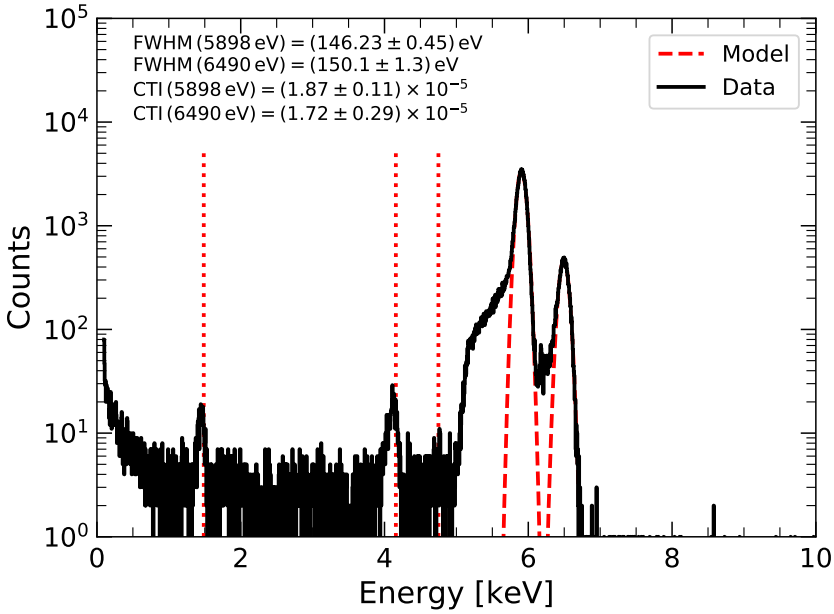

(b)

Figure 3.27 – Gain- and CTE-corrected ^{55}Fe spectrum taken at −80 °C. a) Linear scale. b) Logarithmic scale. The true positions of the Al-K$_\alpha$, Mn-K$_\alpha$ and Mn-K$_\beta$ silicon escape lines are also marked. Only single events were used.

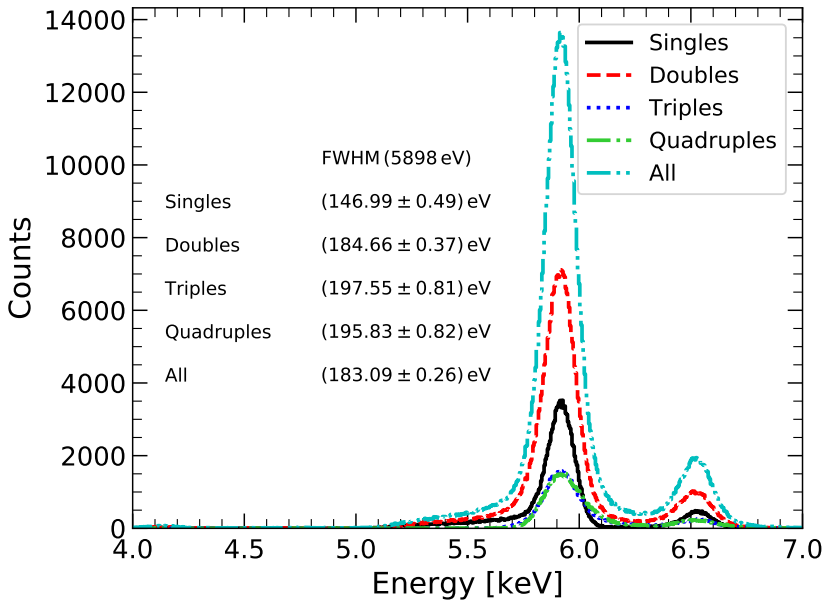

Figure 3.28 – Global ^{55}Fe spectrum at −80 °C. Patterns with different multiplicities were used.

tronic noise is not the only noise source affecting the measurements (this point will be resumed in § 3.4). If one considers the energy of 1.5 keV, ENC ≈ 10 e^-_{rms} translates to a resolution of ≈ 100 eV at the beginning of the mission. This value is beyond the 80 eV specification, but still acceptable within the scope of the expected performance degradation at the end of the mission (i.e. 160 eV after 3 years in orbit and 280 eV after 5 years, § 1.4.1).

The measured Charge Transfer Inefficiency (CTI) is compatible with data found in literature, e.g. Meidinger et al. (2006a), as a value of CTI (5898 eV) ≈ 1.9×10^{-5} is found, to be compared to CTI (6 keV) ≈ 10^{-5}, the latter being the one included in the baseline of MXT.

Finally, a low-level threshold of 100 eV was imposed in the spectral calculations: as already mentioned in § 3.1.1.3, this value is higher than the one used during event extraction (which was 4 times the noise map, i.e. ≈ 40 eV) and this mimics the actual in-orbit operation of MXT, where a first lower threshold is applied by the FEE on the data, followed by a second higher one applied in orbit by the MDPU for localization purposes or on ground during offline analysis. The chosen 100 eV level is compatible with the 200 eV requirement of MXT.

Once all the pixels are calibrated and corrected for CTI, spectra using other

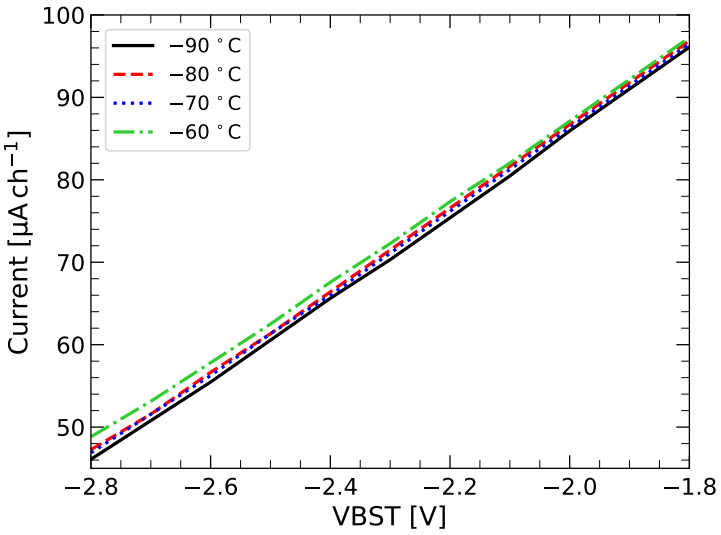

Figure 3.29 – Average drain-source current per channel of the First FETs of the CCD as a function of its working point voltage and temperature.

patterns as well as singles can be calculated. This is done in Fig. 3.28, where one can see the different proportions of the valid events as well as how the charge sharing noise degrades the resolution.

3.3.2.4 Parametric studies

The performances of the PM were studied as a function of a few operational parameters, i.e. CCD high voltage (`VRK`), First FET working point voltage (`VBST`, § 2.4.2.1) and temperature, which were explored in ranges relevant for the MXT mission:

- `VRK` $\in \{-210\,\mathrm{V}, -230\,\mathrm{V}, -250\,\mathrm{V}\}$;
- `VBST` $\in \{-1.8\,\mathrm{V}, -2.2\,\mathrm{V}\}$, corresponding to a current of $96\,\mu\mathrm{A\,ch^{-1}}$ and $48\,\mu\mathrm{A\,ch^{-1}}$ respectively, as shown in Fig. 3.29;
- $T \in \{-90\,^\circ\mathrm{C}, -80\,^\circ\mathrm{C}, -70\,^\circ\mathrm{C}, -60\,^\circ\mathrm{C}\}$.

All the results presented in the following come from single events only.

Spectral gain and offset Fig. 3.30 shows the column-by-column offset and gain as functions of temperature for `VRK` $= -230\,\mathrm{V}$ and `VBST` $= -1.8\,\mathrm{V}$ (other combinations of the voltages provide similar results). In case of the residual offset no trend is apparent, whereas the gain plot reveals a weak dependence on

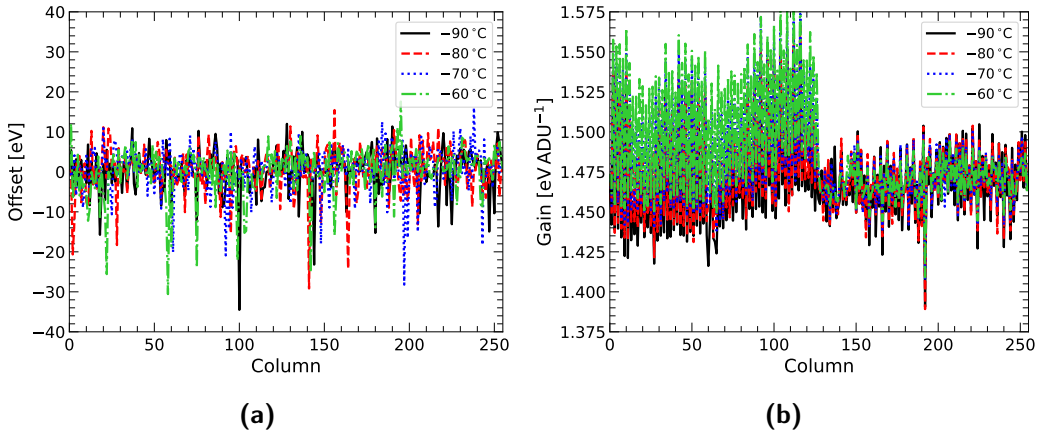

Figure 3.30 – Spectral offset (a) and gain (b) distributions as functions of temperature at VRK = −230 V and VBST = −1.8 V.

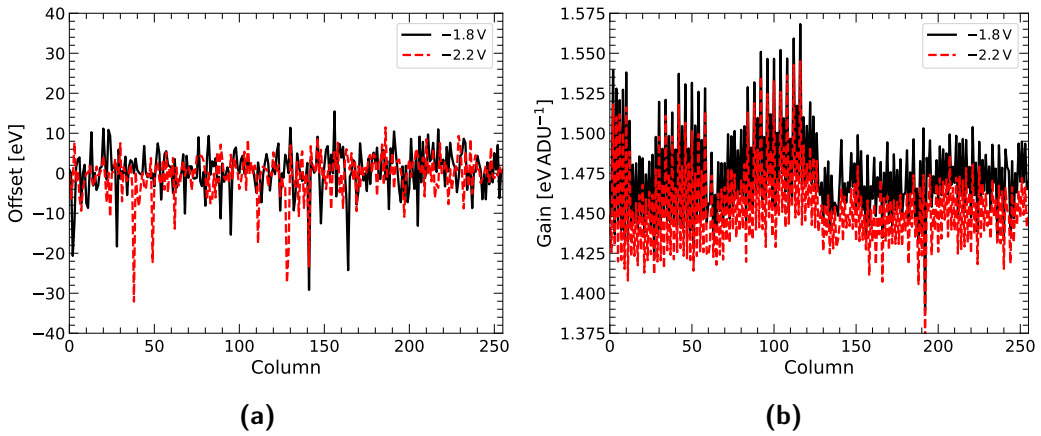

Figure 3.31 – Spectral offset (a) and gain (b) distributions as functions of VBST at VRK = −230 V and $T = -80\,°C$.

temperature, especially for the left ASIC, in which more negative temperatures are associated with smaller spectral gains. This effect is a combination of the temperature dependence of the passive components mounted on the ceramic carrier board as well as of the characteristic curves of the First FETs, their current decreasing with temperature at a given VBST (Fig. 3.29).

Gain and offset for the two values of VBST, given a temperature and an high voltage, are presented in Fig. 3.31. Although once again no clear trend is visible in the offset plot, the gain appears to decrease as VBST becomes more negative. This is an expected behavior as changing this voltage modifies the working point of the First FETs, leading to a change in the overall response of the acquisition chain. It is worth noting that in other setups in which detectors

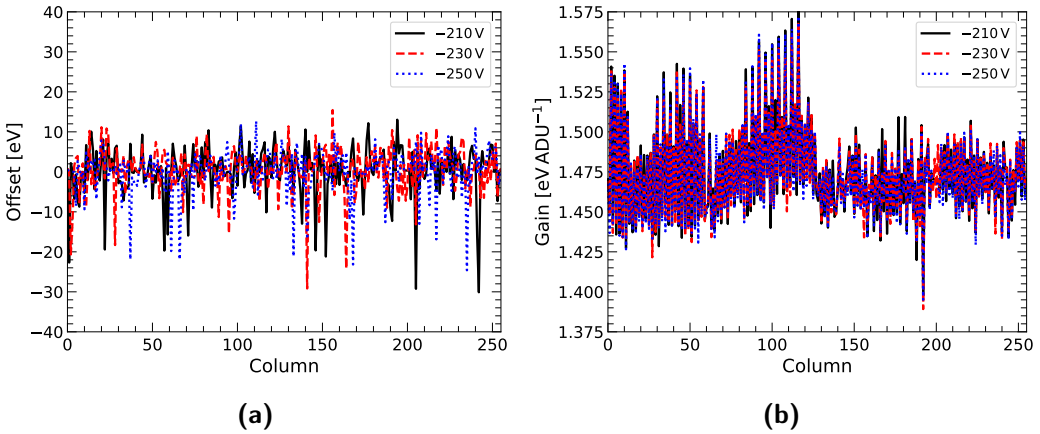

Figure 3.32 – Spectral offset (a) and gain (b) distributions as functions of `VRK` at `VBST` $= -1.8\,\mathrm{V}$ and $T = -80\,^{\circ}\mathrm{C}$.

similar to MXT's are operated, `VBST` $\approx -2.2\,\mathrm{V}$ ensures the higher gain, which is not true here because of voltage drops along the power supply line requiring a higher voltage to be applied to `VBST` to attain the same performances.

Finally, Fig. 3.32 presents spectral gain and offset for different values of the CCD high voltage at `VBST` $= -1.8\,\mathrm{V}$ and $T = -80\,^{\circ}\mathrm{C}$. As expected, no real dependence is visible, as `VRK` is not supposed to affect this aspect of the acquisition chain.

Spectral resolution How the spectral resolution at the Mn-K$_\alpha$ (5898 eV) varies with the parameters under study is presented in Fig. 3.33. Following § 2.3.3.2, the Full Width at Half Maximum (FWHM) of the spectral line is taken as a quantification of the resolution, along with its associated Equivalent Noise Charge (ENC). No trend stands out from the plots, except for a weak tendency for higher-amplitude `VRK`'s to yield better resolutions. However, due to the relatively high uncertainties and the fact that `VRK` $< -250\,\mathrm{V}$ was not recommended by the MPE (provider of the detector assembly) for safety reasons, using this value as a baseline working point is not justified.

Longer measurements at `VRK` $= -230\,\mathrm{V}$ and `VBST` $= -1.8\,\mathrm{V}$ were realized for the plots in Fig. 3.34, where the FWHM for both the Mn-K$_\alpha$ and Mn-K$_\beta$ is shown as a function of temperature. The point at $-90\,^{\circ}\mathrm{C}$ is abnormally high, a behavior not at all confirmed by the measurements discussed so far as well as the data taken in similar conditions. It cannot be explained given the available information and shall thereby be considered an outlier. Apart from

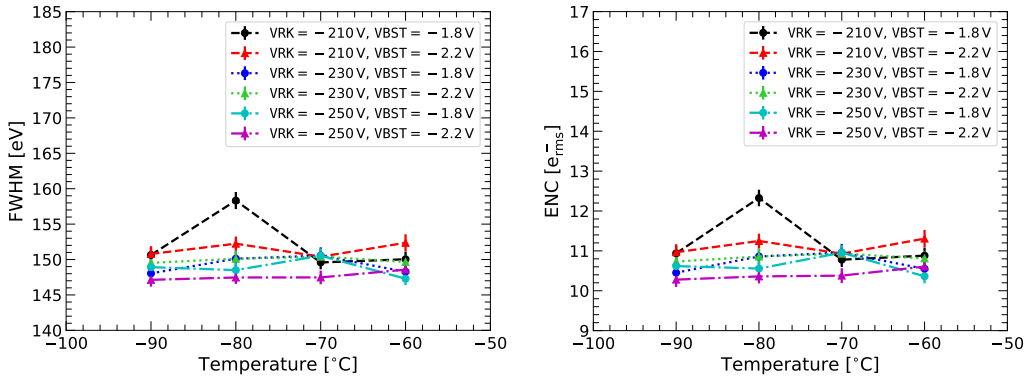

Figure 3.33 – Energy resolution at the Mn-K_α line as a function of temperature, `VRK` and `VBST`. a) Full Width at Half Maximum. b) Equivalent Noise Charge.

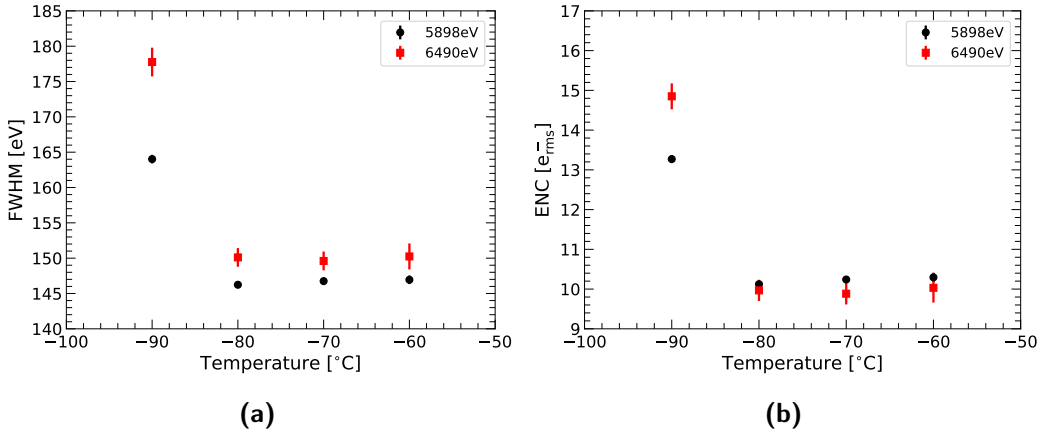

Figure 3.34 – Energy resolution as a function of temperature at the two Mn-K lines. Data acquired at `VRK` = −230 V and `VBST` = −1.8 V. a) Full Width at Half Maximum. b) Equivalent Noise Charge. The point at −90 °C is not confirmed by other measurements and shall be considered an outlier.

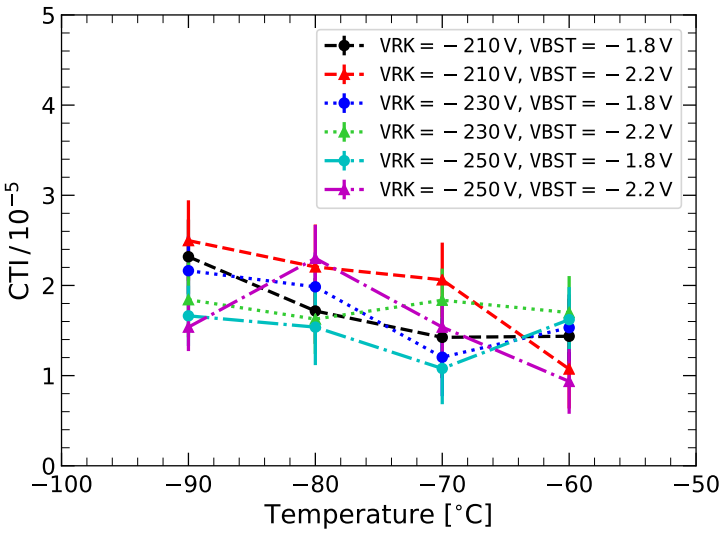

Figure 3.35 – Charge Transfer Inefficiency at the Mn-K$_\alpha$ line as a function of temperature, `VRK` and `VBST`.

that, the small variations in energy resolution and Equivalent Noise Charge (ENC) imply that the temperature-independent noise limit for our system was reached, meaning that leakage current was not a limiting factor of the performances.

Charge Transfer Inefficiency The investigations also dealt with the evolution of the Charge Transfer Inefficiency (CTI) according to the operational parameters. This is shown in Fig. 3.35 for the Mn-K$_\alpha$. No clear trend can be identified on the data points, but the estimates are limited between 1.5×10^{-5} and 2×10^{-5}, in agreement with both our results of § 3.3.2.3 and Meidinger et al. (2006a), where the value of CTI (6 keV) $= 10^{-5}$ is presented.

Once again, higher statistics measurements are used to derive more detailed trends with temperature and energy, which are reported in Fig. 3.36. The value of CTI (5898 eV) $= 1.9 \times 10^{-5}$ is confirmed to be almost constant over a broad temperature range. It is worth noting that CTI (5898 eV, −60 °C) being lower than the others is compatible with the lowering of the charge emission time with increasing temperature (§ 2.3.2.3, Fig. 2.17), which improves the transfer. As already mentioned, both the value and the lack of a strong temperature dependence (at least for sufficiently low T) are in line with the information already available about the detector (Meidinger et al., 2006a).

Although they seem not to influence much the results, temperature varia-

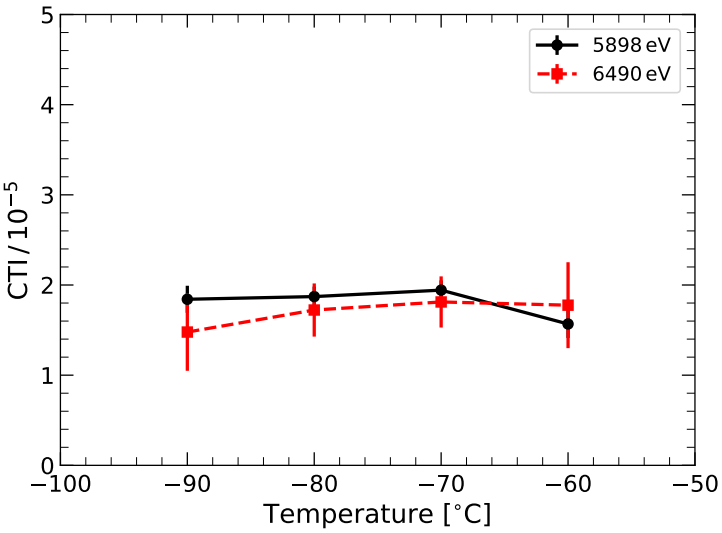

Figure 3.36 – Charge Transfer Inefficiency as a function of temperature at the two Mn-K lines. Data acquired at `VRK` $= -230$ V and `VBST` $= -1.8$ V.

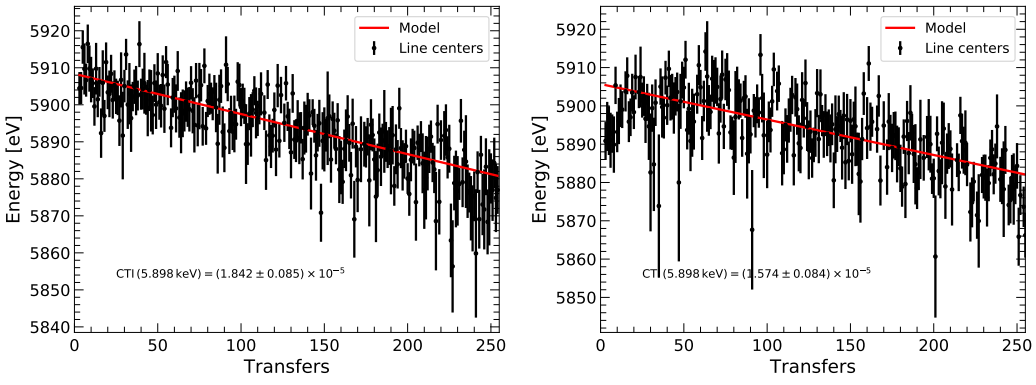

(a) **(b)**

Figure 3.37 – Fitted Mn-K$_\alpha$ line centers of the row-wise spectra, as a function of the number of transfers to reach the anodes. a) $T = -90\,°C$. b) $T = -60\,°C$.

tions do change the shape of the plots over which the CTI is fitted, according to eq. (3.10). Fig. 3.37 shows the Mn-K_α line centers as a function of the number of transfers the charge packets have undergone before reaching the anodes. As can be seen, as temperature increases the points deviate from the quasi-linear trend of eq. (3.10). This phenomenon is compatible with local variations in the CTI formula given in eq. (2.70), which result in the release of charges into the packets. A better understanding may be achieved if a *full* matrix response is measured, meaning that instead of calculating column-wise gain and overall charge efficiency, pixel-by-pixel spectra are analyzed. This is a study to be continued with the next FEE model, that will surpass the data rate limitation of the current prototype, enabling an output of $10\,\mathrm{frame\,s^{-1}}$in event mode (i.e. the list of hit pixels) and $5\,\mathrm{frame\,s^{-1}}$in full-frame mode.

3.4 Discussion

In the following sections, an assessment is given of the main results of the laboratory tests performed on the Engineering and the Performance Models of the MXT Detector Assembly. After a short summary of the main findings (§ 3.4.1), the question of the noise sources affecting the energy resolution of the Performance Model will be tackled (§ 3.4.2), to finally conclude with a few considerations about the future developments of the system (§ 3.4.3).

3.4.1 General considerations

I developed the full offline analysis pipeline of the MXT detector data, to be used in full-frame acquisition mode (§ 3.1). I used the algorithms to test and characterize the two available models of the MXT Detector Assembly. In both cases, experimental needs demanded some modifications of the pipeline to be able to analyze the data: in case of the Engineering Model (EM), the pattern identification needed to be tweaked to overcome the effects of charge trailing; with the Performance Model (PM), a novel correction algorithm had to be implemented to soften the multiplexing trailing that altered the pixel content up to $\approx 20\,\%$.

The Engineering Model (§ 3.2) suffered from performance issues and also experienced a fatal mechanical failure. Although a clear cause of the below-expectation response was not unequivocally identified nor was a solution found,

the EM allowed the experimental setup, the procedures and the fabrication process to be validated and upgraded for the next DA models.

The Performance Model (§ 3.3) featured a fully functional matrix, with uniform offset, gain and noise across all the 256×256 pixels. For the first time, the spectral performances of the MXT Detector Assembly were demonstrated in close compliance with the beginning-of-life mission requirements (FWHM (5898 eV) $\approx$ 146 eV instead of $\approx$ 130 eV expected) and in full compliance with the broader end-of-life specifications of the instrument. The low-energy threshold is also fully within the 200 eV specification.

3.4.2 Energy resolution of the Performance Model

Special attention should be dedicated to the energy resolution of the detector. As already pointed out during the presentation of the results, the Equivalent Noise Charge associated with the ^{55}Fe spectral lines is 10 e^-_{rms}, much higher than the 3 e^-_{rms} that can be calculated from the noise map. This means that electronic noise has to be ruled out as a major contributor to the line widths. Moreover, the almost complete absence of any temperature dependence demonstrates that leakage current is not an issue for the setup. Those considerations imply that the limiting noise source for the system must be searched elsewhere, as it apparently intervenes equally at the two studied energies and it is independent of other parameters. Since CTI is corrected for in the analysis, charge transfer noise such as in eq. (2.83) should be excluded too from the list of possible causes. This leaves room for two possible explanations, i.e. incorrect energy calibration or residual influence of the multiplexing trailing.

It is important to point out again that energy-dependent effects such as non-linearity, which may also depend on the ASIC channel, i.e. the column of the CCD, cannot be really quantified from the experimental data analyzed in this chapter. Indeed, all the algorithms used so far assume that a linear calibration can be estimated for all channels, which may not be the case. To assess this point, a multi-energy approach is necessary, which will be provided in § 5.4.

3.4.2.1 Energy calibration

In order to assess the hypothesis of incorrect energy calibration, the ECC algorithm (§ 3.1.2.1) was employed to calibrate the data. The synthetic

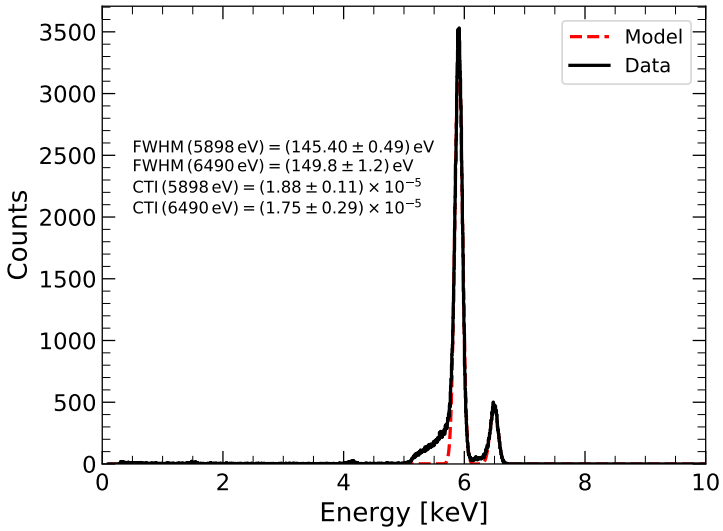

Figure 3.38 – Gain- and CTE-corrected ^{55}Fe spectrum taken at −80 °C. The data are the same as in Fig. 3.27, but the calibration was performed by use of the ECC algorithm (§ 3.1.2.1).

spectrum used was that of ^{55}Fe detected by a 450 µm-thick silicon detector, with the inclusion of the two escape lines. The result is shown in Fig. 3.38 for the same data set as Fig. 3.27. Even though the energy resolution does change a little, the variation is not enough to explain the increase from the $3\,e^-_{rms}$ of the noise map to the $10\,e^-_{rms}$ derived from the FWHM of the spectral lines.

3.4.2.2 Residual multiplexing trailing

A significant help comes from the possibility to put a radioactive X-ray source on the front side as well as on the back side of the detector, thanks to the specifically designed inlets of the cryostat (§ 3.3.1). Despite not being the nominal mode of operation for MXT, front-side illumination may allow to quantify how much charge splitting between pixels affects the spectral response, especially when coupled with multiplexing trailing. Two effects are expected. The first one is a decreased quantum efficiency, especially at lower energies, due to the p^+-structures of the shift registers as well as layers such as aluminum depositions and MIS structures present on the front side (§ 2.4.1.1). The second one is an alteration of the pattern statistics in favor of lower multiplicities: since photons are absorbed soon after they enter the detector (90 % of Mn-K$_\alpha$ photons are absorbed within 100 µm from the surface of the detector), the resulting electron clouds drift on average over smaller distances to reach the

potential minima placed at $\approx 7\,\mu m$ from the front side, thus resulting in fewer charge splits between neighboring pixels.

Fig. 3.39 shows an example of a ^{55}Fe front-side spectrum of single events taken at $-75\,°C$. Although multiplexing trailing was still present and was consequently corrected via the same method described in § 3.3.2.2, the low-energy tails of the spectral lines are much less prominent than in the back-illumination case (Fig. 3.27). This occurs because the pattern correction algorithm of § 3.3.2.2 has a smaller probability of wrongly identifying pixels from genuinely multiple events as multiplexing trailing, due to the fact that the total number of charge splits is smaller, as evidenced by plots such as Fig. 3.22. As a consequence, less double events (`TYPE` $= 2$) have one of their pixels forced to zero and end up being misclassified as single events, creating a *charge-loss* tail.

In terms of energy resolution, a performance improvement is experienced, with sharper lines than in the previous case, i.e. FWHM (5898 eV, front) $\approx$ 134 eV against FWHM (5898 eV, back) $\approx$ 146 eV. This again is at least partly due to the smaller presence of misattributed events in the spectrum and strongly suggests the fact that the spectral resolution limit is determined more by effects related to charge splits and multiplexing trailing than by electronic noise, leakage current and incorrect calibration.

3.4.2.3 Charge split

To understand how charge sharing among pixels can affect the energy resolution even in the case only single events are considered and no other phenomena contribute to the overall noise, two simulations were carried out. The first one relies on a focal plane simulator developed to generate synthetic detector data to be used for code validation purposes. The second one is a more restricted approach to the problem, aiming at investigating the relationship between the dimensions of photon-generated charge packets and CCD pixels. Both methods provide similar results, but the discussion will be limited to the latter for the moment, as the focal plane simulator will be thoroughly described in § 5.1.

The scenario of the simulation consists of a charge cloud, taken as a square for simplicity, whose dimensions are the same as a single pixel of the detector. A set of four neighboring pixels is considered, as all valid X-ray event patterns

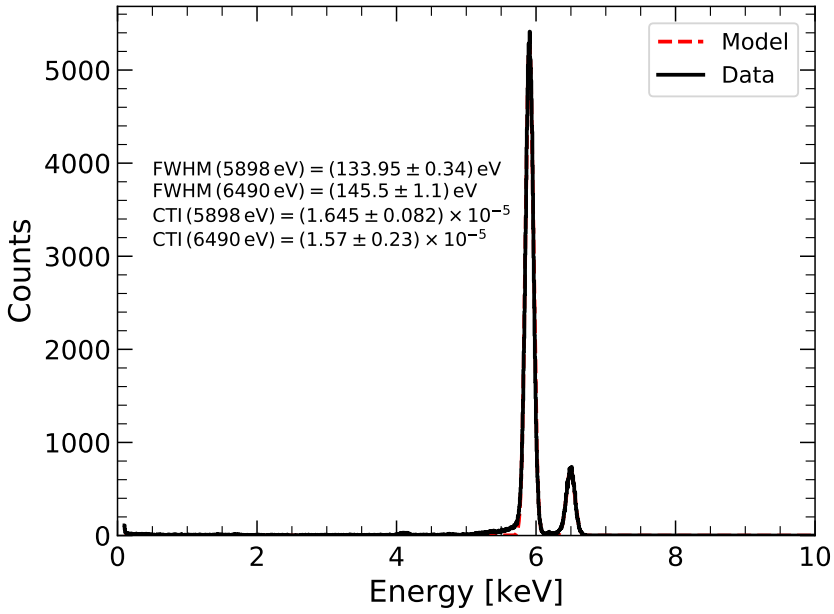

(a)

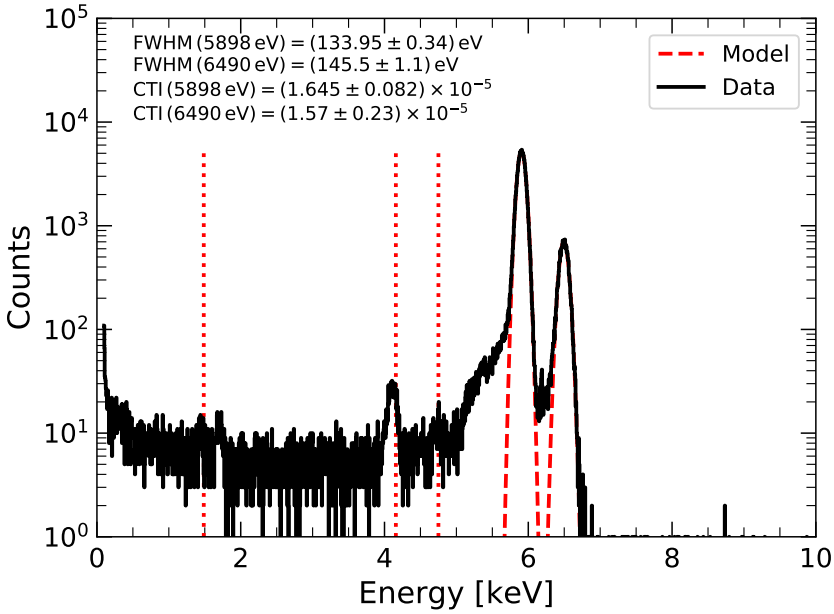

(b)

Figure 3.39 – Front-illuminated gain- and CTE-corrected ^{55}Fe spectrum taken at −75 °C. a) Linear scale. b) Logarithmic scale. The true positions of the Al-K$_\alpha$, Mn-K$_\alpha$ and Mn-K$_\beta$ silicon escape lines are also marked. Only single events were used.

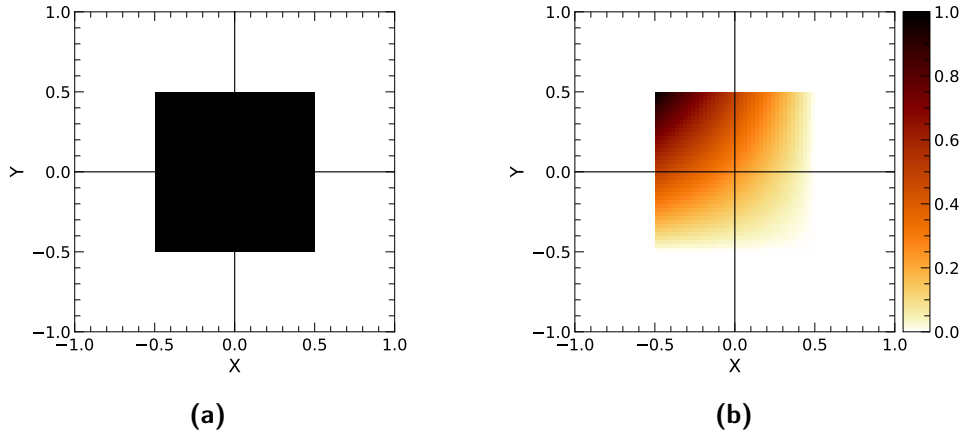

Figure 3.40 – Four-pixel system used in the simulation. a) Region covered by the centers of the charge cloud ensuring it stays fully included within the four pixels. b) Fraction of the area of the charge cloud included in the top-left pixel as a function of the position of the cloud center.

are obtained from a structure like this (Fig. 3.4). The center of the charge cloud is then randomly and uniformly moved so that the cloud is always entirely included within the four pixels (Fig. 3.40). For each position, the energy E contained in the top-left pixel is recorded, calculated as the energy of the incident photon E_γ multiplied by the fraction of the area of the square charge cloud included in the pixel itself. E_γ is drawn from a Gaussian distribution centered at 5898 eV (Mn-K$_\alpha$) and width due to the associated Fano noise, i.e. eq. (2.82). Finally, an energy threshold E_{thr} is defined to detect when a pixel is considered to be hit. In line with the 4σ level used in the analysis of the detector data, $E_{\text{thr}} = 40\,\text{eV}$ was chosen.

As the cloud moves, its charge is split among the pixels. Since the investigation focuses on single events occurring in the top-left pixel, I decided to retain only the energy values satisfying $E > E_0 - nE_{\text{thr}}$, where n is the number of pixels (other than the one under consideration) holding a portion of the charge cloud ($n \leq 3$). This corresponds to the situation in which the charge contained in the other pixels is under threshold and therefore not detected, leading to a single count as intended. Lower values than $E_0 - nE_{\text{thr}}$ coincide instead with a multiple event.

Fig. 3.41 shows the histogram of the surviving energies E. Although no noise source was added to the simulation except for Fano noise, the result is not Fano-limited: instead, the simulated spectral line is wider than expected (corresponding to an apparent ENC of $7\,e^-_{\text{rms}}$), a phenomenon that results

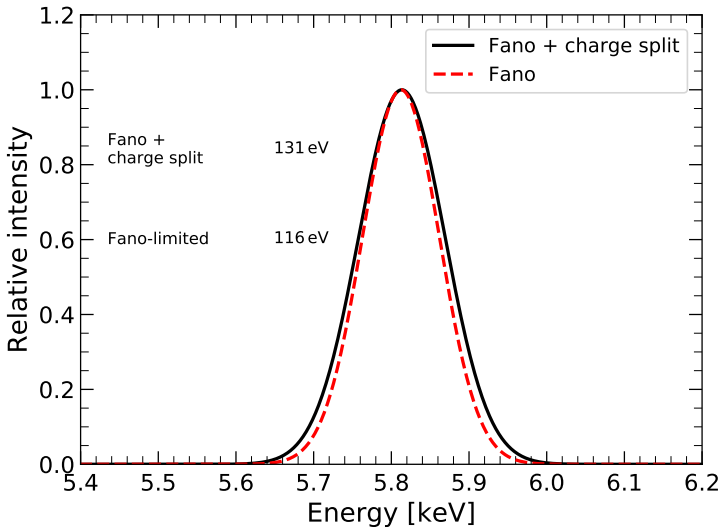

Figure 3.41 – Spectral line made out of single events, for which only Fano noise and charge split are taken into account. It is clear that despite the absence of any other noise contributions (most notably electronic noise), the line resolution differs from the expected Fano-limited case. The shift of the line center towards lower energies is addressed in § 5.4.2.3.

entirely from the fact that single counts are in reality usually split events for which the contributions of the neighboring pixels are under threshold. Indeed, the simulation also allowed to prove that, if the dimensions of the charge cloud are decreased, the energy resolution approaches the theoretical limit. It is worth noting that the use of a square charge cloud instead of a more realistic spherical Gaussian cloud (circular cross-section) does not undermine the final conclusion, as the objective was to demonstrate that sub-threshold signal can contribute to the degradation of the energy resolution.

The findings described above enable to safely state that a significant limiting contribution to the energy resolution of the PM Detector Assembly is represented by charge splits, which in turn depend on the relative dimensions of the photon-generated charge clouds and the pixel dimensions. As already mentioned at the beginning of § 3.4.2.2, those results can also explain the difference in the energy resolution between spectra acquired with front and back illumination: as the charge packets are created roughly at the same depth from either side of the detector, those generated by photons coming from the front spend less time diffusing and therefore are smaller compared to the pixels, which improves energy resolution.

It is useful to remind that the more thorough approach based on the focal

plane simulator provided completely compatible results. This will be dealt with in § 5.1.

3.4.3 Perspectives

The future steps in the characterization of the MXT acquisition chain include the confirmation of the performances and their compliance with the mission specifications in case the DA is coupled with the next model of the Front-End Electronics. This will be a crucial point, as the proto-FEE used in the previous tests does not obey the US-free requirement. This difference will be particularly felt in relation to the Analog-to-Digital Converters (ADCs) which allow the digitization of the CAMEX analog output: due to US-free components, the Effective Number of Bits[9] of the system will be of 10.5 instead of the 11.8 of the proto-FEE, a fact that is expected to degrade the performances in comparison to the results presented in the previous sections. As hinted previously, however, the preliminary results of the first tests are encouraging, suggesting that the overall noise contribution might only slightly increase ($4\,e^-_{rms}$ compared to $3\,e^-_{rms}$ of the proto-FEE).

The next models of FEE will be also used to investigate aspects of the response the knowledge of which is currently limited by the setup itself: one example is the pixel-by-pixel calibration, which requires much higher statistics than achievable at the moment, especially due to the data transfer rate to the interface PC.

[9]The Effective Number of Bits quantifies the impact of non-linearity, system noise and signal distortions on the performances of an ADC. Its definition is provided in IEEE (2011).

Chapter 4

Radiation effects on the spectral performances

In this chapter, an attempt will be made to answer some of the main questions of this thesis, i.e. how much space radiation the MXT detector will be exposed to during its operation in orbit and how said exposure will affect its response as a function of the mission lifetime. Particular interest will be dedicated to the study of the compliance with the scientific requirements of the mission. To tackle this topic, simulations will be mainly used, always firmly rooted in the physics behind all the relevant processes, along with some of the experimental results obtained previously.

After introducing the space radiation environment MXT will be operating in (§ 4.1), a review of the physics behind the interaction between radiation particles and detectors will be laid out, with the intent to quantify the effects on the performances (§ 4.2). In the second part of the chapter, a detailed description of the simulations performed in order to evaluate the expected in-orbit damage of the MXT detector will be provided (§ 4.3). Furthermore, the evolution of its performances will be predicted both from a theoretical and from an experimental point of view (§ 4.4).

4.1 Space environment

Scientific detectors which are exposed to levels of radiation capable of affecting their performances are usually operated in three possible environments: particle accelerators, nuclear reactors or space. Since the topic of

this manuscript is the study of the performances of the focal plane of MXT, that will be mounted on the SVOM satellite in orbit around the Earth, the properties of the space environment are here detailed, putting aside completely the other two scenarios, as they are not relevant to the discussion at hand.

This section is therefore divided into three parts, each corresponding to a particular component of space radiation: solar particles (§ 4.1.1), particles trapped in Earth's magnetosphere (§ 4.1.2) and galactic cosmic rays (§ 4.1.3).

4.1.1 Solar particles

According to the model first devised by Parker (1958a,b), the Sun's outer atmosphere, the *corona*, is constantly expanding and extends over several solar diameters in interplanetary space. Due to its high temperature ($\sim 10^6\,\mathrm{K}$), the corona is composed of neutral plasma (totally ionized gas) and can provide its electrons with enough energy to escape the gravitational attraction of the Sun. Due to its overall charge neutrality, the corona consequently also emits positive particles, in the form of protons and alpha particles, with traces of other heavier ions. The result is a continuous outward stream of particles named *solar wind*. The solar wind, which changes over time according to the solar cycle (Xapsos, 2006), has an average density of $1 - 30\,\mathrm{part\,cm^{-3}}$ with energies in the $0.5 - 2\,\mathrm{keV\,nucleon^{-1}}$, a temperature of $10^4 - 10^6\,\mathrm{K}$ and a speed of $300 - 900\,\mathrm{km\,s^{-1}}$ (Barth, 2009). The latter, coupled with a speed of sound of $50 - 60\,\mathrm{km\,s^{-1}}$, makes it *supersonic*. Due to magneto-hydrodynamic effects, the solar wind transports part of Sun's magnetic field, which then expands into the interplanetary space, eventually interacting with the galactic environment and forming the *heliosphere*, with similar properties to Earth's magnetosphere (to be discussed below in § 4.1.2).

In addition to solar wind, the Sun may produce *Solar Energetic Particle* events (SEPs) in which particles are accelerated through magnetic effects near its surface or even as they move through space, in case of the most violent ones. Energies for SEP particles may reach hundreds of MeV.

On the basis of what was explained above, both solar wind and SEPs depend directly on the Sun's magnetic field, which, according to data, undergoes a 22-year cycle, reversing polarity roughly every 11 years. This cycle is coupled with the Sun's activity in the form of X-ray flares, particle events and, most notably sunspots. For modeling purposes, the Sun's 11-year period is usually

divided up into 7 years of *solar maximum* followed by 4 years of *solar minimum*, the former being characterized by a high number of sunspots and other events, whereas the latter by a lower number of both.

4.1.2 Earth's magnetosphere

Earth's magnetic field $\vec{B}$ results from two contributions, one *internal* and the other *external*, each of which may be described as a scalar potential Φ:

$$\vec{B} = -\nabla\Phi = -\nabla\big(\Phi_{\text{int}} + \Phi_{\text{ext}}\big). \tag{4.1}$$

According to the dynamo model, the internal field is generated by convective currents flowing in the Earth's liquid outer core. It has an approximately dipolar shape, slightly offset from the planet center ($\sim 500\,\text{km}$) and tilted 11° with respect to Earth's rotational axis. This results in the north magnetic pole being located at $\sim 76^\circ\,\text{N}\,100^\circ\,\text{W}$ and the south magnetic pole at $\sim 66^\circ\,\text{S}\,100^\circ\,\text{E}$. The magnetic field strength varies between a few nT and $5 \times 10^4\,\text{nT} = 0.5\,\text{G}$ according to latitude and altitude. Although the dipolar component is by far the dominant one, additional orders may be considered, namely quadrupole and time-dependent corrections, linked to the dynamics of the fluids in Earth's core.

The dipolar model is reasonably accurate up to $4 - 5$ Earth's radii, beyond which it is necessary to include the influence of the external components, i.e. Earth's ionosphere, the solar wind and illumination by the Sun, all of which shape the outer layers of Earth's magnetic field. One defines the *magnetosphere* as the cavity in the solar wind caused by its interaction with the geomagnetic field (Fig. 4.1). The magnetosphere is composed of several regions:

- *Bow shock*: the (collisionless) standing shock wave occurring where the solar wind slows down to subsonic speed due to the interaction with Earth's dipolar field.
- *Magnetopause*: the layer in which the magnetic pressure of solar wind and Earth's magnetic field equal each other. It limits the magnetosphere at ~ 10 Earth radii in the sunward direction (~ 5 Earth radii during solar storms) and is mostly empty of solar particles (99.9% of the solar wind is deviated at the shock).

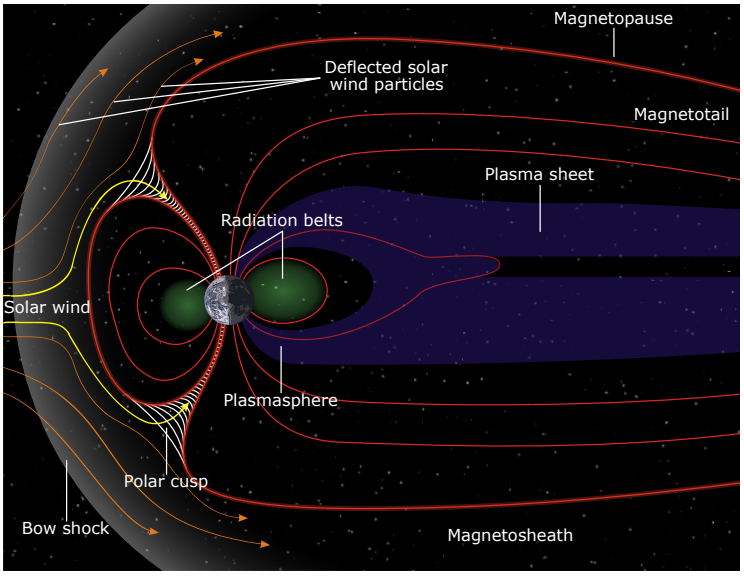

Figure 4.1 – Schematic of the Earth's magnetosphere. Adapted from NASA. Original available at `https://commons.wikimedia.org/wiki/File:Structure_of_the_magnetosphere_LanguageSwitch.svg`.

- *Magnetosheath*: the region between magnetopause and bow shock. It is filled with turbulent subsonic solar plasma which cannot penetrate further due to the magnetic pressure of the inner layers.

- *Magnetotail*: the portion of the magnetosphere extending up to ~ 300 Earth radii in the direction opposite to the Sun, formed by the Earth's magnetic field being deformed by the solar wind. Here not all the field lines are closed on themselves and some are connected directly to the interplanetary magnetic field.

- *Plasmasphere*: portion of the inner dipolar field populated by hot dense plasma, which also extends inside the magnetotail forming the *plasma sheet*.

- *Radiation belts*: regions overlapping with the plasmasphere and the plasma sheet, filled with electrons and protons (and heavy ions) trapped along the magnetic field lines. Two belts may be identified, an *inner belt* ranging from a few hundreds of kilometres up to $\sim 6 \times 10^3$ km, mostly populated by $\sim 10 - 100$ MeV protons and $\sim 1 - 10$ MeV electrons, and an *outer belt* extending up to $\sim 6 \times 10^4$ km and predominantly made up of high energy electrons. The fact that the center of Earth's magnetic

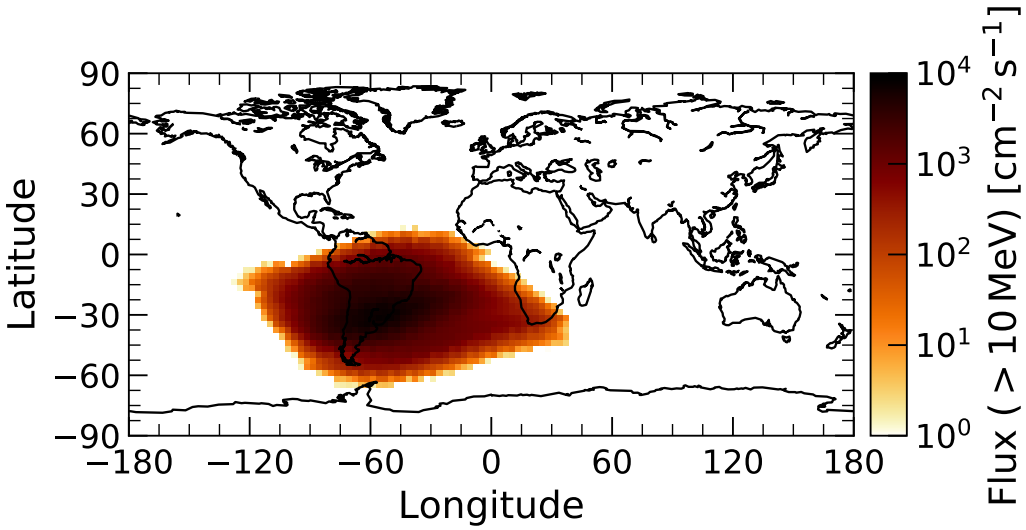

(a)

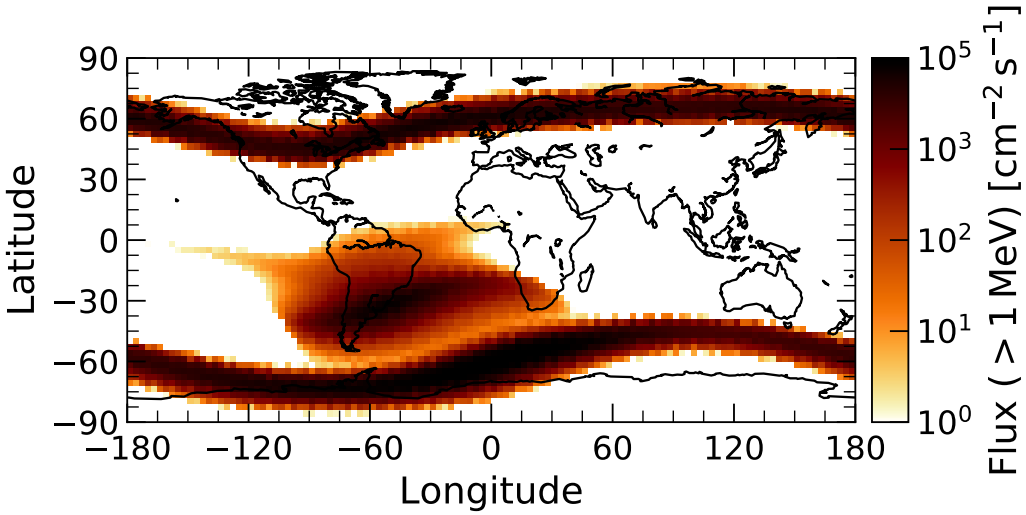

(b)

Figure 4.2 – Trapped particle flux at 800 km from Earth's surface. a) Flux of protons above 10 MeV. b) Flux of electrons above 1 MeV. In both cases, the South Atlantic Anomaly (SAA) is clearly visible.

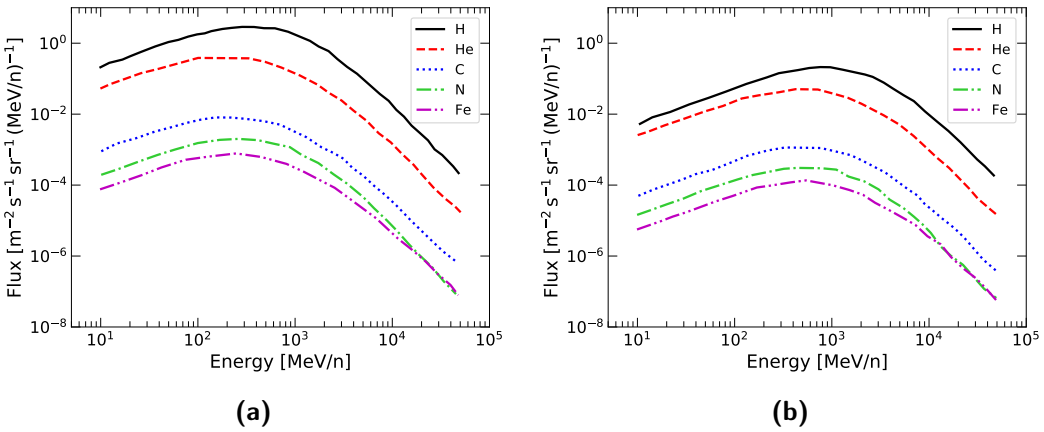

Figure 4.3 – Flux of Galactic Cosmic Rays. a) During solar minimum. b) During solar maximum. Adapted from Shea & Smart (2004).

field does not coincide with the center of the planet itself causes the radiation belts to be closer to the planet surface over the South Atlantic Ocean, where the energetic trapped particles may be found at relatively low altitudes. This region is named *South Atlantic Anomaly* (SAA) and represents the most important space radiation hazard for low Earth orbit missions (Fig. 4.2).

- *Polar cusps*: boundaries between the closed field lines on the day side and the opened lines on the night side, where some particles may penetrate the magnetopause. Indeed those are thought to be an entry point for solar particles to get trapped in Earth's magnetic field.

Due to the shielding effect of Earth's magnetic field, the most direct action of Sun's activity (solar wind and solar events) is less felt the lower the altitude.

4.1.3 Galactic cosmic rays

Galactic Cosmic Rays (GCRs) are particles from outside the solar system, believed to be produced in supernova explosions. Except for a small fraction of electrons (3%), they are composed of protons (83%), alpha particles (13%) and heavy nuclei (1%). Elements up to Uranium are present, even though a steep drop in abundance may be seen after Iron. Fluxes are low ($\sim 1\,\mathrm{part\,s^{-1}\,cm^{-2}}$) and energies range from a few MeV to $\sim 10^{11}$ GeV, with a maximum at $\sim 1\,\mathrm{GeV\,nucleon^{-1}}$ (Barth, 2009). In general, particles with energy $\lesssim 10\,\mathrm{GeV\,nucleon^{-1}}$ may be deflected by the magnetic field of the Sun

and the solar wind. This results in the GCRs being modulated by solar cycles, with lower and harder fluxes during solar maxima (Fig. 4.3). For an analogous reason, the flux of GCRs is less important the closer to Earth's surface the orbit, thanks to the screening effects of the planet's magnetic field.

4.2 Radiation damage

This section shall now delve into the physics of the interactions between semiconductor detectors and radiation, focusing on how the latter affects the performances of the former and how to quantify said evolution. After an overview of the different components the interaction can be broken down to (§ 4.2.1), the ones that are most relevant to this work will be discussed, i.e. ionization damage (§ 4.2.2) and displacement damage (§ 4.2.3).

4.2.1 Energy losses

Particles traversing a medium may lose energy by:

- interactions with the electron clouds surrounding the atoms of the medium, by means of excitation or ionization (*inelastic*, *ionizing* or *electronic energy loss*);
- elastic collisions with the nuclei, which may result in their displacement from their lattice site (*elastic*, *non-ionizing* or *nuclear energy loss*);
- action of the electric field of the nuclei, which may cause the incoming particle to deviate and therefore emit electromagnetic radiation (*Bremsstrahlung* or *radiative energy loss*).

If the three contributions are taken into account, one may write the energy loss $\mathrm{d}E/\,\mathrm{d}x$ of a particle with energy E moving along a path x through a medium as the sum of three terms

$$\frac{\mathrm{d}E}{\mathrm{d}x} = \left.\frac{\mathrm{d}E}{\mathrm{d}x}\right|_{\mathrm{elec}} + \left.\frac{\mathrm{d}E}{\mathrm{d}x}\right|_{\mathrm{nucl}} + \left.\frac{\mathrm{d}E}{\mathrm{d}x}\right|_{\mathrm{rad}}. \tag{4.2}$$

Usually, the energy loss $\mathrm{d}E/\,\mathrm{d}x$ is also referred to as *stopping power*, which may therefore be electronic, nuclear of radiative in nature. Of course, this separation into three independent components does not consider possible correlations

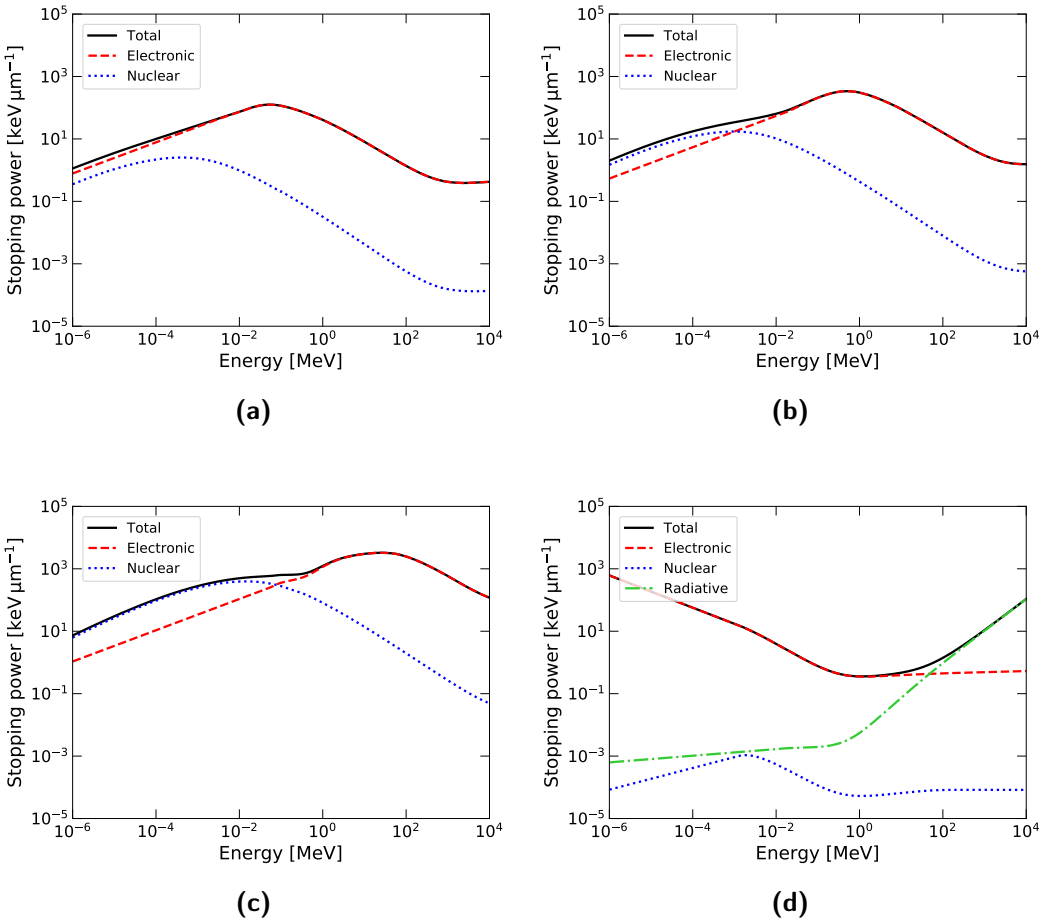

Figure 4.4 – Stopping power as a function of energy for particles in silicon, broken down into its components. a) Protons. b) Alpha particles. c) Silicon ions. d) Electrons. Models obtained from Boschini et al. (2014).

between the phenomena, which are considered to be negligible (Ziegler et al., 2008).

Fig. 4.4 shows the total stopping power for several particles in silicon. It is clear that the electronic component is dominant in most cases, with the nuclear one becoming relevant only for the more massive particles and only at low energy. On the other hand, the radiative emission is reported for electrons only, as it is negligible for other particles, due to the mass difference.

From the total stopping power, one can calculate the *range* $x_{\max}$ of a particle in a medium, defined as the length of the path over which it passes from an initial energy E to rest:

$$x_{\max}(E) = \int_0^E \left[-\frac{\mathrm{d}E}{\mathrm{d}x}(e) \right]^{-1} \mathrm{d}e, \tag{4.3}$$

where the integration is performed on the energy. Equivalent to the range is also the *projected range*, i.e. the projection of the traveled distance onto the initial incoming direction. Due to scattering, the two may not match, especially at low energies, when the deviations per collision are larger.

From Fig. 4.4 it is evident that, as a particle slows down from high energy, it loses more and more energy, to the point that most of it is deposited just before stopping. This feature is called *Bragg peak* and it is peculiar to charged particles.

In the following, the ionization and displacement damage will be examined in more detail in § 4.2.2 and § 4.2.3, with more attention being dedicated to the latter, as it is more intimately connected with the subject of this work. Radiative processes will be left out of the discussion, since they are relevant for electrons (and positrons) only, as previously stated, and only at high energies. Furthermore, photons produced through those phenomena obey the same physics already discussed in § 2.3.1.2.

4.2.2 Ionization damage

In the next sections, the ionization damage a detector suffers when operated in a radiation environment will be described. Firstly, the electronic (or inelastic) energy loss will be dealt with in general terms (§ 4.2.2.1) and then the results will be used to quantify the exposure of a device to radiation (§ 4.2.2.2). Finally, the effects of said exposure which are most relevant to this work will be reviewed (§ 4.2.2.3).

4.2.2.1 Electronic energy losses

Let us consider a particle with mass M_1, charge $Z_1 q$, traversing with velocity $v = \beta c$ and energy E a solid of density ρ made out of atoms of atomic number Z_2 and atomic weight A. The electron clouds of the medium can be considered as a gas of free particles, which, if their velocity is negligible with respect to that of the incoming particle, can be seen as static during the interaction. Under those hypotheses, the rate at which the projectile loses energy is given by (Leo, 1994; Leroy & Rancoita, 2009)

$$-\frac{\mathrm{d}E}{\mathrm{d}x} = 2\pi N_\mathrm{A} r_\mathrm{e}^2 m_\mathrm{e} c^2 \rho \frac{Z_2}{A} \frac{Z_1^2}{\beta^2} \left[\ln\left(\frac{2 m_\mathrm{e} \gamma^2 v^2 W_\mathrm{max}}{I^2} \right) - 2\beta^2 - \delta - 2\frac{C}{Z_2} \right], \quad (4.4)$$

where the minus sign indicates that the energy is being lost, $\gamma = 1/\sqrt{(1-\beta^2)}$, m_e is the electron mass, $r_\mathrm{e} = q^2/(4\pi\varepsilon_0 m_\mathrm{e} c^2)$ the classical electron radius, $N_\mathrm{A} = 6.022 \times 10^{23}\,\mathrm{mol}^{-1}$ Avogadro's number, W_max is the maximum energy transfer in a single collision and I the *mean ionization potential* of the medium. The *density effect correction* δ takes into account the polarization induced on the surrounding atoms by the electric field of the traversing particles, which makes it more difficult for farther electrons to be ionized, as they are more shielded. On the other hand, the *shell correction* C is mostly important at low energies, when the particle's velocity becomes comparable to the orbital velocity of the electrons and therefore the electrons can no more be considered static during the interaction. It is also worth noting that in case of moving ions, as they slow down, they tend to pick up electrons from the surrounding medium, which modifies their charge state and hence § 4.4.

In case the particle is moving through a compound with total density ρ, comprised of N elements each one with density ρ_i and present in a fraction w_i, the total stopping power writes

$$\frac{1}{\rho}\frac{\mathrm{d}E}{\mathrm{d}x} = \sum_i \frac{w_i}{\rho_i}\frac{\mathrm{d}E_i}{\mathrm{d}x}, \tag{4.5}$$

where $\mathrm{d}E_i/\mathrm{d}x$ is the stopping power the particle would have if the medium was entirely made out of the element i. Eq. (4.5) is known as *Bragg's rule*.

In case of electrons and positrons, the different cross sections for the interactions with the free electron gas of the medium leads to different forms of eq. (4.4). Details can be found in textbooks such as Leroy & Rancoita (2009).

4.2.2.2 Ionizing dose

The energy a particle loses inside a medium through eq. (4.4) is given to the electrons, which are excited to higher states or even ionized. The most energetic among those electrons, able to travel significant distances from the position where they originated, are called *δ-rays*. Secondary electrons in turn may lead to further ionization according to the process already described in § 2.3.1.3. If however some of the newly-formed electrons are energetic enough to escape the medium, not all the energy lost by the primary particle gets absorbed. Therefore the energy lost by a particle is not necessarily the same as the energy deposited. For this purposes, when dealing with the effects of

ionizing radiation to matter, one refers to the *Linear Energy Transfer* (LET), i.e. the amount of energy per unit length *absorbed* by a medium through ionization processes:

$$\mathrm{LET} = \left.\frac{\mathrm{d}E}{\mathrm{d}x}\right|_{\mathrm{elec}}. \tag{4.6}$$

Given a particle distribution $\mathrm{d}\Phi/\,\mathrm{d}E$ (differential fluence) in the energy range $[E_{\min}, E_{\max}]$, the *Total Ionizing Dose* (TID) is defined as as the energy absorbed by a medium through ionization processes:

$$\mathrm{TID} = \int_S \int_{E_{\min}}^{E_{\max}} \frac{\mathrm{d}\Phi}{\mathrm{d}E}\left(E, \vec{r}\right) \int_0^{X(E)} \mathrm{LET}\left(E\left(x\right)\right)\,\mathrm{d}x\,\mathrm{d}E\,\mathrm{d}S, \tag{4.7}$$

where the integral is extended over the whole irradiated surface S of the device under consideration. The integration along the particle path x is performed up to the maximum penetration $X\left(E\right)$, which depends on the initial energy as well as on the geometry (e.g. particles coming at different angles and positions on the surface may travel different lengths). The dose is measured in *gray* Gy ($1\,\mathrm{Gy} = 1\,\mathrm{J\,kg^{-1}}$) or rad ($1\,\mathrm{rad} = 100\,\mathrm{erg\,g^{-1}} = 10^{-2}\,\mathrm{Gy}$).

4.2.2.3 Ionizing radiation effects

In the following a very brief review of the most important consequences of ionization damage in electronic devices is given. A more detailed treatment is left to specialized texts such as Spieler (2005) or ECSS-E-HB-10-12A.

Cumulative effects Let us consider a charged particle crossing the oxide layer of a MOS structure (§ 2.1.3.3). Due to ionization, it loses some energy inside of it, which results in the creation of some electron-hole pairs, the average energy required for this process being a few times the corresponding value for silicon ($\approx 18\,\mathrm{eV}$ instead of $\approx 3.6\,\mathrm{eV}$). Under the action of the electric field applied across the oxide, the electrons may move ($\mu_{\mathrm{n}} \approx 20\,\mathrm{cm^2\,V^{-1}\,s^{-1}}$ at room temperature) towards the positive electrode and eventually recombine. Holes on the other hand have a much lower mobility ($\mu_{\mathrm{p}} \approx 10^{-4} - 10^{-11}\,\mathrm{cm^2\,V^{-1}\,s^{-1}}$ depending on temperature and electric field) and therefore are mostly fixed or tend to get trapped by defects at the silicon-oxide interface, thereby accumulating in the oxide. This results in a build-up of positive charges with several possible consequences, such as

- voltage threshold shifts in MOSFETs, lower threshold for n-MOSFETs, higher for p-MOSFETs;
- alteration of the depletion voltage of MOS devices;
- modification of the oxide electric field, resulting in poorer isolation in integrated circuits;
- increase in leakage current if the modified voltage causes inversion.

Transient effects As previously discussed, as a charged particles deposits energy along its path, it generates electrons from the ionization of the medium. If the particle happens to move across a sensitive region of a circuit, it may put in contact regions that are normally supposed to be electrically isolated, with potentially dangerous consequences, depending on the type and energy of the incoming particle, the component struck in the circuit and its operation. Since those phenomena depend on the passage of single particles, they are known as *Single Event Effects* (SEEs) and subdivided into different categories.

- Non-destructive events may affect digital electronic components and involve the flip of single bit (*Single Event Upset* or SEU) or multiple bits (*Multiple Bit Upset* - MBU - or *Multiple Cell Upset* - MCU). Recovery is usually possible by simply rewriting the compromised bits.
- Destructive events are associated with high currents flowing between sensitive parts of a circuit: if the current is not managed, the consequent heat dissipation may result in the destruction of the component itself. Examples are *Single Event Latch-ups* (SELs), *Single Event Burnouts* (SEBs) and *Single Event Transients* (SETs).

4.2.3 Displacement damage

The following sections detail the causes and effects of the displacement damage suffered by detectors after exposure to radiation. At first, a phenomenological summary of the physics of defect formation shall be provided (§ 4.2.3.1), followed by the kinematics of collisions between incoming radiation particles and lattice ions (§ 4.2.3.2), and the properties of radiation-induced defects (§ 4.2.3.3). Finally, some ways to quantify displacement damage are

presented, with the goal of establishing a relation with the performances of a device (§ 4.2.3.4).

4.2.3.1 Defect formation

Let us consider a particle of mass M_1, charge $Z_1 q$ and energy E traversing a crystalline medium and colliding with a stationary atom of mass M_2 and charge $Z_2 q$. Let E' and E_R respectively be the energies of the incoming particle and recoil atom after the interaction, and E_d the depth of the potential barrier keeping the lattice atom in its site, i.e. the threshold energy for displacement[1].

- If $E_\mathrm{R} < E_\mathrm{d}$, the target atom cannot leave its position in the lattice and E_R is dissipated through vibrations.
  - If $E' > E_\mathrm{d}$, the primary particle may collide with another atom of the lattice, with the opportunity to displace it.
  - If $E' < E_\mathrm{d}$, the primary particle cannot displace any other atom of the lattice and becomes an *interstitial*, with E' dissipated as phonons.
- If $E_\mathrm{R} > E_\mathrm{d}$, a *displacement* occurs and the target atom is pushed away from its site with an energy $E'_\mathrm{R} = E_\mathrm{R} - E_\mathrm{d}$. In this case, it is referred to as *primary knock-on atom* or PKA.
  - If $E' < E_\mathrm{d}$ and $Z_1 = Z_2$, a *replacement* takes place, whereas with $Z_1 \neq Z_2$ the original projectile becomes an *interstitial*. In both cases, E' is lost to phonons.
  - If $E' > E_\mathrm{d}$, the primary atom can move on and may interact again with the medium. Since no atom occupies the lattice site anymore, a *vacancy* is created. An electrically active vacancy-interstitial complex is known as *Frenkel pair*.

For particles energies $\gg E_\mathrm{d}$ a *cascade* may be generated, with many atoms being displaced and displacing others in turn, all in a tight space. As a consequence, a *cluster of defects* forms (Fig. 4.5). Finally, particles reaching the surface of the solid with energy larger than its *surface binding energy* E_s

[1] Here the potential well is described by a single value, whereas in reality it is a function of position (interatomic potential). Thermal fluctuations also play a role.

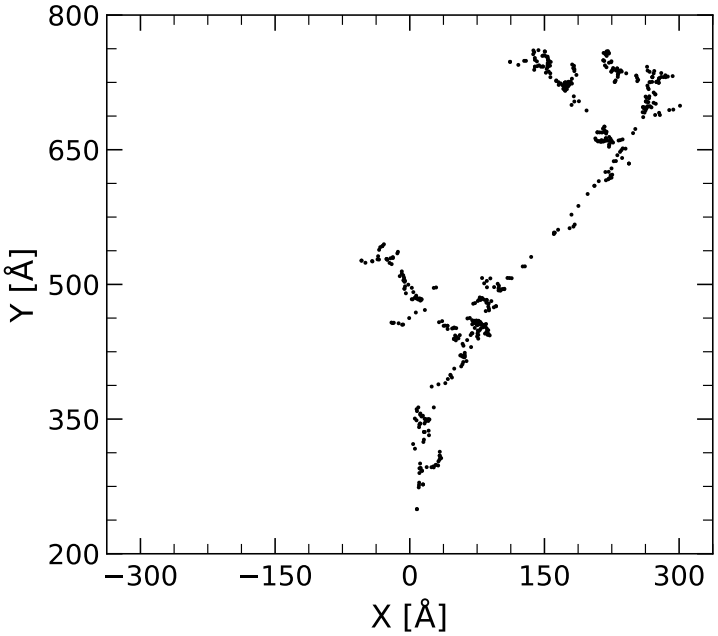

Figure 4.5 – Simulations of the spatial distribution of vacancies created by a recoiling 50 keV silicon ion in silicon. Each dot represents a vacancy. It is clear how some vacancies are concentrated into clusters.

leave the lattice (*sputtering*). It is also worth pointing out that, if the involved energies allow them, *nuclear processes* may occur, such as fragmentation, spallation, neutron capture or transmutation, all of which may be responsible for more impurities and displacements being produced.

Monte Carlo simulations (Wood et al., 1981) show that for recoil energies $< 1-2\,\mathrm{keV}$ ($E < 15\,\mathrm{keV}$ for protons) particles only generate isolated Frenkel pairs. At higher energies, PKAs can originate single cascades and for $E_\mathrm{R} > 12-20\,\mathrm{keV}$ ($E > 150\,\mathrm{keV}$ for protons) tree-like structures with many sub-cascades are produced.

4.2.3.2 Kinematics of displacements

It is useful to calculate the minimum energy a particle must have in order to displace an atom. For this, the maximum energy transferred in a collision $E_\mathrm{R,max}$ and the threshold energy for displacements E_d are required.

$E_\mathrm{R,max}$ can be easily obtained through the application of the *hard-sphere model*, which takes advantage of the well known kinematics of collisions between point masses. If relativistic effects are not important, a classical approach

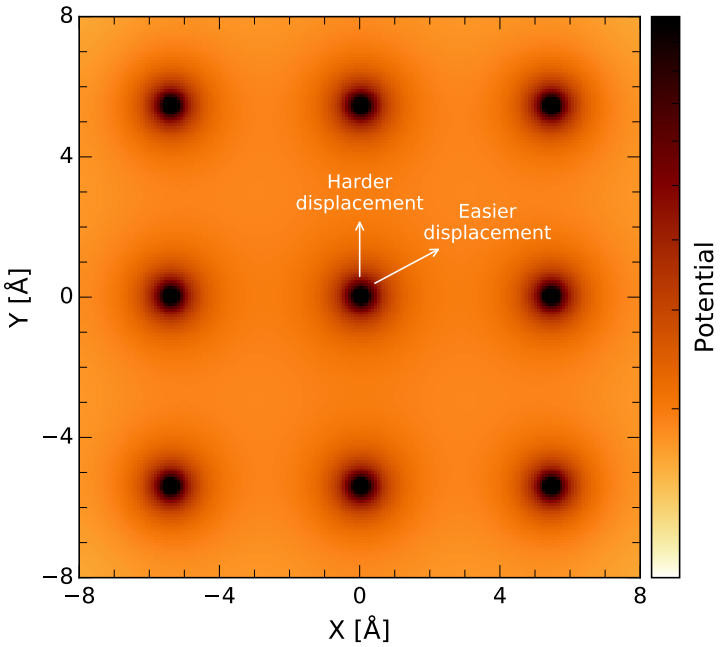

Figure 4.6 – Dependence of displacement energy on recoil direction. An atom is more easily displaced if it moves towards the a saddle point between atoms than towards another lattice site, where the interatomic potential is at its strongest.

yields (Kinchin & Pease, 1955)

$$E_{\mathrm{R,max}} = \frac{4M_1M_2}{(M_1+M_2)^2}E. \tag{4.8a}$$

In case of a relativistic treatment, which is for example necessary for electrons, the maximum transferred energy becomes (Kinchin & Pease, 1955)

$$E_{\mathrm{R,max}} = \frac{2E\,(E+2m_{\mathrm{e}}c^2)}{M_2c^2}. \tag{4.8b}$$

The displacement energy E_{d} is however in principle a function of the direction, because a recoil atom can more easily move towards the gap between lattice nodes than to another atom in the lattice (Fig. 4.6). In silicon, it is about $13-33\,\mathrm{eV}$, but in practice an average over all directions is taken: $E_{\mathrm{d,Si}} = 21\,\mathrm{eV}$.

As a consequence of the above reasoning, one finds that the minimum energy for a proton or an electron to cause a displacement in silicon is 160 eV

and 240 keV respectively.

Ions (including protons) exchange Coulomb interactions with the lattice nuclei, according to their mass and energy, and the electron-screened interatomic potential. They also undergo Coulomb scattering with the electrons in the medium, losing energy through ionizing processes (§ 4.2.2). Since the cross-section for displacements increases as the particles slow down, this implies that more significant damage occurs towards the end of their path.

Electrons, as charged particles, essentially undergo the same processes as other ions. However, in order to displace atoms, electrons have to penetrate their K shell, which, in combination with their small mass, makes the whole displacement process inherently much harder for them. As a consequence, electron radiation is unlikely to cause cascades, and usually its main effect is the generation of isolated defects.

Photons may produce displacements by means of two mechanisms. On the one hand, they can generate Compton electrons or electron-positron pairs, which may in turn go on creating primary knock-ons (§ 2.3.1.2). On the other hand, energetic photons may interact with the nuclei themselves, thus directly originating recoils. In both cases, as in the case of electron radiation, the energies involved are usually not high enough to cause displacement cascades, and thus only Frenkel pairs are created.

In case of neutrons, the absence of any electrical charge means that a complete hard-sphere approach is possible and also that no ionizing energy loss takes place. As a consequence, fast neutrons can penetrate very deeply in a medium, thereby potentially causing heavy damage even very far from the exposed surface. Furthermore, slow neutrons can be involved in nuclear reactions, such as neutron capture, by which atoms recoil so much to leave their position in the lattice.

4.2.3.3 Radiation-induced defects

Regardless of whether they are created in isolation or as part of cascades, most vacancy-interstitial (or $V - I$) pairs diffuse towards the surface or recombine under the action of thermal agitation, as they are both (especially the vacancy) quite mobile even at low temperatures (Marshall & Marshall, 1999; Lutz, 2007). This process usually takes place in less than one millisecond. Some stable defects will nonetheless be created in a characteristic time of about

one second in silicon. The whole phenomenon of evolution from unstable into stable defects is known as *short-term annealing* (Marshall & Marshall, 1999).

Radiation-generated defects are classified in two families.

- *Clusters* were introduced as a way to explain the higher minority carrier recombination rate observable in devices irradiated with heavy particles, as opposed to exposure to gammas and electrons. Apart from the knowledge that they are composed of vacancies and interstitials interacting with each other, no satisfying model has been developed to this day.

- *Point defects* are instead much better understood and, as the name suggests, occur around a single lattice node. They may be composed by replacement atoms, other kind of impurities or vacancies. An important class of point defects is a vacancy interacting with an interstitial (*Frenkel pair*).

The following analysis shall be focused on point defects, as clusters are relevant only in case of heavy irradiation with energetic ions (e.g. particle accelerators).

Let us consider a defect with an energy level E_t in the forbidden band gap. According to the same convention valid in case of doping impurities (§ 2.1.3.1), one defines *acceptors* those defects that are negatively charged when occupied by an electron, whereas *donors* are defects that are neutral when occupied by an electron. Defects may have multiple levels, even acceptor and donor together, in which case their are called *amphoteric*. The position of the energy levels with respect to the Fermi level E_F defines if a defect is neutral or ionized in thermal equilibrium: when $E_\mathrm{t} < E_\mathrm{F}$, donors are neutral and acceptors are negative; when $E_\mathrm{t} > E_\mathrm{F}$, donors are ionized and acceptors are neutral.

The position of the energy level E_t inside the forbidden band gap determines the behavior of the defect, as illustrated in Fig. 4.7.

- *Generation centers* have levels through which electrons move between bands, thus contributing to the leakage current. The most effective generation centers have an energy around the middle of the band gap (§ 2.1.2.1).

- *Recombination centers* capture electrons (holes) from the conduction (valence) band and do not release them until a hole (electron) has been captured as well from the other band. The consequence is a subtraction

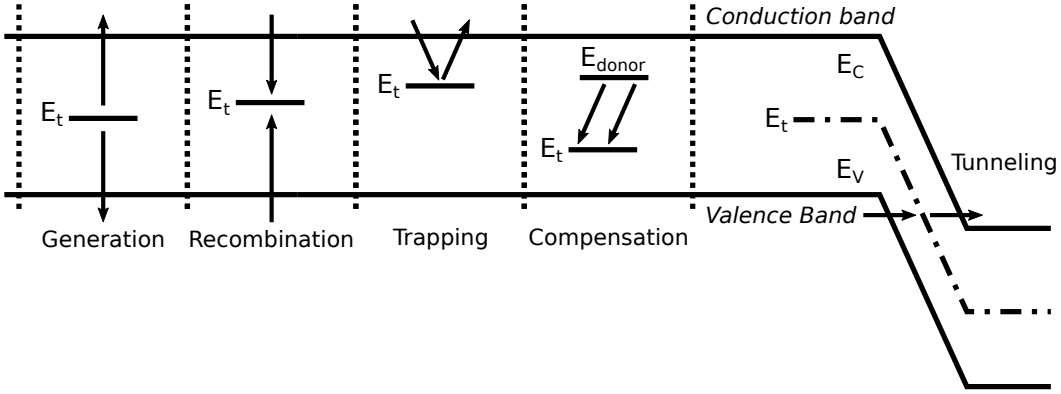

Figure 4.7 – Effects of radiation-induced defect levels in the forbidden band gap. (Marshall & Marshall, 1999)

of the carrier from conduction (§ 2.1.2.1). This process is defined by the minority carrier lifetime.

- *Traps* are defects with an energy level just below the conduction band (above the valence band), in which electrons (holes) can be captured before being released in the conduction (valence) band. If the timing at which charges move is important (e.g. the transport and readout in a CCD), a net charge loss can be measured (§ 2.3.2.3).

- *Compensation* occurs when radiation-generated acceptor defects capture electrons emitted by donor doping impurities in n-type semiconductors, as if the doping concentration had effectively changed. The same effects may happen for holes, with donor defects and acceptor doping impurities in p-type devices.

- *Tunneling* across a potential barrier can also be enhanced by energy levels lying in the middle of it.

Each family of traps can influence the performances of a detector in different ways. For this study, since the focus is on pnCCDs, the attention will be concentrated on traps and generation centers, as they respectively affect important figures of merit such leakage current (§ 2.1.2.1) and Charge Transfer Efficiency (§ 2.3.2.3), the two combined then defining the low-energy threshold and the energy resolution of the instrument.

4.2.3.4 Non-Ionizing Energy Loss

Here will be provided the means to quantify the amount of damage a device suffers after irradiation. This will be done in the framework of the *NIEL scaling hypothesis*, according to which the displacement-induced evolution of a device only depends on the energy deposited through collisions. This hypothesis is backed up by experimental evidence under most circumstances (e.g. in Moll et al. (1999)) and it is valid for study at hand.

Let us consider a particle of energy E moving through a medium of density ρ and atomic weight A. Due to (inelastic) nuclear interactions, it generates a distribution of recoils with energies E_{R}, atomic numbers Z and masses M. One defines the *Non-Ionizing Energy Loss* or NIEL as the energy lost by particles traversing a unit length of a medium through processes resulting in permanent atomic displacements (van Ginneken, 1989)

$$\mathrm{NIEL}\,(E) = \frac{N_{\mathrm{A}}\rho}{A} \sum_{Z,M} \int_{E_{\mathrm{d}}}^{E_{\mathrm{R,max}}} \frac{\mathrm{d}\sigma_{Z,M}}{\mathrm{d}E_{\mathrm{R}}}\,(E_{\mathrm{R}}, E)\, P_{Z,M}\,(E_{\mathrm{R}})\;\mathrm{d}E_{\mathrm{R}}. \tag{4.9}$$

NIEL is usually measured in $\mathrm{keV\,cm^{-1}}$ or $\mathrm{keV\,cm^2\,g^{-1}}$. In eq. (4.9), N_{A} is Avogadro's number, E_{d} the threshold energy for displacements and $E_{\mathrm{R,max}}$ the maximum recoil energy given by eq. (4.8). The differential cross section for the particle to undergo a collision resulting in a recoil with E_{R}, Z and M is given by $\mathrm{d}\sigma_{Z,M}/\,\mathrm{d}E_{\mathrm{R}}$, for which various expression exists, depending on the particular form of the interatomic potential and the inclusion of relativistic effects among other things. Finally, $P_{Z,M}\,(E_{\mathrm{R}})$ is the Lindhard factor, i.e. the total energy going to displacements (Messenger et al., 2004)

$$P_{Z,M}\,(E_{\mathrm{R}}) = \frac{E_{\mathrm{R}}}{1 + k_{\mathrm{d}} g\,(\varepsilon_{\mathrm{d}})} \tag{4.10a}$$

$$k_{\mathrm{d}} = 0.1334\, Z^{2/3} M^{-1/2} \tag{4.10b}$$

$$g\,(\varepsilon_{\mathrm{d}}) = \varepsilon_{\mathrm{d}} + 0.40244\, \varepsilon_{\mathrm{d}}^{3/4} + 3.4008\, \varepsilon_{\mathrm{d}}^{1/6} \tag{4.10c}$$

$$\varepsilon_{\mathrm{d}} = 0.01014\, Z^{-7/3} E_{\mathrm{R}}. \tag{4.10d}$$

The numerical factors in eq. (4.10) make k_{d}, $g\,(\varepsilon_{\mathrm{d}})$ and ε_{d} dimensionless if E_{R} is in eV.

Especially in the field of High Energy Particle Physics, displacement damage for a particle of energy E is expressed in terms of the *displacement damage*

function $D(E)$, defined as

$$D\big(E\big) = \sum_k \sigma_k(E) \int_{E_\mathrm{d}}^{E_\mathrm{R,max}} f_k(E_\mathrm{R}, E)\, L_k(E_\mathrm{R})\, \mathrm{d}E_\mathrm{R}, \tag{4.11}$$

where the sum is intended over all reactions, each one identified by a cross section σ_k and a probability $f_k(E_\mathrm{R}, E)$ of ejecting a recoil of energy E_R, whereas $L_k(E_\mathrm{R}) = P_k(E_\mathrm{R})/E_\mathrm{R}$ with $P_k(E_\mathrm{R})$ having the same meaning as in eq. (4.9). The displacement function is usually measured in units[2] of $\mathrm{MeV\,mb^{-1}}$. If one interprets the sum over Z and M of eq. (4.9) as a sum over all possible reactions as in eq. (4.11), as well as $\mathrm{d}\sigma_{Z,M}/\,\mathrm{d}E_\mathrm{R} \longleftrightarrow \sigma_k f_k$, then

$$\mathrm{NIEL} = \frac{N_\mathrm{A}\rho}{A} D(E). \tag{4.12}$$

In silicon $A = 28.086\,\mathrm{g\,mol^{-1}}$, so

$$100\,\mathrm{MeV\,mb} = 2.144\,\mathrm{keV\,cm^2\,g^{-1}}. \tag{4.13}$$

It is worth noting that in case of a compound made out of elements occurring with fractions w_i, the above equations are still valid for each element separately and they can be combined through Bragg's rule, as in eq. (4.5):

$$\frac{1}{\rho}\mathrm{NIEL} = \sum_i \frac{w_i}{\rho_i}\mathrm{NIEL}_i. \tag{4.14}$$

Fig. 4.8 shows the NIEL in silicon calculated for different particles using a *screened relativistic* approach, in which both screened nuclear potentials and relativistic effects are used (Boschini et al., 2014). It is worth discussing a few features of Fig. 4.8. NIEL for protons is caused by both nuclear and Coulomb interactions, the latter being the dominant ones, especially at lower energy. This explains why the NIEL for protons is so much larger than that for neutrons, to which only nuclear interactions apply, and why the two approach as energy increases, since Coulomb interactions become less and less important. This is also clearly the cause of the NIEL for ions increasing with Z and decreasing with particle energy. Another striking characteristic of Fig. 4.8 is the fact that the NIEL for neutrons increases as the energy decreases for

[2] As customary in nuclear and particle physics, cross-sections are measured in *barns*: $1\,\mathrm{b} = 10^{-24}\,\mathrm{cm^2}$

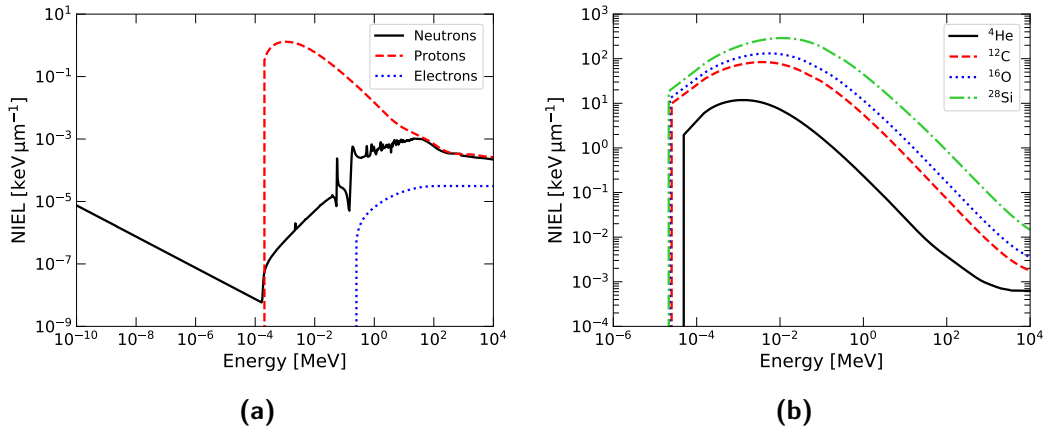

Figure 4.8 – Non-Ionizing Energy Loss (NIEL) for protons, neutrons and electrons (a) and some ions (b). In all the cases, calculations rely on screened relativistic models (Boschini et al., 2014). Following the established convention, $E_\mathrm{d} = 20.5\,\mathrm{eV}$ (ASTM E722-14) for neutrons, whereas $E_\mathrm{d} = 21\,\mathrm{eV}$ in any other case.

$E < 190\,\mathrm{eV}$: this is due to the recoil of nuclei following the emission of a gamma after neutron capture, which gives a recoil energy $\sim 1\,\mathrm{keV}$, much more than the 25 eV threshold for displacements. Finally, one may also notice that the contribution of electrons to displacements is always at least one order of magnitude lower that the corresponding value for hadrons, due to the mass disparity and the different physics behind the interactions.

From eq. (4.9), one can derive the *Kinetic Energy Released to Matter* (KERMA) by a single particle as

$$\mathrm{KERMA} = \int_0^{X(E)} \mathrm{NIEL}\left(E\left(x\right)\right)\,\mathrm{d}x, \tag{4.15}$$

where the integration is performed over the path of length X the particles traverses inside the medium, which depends on the energy E of the particle when it enters, as well as the geometry of the system. In fact, it is easy to see that, if the medium is thick enough for the particle to lose all its energy, $X\left(E\right) = x_\mathrm{max}\left(E\right)$, i.e. the range of the particle, whereas $X\left(E\right) < x_\mathrm{max}\left(E\right)$ if the particle leaves before depositing all its energy. In addition, eq. (4.15) supposes that all the non-ionizing energy lost by the traveling particle is absorbed by the medium, which is only true if all the recoils in turn deposit all their energy, i.e. no recoil leaves the medium. This latter condition may not be fulfilled in case of an energetic particle through a thin absorber.

In case of particles distributed with a differential fluence $\mathrm{d}\Phi/\,\mathrm{d}E$ over an energy range between $E_{\min}$ and $E_{\max}$, the *Total Non-Ionizing Dose* (TNID) will be

$$\mathrm{TNID} = \int_S \int_{E_{\min}}^{E_{\max}} \frac{\mathrm{d}\Phi}{\mathrm{d}E}\left(E, \vec{r}\right) \int_0^{X(E)} \mathrm{NIEL}\left(E\left(x\right)\right)\,\mathrm{d}x\,\mathrm{d}E\,\mathrm{d}S, \tag{4.16}$$

where the outermost integral is extended over all the irradiated surface and the differential fluence is allowed to vary with position $\vec{r}$. One must also be reminded that $X\left(E\right)$ is also a function of the geometry, since a particle with a given energy may have different X according to its trajectory inside the medium. Of course, if the device is exposed to multiple types of radiation, the complete TNID will be the sum of the TNID caused by each species separately. From this definition, it is clear that the TNID is completely analogous to the TID of eq. (4.7), valid for ionizing processes, and it is indeed measured in the same units, although it is common practice to specify the non-ionizing nature of the dose in this case.

In practice it is useful to introduce the concept of *equivalent fluence*, i.e. the fluence of a monoenergetic type of particles (e.g. 10 MeV protons or 1 MeV neutrons) capable of producing the same displacement damage as the population distributed according to $\mathrm{d}\Phi/\,\mathrm{d}E$:

$$\Phi_{\mathrm{eq}}^{\mathrm{part},\overline{E}} = \frac{1}{\int_0^{X\left(\overline{E}\right)} \mathrm{NIEL}_{\mathrm{part}}\left(E\left(x\right)\right)\,\mathrm{d}x} \times \\ \times \int_{E_{\min}}^{E_{\max}} \frac{\mathrm{d}\Phi}{\mathrm{d}E}\left(E\right) \int_0^{X(E)} \mathrm{NIEL}\left(E\left(x\right)\right)\,\mathrm{d}x\,\mathrm{d}E, \tag{4.17}$$

where part indicates the reference particle and $\overline{E}$ its energy. The equivalent fluence enables the comparison of different setups and experiments, each one characterized by its own geometry and particle distribution. This approach was first pioneered in terms of TNID to quantify in-orbit prediction of CTE evolution in CCDs, as an extension of the concept of TID, already familiar to design engineers (Marshall & Marshall, 1999).

In accordance with the NIEL scaling hypothesis, one finds that many parameters characterizing the performance of a device change *linearly* with the (equivalent) fluence. In general, the change observed in an instrument feature

P can be expressed by

$$\Delta P = P_{\text{irr}} - P_0 = k\Phi_{\text{eq}}, \tag{4.18}$$

where the factor k depends on the physical properties of the device, e.g. material and doping concentration, as well as the type and energy of the radiation, as particles of different energies may induce different kinds of defects, even though the overall equivalent fluence stays the same.

As a final remark, it is interesting to comment on the fact that eq. (4.17) may be simplified in case the energy of the incoming particles stays roughly the same when traversing the detector, e.g. in case of very energetic particles and/or thin devices:

$$\Phi_{\text{eq}}^{\text{part},\overline{E}} = \frac{1}{\text{NIEL}_{\text{part}}\left(\overline{E}\right)} \int_{E_{\min}}^{E_{\max}} \frac{\mathrm{d}\Phi}{\mathrm{d}E}\left(E\right) \text{NIEL}\left(E\right)\, \mathrm{d}E. \tag{4.19}$$

This expression is usually found in texts of High Energy Particle Physics and Accelerator Physics, but it is clearly not applicable when particles lose a significant portion of, or even all, their energy as they travel through a medium.

4.3 Simulations of in-orbit conditions

Regulations in the field of space engineering are dictated by space agencies, such as NASA and ESA. In this work the directives of the *European Cooperation for Space Standardization* (ECSS) are followed, which provide some standards for how space environment should be modeled (ECSS-E-ST-10-04C) and radiation effects should be calculated and taken into account during mission design (ECSS-E-ST-10-12C and ECSS-E-HB-10-12A).

4.3.1 Model of the space environment

To assess the conditions of the in-orbit environment, two simulation tools are used: ESA's *SPace ENVironment Information System* (SPENVIS) web service and TRAD's OMERE freeware. Relying on the same physical models for most calculations, their results are entirely compatible within the framework of this thesis, and therefore can be used interchangeably according to the specific functionality each software provides.

Table 4.1 – Main orbital parameters of SVOM.

Parameter	Value
Launch date	2021
Duration	3 yr
Extended duration	5 yr
Perigee	600 km
Apogee	650 km
Inclination	29°
Argument of Perigee	90°
Longitude of Ascending node	0°
True Anomaly	0°
Period	5826 s ($\approx$ 97 min)

Following ECSS-E-ST-10-04C, a model of the space environment is realized in four steps, comprised of the orbit definition and the assessment of the contributions of trapped particles, solar radiation and galactic cosmic rays.

4.3.1.1 Orbit

Tab. 4.1 resumes the main parameters of the orbit of the SVOM satellite. As stated in § 1.2.3.1, SVOM will be place on a Low Earth Orbit (LEO) with low eccentricity and inclination for an optimized pointing strategy.

4.3.1.2 Trapped particles

The ECSS standards for estimating the contribution of protons and electrons trapped in the radiation belts (§ 4.1.2) in case of non-specific orbits (i.e. other than, say, geostationary orbits) are NASA's AP-8 (Sawyer & Vette, 1976) and AE-8 (Vette, 1991) models respectively. Based on experimental data collected mostly between 1959 and 1970, they are mostly static models that take into account only limited time variations.

Due to the interactions between solar activity and Earth's magnetosphere, both models have a built-in dependency on the Sun's cycle. In particular, during solar maxima, Earth's (neutral) atmosphere expands (Huston et al., 1996), so that the inner edges of the radiation belts are eroded away. At the same time, the stronger solar wind feeds the outer belt with electrons. Since the main goal of the calculations is to provide a worst-case scenario, the AP-8 model is used in conditions of solar minimum (AP-8 MIN) whereas the opposite

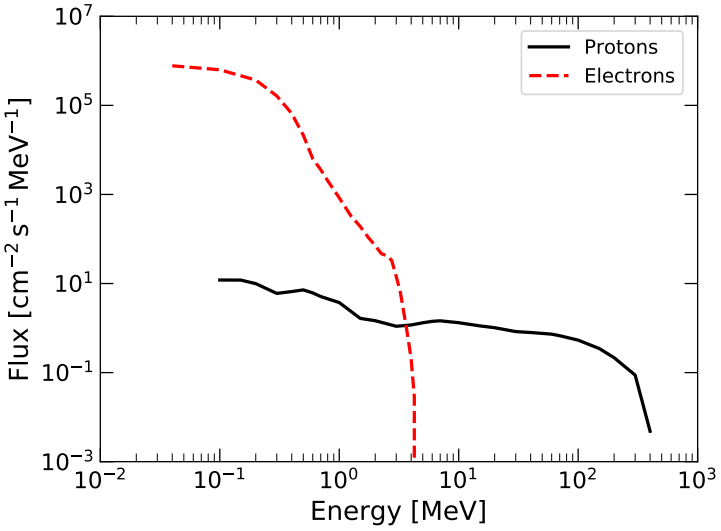

Figure 4.9 – Average differential spectra for trapped proton and electrons. Details about the models are contained in the text.

is true for the electron model (AE-8 MAX): this strategy allows to maximize the contribution of each component.

Trapped particle models are used in combination with the standard internal geomagnetic model developed by Jensen & Cain (1962) and Cain et al. (1965). No external geomagnetic field field is taken into account.

It is worth noting that despite their age NASA's AP-8 and AE-8 models are still considered the standards because they are the only providing a full coverage of the radiation belts as well as a wide enough energy range for both protons and electrons. However, uncertainties must be taken into account nonetheless in the calculations. ECSS-E-ST-10-04C suggests a factor of 2 for most scenarios, including the one under study, although in some cases models and data may differ by a factor of 5 or even a few orders of magnitude, especially in case of electrons. Newer models, such as NASA's AP-9 and AE-9, provide built-in uncertainty estimation methods, but the models themselves are still limited and unreliable to be made standards for space engineering.

Fig. 4.9 shows the average spectrum of the trapped protons and electrons to which SVOM will be exposed along its orbit, whereas Fig. 4.10 presents maps of the integral proton and electron flux as a function of the satellite position. Two things are clear from the figures. Due to their energy range, electrons do not pose a threat to the correct functioning of MXT, since their

are easily absorbed by the instrument shielding and that of the satellite[3] (range $x^{e^-}_{\max}(1\,\mathrm{MeV}) = 2\,\mathrm{mm}$ in aluminum). On the other hand, trapped protons are energetic enough to penetrate the shielding, contributing with both ionizing and non-ionizing dose, and therefore affecting the performances of the instrument. In addition to all that, it is evident from Fig. 4.10 that the trapped particles interacting with the satellite are entirely concentrated in the South Atlantic Anomaly § 4.1.2, with negligible contributions outside of it, proving the necessity of closing the aperture and shutting down the system (§ 1.2.3.1).

4.3.1.3 Solar particles

Solar particles (§ 4.1.1) are another potential hazard for space instrumentation. To assess their importance, NASA's model for *Emission of Solar Protons* (ESP) was used (Xapsos et al., 1999, 2000). Originally based on data gathered between 1963 and 1996, and now periodically updated, the model provides a technique to calculate the probability of exceeding a given fluence Φ of solar protons above a certain energy E, over a duration T.

The spectrum of the particles that actually reach the spacecraft depends on the local configuration of the geomagnetic field. Strømer's theory provides the *geomagnetic cut-off rigidity*[4] as a function of Earth's dipole, magnetic coordinates and angle of arrival (Adams et al., 1981). The solar particle flux is then calculated at each energy and point along the orbit: the fraction of solid angle over which the particles can reach the detector, called the *attenuation* or *exposure factor*, is obtained at a function of energy and location (i.e. if particles coming from all directions at a certain energy arrive at the detector when the spacecraft is at a particular point of the orbit, the exposure factor at that energy and orbital point is 1). In this calculation, one must take into account the fact that the Earth is a solid body with finite physical dimensions, that can therefore block particles along certain paths (*Earth's shadow*).

If the complete model is applied to the case under study, one finds that the contribution of solar protons is completely negligible along the orbit, over the entire extended lifetime of the mission (up to a 90 % confidence level). This is understandable as the satellite's orbit lies completely deep inside Earth's

[3]Electron radiation is usually a concern for solar panels, which are outside the shielding.
[4]The *magnetic rigidity* is the ratio between the particle's momentum and charge.

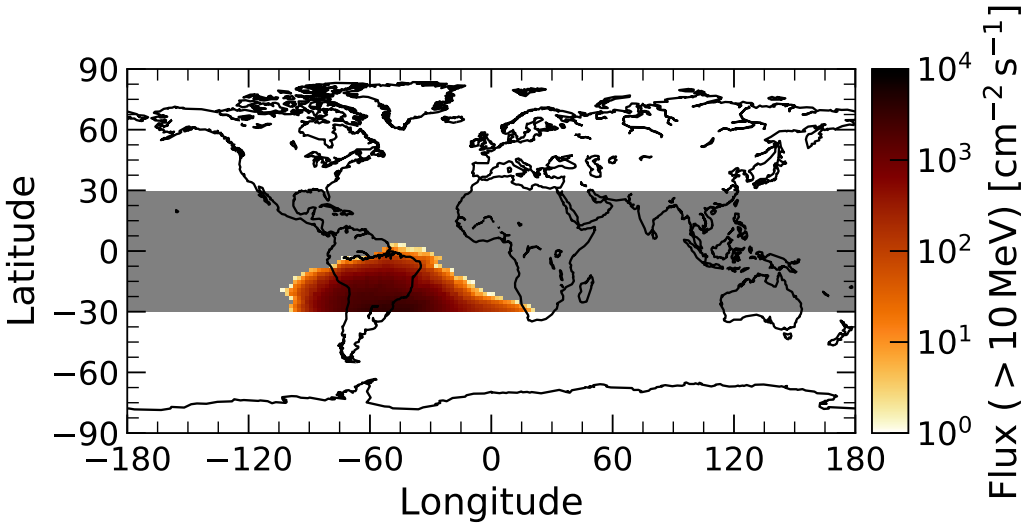

(a)

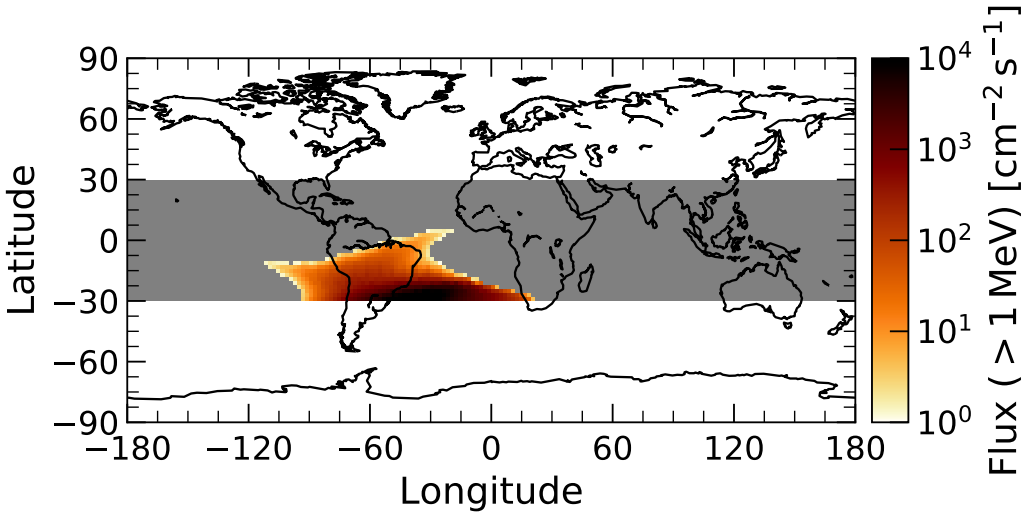

(b)

Figure 4.10 – Integral flux of trapped particles as a function of orbital position. a) Protons above 10 MeV. b) Electrons above 1 MeV. In both cases, the grey band represents the geographical coordinates spanned by the satellite.

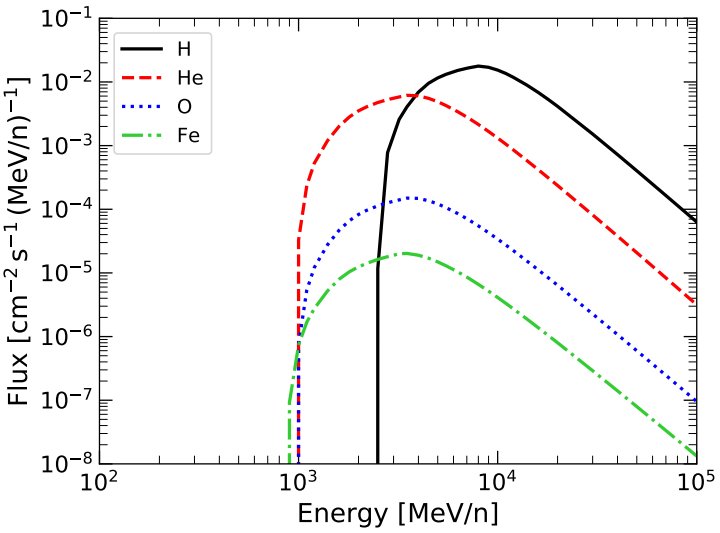

Figure 4.11 – Average differential flux of Galactic Cosmic Rays along the SVOM orbit. Only a few elements are shown.

magnetic field, making the possibility that solar particles reach the spacecraft extremely unlikely. The same result holds in case solar ions are considered.

4.3.1.4 Galactic Cosmic Rays

Galactic cosmic rays (§ 4.1.3), or GCRs, are the last source of background particles to be included in the simulations. Their contribution is defined according to ISO-15390, based on the semi-empirical GCR models developed by the Moscow State University. The model calculates the GCR flux according to the solar cycle, as it defines a cut-off rigidity due to variation is Sun's magnetic field, in a way analogous to case of solar particles moving in Earth's magnetosphere. To obtain a worst-case scenario, it is considered as if the Sun is at its minimum throughout the mission. Finally, the presence of the Earth in terms of magnetic field and shadow are taken into account as well.

Fig. 4.11 shows the results in terms of energy spectrum for some elements. From a quick comparison with Fig. 4.9, it is clear that even though the energy is much higher than that of the trapped particles, the flux is so low that their contribution to the total mission fluence is negligible.

4.3.2 Displacement damage

The amount of displacement damage the MXT detector will suffer during its time in orbit was assessed by first calculating the total equivalent fluence the detector will be exposed to, as described in § 4.2.3. Those calculations take into account also the contribution of secondary particles generated as a consequence of the interaction with the materials surrounding the device.

In order to accurately estimate the particle fluence on the MXT focal plane at various points during the mission lifetime, I carried out Monte Carlo simulations with the use of the Geant4 toolkit (Agostinelli et al., 2003; Allison et al., 2006, 2016). The simulations consisted of several steps:

- definition of the space environment outside the spacecraft;
- definition of the geometrical structure surrounding the MXT detector;
- propagation of the in-orbit particle environment through the geometry, down to the focal plane;
- normalization of the results;
- determination of the total displacement damage and calculation of an equivalent proton fluence.

4.3.2.1 Environment

As previously hinted, from the results of § 4.3.1, it is clear that the particle flux outside the spacecraft is essentially caused by the passages through the SAA. I chose to use the average flux along the orbit instead of the flux at a specific point in the SAA, which would have been an option, e.g. for comparison with a corresponding point outside: results would have otherwise been highly dependent on the location. An isotropic distribution of protons with the same energy spectrum as in Fig. 4.9 was generated from a spherical surface centered on the MXT detector and encompassing all the geometry, and then tracked as it propagated through the solids.

It is worth noting that trapped electrons do not have enough energy to cross the shielding and therefore are not considered in the following.

4.3.2.2 Geometry

Two geometrical configurations were selected for the simulations: the MXT camera alone, directly exposed to the space environment, and the camera inside the scientific payload of the SVOM satellite. This twofold approach served two purposes. On the one hand, in the domain of space instrumentation, simulations usually involve only the shielding immediately around the detector under study. On the other hand, an increasing degree of complexity enabled the identification of the solids most affecting the end results in terms of spatial and energy distributions of the particles on the focal plane. This in turn limited the load of the simulation if compared to a scenario in which the whole spacecraft is considered right from the start.

The running time of the simulations was of primary concern for a very simple reason. The object of the calculation was the assessment of the particle flux on a small detector ($\approx 2\,\text{cm} \times 3\,\text{cm} \times 450\,\mu\text{m}$) placed inside a large volume ($\approx 25\,\text{cm} \times 25\,\text{cm} \times 25\,\text{cm}$ for the camera and $\approx 180\,\text{cm} \times 160\,\text{cm} \times 160\,\text{cm}$ for the payload), outside of which an isotropic radiation environment was simulated. Such a geometric configuration required the vast majority of the particles to be tracked even though they did not contribute to the end result, as they never reached the detector. Moreover, the main role of most of the solids (as far as this analysis is concerned) was to shield the detector from the incoming radiation, further increasing the number of particles that had to be simulated in order to reach a satisfying statistics on the detector. A consequence of all this was an extension of the computation time. Several expedients were therefore implemented to tackle this issue, one of which was the one described above, i.e. the choice to gradually increase the complexity of the overall geometry instead of using the most complete version of it right from the start.

The simplified geometry The geometrical models of the MXT camera and of the camera inside the scientific payload used in the calculations are shown in Fig. 4.12. In both cases the number of volumes was greatly decreased relatively to the baseline geometry: for example, in case of the camera model, used in both scenarios, the number of solids was decreased from 762 to 66. This falls in line with what was stated above, as not all solids have the same ability to influence the final particle distribution, mainly due to their dimensions and

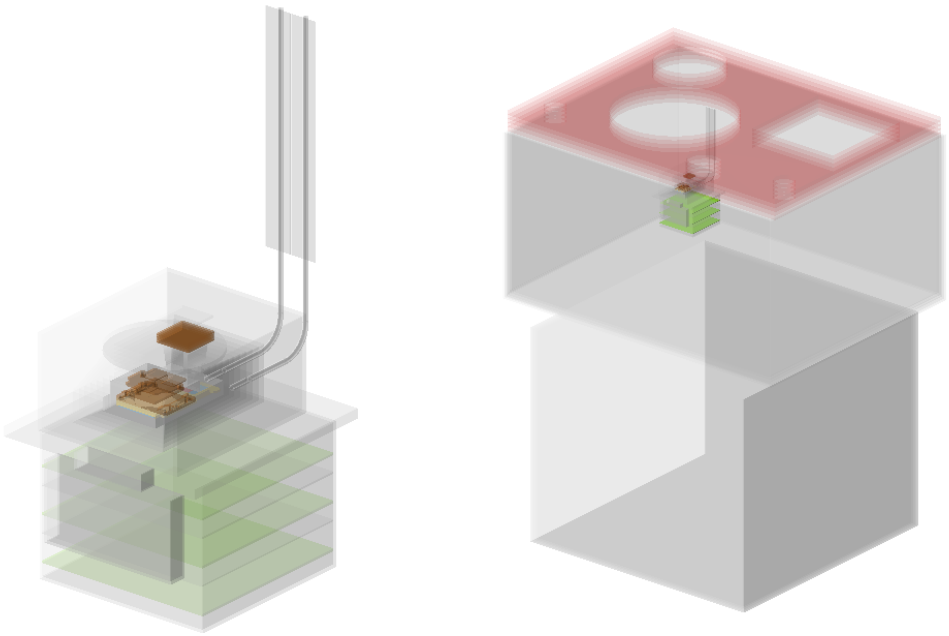

(a) **(b)**

Figure 4.12 – Simlified geometrical models used in the Monte Carlo simulations. a) Camera alone. b) Camera placed inside the satellite. Copper parts (such as the shutter and the TEC plates) are highlighted, as are the three boards of the FEE underneath.

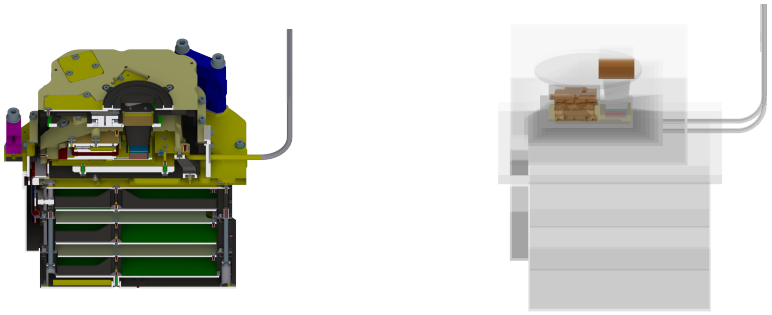

(a) (b)

Figure 4.13 – Comparison between the original geometry of the camera (a), in cross-section, and the simplified version used in the Geant4 simulations (b).

composition (notable examples are screws and thin layers of light materials), but all intervene in the tracking of particles. As a consequence, indiscriminately including everything would enormously increase the computation time of the simulation without any significant benefit in terms of the accuracy of the results.

The same reasoning lies behind the choice not to simply import in the Geant4 application the geometry from files created by Computer Aided Design software, which is the standard in engineering. Although direct importation is in principle possible, the way this kind of geometries are handled in Geant4 (as *tessellated solids*, i.e. solids made out of a mesh of triangles), greatly slows down the computation. Instead, I opted for translating everything into optimized Geant4 native volumes, mainly consisting of boxes, pyramids, spheres etc. and logical operations between them. During this process, the shape of many solids was simplified, although their main parameters, such as overall dimensions and material composition, were kept as realistic as possible. It is worth noting that the operation was carried out without the aid of any specialized software, as none was available. By comparing Fig. 4.13a and Fig. 4.13b, one can see the results of this simplification process. It is finally important to point out that the volumes making up the focal plane structure itself (MoCu and ceramic carrier board described in § 1.3.3.2) were indeed imported as tessellated solids, as their effect on the overall performances was negligible and more importantly a more rigorous geometric representation was preferred next to the detector. The latter was however changed to a Geant4 solid to take full advantage of its functionalities.

The multiplication algorithm As previously mentioned, arising from mere geometrical considerations of the configuration is the fact that most of the primary particles that leave the spherical surface from which they are tracked do not arrive anywhere near the detector, due to its very small dimensions, with a consequent impact on the speed of the simulation.

One possible solution is the adoption of a so-called *reverse Monte Carlo* method, in which the tracking is performed backwards from the detector towards the outside sphere, thus drastically reducing the waste of computation time. However, this method suffers from two major drawbacks, as it is difficult to implement in practice and is very dependent on the way the normalization of the results is performed.

In my work, I opted for a more manageable *split-and-kill multiplication algorithm*. This method is mainly useful in shielding applications, i.e. when one is interested only in the very few particles that successfully traverse a large absorber (the shield). Understandably, this scenario shares many similarities with case under study. The split-and-kill algorithm acts on the particles passing through the shield and selects those moving in the direction of interest, while removing (*killing*) the others from the simulation, in order to save computing resources. A particle that does get selected is *split*, i.e. N particles are created in its place, all sharing the same parameters as the original one, except for a *weight* $w = 1/N$, by means of which one can keep track of the multiplication process. The selection takes place at the interface between volumes and for this reason the shield is segmented into M sections. Fig. 4.14 sums up the rationale behind this algorithm. Thanks to this algorithm, one can increase the number of particles that eventually reach the detector, while at the same time saving computation time, as particles moving away from it are not tracked.

In the case under study, the use of Geant4 native solids delivers an important advantage, because the main shield of the camera (§ 1.3.3) can be segmented into concentric shells, which allows the implementation of the split-and-kill approach. As for the selection criterion, particles moving towards the detector are multiplied, whereas those moving away are suppressed. Selected particles were multiplied by $N = 2$, as suggested by Geant4 guidelines, based on considerations about the reliability of this method. The number of layers M was chosen to maximize the number of splits (the particles must survive the gap between two successive interfaces to undergo another multiplication step) without resulting in a runaway number of particles to track (exponential

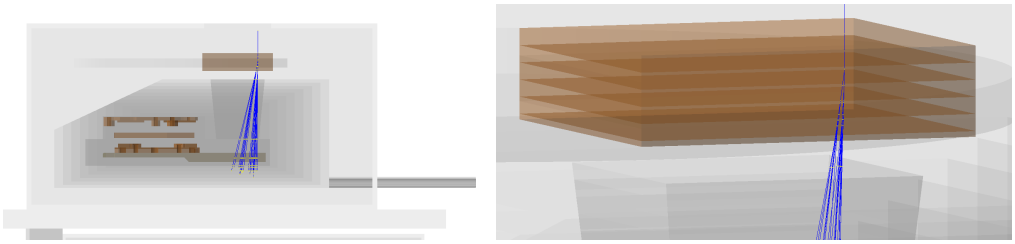

(a) (b)

Figure 4.14 – Multiplication algorithm applied to the simulations of the MXT camera. A single 100 MeV proton (blue track) is generated and propagated vertically downwards. a) Overall view from the side. b) Close-up view: it is clear how the multiplication occurs at the interfaces between successive layers of the shielding.

behavior). The same logic was applied to the spacecraft, during the second run of simulations.

In all the calculations the `Shielding_EMZ` physics list was chosen. This list contains the most detailed descriptions of the physics of radiation in matter and uses high precision models for neutron reactions. Furthermore, the `EMZ` suffix implies that it implements the most accurate curves for energy deposition and electromagnetic processes in general. Although it achieves the best results, those features make it slow to use and therefore it is suggested only when the number of secondary particles is limited, e.g. with respect to the hadronic cascades simulated in high energy particle physics.

The output of the Geant4 simulations was a list of particles that entered the detector (not necessarily interacted with it), of which the type, position, direction and kinetic energy were recorded.

4.3.2.3 Particle spectrum

Geant4 has (almost) no information of time, meaning that increasing the number of simulated particles is mainly a tool to increase statistics, not to represent a longer operation. It is therefore mandatory to turn the list of particles that have reached the detector into a physical flux and then into a fluence.

First of all, let us consider an isotropic particle (proton) source of intensity $I(E)$, measured in $\mathrm{cm}^{-2}\,\mathrm{s}^{-1}\,\mathrm{MeV}^{-1}\,\mathrm{sr}^{-1}$. Its integral over all the directions of

emission from a flat surface leads to a flux

$$\mathcal{F}(E) = \int_{2\pi} \mathrm{d}\phi \int_{\pi} \mathrm{d}\theta\, I(E) \sin\theta \cos\theta = \pi I(E), \tag{4.20}$$

because it does not depend on the solid angle. Such a flux is exactly what simulations of the particle environment provide (Fig. 4.9).

As described above, in the simulations the particles are tracked from a spherical surface centered on the detector. Let R be its radius. The *simulated rate* $\mathcal{R}$ can be calculated as

$$\mathcal{R} = \int_{4\pi R^2} \mathrm{d}\sigma \int_{\Delta E} \mathrm{d}E \int_{2\pi} \mathrm{d}\phi \int_{\pi} \mathrm{d}\theta\, I(E) \sin\theta \cos\theta = 4\pi R^2 \mathcal{F}, \tag{4.21}$$

where $\mathcal{F} = \int_{\Delta E} I(E)\, \mathrm{d}E$ and the integration is performed over the entire energy range of the spectrum. Accordingly, the *simulated time* $\mathcal{T}$ equals

$$\mathcal{T} = \frac{\mathcal{N}}{\mathcal{R}} = \frac{\mathcal{N}}{4\pi R^2 \mathcal{F}}, \tag{4.22}$$

with $\mathcal{N}$ being the number of simulated primary particles (protons). If N particles are observed on the detector of area A_{det} at the end of the simulation, the observed flux F therefore becomes

$$F = \frac{N}{A_{\mathrm{det}} \mathcal{T}} = \frac{4\pi R^2 \mathcal{F}}{A_{\mathrm{det}}} \frac{N}{\mathcal{N}}. \tag{4.23}$$

An expression for the spectrum $F(E)$ can be straightforwardly derived as

$$F(E) = \frac{4\pi R^2 \mathcal{F}}{A_{\mathrm{det}} \mathcal{N}} \frac{\mathrm{d}N}{\mathrm{d}E}, \tag{4.24}$$

where $\mathrm{d}N/\mathrm{d}E$ is the number of observed counts per energy bin. In general, the factor

$$\mathcal{C} = \frac{4\pi R^2 \mathcal{F}}{A_{\mathrm{det}} \mathcal{N}}, \tag{4.25}$$

measured in $\mathrm{cm}^{-2}\,\mathrm{s}^{-1}$, allows to convert values derived from the simulations into physical quantities. Fig. 4.15 shows the particle spectra on the detector obtained from the simulations through this method.

As explained in § 4.3.2.1, a distribution made out of only protons was simulated outside the geometry. This implies that all the other particles visible in Fig. 4.15, as well as some protons, are secondaries, due to electromagnetic

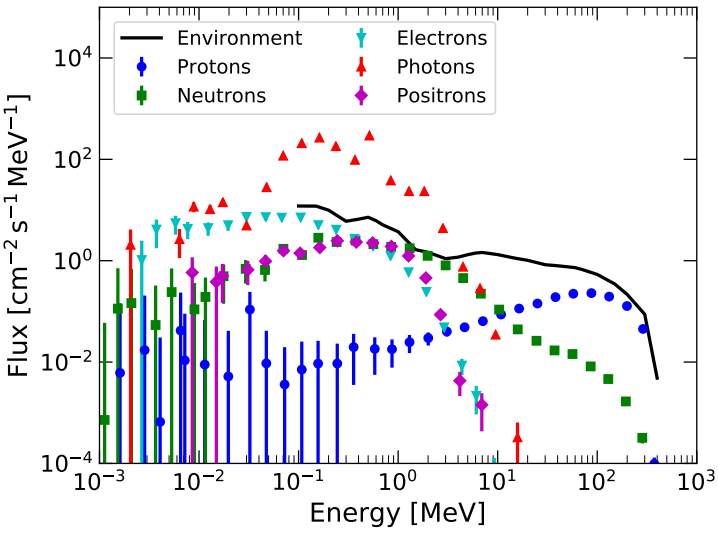

(a)

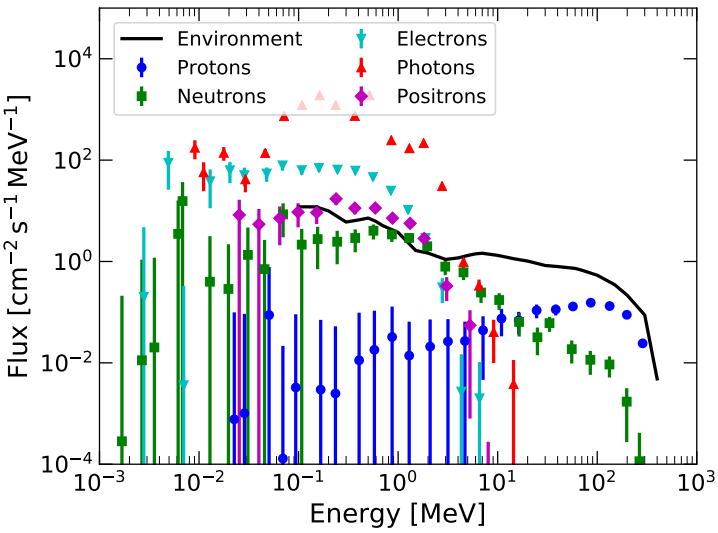

(b)

Figure 4.15 – Total differential particle flux on the MXT focal plane, broken down into its components. a) Configuration with the MXT camera alone. b) Configuration with the MXT camera inside the simplified spacecraft. In both cases, the curve labeled as *Environment* is the spectrum outside the geometry, which is propagated to the detector.

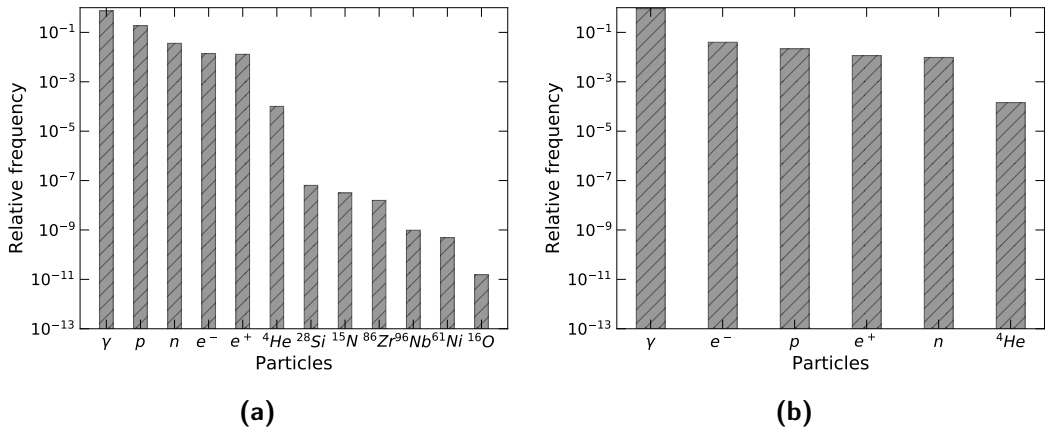

Figure 4.16 – Fractional distribution of particles reaching the detector. a) Configuration with the MXT camera alone. b) Configuration with the MXT camera inside the simplified spacecraft.

and nuclear interactions between primaries and the solids surrounding the detector. Fig. 4.16 shows the fractional distribution of the different species. It is worth noting that, when the camera is surrounded by the payload, far fewer ions reach the detector, a testimony of the fact that the energy with which the primaries reach the shielding just around the detector, where most of the ions are generated, does not favor any more the same nuclear processes that take place in the scenario with the camera alone.

Let us now focus the attention on the protons. As predictable, the primary spectrum gets modified by the layers of materials through which it has to propagate before reaching the detector, with the lower-energy end being more heavily modified than the higher-energy one, which stays almost unaffected. The shape of the calculated proton spectrum can be used to estimate the *equivalent shielding* around the detector, i.e. the thickness of an aluminum sphere through which the outside spectrum has to propagate in order to match the above results. This is a useful value that enables comparisons with other experiments, which obviously have different geometries and materials involved. Fig. 4.17 shows the proton spectrum of each configuration compared with the spectra resulting from the primary proton distribution being propagated through aluminum layers of several thicknesses (*residual spectrum*). In particular, the data points of Fig. 4.17a are closer to the 40 mm-curve most of the time, which is compatible with the fact that the main camera shield alone was designed to present a 30 mm-thickness over most directions. To this one must obviously add the simplification of the geometry and the presence of

other volumes besides the shield itself, which increase the amount of material particles have to cross. As far as high energy particles are concerned, however, the equivalent thickness becomes as small as $\approx 20\,\mathrm{mm}$. On the other hand, Fig. 4.17b shows the impact of including the main structure of the satellite.

As was said at the end of § 4.3.2.2, the position of each particle on the detector surface, as well as their direction, is recorded, which allows to draw hit maps, per particle species and per traveling direction (particles going *down* move along the direction of the telescope, entering the photon window, whereas *up* means from the bottom shielding to the shift-register side of the detector). Fig. 4.18, 4.19 and 4.20 show such maps for protons, photons and neutrons respectively for the camera alone, those for the other scenario being equivalent except for the lower flux. In each figure, particles are considered regardless of their energy. Furthermore, the whole surface of the detector is considered, i.e. image and frame-store areas: each pixel of the map corresponds to four pixels of the detector, with the relative dimensions between the two regions respected.

The flux appears to be essentially uniform across each side and between the two sides as well, implying that the detector is exposed to an equivalent thickness along all directions. Notable exceptions to the uniformity are Fig. 4.18a and Fig. 4.19a, the former presenting a lower flux in correspondence to the frame-store area, whereas the latter showing a higher flux in the same region. Both effects are likely to be caused by the MoCu shielding of the frame-store itself, which absorbs low-energy protons in the first case and stimulates the emission of photons in the second case, as it is a thin layer of absorbing material. This interpretation is supported by the fact that those features are absent from the other side of the detector.

4.3.2.4 Equivalent fluence

I experienced some difficulties in correctly recording the energy deposits of the particles interacting with the detector in Geant4 in combination with the multiplication algorithm. Even though it is normally possible to register the amount of energy lost by a particle to a medium through ionization and non-ionization processes, when this feature is used in conjunction with the split-and-kill method, results appear to become nonphysical, e.g. a particle losing order of magnitudes more energy than it possesses before the interaction.

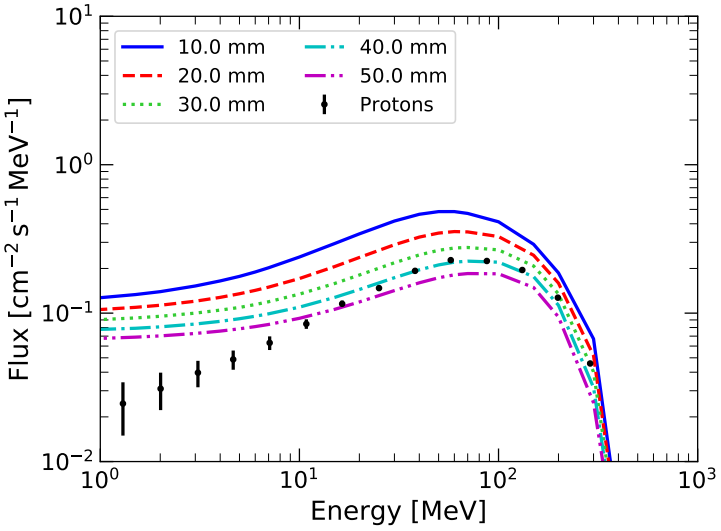

(a)

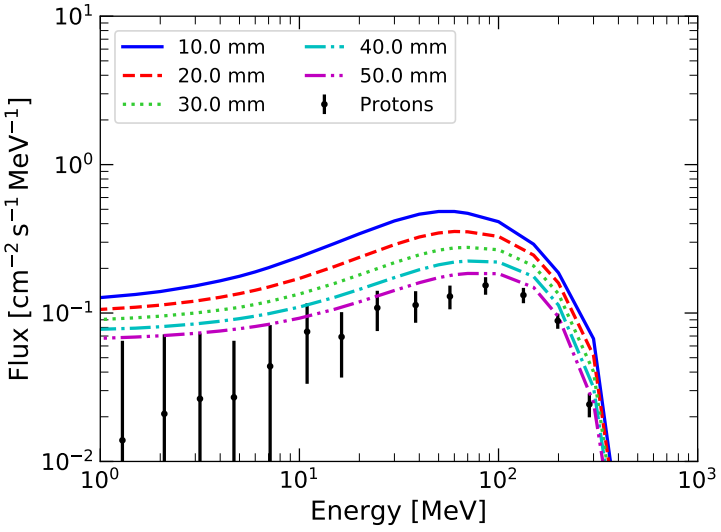

(b)

Figure 4.17 – Proton spectrum compared with the residual spectrum through a spherical aluminum shielding of varying thickness. a) Configuration with the MXT camera alone. b) Configuration with the MXT camera inside the simplified spacecraft.

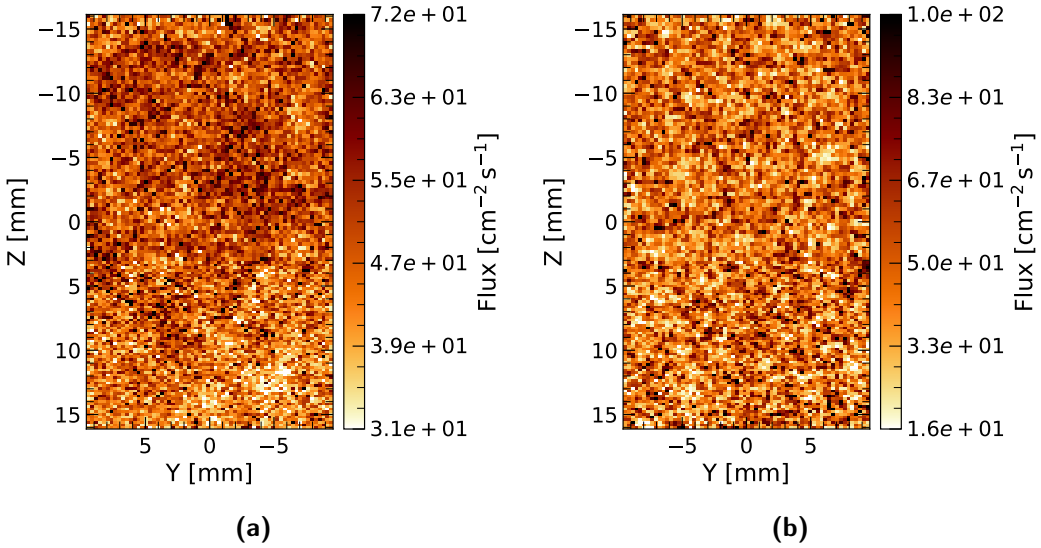

Figure 4.18 – Proton flux in the case of the camera alone. a) Downward flux. b) Upward flux.

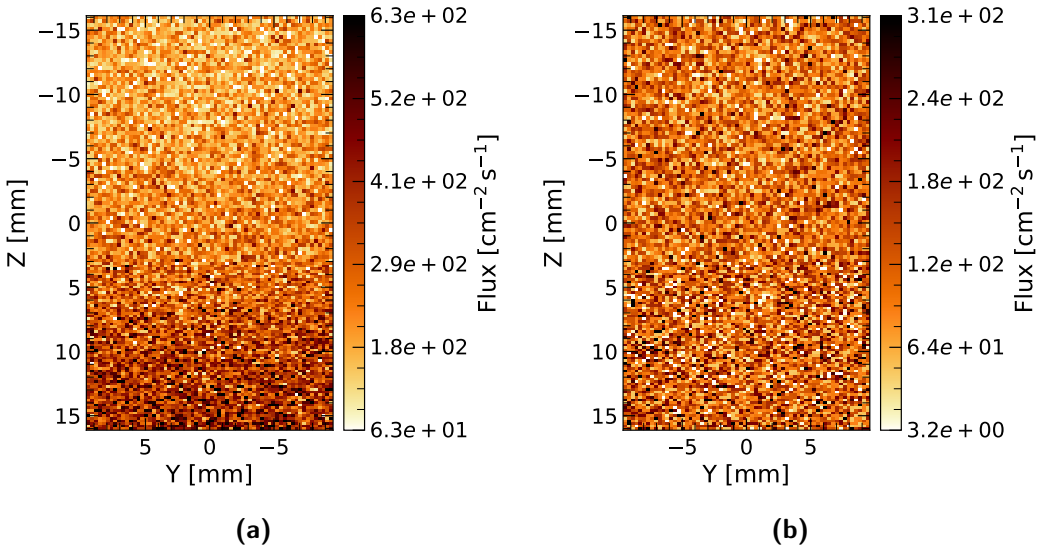

Figure 4.19 – Photon flux in the case of the camera alone. a) Downward flux. b) Upward flux.

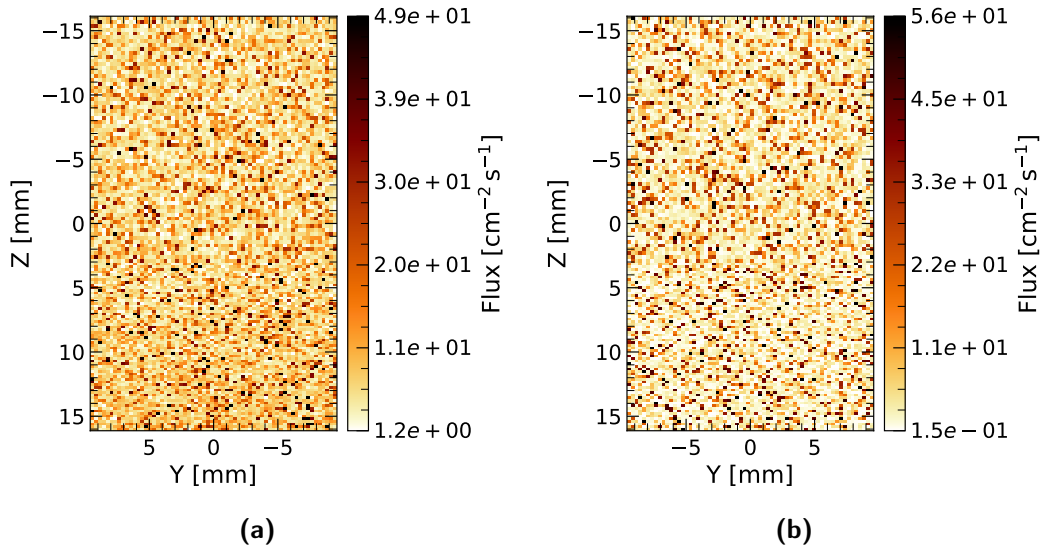

Figure 4.20 – Neutron flux in the case of the camera alone. a) Downward flux. b) Upward flux.

For this reason I adopted a different approach, which also allows to utilize more accurate models of NIEL than those implemented in Geant4, without the need to modify the physics list.

Energy deposit If, say, a proton knocks on a silicon nucleus with so much energy that the latter leaves the solid before losing all its kinetic energy, not all the energy lost by the particle is actually absorbed by the medium (§ 4.2.3.4). In order to assess this scenario, firstly the maximum energy $E_{\mathrm{Si,max}}$ a silicon atom may acquire from a collision must be estimated. With the help of eq. (4.8) and Fig. 4.15, one obtains that for an incoming 500 MeV-proton $E_{\mathrm{Si,max}} \approx 67\,\mathrm{MeV}$. This result can now be compared with the range of silicon atoms in silicon, from which one derives that the maximum range of a silicon atom is $R_{\mathrm{Si,max}} \approx 25\,\mu\mathrm{m}$. Given the dimensions of the simulated detector of $\approx 2\,\mathrm{cm} \times 3\,\mathrm{cm} \times 450\,\mu\mathrm{m}$, it can safely be said that for the vast majority of interactions, the energy lost by the incoming radiation is entirely deposited in the detector, implying the applicability of the formulas in § 4.2.3.4.

The algorithm The goal of the calculations is to apply eq. (4.17) in order to calculate the equivalent fluence in terms of 10 MeV and 50 MeV protons, as those are two widespread references in literature and in experimental irradiation campaigns.

The main issue with eq. (4.17) is $X(E)$, i.e. the length of track made by each particle inside the detector, along which the particle energy $E(x)$ varies. Let us consider a particle that slows down inside a medium from an initial energy E. If the medium is thick enough that the particle stops, then $X(E) = x_{\max}(E)$ ($x = 0$ at the entrance point), i.e. the particle track equals its range in the medium. Let us now consider an arbitrary point $\overline{X}$ along the path, where the particle has an energy $\overline{E}$: by construction, if the particle had to enter the medium at this point $x = \overline{X}$ with energy $\overline{E}$, it would stop at the same place as the particle starting at $x = 0$ with energy E. In formulas,

$$X(E) = x_{\max}(E) = \overline{X} + x_{\max}\left(\overline{E}\right). \tag{4.26}$$

This implies that if the detector is too thin for a particle of energy E to stop inside of it, then the particle leaves with energy $\overline{E}$ so that

$$x_{\max}\left(\overline{E}\right) = x_{\max}(E) - \Delta x, \tag{4.27}$$

where Δx is the path inside the detector. This result can be applied to eq. (4.17) with the substitution

$$\int_0^{X(E)} \mathrm{NIEL}\left(E(x)\right) \mathrm{d}x = \int_{x_{\max}(E)-\Delta x}^{x_{\max}(E)} \mathrm{NIEL}\left(E(x)\right) \mathrm{d}x. \tag{4.28}$$

At this point, the issue becomes the determination of Δx. To estimate the path a particle covers inside the detector, one can turn to geometry and simply consider the length of the intersection between a straight line parallel to the direction of the particle (one of the outputs of the simulations) and a box with the same dimensions as the detector: the line must pass through the entrance point of the particle in the detector, which is among the output values as well. The result is the maximum geometrical projected range a particle may cover inside the detector (Fig. 4.21). Of course, $x_{\max}(E) - \Delta x < 0$ in eq. (4.28) means that the particle stops inside the detector, depositing all its energy.

As previously hinted, the geometrical calculations do not deliver a value for the actual range of the particle, but only its projection along the direction of arrival: due to scatterings, the two values may differ greatly. From Fig. 4.22, where range and projected range of a proton in silicon are both shown, one can observe that the two curves differ from each other only for energies $\lesssim 0.1\,\mathrm{MeV}$,

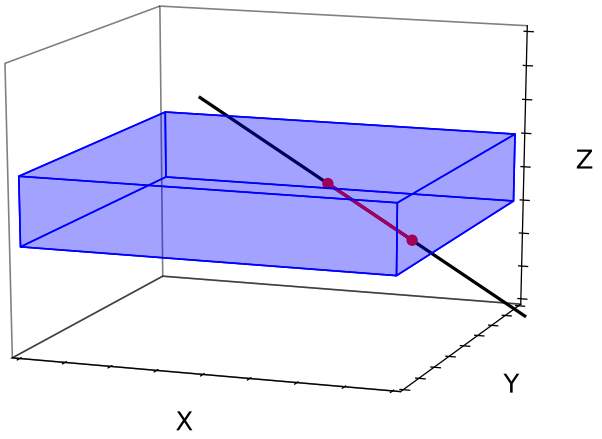

Figure 4.21 – Schematic of the geometrical calculation of the maximum projected range of a particle traversing the detector.

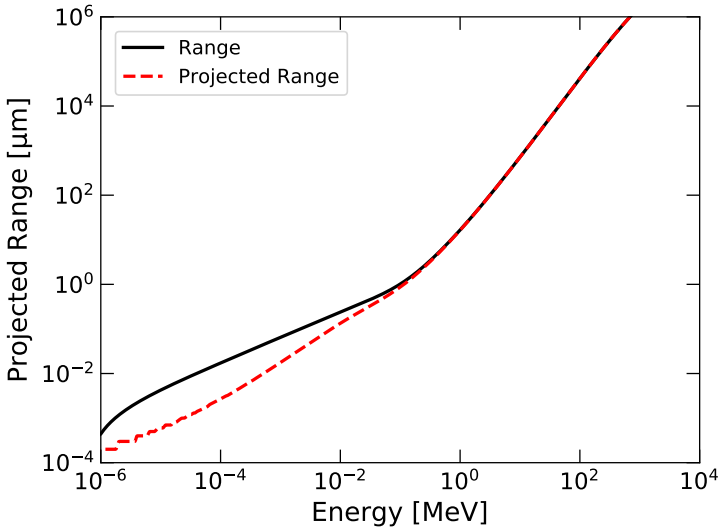

Figure 4.22 – Range and projected range of a proton in silicon. Models obtained from Boschini et al. (2014).

at which protons are already essentially totally absorbed by the detector. As a consequence, it can be said that either a particle deposits all its energy or the estimate based on its trajectory is a reasonable evaluation of its range.

Other than to protons, this procedure can be applied to electrons, positrons[5] and ions, for which the range is usually so small that they are totally absorbed. However, if one is interested in a complete treatment of the damage suffered by the detector, two components are yet to be taken into account, i.e. photons and neutrons.

As mentioned in § 4.2.3, photons can generate electrons (and positrons) thanks to photoelectric effect, Compton scattering and pair production (§ 2.3.1.2), which may in turn be energetic enough to displace atoms. This mechanism is considered in the algorithm. Photons are extracted from the list of particles reaching the detector and a random number smaller than 1 is drawn for each one: an interaction happens if it is less than the interaction probability, which is defined as

$$P_\gamma = 1 - e^{-\rho_{\mathrm{Si}} \sigma x_{\mathrm{det}} / \cos\theta}, \tag{4.29}$$

where ρ_{Si} is the silicon density, x_{det} is the thickness of the detector, θ the angle of arrival with respect to the vertical, and σ the interaction cross section. I made the choice of only considering Compton interactions, as they are dominant in the energy range over which the photons are distributed (Fig. 4.15). For each interacting photon of energy E_γ, the scattering angle of the electron ψ_{e} is randomly determined according to the Compton formulas, and this in turn defines the electron energy E_{e}. Finally, the traveling direction of the Compton electron is calculated on the basis of the direction of the primary photon along with ψ_{e}. Once the electron energy, direction and position on the surface of the detector (taken to be the same as the photon) are known, the integral of eq. (4.28) can be applied.

As far as neutrons are concerned, the detector is almost transparent to the incoming neutron flux of Fig. 4.15, as it is clearly visible in Fig. 4.23, where the transmission of neutrons in a 450 µm silicon layer is presented. With this knowledge, I made the decision to apply eq. (4.19) instead of eq. (4.17).

At this point the contributions from each particle may be computed, multiplied by the weight of the particle (§ 4.3.2.2) and added up. By multiplying by the conversion factor of eq. (4.25) and by the mission duration, and dividing by

[5] The NIEL of positrons is considered equal to that of electrons.

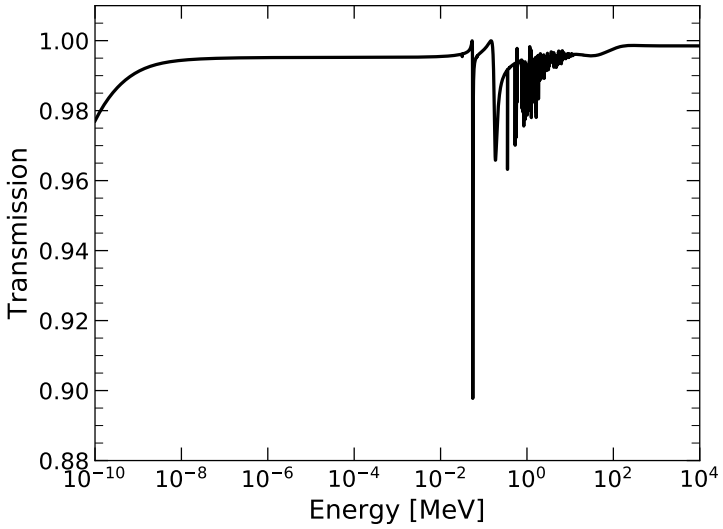

Figure 4.23 – Neutron transmission through 450 µm of silicon. Cross section data are part of the JENDL/HE-2007 catalog, retrieved from the *Java-based Nuclear Information Software* (Soppera et al., 2014).

Table 4.2 – Contributions to the 10 MeV proton equivalent fluence for the simulations with the camera alone for four values of the time in orbit.

	$\Phi_{\mathrm{p,10\,MeV}}$ / cm^{-2}			
	1 yr	3 yr	5 yr	10 yr
H	8.04×10^8	2.41×10^9	4.02×10^9	8.04×10^9
γ	1.86×10^7	5.59×10^7	9.32×10^7	1.86×10^8
e^-	2.71×10^5	8.14×10^5	1.36×10^6	2.71×10^6
e^+	4.07×10^5	1.22×10^6	2.04×10^6	4.07×10^6
n	6.62×10^7	1.98×10^8	3.31×10^8	6.62×10^8
He	1.52×10^6	4.56×10^6	7.59×10^6	1.52×10^7
Ions	3.06×10^5	1.08×10^6	1.80×10^6	3.06×10^6
Total	8.91×10^8	2.67×10^9	4.45×10^9	8.91×10^9

Table 4.3 – Contributions to the 50 MeV proton equivalent fluence for the simulations with the camera alone for four values of the time in orbit.

	$\Phi_{\mathrm{p,50\,MeV}}$ / cm^{-2}			
	1 yr	3 yr	5 yr	10 yr
H	1.98×10^{9}	5.95×10^{9}	9.91×10^{9}	1.98×10^{10}
γ	4.60×10^{7}	1.38×10^{8}	2.30×10^{8}	4.60×10^{8}
e^-	6.69×10^{5}	2.01×10^{6}	3.34×10^{6}	6.69×10^{6}
e^+	1.00×10^{6}	3.01×10^{6}	5.02×10^{6}	1.00×10^{7}
n	1.63×10^{8}	4.90×10^{8}	8.16×10^{8}	1.63×10^{9}
He	3.75×10^{6}	1.12×10^{7}	1.87×10^{7}	3.75×10^{7}
Ions	8.87×10^{5}	2.66×10^{6}	4.43×10^{6}	8.87×10^{6}
Total	2.20×10^{9}	6.59×10^{9}	1.10×10^{10}	2.20×10^{10}

Table 4.4 – Contributions to the 10 MeV proton equivalent fluence for the simulations with the camera inside the satellite for four values of the time in orbit.

	$\Phi_{\mathrm{p,10\,MeV}}$ / cm^{-2}			
	1 yr	3 yr	5 yr	10 yr
H	5.25×10^{8}	1.58×10^{9}	2.63×10^{9}	5.25×10^{9}
γ	1.32×10^{8}	3.96×10^{8}	6.60×10^{8}	1.32×10^{9}
e^-	3.78×10^{6}	1.13×10^{7}	1.89×10^{7}	3.78×10^{7}
e^+	1.77×10^{6}	5.30×10^{6}	8.83×10^{6}	1.77×10^{7}
n	1.30×10^{8}	3.90×10^{8}	6.50×10^{8}	1.30×10^{9}
He	3.09×10^{7}	9.27×10^{7}	1.54×10^{8}	3.09×10^{8}
Total	8.24×10^{8}	2.47×10^{9}	4.12×10^{9}	8.24×10^{9}

Table 4.5 – Contributions to the 50 MeV proton equivalent fluence for the simulations with the camera inside the satellite for four values of the time in orbit.

	$\Phi_{\mathrm{p,50\,MeV}}$ cm^{-2}			
	1 yr	3 yr	5 yr	10 yr
H	1.30×10^{9}	3.89×10^{9}	6.48×10^{9}	1.30×10^{10}
γ	3.25×10^{8}	9.76×10^{8}	1.63×10^{9}	3.25×10^{9}
e^-	9.31×10^{6}	2.79×10^{7}	4.66×10^{7}	9.31×10^{7}
e^+	4.35×10^{6}	1.31×10^{7}	2.18×10^{7}	4.35×10^{7}
n	3.21×10^{8}	9.62×10^{8}	1.60×10^{9}	3.21×10^{9}
He	7.62×10^{7}	2.29×10^{8}	3.81×10^{8}	7.62×10^{8}
Total	2.03×10^{9}	6.09×10^{9}	1.02×10^{10}	2.03×10^{10}

Table 4.6 – Summary of the estimations of the 10 MeV and 50 MeV proton equivalent fluence for the simulations with the camera alone and inside the satellite for four values of the time in orbit. The values reported here are those in the *Total* row of Tab. 4.2 to 4.5.

		1 yr cm^{-2}	3 yr cm^{-2}	5 yr cm^{-2}	10 yr cm^{-2}
$\Phi_{\mathrm{p,10\,MeV}}$	Camera	8.91×10^{8}	2.67×10^{9}	4.45×10^{9}	8.91×10^{9}
	Satellite	8.24×10^{8}	2.47×10^{9}	4.12×10^{9}	8.24×10^{9}
$\Phi_{\mathrm{p,50\,MeV}}$	Camera	2.20×10^{9}	6.59×10^{9}	1.10×10^{10}	2.20×10^{10}
	Satellite	2.03×10^{9}	6.09×10^{9}	1.02×10^{10}	2.03×10^{10}

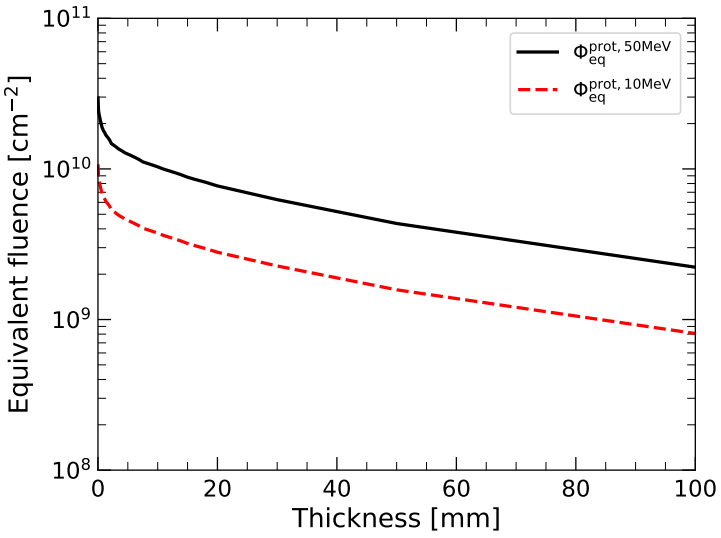

Figure 4.24 – Equivalent fluence in 10 MeV and 50 MeV protons as a function of Al thickness.

the energy deposited by a 10 MeV or 50 MeV proton in 450 µm of silicon[6], as in eq. (4.17), I derived estimates for the equivalent fluence, which are reported in Tab. 4.2 to 4.5, and in summary in Tab. 4.6. The considered time periods are 1 year (for reference), 3 and 5 years (for comparison with the mission performance constraints) and 10 years (to account for uncertainties in the models of the environment, as explained in § 4.3.1.2).

Discussion When looking at the results of Tab. 4.2 to 4.5, two features are evident.

Firstly, one notices the importance of considering secondary particles. Even though they globally make up approximately 10 % of the total equivalent fluence in the case of the camera alone (Tab. 4.2 and 4.3), their contribution rises up to 36 % when the spacecraft is included (Tab. 4.4 and 4.5). This is a consequence of the material of the satellite itself, which blocks protons at the cost of producing a large amount of secondary particles. It is worth noting that this result cannot be achieved with standard simulation tools (e.g. SPENVIS and OMERE) that do not rely on detailed Monte Carlo simulations.

The second peculiarity is that the equivalent fluence obtained in the second scenario is only $\approx$ 10 % smaller than the first one (Tab. 4.6). This can be

[6]For the sake of comparison with experimental data in accelerator facility, the protons are considered to reach the surface perpendicularly

explained by considering Fig. 4.24. It shows the 10 MeV and 50 MeV proton equivalent fluence on a detector placed at the center of an aluminum sphere. The radius of the sphere is indicated on the x-axis of the plot and the input spectrum is the same as the one used in the Geant4 simulations discussed so far and the permanence in orbit is 5 years. One can see that the transmitted fluence tends to decrease slowly as a function of the thickness of the shield, so that an increase of the Al protection from 35 mm to 80 mm (i.e. $\approx 130\,\%$) only corresponds to a 50 % decrease in the total fluence. By design the MXT camera presents ≈ 30 mm of Al along all directions, to which the ≈ 30 mm thickness of the rest of the spacecraft must be added in the second scenario. It must be taken into account however that the satellite is not made of solid aluminum, but it has a honeycomb structure to optimize between mass and mechanical resistance: this is simulated in Geant4 by a custom material with the same composition as aluminum but a density of just $1.8\,\mathrm{g\,cm^{-3}}$ instead of the canonical $2.7\,\mathrm{g\,cm^{-3}}$. With this in mind, I could roughly estimate a total shielding (focal plane and satellite) of 45 mm: the curves of Fig. 4.24 show therefore that the associate decrease in fluence should be $\approx 20\,\%$. Since the complex geometry of the Geant4 simulations is ignored in Fig. 4.24 as well as the generation of secondaries, one can safely say that the fluence decrease obtained by surrounding the camera with the satellite structure is as limited as expected.

A third detail is that, even though the particle distribution on the detector is dominated by photons (Fig. 4.15 and Fig. 4.16), their energy (and the physics of displacement damage) is such that protons still provide the main contribution to the equivalent fluence.

Finally, it is interesting to compare the results with the fluence other missions have been or are predicted to be exposed to. To make a meaningful comparison, experiments using similar detectors should be considered: for this reason, only EPIC-pn on board XMM-Newton (Strüder et al., 2001) and the eROSITA mission (Meidinger et al., 2010b), both of which mount pnCCDs of a similar design to MXT's, are considered here. In case of EPIC-pn, a prediction of $5 \times 10^8\,\mathrm{cm^{-2}}$ 10 MeV protons was made for a 10-year mission (Strüder et al., 2003): this value can be extrapolated to $10^9\,\mathrm{cm^{-2}}$ to consider the successful 20 years in orbit (i.e. $\approx 0.5 \times 10^8\,\mathrm{cm^{-2}\,yr^{-1}}$). For eROSITA, the expected fluence is $2.5 \times 10^8\,\mathrm{cm^{-2}}$ 10 MeV protons in 7 years (i.e. $\approx 0.4 \times 10^8\,\mathrm{cm^{-2}\,yr^{-1}}$). The predicted fluence for MXT per year of operation is therefore more than one

order of magnitude larger than for both those missions. If one also factors in the fact that both those detectors are operated at temperatures which are far lower than the baseline for MXT ($\leq -90\,^{\circ}\mathrm{C}$ compared with $\approx -65\,^{\circ}\mathrm{C}$), it becomes apparent the necessity to carry out a dedicated study to predict the evolution of the performances of MXT, since the results already available in the literature for XMM/EPIC-pn and eROSITA cannot be straightforwardly generalized.

4.3.2.5 Total ionizing dose

The same algorithm described above also allows for the calculation of the Total Ionizing Dose of the mission as a function of the in-orbit time. The only differences with the case of the displacement damage are the substitution of the NIEL tables with the stopping power and the fact that no contribution from neutrons is taken into account. Moreover, the results are provided in rad instead of equivalent fluence.

Tab. 4.7 shows the summary of the calculations. The dose the detector is exposed to is quite small according to the results, especially considering that prototypes of pnCCDs were exposed to doses of $1-5$ Mrad without experiencing any major change in the performances (Strüder et al., 1990). Furthermore, one must remember that pnCCDs are naturally resilient to ionization damage, on the basis of the conclusions of § 2.2.2.3 and the possibility to apply a voltage to the MIS structures in order to counteract the effects of the accumulation of holes (§ 2.4.1.1). On the other hand, CAMEX are fabricated with standard 0.35 µm CMOS technology in a 5 V process: no change in electrical parameters or performances is expected for TID $\lesssim 10$ krad (Herrmann et al., 2007, 2008).

It is finally worth noting that the one above might even be overestimation, since the δ-rays produced in the interactions were considered to be fully absorbed by the device, which is not necessarily true, especially for higher energy particles, as already pointed out in § 4.2.2.2.

4.4 Prediction of the in-orbit performances

As previously discussed (§ 4.2.3.3), interactions between radiation and the material of a detector may affect its performances. In particular, in line with the NIEL scaling hypothesis (§ 4.2.3.4), one finds that some parameters, such

Table 4.7 – Summary of the estimations of the Total Ionizing Dose (TID) for the simulations with the camera alone and inside the satellite for four values of the time in orbit.

		1 yr krad	3 yr krad	5 yr krad	10 yr krad
TID	Camera	0.31	0.94	1.57	3.14
	Satellite	0.21	0.63	1.05	2.10

as the defect concentration, scale linearly with the (equivalent) fluence the detector is exposed to during its time in orbit. Since the fluence was calculated in § 4.3.2.4, it becomes possible to estimate the evolution of the performances of the detector during the mission lifetime.

Normally, this kind of study requires the actual irradiation of a prototype of the detector in an accelerator facility, in order to expose it to a fluence representative of the in-orbit one. However, in the case of MXT, this approach was not possible, since no device was available for radiation tests at the time of this work. As a consequence, hereafter an analysis is attempted based on studies carried out on previous versions of the same detector, as well as on the known working parameters of the MXT system itself (§ 4.4.1). After that, a plan for future proton radiation tests will be outlined, to be carried out whenever a model of the MXT focal plane is available for this kind of study (§ 4.4.2).

4.4.1 Analytic performance assessment

In the following, an analytic approach is undertaken to assess the evolution of various figures of merit of the MXT detector as a function of the mission lifetime. The study is based on the theoretical framework established in § 2, the Monte Carlo simulations described above as well as the literature.

In § 4.4.1.1, Charge Transfer Efficiency shall be explored, followed by low-level threshold in § 4.4.1.2 and energy resolution in § 4.4.1.3.

4.4.1.1 Charge Transfer Inefficiency

As discussed in § 2.3.2.3, a Charge Coupled Device, such as the one at the focal plane of MXT, suffers from some degree of inefficiency in transferring the charges from pixel to pixel towards the anodes for readout, i.e. Charge

Transfer Inefficiency (CTI). As clear from the theoretical model described in the same section and summarized in eq. (2.70), CTI depends, among other things, on the properties of the defects interfering with the charge transfer, i.e. their electron capture cross-section σ, their energy depth $E_\mathrm{t} - E_\mathrm{C}$ and their concentration N_t.

As already stated in § 3.1.2.2, the presence of a frame-store region in the detector (§ 2.4.1) and the dependence of the CTI on many parameters (eq. (2.70)) implies that there are three CTI values to be determined. Indeed, as seen in eq. (3.9), if one considers a charge packet generated by a photon of energy E_γ and separated by n shifts from the bottom of the image region, which comprises of N rows in total (the same number making up the frame-store area, of course), then the measured energy is

$$E_n = E_\gamma \left(1 - \mathrm{CTI}_{\mathrm{fs,fast}}\right)^N \left[\frac{\left(1 - \mathrm{CTI}_{\mathrm{im,fast}}\right)\left(1 - \mathrm{CTI}_{\mathrm{fs,slow}}\right)}{\left(1 - \mathrm{CTI}_{\mathrm{fs,fast}}\right)}\right]^n , \qquad (4.30)$$

where the subscripts im and fs indicate the image and the frame-store areas respectively, whereas fast and slow stand for fast and slow transfer. For completeness, it is useful to be reminded that the CTI is linked to the Charge Transfer Efficiency CTE by $\mathrm{CTE} = 1 - \mathrm{CTI}$.

In order to apply eq. (2.70), several parameters are needed, which are divided into *physical*, *operational* and *defect* parameters.

Physical parameters are those depending only on the detector, such as pixel dimensions and clock timing. Those were reported in § 2.4. A critical value among those is the volume occupied by the charge cloud as it is stored underneath a pixel, because it influences the number of defects the electrons interact with as they move to the anode. It is worth noting that the dimensions of the charge cloud considered here are not the same as those expressed by eq. (2.75). Indeed, after the charges drift from the interaction point to the transfer channel (§ 2.3.2.4), possibly splitting among multiple pixels, the spread of the electrons below each pixel gets limited by technological features such as varying doping concentrations (§ 2.4.1.1), in order to limit the interactions between signal electrons and lattice defects, thus improving the CTI. Unfortunately, the detailed internal electric configuration of the device, normally required for this kind of estimation, was not available. By taking advantage of some simulations contained in Schmaler (2012), I was nonetheless

Table 4.8 – Summary of the parameters of the defects used in the estimations of the CTE. The cross-section is expressed as $\sigma = \sigma_0 e^{-E_\sigma/kT}$, where T is the temperature. The enthalpy variation ΔH and the entropy factor X are defined in eq. (2.61). Values were retrieved from Brotherton & Bradley (1982) and Holland (1993).

ΔH eV	σ_0 $10^{-14}\,\mathrm{cm}^2$	E_σ eV	X
0.169	1	0	0.4
0.230	0.04	0.017	8
0.3	1	0	1
0.39	0.4	0	0.3

able to estimate a volume of the charge cloud equal to

$$V = \frac{\pi}{6}\,(5.2\,\mu\mathrm{m})^3\,\frac{X_{\mathrm{pix}}Y_{\mathrm{pix}}}{75\,\mu\mathrm{m}\times 75\,\mu\mathrm{m}}, \tag{4.31}$$

where X_{pix} and Y_{pix} are the two dimensions of a single pixel.

The CTI also depends on the way the detector is operated in terms of integration time, photon flux and, most importantly, temperature. As for the first parameter, the baseline value for MXT of $t_{\mathrm{int}} = 100\,\mathrm{ms}$ was adopted in all the calculations, with a photon flux of $100\,\mathrm{cm}^{-2}\,\mathrm{s}^{-1}$, the latter influencing the result very weakly. The temperature range was again taken equal to the baseline, i.e. between $-60\,^\circ\mathrm{C}$ and $-80\,^\circ\mathrm{C}$, in agreement with the expected in-orbit performances of the cooling system (§ 1.3.3.2).

Finally, the defects play the most important role in the determination of the CTI, as the efficiency depends linearly on their concentration and they also define all the capture and emission rates. It is known (Meidinger et al., 1996, 1998, 2000) that the performances of pnCCDs are affected principally by two kinds of defects, i.e. A-centers and divacancies, which are complexes composed of a vacancy and an oxygen atom, and two vacancies respectively. They are created at different rates according to the concentration of oxygen atoms in the device (A-centers) and to the NIEL of the radiation (divacancies). By applying eq. (2.70) to the data presented in those papers, I was able to identify the most relevant defects, as well as estimate their concentration. By fitting a straight line (NIEL scaling hypothesis) to the latter as a function of the fluence to which the prototypes had been exposed before the measurements, I could extrapolate values relevant to the scenario at hand, thanks to the

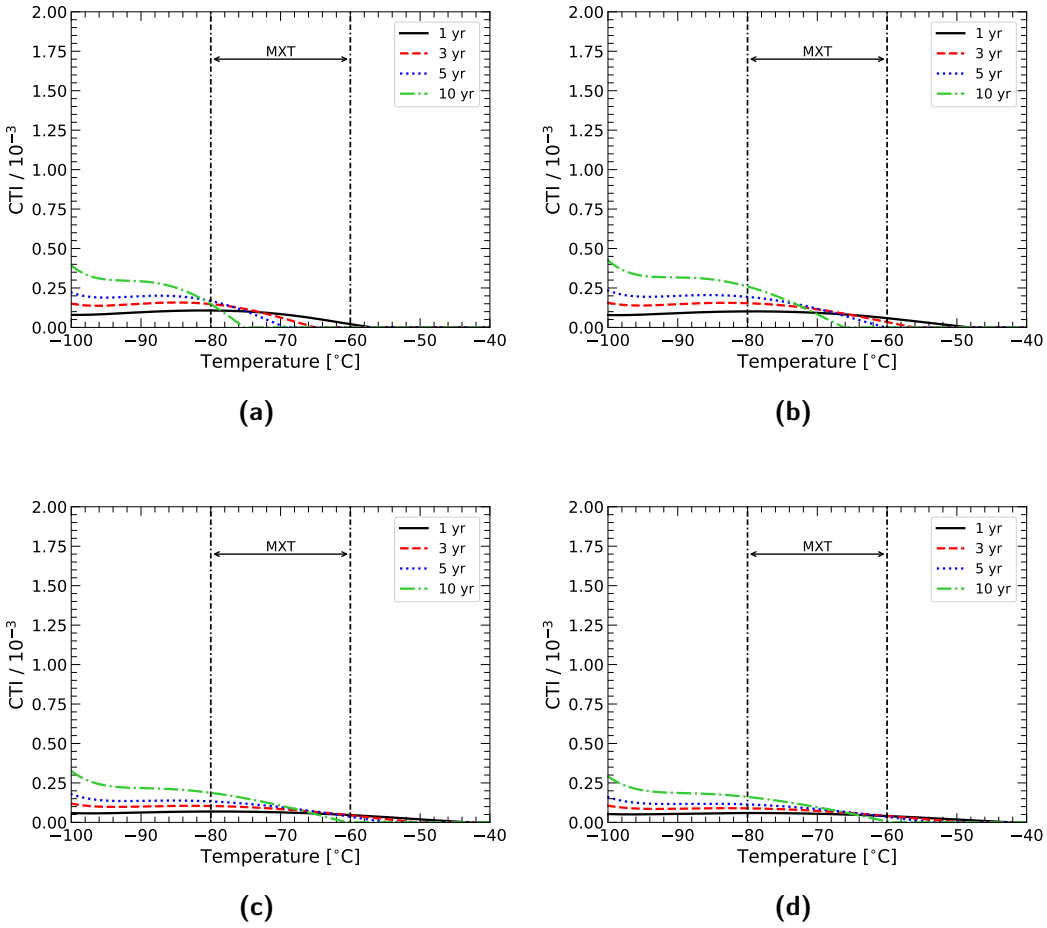

Figure 4.25 – Charge Transfer Inefficiency (CTI) for fast transfer in the image region after 1, 3, 5 and 10 years in orbit. Several energies are presented: a) 277 eV (C-K); b) 1486 eV (Al-K$_\alpha$); c) 5898 eV (Mn-K$_\alpha$); d) 8040 eV (Cu-K$_\alpha$).

10 MeV proton fluence I calculated in § 4.3.2.4: to operate in a worst-case scenario, I used the results pertaining to the camera alone, as the fluence is higher. Tab. 4.8 summarizes the parameters.

The results of the calculations are presented in the plots of Fig. 4.25 for the CTI associated with the 75 µm × 75 µm pixels of the image area during the fast transfer, i.e. $CTI_{im,fast}$ of eq. (4.30), whereas Fig. 4.26 shows the CTI of the 75 µm × 51 µm pixels of the frame-store area during readout, i.e. $CTI_{fs,slow}$ of eq. (4.30). For the sake of clarity, the CTI of the frame-store area during fast transfer, i.e. $CTI_{fs,fast}$ of eq. (4.30), will not be presented here, since the results are very similar to $CTI_{im,fast}$.

Several trends are evident in the plots. First of all, as already discussed in

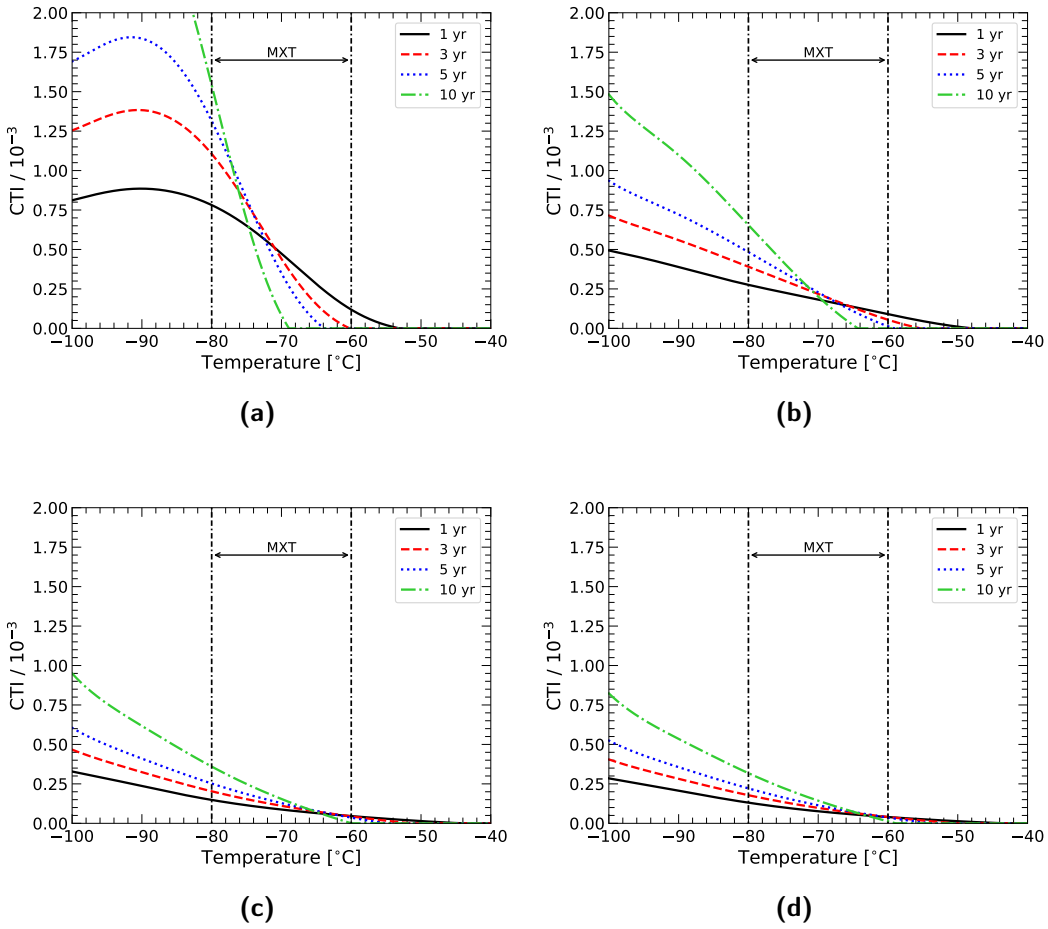

Figure 4.26 – Charge Transfer Inefficiency (CTI) for slow transfer in the frame-store region after 1, 3, 5 and 10 years in orbit. Several energies are presented: a) 277 eV (C-K); b) 1486 eV (Al-K_α); c) 5898 eV (Mn-K_α); d) 8040 eV (Cu-K_α).

§ 2.3.2.3, the CTI depends strongly on the photon energy, since this determines the amount of charge that is transferred (and therefore trapped) from one pixel to another.

The second feature is the fact that the CTI in the image (but also frame-store) region during fast transfer is smaller than the CTI in the frame-store area during slow transfer. This phenomenon depends on the different time a charge packet spends inside a pixel in the two cases (900 ns for fast transfer and 32 µs for slow transfer), as the longer it stays the more interactions it has with the defects in the pixels and thus the worse the CTI.

Finally, one can notice that the CTI decreases at higher temperatures for longer lifetimes. This is the results of the inclusion of the leakage current[7] in the CTI model of eq. (2.70). Indeed, as time progresses (and the equivalent fluence increases), the leakage current becomes higher as well with the consequence that traps are filled with dark electrons before the arrival of photon packets, resulting in a high transfer efficiency.

After 5 years in orbit, at 1.5 keV, where the MXT telescope is the most sensitive, one can expect CTI $\lesssim 2.5 \times 10^{-4}$ for fast transfer and CTI $\lesssim 6 \times 10^{-4}$ for slow transfer.

4.4.1.2 Low-energy threshold

As explained in § 2.3.3.3, an important figure of merit for a detector (and for the SVOM mission in particular) is its low-energy threshold, defined as a number k of times the noise due to the leakage electrons accumulated in each pixel of area A_{pix} during integration time t_{int}:

$$E_{\text{thr}} = k\epsilon\sqrt{\frac{J}{q}A_{\text{pix}}t_{\text{int}} + \text{ENC}^2}. \tag{4.32}$$

where J/q is the leakage current density measured in electrons per unit time and surface and ENC is the electronic noise of the complete readout chain (§ 2.3.2.2). This equation is the same as eq. (2.88). One should remember that in eq. (4.32), both ϵ and J depend on the temperature.

As space radiation is responsible for the onset of defects that worsen the charge transfer efficiency, it also creates generation centers that release electrons

[7]The in-orbit evolution of the leakage current is assessed in § 4.4.1.2 when discussing the low-level threshold and in § 4.4.1.3 when dealing with the energy resolution.

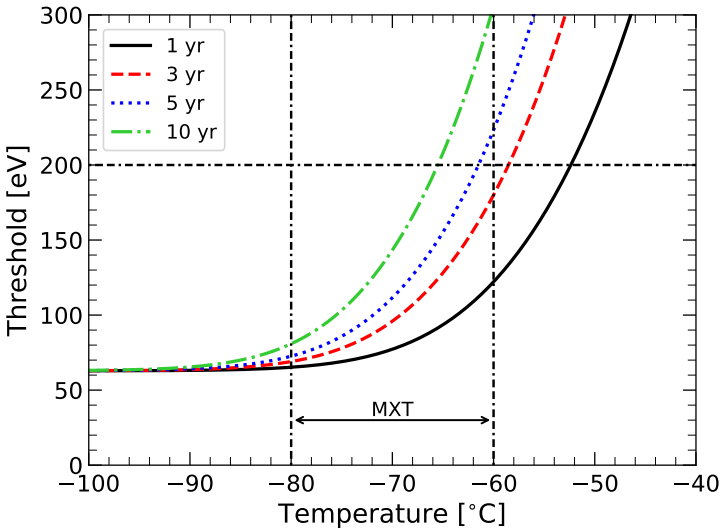

Figure 4.27 – Evolution of the low-energy threshold in MXT as a function of temperature and time in orbit. In applying eq. (4.32), $k = 4$ was chosen. The mission specification of $E_{\mathrm{min}} = 200\,\mathrm{eV}$ is marked for reference.

during integration, therefore changing the applicable low-energy threshold. In order to estimate its evolution, I relied again on the studies carried out by Meidinger et al. (2000) which provide measurements of the leakage current as a function of temperature T after exposure to various amount of radiation in the form of 10 MeV protons. Data points were fitted with a law in the form of

$$J\left(T\right) = J_0 + C_J T^2 e^{-\frac{E_{\mathrm{G}}(T)}{2kT}} \tag{4.33}$$

with J_0 and C_J fitting parameters, $E_{\mathrm{G}}\left(T\right)$ silicon band gap and k Boltzmann constant. In particular, J_0 represents the residual infrared emission that depends on the CAMEX ASIC. In an approach similar to the one already described in § 4.4.1.1, the parameters C_J were plotted against their associated 10 MeV proton fluence and then fitted with a straight line in order to extrapolate to the fluence range interesting for MXT. It is worth noting that the leakage current calculated above was multiplied by a factor W/W_{ref} before using it in the calculations, with $W = 450\,\mu\mathrm{m}$ and $W_{\mathrm{ref}} = 300\,\mu\mathrm{m}$ to take into account the different thickness of the detector tested in Meidinger et al. (2000) and MXT.

From the tests on the Performance Model of the MXT detector discussed in § 3.3, I estimated ENC $= 3\,\mathrm{e}^-_{\mathrm{rms}}$ for the noise of the complete readout chain.

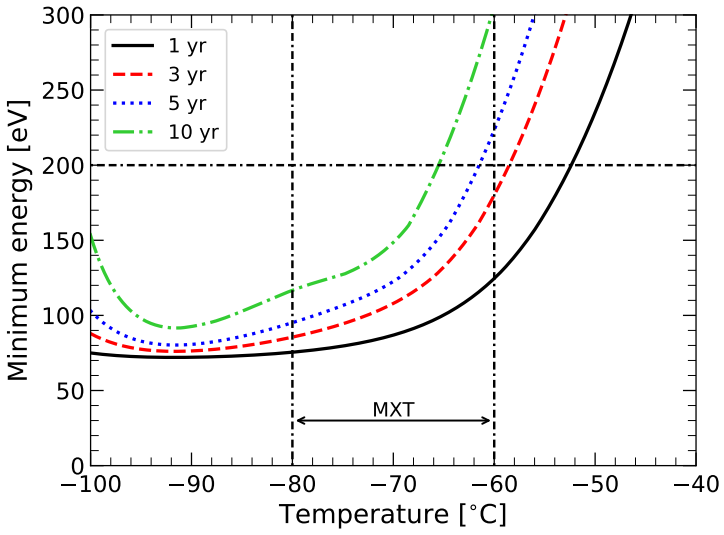

Figure 4.28 – Minimum detectable energy as a function of temperature and time in orbit once both low-level threshold and CTE are taken into account. The mission specification of $E_{\mathrm{min}} = 200\,\mathrm{eV}$ is marked for reference.

The preliminary measurements on the same detector model coupled with the Engineering Model of the Front-End Electronics, instead of the prototype FEE previously used, suggests that the noise associated with the final design is closer to ENC $= 4\,\mathrm{e^-_{rms}}$. The latter value will be used in the following assessment.

Fig. 4.27 shows the results of the calculations described above as a function of temperature and time spent on orbit. A value of $k = 4$ was chosen in eq. (4.32). As one can see, for temperatures below $-65\,^{\circ}\mathrm{C}$, the 200 eV requirement can be satisfied for the whole duration of the mission.

It is worth addressing that the curves of Fig. 4.27 do not really represent the minimum energy to which the detector is sensitive. This derives from the fact that in the event extraction pipeline, outlined in § 2.4.3.5 and discussed more thoroughly in § 3.1 for laboratory measurements, single pixels are compared to the threshold *before* any correction of the CTI can take place. If a photon with an energy close to the threshold itself deposits its energy in a pixel[8] far from the anode, when it is read out, it will be assigned a lower energy if the CTI is important (which is most probably the case, as was seen in § 4.4.1.1). If due to this phenomenon it falls below the threshold, then it will be misidentified as noise. At most, a pixel may undergo $n = 256$ shifts in the image area as well

[8] I am considering only single events, where only one pixel is involved, since the energy is so low that in case of split events all involved pixels end up confused with the noise.

as the usual $N = 256$ transfers in the frame-store region. As a consequence of eq. (4.30), the minimum detectable energy will be

$$E_{\mathrm{min}} = \frac{E_{\mathrm{thr}}}{\mathrm{CTE}_{\mathrm{im,fast}}^{256}\mathrm{CTE}_{\mathrm{fs,slow}}^{256}}. \tag{4.34}$$

This is reported in Fig. 4.28. The result confirms that the 200 eV specification on the energy threshold is likely to be satisfied throughout the mission lifetime for temperatures below −65 °C. This justifies the temperature requirement on the thermal control of the MXT camera.

4.4.1.3 Energy resolution

Another important figure of merit whose evolution must be assessed is the instrument energy resolution, as defined in § 2.3.3.2. For the estimations, I adopted the same leakage current and electronic noise calculated in § 4.4.1.2 and I coupled it with the Fano noise for the energy under consideration (§ 2.3.2.1). For simplicity, the analysis is limited to single events, i.e. photons depositing their charge in a single pixel. Moreover, the effects of CTE are not considered, as this phenomenon will be corrected for in the MXT data analysis pipeline, as outlined in § 2.4.3.6 and § 3.1. Fig. 4.29 shows the estimates of the energy resolution in terms of the Full Width at Half Maximum (FWHM) of selected spectral lines, as a function of temperature and time spent in orbit. For all the curves, the value of ENC = $10\,\mathrm{e}^-_{\mathrm{rms}}$ calculated from the measurements carried out on the Performance Model of the MXT detector (§ 3.3) was employed. This ENC value was preferred to ENC = $4\,\mathrm{e}^-_{\mathrm{rms}}$ used for the low-level threshold (§ 4.4.1.3) because it derives from spectral studies and, as explained in § 3.4.2, it takes into account noise sources not limited to readout noise and leakage current.

It is evident from Fig. 4.29 that the leakage current of the detector plays a pivotal role in determining the energy resolution, as the widening of the FWHM due to the current occurs right in the temperature range in which the MXT detector will be operated.

From this study one can conclude that, in order to comply with the energy resolution requirements of 160 eV at 1.5 keV after 3 years of operation and of 280 eV after 5 years, the detector must be kept cooler than −60 °C. Thus, as in the case of the low-level threshold (§ 4.4.1.2), the temperature constraint on

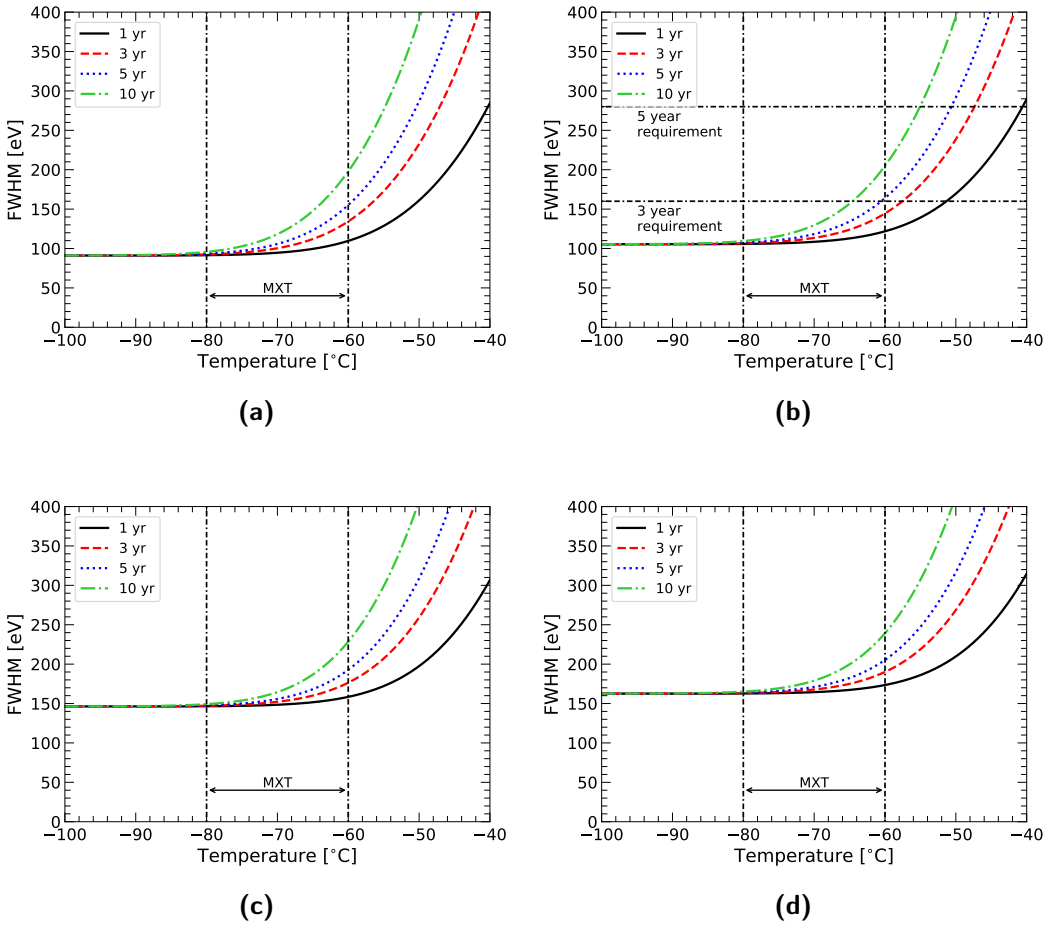

Figure 4.29 – Energy resolution, in terms of the Full Width at Half Maximum of a spectral line made out of single events, as a function of temperature after 1, 3, 5 and 10 years in orbit. Several energies are presented: a) 277 eV (C-K); b) 1486 eV (Al-K_α); c) 5898 eV (Mn-K_α); d) 8040 eV (Cu-K_α). For reference, the 3 year and 5 year requirements on energy resolution at the Al-K_α line are reported.

the cooling system of the camera is confirmed to be of the utmost importance to ensure the fulfillment of the mission specifications.

4.4.2 Radiation tests

The results of § 4.4.1 are based on modeling with several assumptions and approximations about the detector and how its performances degrade with radiation damage. They demonstrate that the technical specifications in terms of noise and temperature are coherent with the science requirements on low-level threshold and energy resolution. However, some features, such as the type and concentration of defects that are formed by radiation, are highly dependent on the specific device, e.g. in terms of the amount of impurities present in the silicon lattice. An experimental investigation is thus required to consolidate the findings obtained so far.

In the following sections, I shall propose a proton irradiation campaign of the MXT detector to investigate the evolution of its response with radiation damage. After an overview of test facility and setup (§ 4.4.2.1), I am going to describe the Monte Carlo simulations used to optimize the experiment (§ 4.4.2.2), followed by a proposed test plan (§ 4.4.2.3).

4.4.2.1 Setup

The facility selected to carry out the proton radiation tests of the MXT focal plane is the Proton Irradiation Facility (PIF) of the Paul Scherrer Institute (PSI), Switzerland (Paul Scherrer Institute (PSI), 2019). PIF is a member of the ESA-supported European Component Irradiation Facilities (ECIF) and provides scientists with a user-friendly infrastructure and long experienced personnel to conduct tests with realistic space proton environments and mono-energetic proton beams.

On this beam line, the irradiation is customarily performed in air. However, since the intention is to irradiate the MXT focal plane under conditions as close as possible to those in orbit, the MXT team will provide a vacuum chamber where the detector can be supplied with high voltage and cooled down to $-65\,^{\circ}\mathrm{C}$. Fig. 4.30 shows the setup designed for the campaign, with the detector placed inside a copper case to ensure both mechanical stability and thermal conductivity.

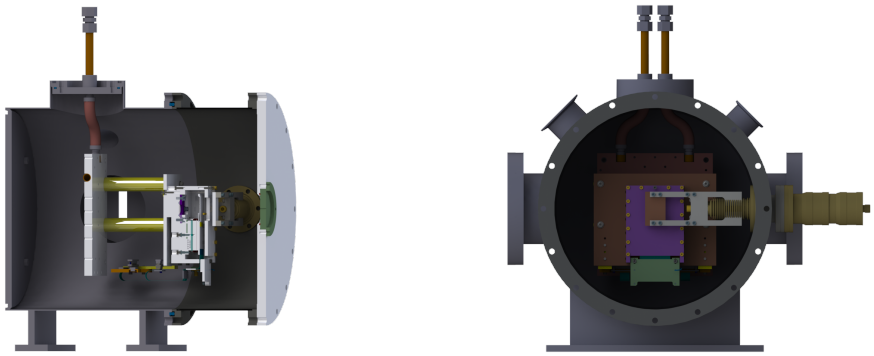

(a) (b)

Figure 4.30 – Setup devised for the irradiation tests. a) Longitudinal section of the cryostat. b) Front view of the interior of the cryostat. In both cases, gravity points downwards.

The beam line configuration involves primary protons exiting the accelerator at 72.8 MeV, then moving through a series of copper degraders for the purpose of selecting the energy of interest, and finally arriving at the MXT vacuum chamber, where they reach the detector after going through a 500 µm-thick beryllium window. A copper collimator just after the degraders helps keeping the beam focused.

It is important to point out that the tests are to be performed on the front side of the detector. The reason for this is the desire to expose the whole of the detector (image and frame-store areas) to an equal amount of radiation. Since in the case of MXT the MoCu X-ray shielding in front of the frame-store region also provides mechanical support to the whole focal plane, its removal is not possible, hence the flipping of the detector. The detector assembly is mounted in a copper case which allows to protect the ASICs, which are mounted on the same side of the ceramic carrier board as the front of the CCD, and therefore in principle directly exposed to the particle flux. It is worth noting that the eROSITA team already irradiated the CAMEX with $2 \times 10^9\,\mathrm{cm}^{-2}$ 10 MeV protons, measuring neither temporary nor permanent effects (Meidinger et al., 2010a).

In Fig. 4.30b, a copper plate is visible in front of the aperture in the detector case through which the particles are to pass. This plate works as a sliding shield thanks to the micrometric screw on which it is mounted (visible on the right in the picture). This enables the irradiation of only a portion of the CCD,

which in turn allows for the possibility of creating zones of different exposure[9]. This is an important step to obtain a meaningful relationship between particle fluence (i.e. in-orbit time) and device performances, as laboratory tests can be performed thoroughly after the irradiation campaign.

4.4.2.2 Simulations

The geometrical configuration outlined in § 4.4.2.1 must be validated through Monte Carlo simulations, which allow to optimize the geometry itself, as well as develop a realistic test plan for the irradiation campaign, in terms of choice of energy and flux of the primary particles, and schedule.

Rationale The simulations were carried out through a Geant4 application, in which the whole system was recreated, from the exit of the beam line to the detector inside the cryostat, passing through the copper degraders and the beryllium window. The whole system was placed in air, with the exception of the interior of the cryostat of course being under vacuum.

With an approach similar to the one described in § 4.3.2.2, the setup of § 4.4.2.1 was simplified and reduced to its most important solids (Fig. 4.31). This again allowed to speed up the simulations. Unlike the earlier simulations, however, there was no need for the implementation of a multiplication algorithm, since the particular configuration ensured high statistics. Furthermore, the fewer performance constraints allowed for the use of a large part of the original CAD model, i.e. not only the focal plane (MoCu and ceramic carrier board as in § 4.3.2.2), but also the whole structure encasing it, as well as the sliding shield (the movable arm was nonetheless removed). However, the detector was substituted with a native Geant4 solid for the same reasons as before.

Aspects such as the chosen physics list (`Shielding_EMZ`) and the list of registered parameters per particle are the same as in the previous case, as are the algorithms employed to extract useful information from the data (§ 4.3.2.3 and § 4.3.2.4).

Different setups were studied:

- 50 MeV proton primaries with unshielded detector;
- 10 MeV proton primaries with unshielded detector;

[9]Of course, the detector can be irradiated all at once, if desired.

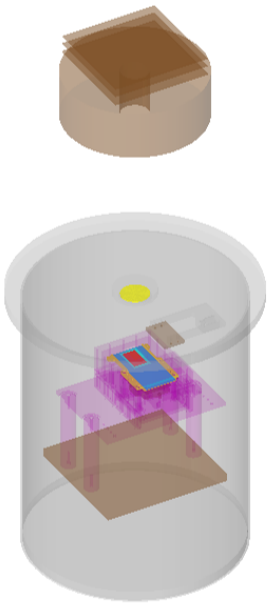

Figure 4.31 – Simplified geometry used in the simulations of the radiation tests. The detector (front-side up in the figure) is placed in the simplified cryostat and encased in its module. The movable shutter is also visible in the vacuum chamber. At the top of the image are the copper collimator and a set of degraders.

- 50 MeV proton primaries with half-shielded detector;
- 10 MeV proton primaries with half-shielded detector.

Besides the obvious necessity to understand the behavior of primary particles of different energy, the simulations were intended to assess the feasibility of the movable shield system, especially with respect to the presence of an eventual *transition zone* between two successive regions of different fluence.

It is important to point out that, in order to keep the scenario as faithful to reality as possible, 50 MeV and 10 MeV protons were in fact generated by a 72.8 MeV proton beam passing through a succession of copper degraders, as it is the case at PIF (§ 4.4.2.1).

Results Fig. 4.32 and 4.33 show the particle spectra in the case of an unshielded detector exposed to 50 MeV and 10 MeV protons respectively. The most striking feature is the comparison between the width of the spectral line of the primary particles in each plot: the 10 MeV beam is much more energetically dispersed than the other one. This is a consequence of the interaction with the

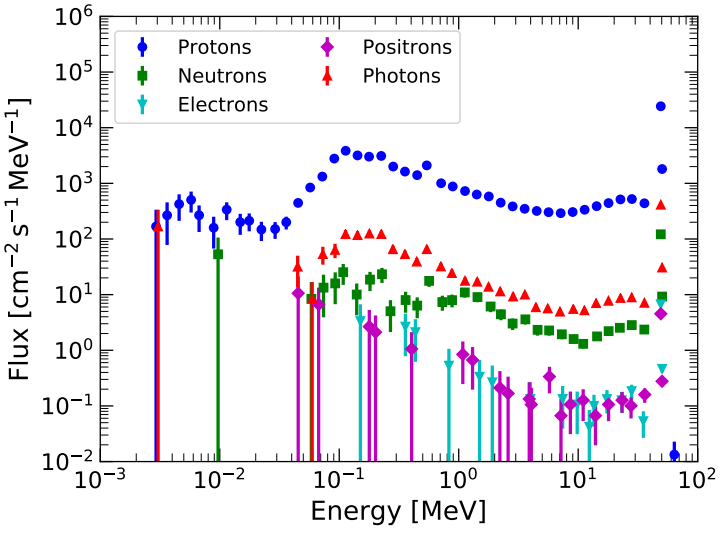

(a)

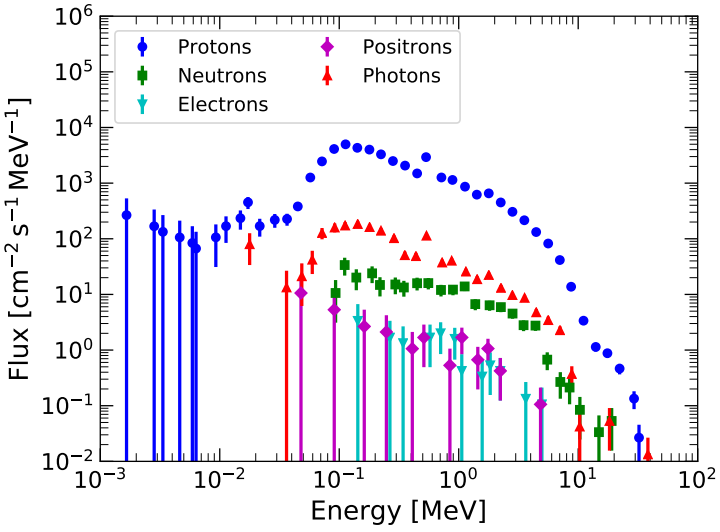

(b)

Figure 4.32 – Simulated differential particle flux on the MXT focal plane during 50 MeV proton irradiation, broken down into its components. a) Flux on the front-side (from the beam line). b) Flux from the back-side (back-scattered).

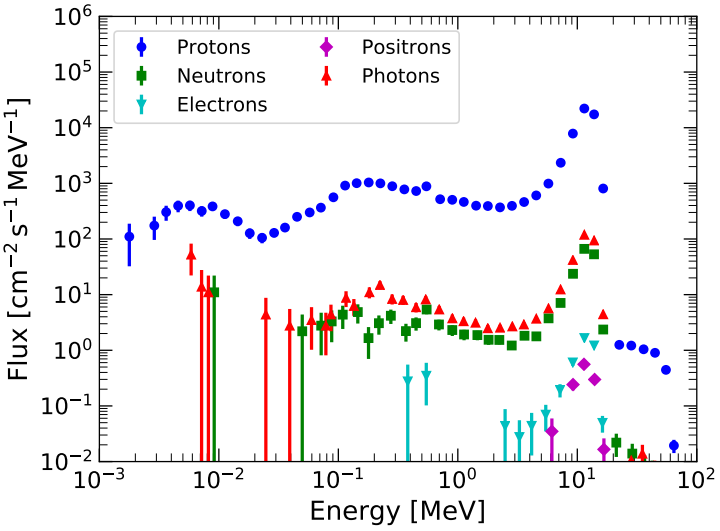

(a)

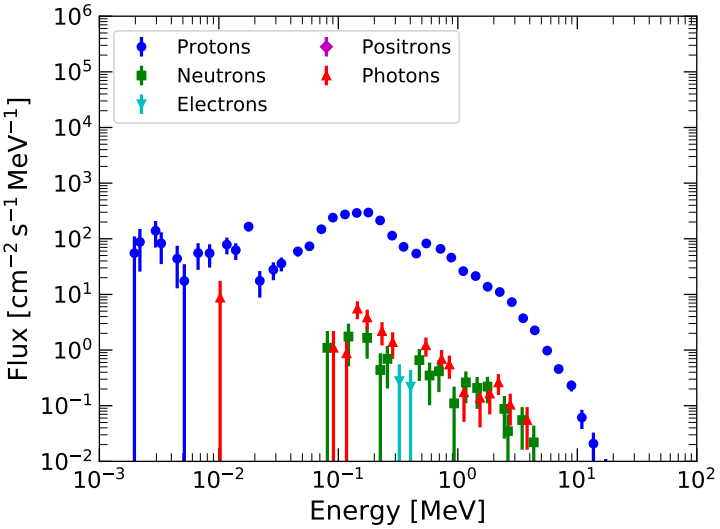

(b)

Figure 4.33 – Simulated differential particle flux on the MXT focal plane during 10 MeV proton irradiation, broken down into its components. a) Flux on the front-side (from the beam line). b) Flux from the back-side (back-scattered).

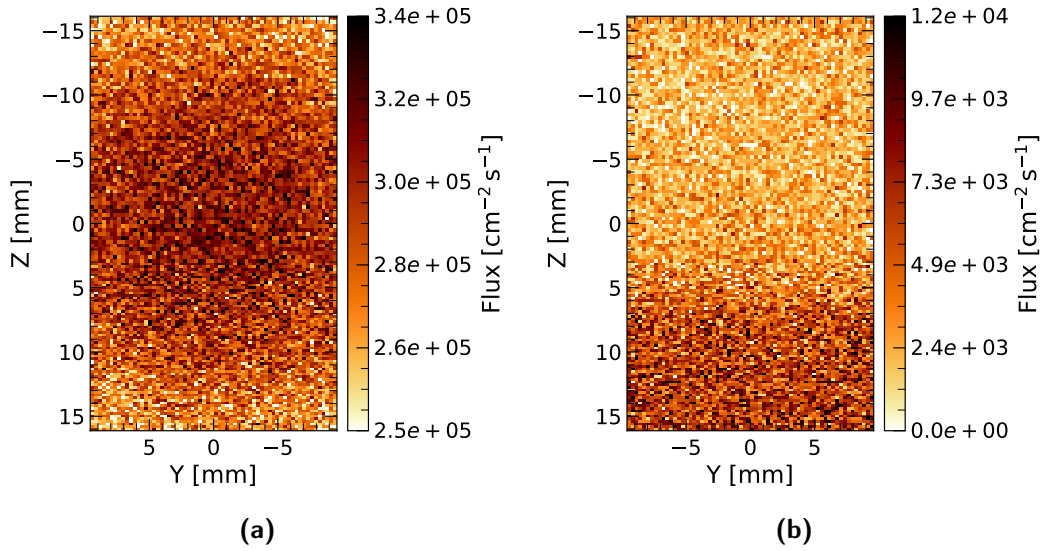

Figure 4.34 – Proton flux in the 50 MeV configuration. a) Flux on the front-side (from the beam line). b) Flux from the back-side (back-scattered).

air, as well as the action of the degraders, because at that energy the amount of air traversed by particles can significantly alter their energy, also implying that the correct positioning of the setup may influence the proton spectrum the detector is exposed to, especially in the second case. The fact the 50 MeV and 10 MeV protons come from the degradation of a 72.8 MeV proton beam also explains why there are particles more energetic than 50 MeV and 10 MeV respectively, as they are the residues of the primary beam.

Fig. 4.34, 4.35 and 4.36 show the proton, photon and neutron maps for the 50 MeV configuration, whereas Fig. 4.37 presents the proton map for the 10 MeV configuration (the other maps for the second scenario are analogous to the first ones, but with fewer secondaries, especially on the back-side). The irradiation is essentially uniform across the detector, with the proton beam being more intense around the center, a trend less evident in case of the 10 MeV setup, due to stronger scattering in air. A non-zero flux is registered on the back-side of the detector, implying that back-scattering takes place behind the detector to some degree. Most notably, the proton flux from the rear in correspondence to the frame-store area is higher than in the image region. This can be explained with the interaction between the main (back-scattered) proton (and neutron) flux and the thin layer of the MoCu X-ray shielding over the frame-store, which stimulates proton emission. This interpretation is confirmed by the fact that if half the detector is covered by the sliding shield,

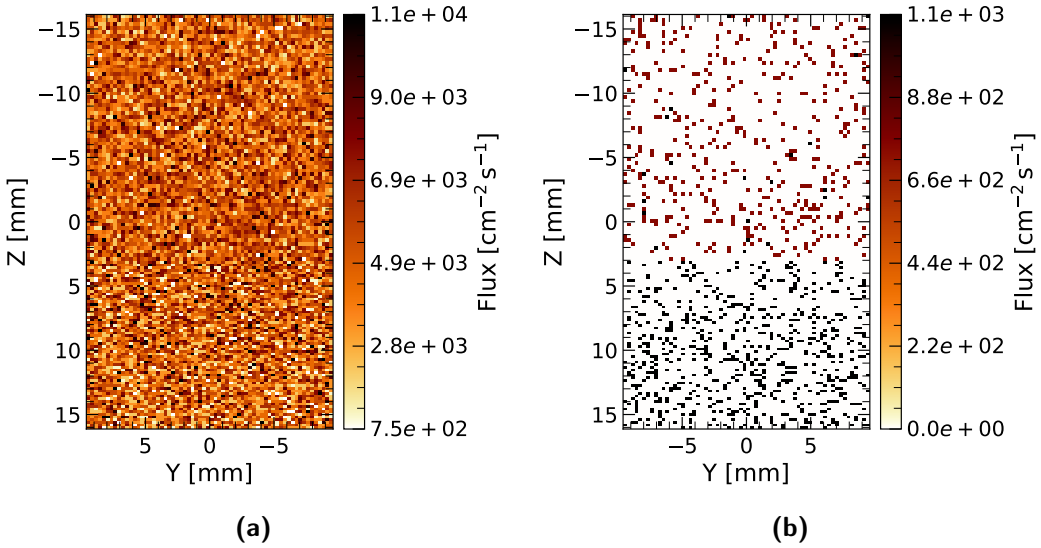

Figure 4.35 – Photon flux in the 50 MeV configuration. a) Flux on the front-side (from the beam line). b) Flux from the back-side (back-scattered).

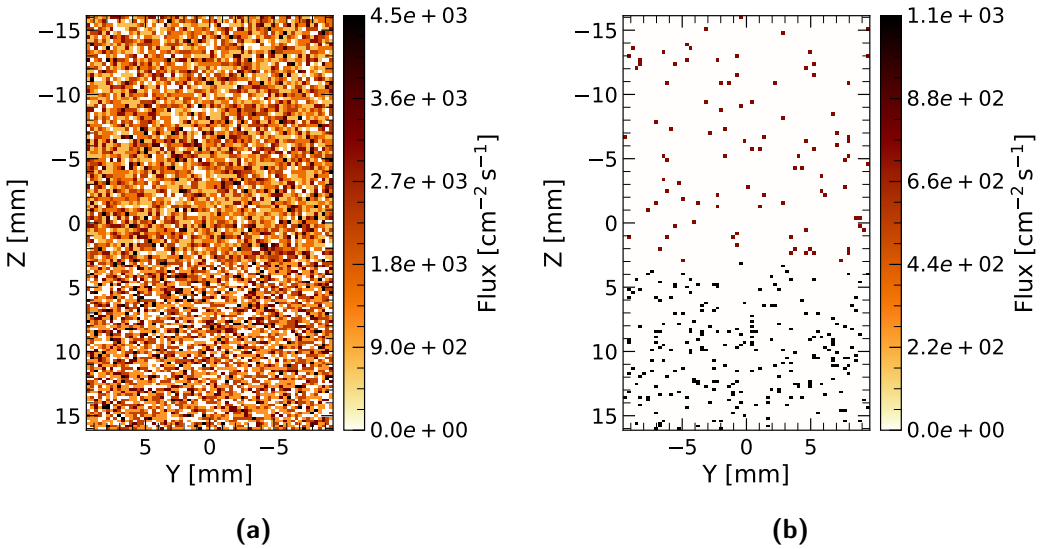

Figure 4.36 – Neutron flux in the 50 MeV configuration. a) Flux on the front-side (from the beam line). b) Flux from the back-side (back-scattered).

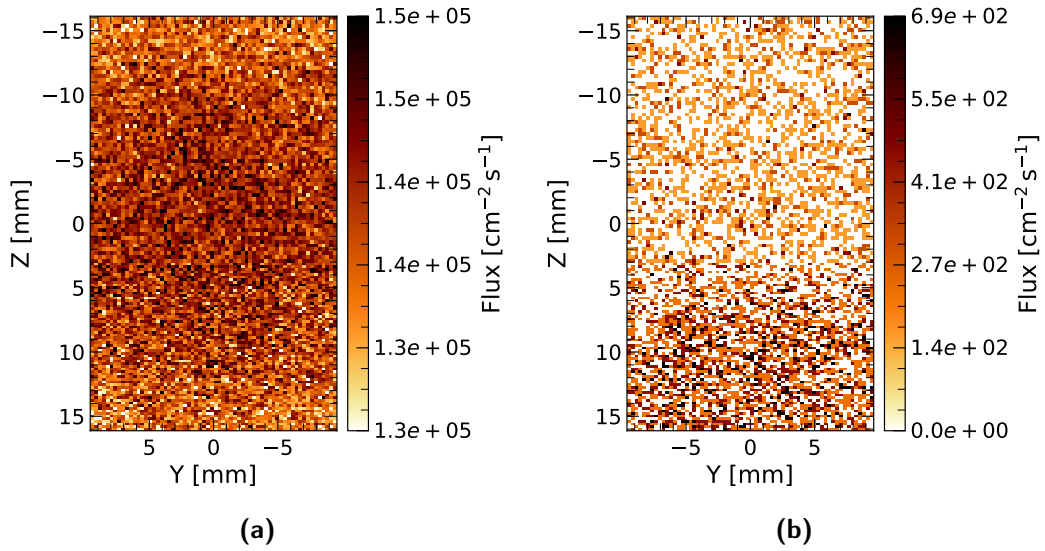

Figure 4.37 – Proton flux in the 10 MeV configuration. a) Flux on the front-side (from the beam line). b) Flux from the back-side (back-scattered).

the flux from the rear is cut as well, only remaining in the irradiated half. This is visible in Fig. 4.38.

Fig. 4.38 shows that, when the detector is partially covered by the movable shutter, a transition region arises between the covered and exposed part of the detector, an expected phenomenon and indeed one of the drivers of the simulations. To be more specific, one can see from the image that the transition[10] takes place across about 20 columns of the CCD (each pixel of the maps corresponds to 4×4 pixels of the detector), where consequently the fluence cannot be easily determined. This scenario is further worsened by eventual misalignment issues between the detector and the shutter. The situation described so far limits the number of regions of different exposure the device can be divided into, because a reasonable number of columns of known fluence must remain available for laboratory tests to ensure the required statistics necessary for a meaningful performance-fluence relation. Those findings are still valid in the case of the 10 MeV proton irradiation, because the number of columns of uncertain exposure is the same, although the flux on the covered region (and back-side) is about one order of magnitude lower than in the 50 MeV case (Fig. 4.39).

[10]The transition region is defined here as the group of columns included between where the flux raises between 5 % and 95 % of its maximum.

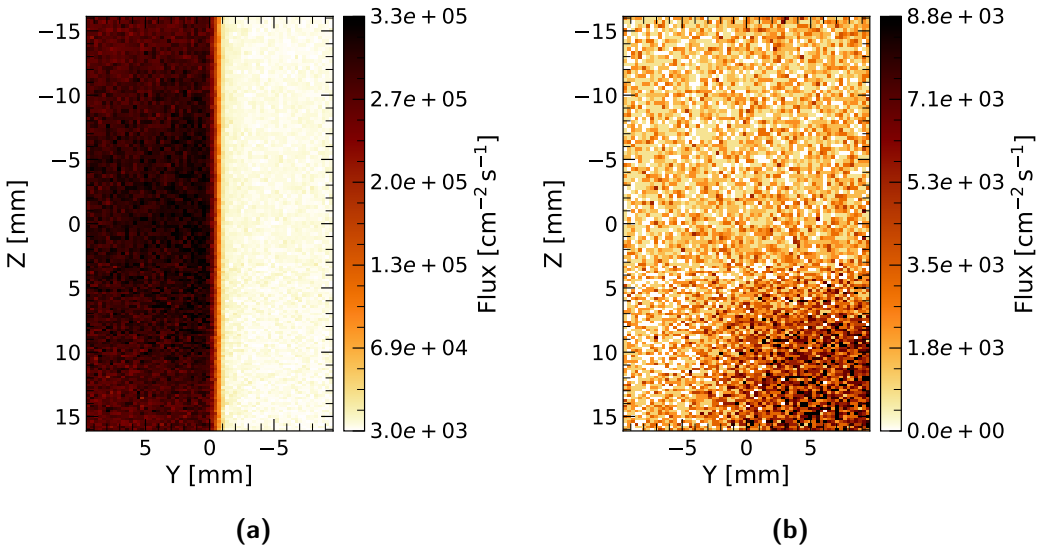

Figure 4.38 – Proton flux in the 50 MeV configuration with the sliding shield covering half the detector. a) Flux on the front-side (from the beam line). b) Flux from the back-side (back-scattered).

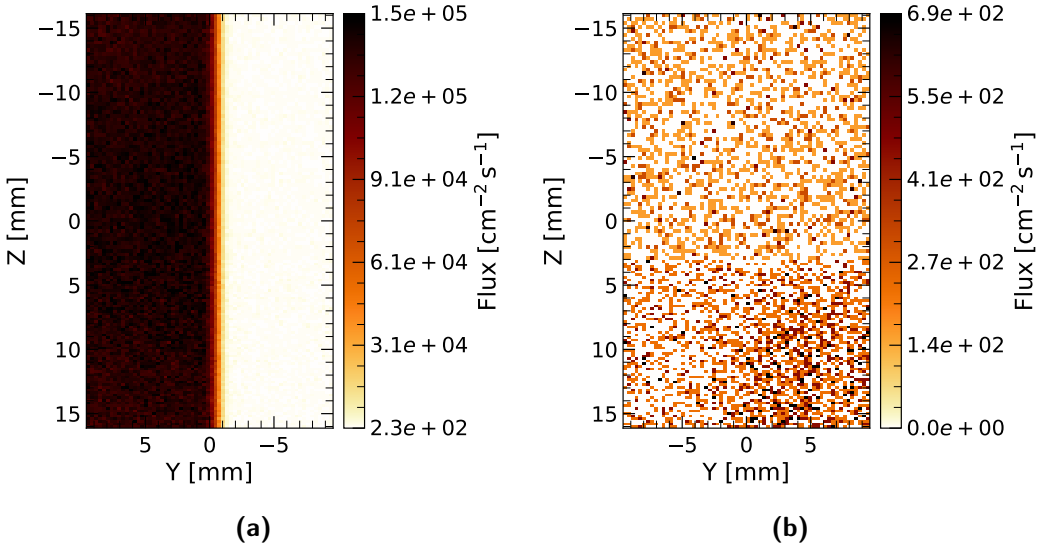

Figure 4.39 – Proton flux in the 10 MeV configuration with the sliding shield covering half the detector. a) Flux on the front-side (from the beam line). b) Flux from the back-side (back-scattered).

Table 4.9 – Summary of the proposed test plan. For each region, the equivalent years of exposure to the orbital environment are presented per run.

Run ID	Duration h	Region 1 yr	Region 2 yr	Region 3 yr	Region 4 yr
1	20	0	0	0	5
2	8	0	0	2	7
3	12	0	3	5	10

4.4.2.3 Test plan

On the basis of the considerations made above, I hereby propose a test plan in which the MXT detector is divided into 4 areas, with three transition regions in between. This implies that the fluence cannot be easily measured for 60 columns, leaving an average of 49 channels in each of the 4 regions where thorough spectroscopic tests can be performed after irradiation. Three of the four regions should have an exposure corresponding to 3, 5 and 10 years in orbit, while the fourth one should remain protected throughout the tests to be kept as a reference.

I recommend 50 MeV energy for the primary protons. Although the 10 MeV configuration provides similar performances in terms of the exploitability of the piece-wise irradiation, along with a lower background flux (by an order of magnitude) on the areas that are not supposed to be directly exposed to radiation, the poor energy resolution of the primary protons is a point of concern, as it means that not all of the particles are able to cross the detector, consequently creating an uneven energy deposition in it, whereas a uniform irradiation across the thickness of the detector is sought. For the same reason, the measurement of the beam intensity provided by PIF delivers a more accurate estimate of the total fluence in the case of a 50 MeV proton beam.

The flux should be high enough to achieve the desired fluence in about 40 hours, which is compatible with the usual allocated beam time at the accelerator facility. This approximately corresponds to one year of exposure every four hours, or, from the results of Tab. 4.3 or Tab. 4.6, a proton flux of $1.53 \times 10^5\,\mathrm{cm^{-2}\,s^{-1}}$. Three irradiation runs can be envisaged, each associated with a different position of the sliding shield, in order to progressively build up the fluence in each region, as summarized in Tab. 4.9.

Chapter 5

Focal plane calibration and response modeling

This chapter will tackle the topic of calibration of the MXT detector from several different angles, with the goal of estimating how reliably one can characterize the response of the device, especially when it is far from a laboratory environment, i.e. during in-orbit operation.

After the description of a simulation tool that could be integrated in more complex pre-existing pipelines in order to deliver results rooted in the physics of the detector (§ 5.1), two calibration scenarios that will occur periodically during the lifetime of the mission will be examined, i.e. the energy (§ 5.2) and flux (§ 5.3) calibration of the detector. The chapter will be concluded by a closer and more detailed look at the response of the detector, with the intent of studying how uncertainties may affect the overall performances (§ 5.4).

5.1 Focal plane simulator

In the following sections is detailed a focal plane simulator I developed in order to reproduce the scientific output of the Front-End Electronics of MXT, i.e. the stream of frames and/or hit pixels[1]. Originally developed to generate synthetic laboratory data for validation of the analysis pipeline described in § 3.1, this simulator is based on the physics of all the phenomena involved in the readout chain, from the interactions between incoming photons and the detector, to the readout process. It may be used in combination with more

[1] Housekeeping data are not simulated.

sophisticated tools and, for example, incorporated in complete simulations of the data flow from the MXT instrument.

5.1.1 Description

Written entirely in Python 3.6, the program allows to simulate the complete MXT acquisition chain, from photons interacting with the detector to the output of the Front-End Electronics. Being based on the proto-FEE, the main output of the simulator consists of raw data frames (matrices of ADU values). However, event lists are still produced, essentially enabling to simulate the operation of the FEE in *event mode* as well as *full-frame mode* (§ 2.4.3.6).

In the next paragraphs are discussed the input parameters the system requires to perform the simulation (§ 5.1.1.1), followed by the detailed description of all the steps of the calculations, each one based on the relevant physical processes (§ 5.1.1.2).

5.1.1.1 Initialization

To set up the simulation, several information must be provided via a parameter file, which includes settings that stay the same throughout the calculations. Those are divided into different categories:

- detector properties: number and dimensions of the pixels, quantum efficiency, Charge Transfer Inefficiency;
- source properties: spectrum from which the photons are to be extracted, spatial distribution of them across the detector, flux;
- detection chain properties: energy threshold, gain, offset, electronic noise and common-mode noise (per ASIC);
- simulation-specific properties: exposure time in the form of number of output files and frames per file.

Output file names and paths as well as plot properties are also handled via a list of parameters.

It is worth noting that since the program was originally intended to just generate synthetic laboratory data, it does not include all the features of a full telescope simulator: most notably, it only accepts a flat energy spectrum

or a list of spectral lines from which to draw the photons, which are either scattered uniformly across the detector or follow some user-defined distribution (in theory, the PSF of MXT may be used for this); finally, the flux is provided as the average number of photons per frame, implying that no information of the effective area of the optical system is explicitly set.

5.1.1.2 Simulation

An interactive *inspection mode* is provided to ensure the output is in the desired form. This executes a first run and returns the spectral and spatial distributions of the generated photons to be visually checked by the user, along with examples of the output files.

After the successful setup, the simulation may be launched. To optimize the processing speed, the program may run in multi-threaded mode so that as many output files as the available (or provided) cores of the machine are generated at the same time.

Photon generation By combining the source spectrum with the quantum efficiency of the detector and Fano noise, the spectral distribution from which to extract the photons is determined. As many photons are then drawn from it as given by the number of frames to be simulated and the average number of photons per frame: this essentially means that the source flux is supposed to be constant throughout the simulation. Spatial coordinates for each photons are determined according to the provided PSF. Flat fields can also be simulated (useful to represent the exposure to an unfocused radioactive X-ray source).

Charge splitting As extensively discussed on several occasions in the previous chapters, the charge cloud created by a single photon may be shared among the pixels surrounding its impact position. To account for this, the four pixels closest to the coordinates of each photon are first identified, the charge being split among those. According to what was stated in § 2.3.2.4, the four pixels need to be arranged in a square configuration (Fig. 5.1a). Photons interacting near the borders of the detector are allowed to share their charge with a ring of pixels placed outside the sensitive area: this simulates charge splits between the border pixels and the surrounding guard rings. The charge that ends up in those external pixels is considered lost.

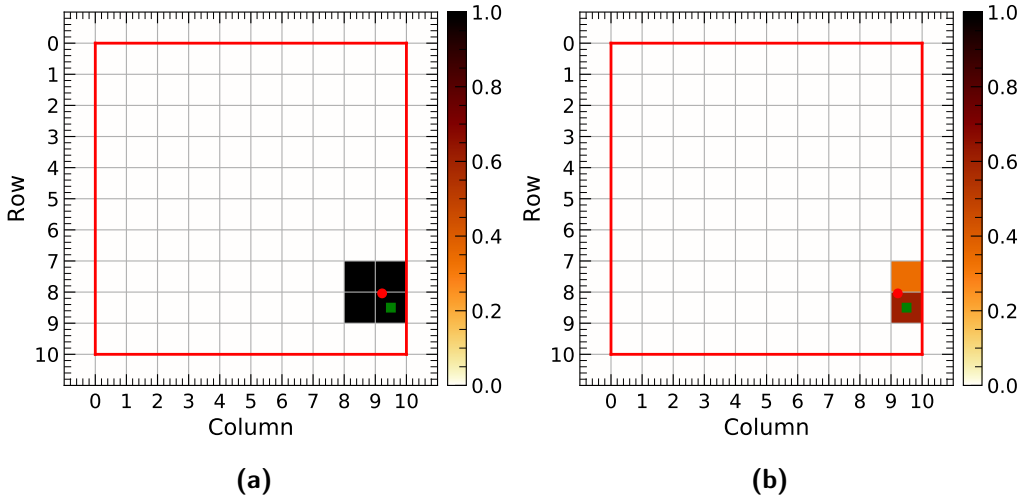

Figure 5.1 – Charge splits among neighboring pixels. a) Hit pixels participating in the charge sharing event. b) Pixels surviving after the charge has been partitioned and the threshold applied. In both plots, the red circle represents the coordinates of the photon interaction whereas the green square the center of the closest pixel, where the maximum charge is expected. An additional ring of pixels outside the sensitive area of the detector (marked by the red line) represents the guard ring.

The amount of charge, expressed as energy, to be assigned to each of the four pixels involved in a multiple event is calculated on the basis of the sub-pixel algorithm described by Dennerl et al. (2012) for a detector sharing a very similar design to MXT and originally developed to enhance the localization accuracy of the eROSITA telescope. Given a photon of energy E_γ interacting at (x_0, y_0), the energy E_i deposited in each surrounding pixel at position (x_i, y_i) is calculated as

$$E_i = E_\gamma \frac{\exp\left(-\frac{\Delta x_i^2 + \Delta y_i^2}{a^2}\right)}{\sum_{j=0}^{3} \exp\left(-\frac{\Delta x_j^2 + \Delta y_j^2}{a^2}\right)}, \tag{5.1}$$

where $\Delta x_i = x_i - x_0$ and $\Delta y_i = y_i - y_0$. The parameter a was experimentally determined to match the measured event multiplicities and was found to be around $a = 0.35$.

At this stage in the simulation, an energy threshold $E_{\rm thr}$ corresponding to the one that allows the event extraction (§ 3.1.1.3) can be applied so that only the pixels above it are retained.

Pile-up and charge transfer During the previous steps, photons are considered isolated on the matrix, i.e. no interaction is taken into account. After

the charge splits have been resolved, however, the contents of hit pixels with the same coordinates (row, column and frame) are summed up in order to simulate pile-up (§ 2.3.2.5).

The charge in each pixel is then transferred to the bottom of the matrix, a process represented by the application of the provided Charge Transfer Efficiency:

$$E_i(n) = E_i \mathrm{CTE}^n. \tag{5.2}$$

For the moment, only a single CTE value may be set, although the possibility of providing a tabulated function (e.g. for energy-dependence) is surely envisaged.

Readout To reproduce the noise added during readout, the content of each pixel is redrawn from a Gaussian distribution centered on each E_i and width determined by the Equivalent Noise Charge provided by the parameter file

$$E'_i \sim G(E_i, \epsilon\mathrm{ENC}). \tag{5.3}$$

Since this procedure is applied to every pixel, it follows that multiple events become inherently noisier than single photon counts, as expected.

Afterwards, energies are converted to ADU via the application of column-dependent gains, drawn from a Gaussian distribution whose center and width are user-defined. It is worth noting that the gain configuration is determined during the initialization of the simulator and therefore stays the same throughout the calculations (i.e. all the files simulated in a single run).

If desired, the pixel list may be arranged in a series of images, to which offset and common-mode noise are added.

Output FITS output files are generated at the end of the simulation, containing final frames, pixel list and original event list, as well as the table of the used gains. To allow the analysis of full frames, dark files files with no photons are saved as well.

When run on a HP laptop equipped with a quad-core Intel$^{\mathrm{R}}$ Core$^{\mathrm{TM}}$ i5-5300U CPU (2.30 GHz) in multi-threading mode, the simulator can output a complete 1000-frame file per minute.

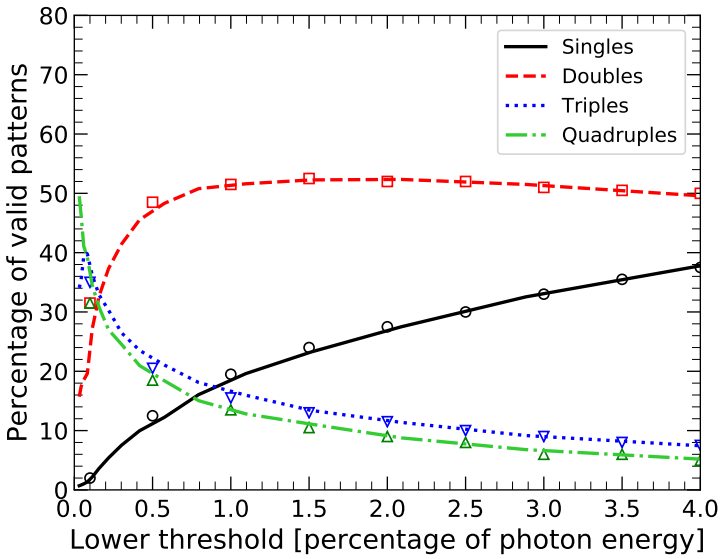

Figure 5.2 – Fractions of valid patterns as functions of the ratio between photon energy E_γ and low-level threshold E_{thr}. Superposed to the curves are the corresponding data points from Dennerl et al. (2012).

5.1.2 Validation

The validation of the simulator proceeded along two lines: the study of the distribution of allowed multiple events (§ 5.1.2.1) and the spectral analysis of simulated data (§ 5.1.2.2).

5.1.2.1 Multiplicity

The first step was to make sure that the split-charge algorithm was working properly and was able to correctly reproduce experimental data. For this reason, I turned to Dennerl et al. (2012), which provide measured curves for the event multiplicity as a function of the ratio between the photon energy E_γ and the threshold E_{thr}: indeed, as previously stated in § 2.3.2.4, E_γ/E_{thr} is the parameter defining the relative abundances of multiple events, as E_γ determines the total charge available for splitting and E_{thr} the level below which a signal cannot be detected.

Fig. 5.2 shows the curves obtained thanks to the simulator described above and how they relate to the experimental points from Dennerl et al. (2012). The superposition demonstrates that the physics of charge sharing is well implemented in the code.

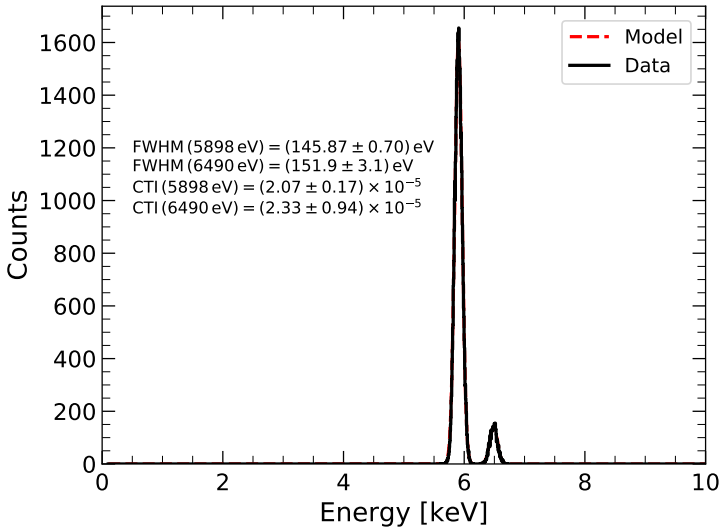

Figure 5.3 – ^{55}Fe spectrum after the same analysis described in § 3 was applied to the frames obtained with the focal plane simulator. The correspondence with Fig. 3.27 is apparent. The low-energy trails of Fig. 3.27 are of course not visible here, as they arise from the correction of the multiplexing trailing (§ 3.3.2.2).

5.1.2.2 Spectral analysis

The output of the simulator was tested against the experimental data acquired with the Performance Model of the MXT Detector Assembly, whose tests were described in detail in § 3. Parameters derived from measurements, such as CTI, noise and offset, were provided to the program and a series of acquisitions were simulated to go through the same analysis pipeline as laboratory data. At the end of the analysis, the results matched the input parameters, e.g. CTI $= 2 \times 10^{-5}$.

Fig. 5.3 shows the ^{55}Fe spectrum provided by the pipeline applied to the simulated frames and it closely resembles the findings of § 3.3.2.3 (e.g. Fig. 3.27). This similarity has a twofold consequence. On the one hand, it indicates that the simulator is able to correctly reproduce experimental data. On the other hand, it confirms the findings of § 3.4.2.3, regarding the relationship between energy resolution and noise level. Indeed, even though the same ENC $= 3\,\mathrm{e^-_{rms}}$ derived in § 3.3.2.1 was used as input, the resulting spectral resolution of 146 eV is far from the 120 eV value pertaining to that noise level, corresponding instead to ENC $= 10\,\mathrm{e^-_{rms}}$. Since no additional contribution was added in the simulation, it is clear that this loss of resolution is intrinsic to

the physics of the detector, as was already established at the end of § 3.4.2.3.

5.2 Energy calibration

The energy calibration of the MXT detector during its in-orbit operation shall now be explored. As was seen in § 3, the relation between the measured signal and the energy of the incoming photons is a fundamental figure of merit of the device and being able to precisely measure it is necessary to ensure the best possible performances. If one also considers that, according to § 4, said relation is bound to degrade under the effect of space radiation, to be able to periodically and accurately assess the response gains even more importance.

In the next sections, two approaches to in-orbit calibration will be examined, i.e. by use of the radioactive source embedded in the MXT camera itself (§ 5.2.1) and by observing selected astrophysical sources (§ 5.2.2).

5.2.1 Calibration source

As first introduced in § 1.3.3.3, the Calibration Wheel Assembly, part of the MXT camera, will provide four configurations: an open position and a UV filter to perform observations of astrophysical sources, a copper shutter to protect the detector during the South Atlantic Anomaly crossings (§ 4) and a radioactive calibration source.

The fact that the source is housed on the calibration wheel implies that, when it is in use, no observation of astrophysical sources can be performed. However, this is still compatible with the scientific program of the mission if one considers that the attitude law of the SVOM satellite combined with its Low-Earth Orbit (§ 1.2.3.1) results in a 50 % duty cycle for the narrow field-of-view instruments MXT and VT. If the $13 - 17$ % dead time per orbit due to the passage through the South Atlantic Anomaly is factored in as well, one obtains that ≈ 40 min per orbit are not suitable for astrophysical observations and can therefore be dedicated to calibration.

Starting from these premises, two configurations of the radioactive source will be assessed via a series of simulations in order to identify the better one that allows to attain both high calibration accuracy and low exposure time required to achieve it, with the intention of not negatively affecting the scientific program of the mission.

After a general description of the two scenarios (§ 5.2.1.1), the description of the Monte Carlo simulations will be provided (§ 5.2.1.2), finishing with the prediction of the in-orbit performances and the selection of the configuration (§ 5.2.1.3).

5.2.1.1 Configuration

For both setups, the baseline of the source is radioactive ^{55}Fe, encased in a package behind a 250 µm beryllium window. Despite emitting spectral lines in the middle of the sensitive energy range of MXT, the isotope has the important disadvantage of a 2.737 yr half-life, which is rather short when compared to the 5 yr lifetime of the extended mission and even more so if one considers the 2.5 yr lapse between fabrication and launch. This implies that, at the end of the extended SVOM mission, a ^{55}Fe source will have only 15 % of its original activity. To this, one must also add that the source activity is limited to 1 MBq at its strongest because of export regulations to China.

Indirect illumination In the first scenario, the source is directed against a target made of aluminum and titanium, that, upon excitation by the X-ray source, emits fluorescence photons, some of which eventually reach the detector together with those coming from the source itself (Fig. 5.4). The result is the availability of at most five spectral lines for calibration purposes, which cover most of the operating energy range of MXT: 1486 eV (Al-K_α), 4509 eV (Ti-K_α), 4932 eV (Ti-K_β), 5898 eV (Mn-K_α) and 6490 eV (Mn-K_β). The main drawback of this configuration is the low rate when compared with the activity of the primary source. As a matter of facts, only a fraction of Mn photons excite the fluorescence of the target, with much lower efficiency on aluminum than titanium, and only a fraction of those secondary photons reach the detector, due to the isotropic nature of the emission. Furthermore, few X-rays from the radioactive source manage to travel to the CCD because of the geometric configuration.

The fluorescence target is composed of a 2.3 mm-diameter Ti disk surrounded by an Al ring for a total of 3.8 mm in diameter and 200 µm in thickness. The target is tilted by 45° towards the radioactive source and the MXT detector to ensure maximum illumination of the latter. The distance between the source package and the top of the target is optimized to ensure maximum

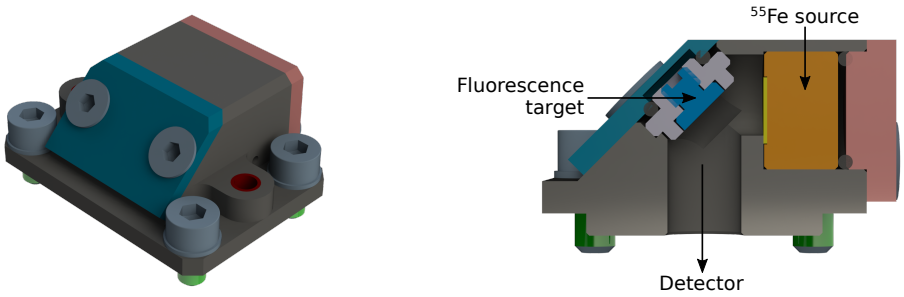

Figure 5.4 – Configuration with the radioactive ^{55}Fe source illuminating the Al–Ti fluorescence target. a) Three-dimensional view of the source holder. b) Cross-sectional view of the source holder.

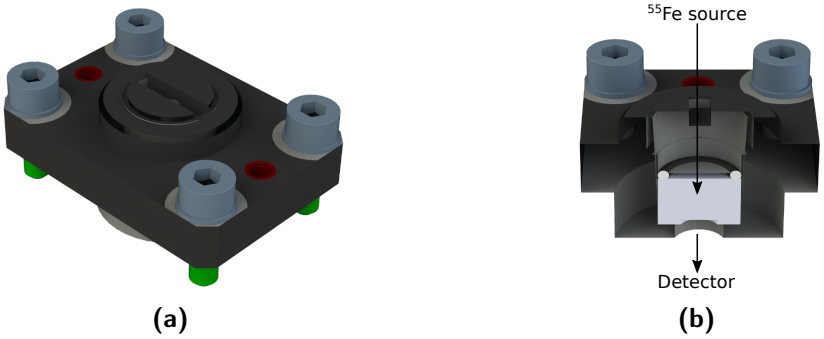

Figure 5.5 – Configuration with the radioactive ^{55}Fe source directly illuminating the detector. a) Three-dimensional view of the source holder. b) Cross-sectional view of the source holder.

fluorescence efficiency without resulting in an excessive direct illumination of the detector, that can easily outshine the spectral lines from the target.

Direct illumination An alternative approach is to expose the detector directly to the ^{55}Fe source, in order to achieve the maximum count rate given its activity (Fig. 5.5). The main disadvantage of this is of course the presence of only two spectral lines to calibrate with, i.e. the two Mn-K lines at 5898 eV and 6490 eV respectively. It is important to point out that, due to the layered interior of the shielding of the MXT Focal plane Assembly (§ 1.3.3.2), aluminum fluorescence lines from the shielding itself cannot be excited.

5.2.1.2 Monte Carlo simulations

Both designs were investigated via Geant4 Monte Carlo simulations. In case of the indirect illumination, a three-dimensional model of the source housing

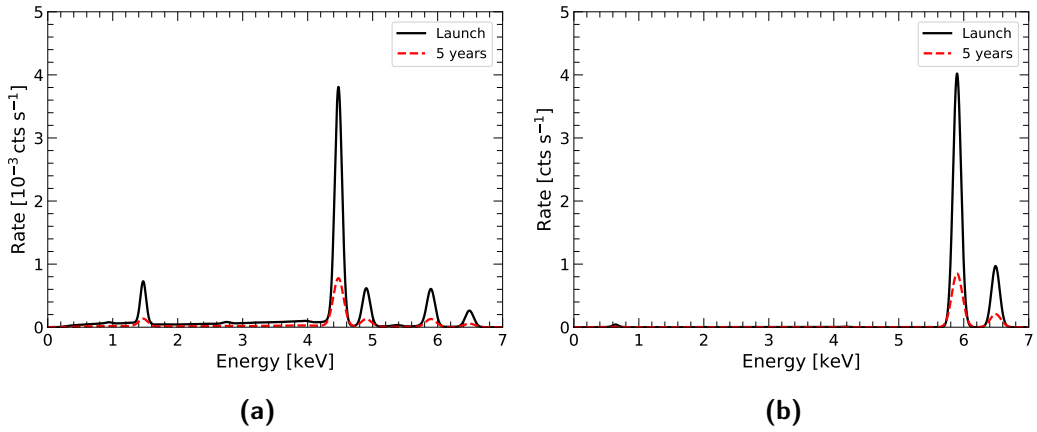

Figure 5.6 – Detector-wide spectrum of the ^{55}Fe calibration source at launch and at the end of the extended mission (pessimistic case). a) Indirect illumination via the fluorescence target. b) Direct illumination. In the second plot, the small Mn-L$_\alpha$ emission is visible at 637 eV, although in an experimental scenario this emission would be absorbed by the source packaging (not simulated in this instance). It is important to point out that the vertical axes on the two plots differ by three orders of magnitude.

was imported into the simulation and coupled with a simple silicon volume representing the detector. All distances and dimensions were kept the same as in the final MXT camera design. For the second scenario, the same model of the MXT camera as used in § 4.3.2.2 for the study of the effects of space radiation was employed.

The reason the whole camera was adopted in the latter case but not in the former is the aforementioned coating of the interior of the shielding of the MXT Focal plane Assembly (§ 1.3.3.2), which by design prevents excited Al fluorescence lines of the shielding itself from reaching the CCD. This means that the absence of any other volume apart from the calibration source and the detector in the first configuration does not affect the validity of the results, as by a spectroscopic point of view those are the only bodies which are supposed to emit lines. Moreover, any Al emission arising from uncoated bodies would be dwarfed by the aluminum fluorescence of the source target. On the other hand, since only two lines are generated by the X-ray source for the case of direct illumination, any contribution from the surrounding environment becomes important to fully assess the validity of the configuration.

Fig. 5.6 shows how the detector-wide spectrum of single counts would appear at the beginning and at the end of the mission for the two designs. For

the spectra at launch, energy resolution and low-level threshold are based on what was measured with the Performance Model (PM) of the MXT Detector Assembly (§ 3.3), i.e. ENC = $10\,e^-_{rms}$ and $E_{thr} = 40\,eV$. For the end of the mission, pessimistic values of ENC = $18\,e^-_{rms}$ (Fig. 4.29b, corresponding to FWHM (1486 eV) = 160 electronvolt) and $E_{thr} = 200\,eV$ (Fig. 4.27) were taken.

The count rate is also based on the PM tests with ^{55}Fe. The flux of the $\approx 1\,MBq$ laboratory source was calculated from cumulative maps such as Fig. 3.19 and then used to rescale the output of the Monte Carlo simulations[2]. To take into account the decay of the radio-isotope, the activity of the laboratory source was supposed the same as that of the MXT source two years before launch. Furthermore, the transmission of the on-chip filter was considered (Fig. 2.24).

The fraction of single counts out of the total of incoming photons was calculated thanks to the curves derived in § 5.1.2.1 from the focal plane simulator, which provide the multiplicity as a function of energy for a given threshold E_{thr}.

From Fig. 5.6 one finds that, as expected, five spectral lines at most are available for calibration in case the fluorescence target is present, whereas only two are visible in the second case.

Fig. 5.7 and Fig. 5.8 instead show the spatial distribution of photons interacting with the detector. In both configurations, the flux is uniform, even when separate energy bands are considered, as in Fig. 5.7. This means that one can expect all columns and rows of the matrix to receive roughly the same amount of photons, which facilitates the calibration of the whole CCD.

It is worth underlining how striking the difference is in the count rate in the two scenarios, with the presence of more spectral lines due to indirect illumination coming at the expense of a flux loss of more than two orders of magnitude.

5.2.1.3 Estimated performances and acquisition time

Before being able to estimate the calibration time of the MXT detector via the radioactive source in the two scenarios under consideration, one must

[2]The laboratory source had not been calibrated before delivery therefore its flux, which is affected by factors such as packaging, was not known beforehand.

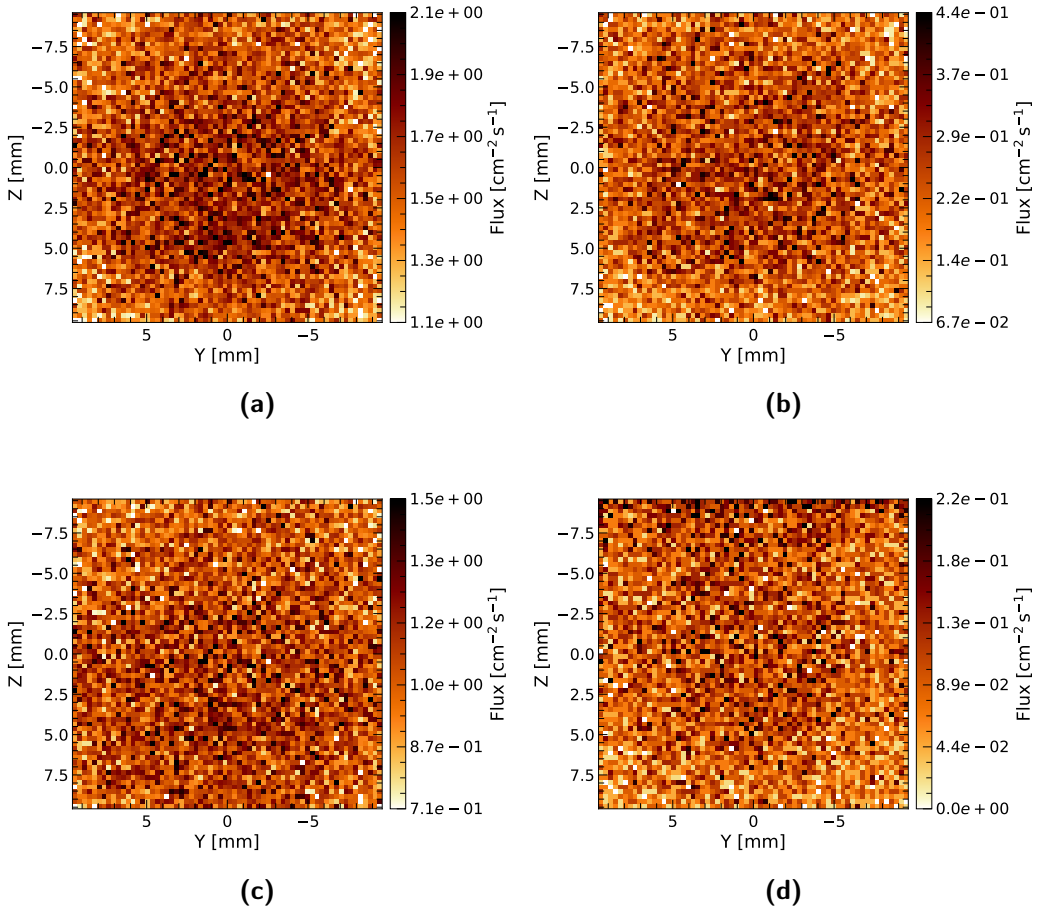

Figure 5.7 – Hit map in the case of indirect illumination via the fluorescence target. a) $0-10\,\mathrm{keV}$. b) Al line. c) Ti lines. d) Mn lines.

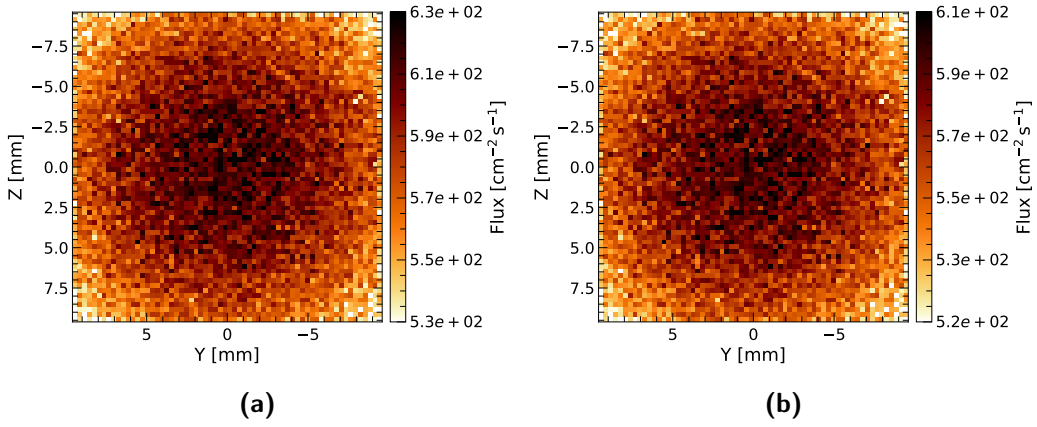

Figure 5.8 – Hit map in the case of direct illumination. a) $0-10\,\mathrm{keV}$. b) Mn lines.

determine the minimum amount of photons needed for an accurate calibration. This is of course dependent on both the shape of the spectrum (number of spectral lines, resolution, background) and the algorithms used for the calculations. Since the codes that will be employed to analyze the scientific data of MXT during the SVOM mission are not available, the study relies on the ones developed for the laboratory tests of the Engineering and Performance Models of the MXT detector, described in detail in § 3.1.

Because of the modularity of the analysis (it constructs line-by-line and row-by-row spectra), I operated on a single spectrum, to be intended as a single column or row, instead of the whole detector. Photons extracted from either of the two simulated energy distributions of Fig. 5.6 were converted to ADU by imposing a fixed gain (and zero offset). The analysis algorithm was then applied to calibrate the data and the accuracy of the fitted line centers was evaluated as a function of the number of generated photons N_γ. For each N_γ, $N_{\rm rep}$ repetitions were carried out, i.e. N_γ photons were extracted $N_{\rm rep}$ times, to assess the uncertainties. Based on the predictions of the energy resolution of the detector during the mission lifetime that were presented in § 4.4.1.3 (Fig. 4.29), the analysis was limited to the ENC $= 10\,{\rm e}^-_{\rm rms}$ case measured in laboratory, since the performances are not predicted to change significantly as long as the detector is kept sufficiently cold. The fact that the primary spectrum was supposed to consist of single counts only does not really influences the shape of the spectrum itself (line ratios), apart from its resolution, at the energies of interest. Finally, it is important to notice that CTI was not included nor estimated in the simulations. The accuracy of the line centers is however relevant for the calculation of the CTI as well, as the latter requires a fit on the line centers as a function of the number of transfers in the CCD (§ 3.1.2.2).

Fig. 5.9 shows the calibration error for the three main spectral lines (Al-K$_\alpha$, Ti-K$_\alpha$ and Mn-K$_\alpha$) of the configuration with the fluorescence target, whereas Fig. 5.10 shows the equivalent plots in the case of the two Mn lines for direct exposure. All the plots are expressed as functions of the height of the Mn-K$_\alpha$ rather than the total number of counts in the spectrum. This implies that they continue to be representative even if the resolution changes significantly compared to the one used in the simulations (e.g. if multiple counts are considered instead of singles) or if a background source is added, provided that the ratios of the spectral lines stay the same.

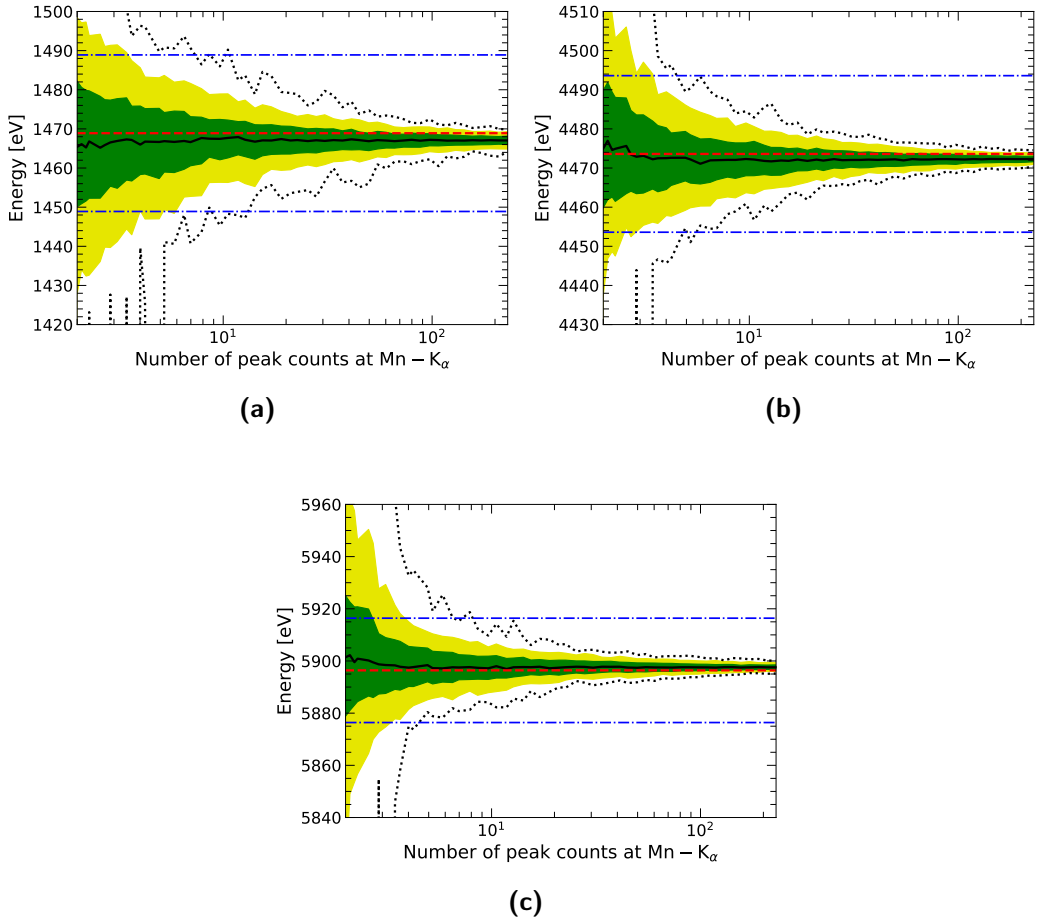

Figure 5.9 – Calibration error as a function of the height of the Mn-K_α line for the case of indirect illumination via the fluorescence target. a) 1486 eV (Al-K_α). b) 4509 eV (Ti-K_α). c) 5898 eV (Mn-K_α). In all the cases, the solid black curve represents the median, while the inner green (outer yellow) region indicates where 64 % (95 %) of the results lie. The black dotted curves identify the 99 % interval. The ±20 eV requirement is marked by the blue dash-dotted lines. The red dashed line corresponds to the true line energy.

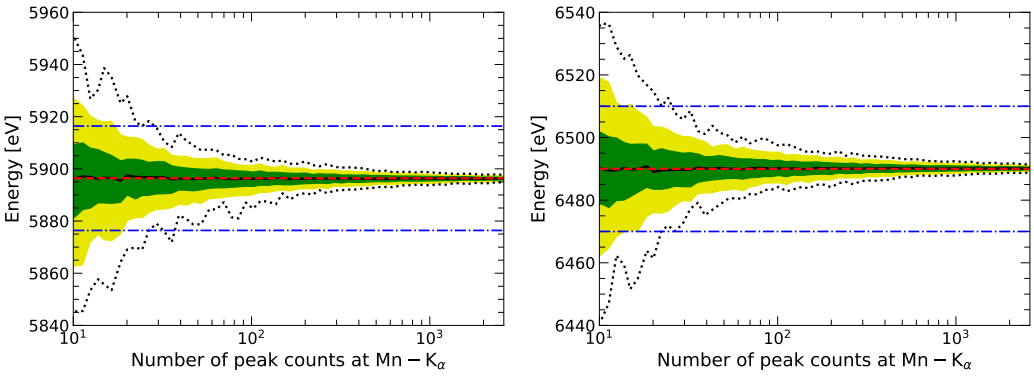

Figure 5.10 – Calibration error as a function of the height of the Mn-K$_\alpha$ line for the case of direct illumination. a) 5898 eV (Mn-K$_\alpha$). b) 6490 eV (Mn-K$_\beta$). In both cases, the solid black curve represents the median, while the inner green (outer yellow) region indicates where 68 % (95 %) of the results lie. The black dotted curves identify the 99 % interval. The ±20 eV requirement is marked by the blue dash-dotted lines. The red dashed line corresponds to the true line energy.

Table 5.1 – Estimated calibration time for the two source configurations (indirect illumination via the fluorescence target and direct exposure to the ^{55}Fe radionuclide) at the beginning and end of the mission. The number of orbits is calculated by supposing ≈ 40 min per orbit can be dedicated to calibration. The 5 year scenario is based on the pessimistic case of ENC = 18 e^-_{rms} and E_{thr} = 200 eV, although the result is mainly dependent on the decay of the ^{55}Fe.

Configuration	Launch		5 years	
	ks	orbits	ks	orbits
Indirect	3.7×10^3	1.5×10^3	20×10^3	8×10^3
Direct	2.6	1.1	12	5

The mission specifications require the energy scale to be correct within 20 eV over the entire detector. The minimum height of the Mn-K_α line for the deviation to be smaller than 20 eV at least 99 % of the time is around 10 counts (respectively 40 counts) per spectrum (i.e. per detector row/column) for the indirect (respectively direct) illumination. One can then derive an estimate for the calibration time if the value is compared to the detector-wide spectra of Fig. 5.6. Results are listed in Tab. 5.1.

From the estimates in Tab. 5.1 it is apparent that the only viable configuration is the one in which the detector is directly illuminated by the ^{55}Fe source, as the other case would require a huge amount of calibration time. It is worth stating that, had the activity of the radioisotope not been restricted to just 1 MBq, the conclusions would have been reversed, since the availability of spectral lines across the entire operating energy range of the telescope would have been more valuable that a reduced calibration time.

5.2.2 Astrophysical sources

If using a fluorescent target is not a realistic option, then a major drawback of the radioactive source on the Calibration Wheel Assembly has to be addressed: it does not provide any spectral line in the range of maximum sensitivity of the telescope, i.e. around 1.5 keV (Fig. 5.15). One may therefore turn the attention to astrophysical sources for low-energy calibration.

In the following, a suitable astrophysical source shall be selected for this task (§ 5.2.2.1) and then the expected resulting performances, such as the required calibration time, shall be assessed.

5.2.2.1 Target selection

In order to be usable for the purposes of spectral calibration, an astrophysical source should fulfill two requirements: it should have a stable flux so that varying results of the calibration process would only depend on the evolution of the instrument performances, and it should have enough *resolvable* spectral lines (more than two in practice) to allow calibration itself. Supernova Remnants satisfy both the aforementioned criteria.

Supernova Remnants (SNRs), as their name suggest, are the leftover of supernova explosions. The structure of a SNR can be very roughly schematized as a hot ($kT \approx 1$ keV) sphere of gas expanding at supersonic speeds into the

surrounding interstellar medium. As a consequence, its emission is composed of a continuum produced by the ionized gas and the shock along with emission lines generated by recombining atoms in the inner portion of the SNR. Since they can extend across several parsecs and their emission can be influenced only by their central neutron star (if present), SNRs are usually characterized by a stable flux.

In this context, I decided to focus on 1E 0102.2-7219, a SNR in the Small Magellanic Cloud and also the strongest soft X-ray source in that galaxy. 1E 0102.2-7219 is listed as one of the astrophysical sources used for the routine gain, offset and CTI calibration of the EPIC instruments on board ESA's XMM-Newton (Smith, M. J. S., 2017): this fact is appealing due to the already discussed similarities between the MXT detector and XMM/EPIC-pn. With an angular diameter of 44 arcsec, 1E 0102.2-7219 is a point-like source for MXT, although the PSF of the instrument will widen its image on the detector, causing many pixels to be hit by photons in a single exposure, which facilitates the calibration process, as the latter requires several (ideally all) CCD columns and rows to contain counts.

In the following, the analysis will be limited to this single astrophysical source because it is the most intense in the aforementioned list (compared with e.g. Tycho SNR or Cas-A), an important feature if the difference in the effective areas between the two telescopes is taken into account, i.e. $23\,\mathrm{cm}^2$ ($57\,\mathrm{cm}^2$) at 1 keV for the central spot (central spot and cross-arms) of MXT's PSF against $> 1000\,\mathrm{cm}^2$ for XMM/EPIC-pn.

5.2.2.2 Estimated performances and acquisition time

The emission of 1E 0102.2-7219 was modeled after the XSPEC spectrum provided by Plucinsky et al. (2017) and developed after a cross-calibration study involving the instruments on board Chandra, Suzaku, Swift and XMM-Newton, carried out within the framework of the International Astronomical Consortium for High Energy Calibration (IACHEC).

Fig. 5.11 shows the spectrum MXT should measure at the beginning and at the end of the mission once the effective area of the instrument and the energy resolution are taken into account. The spectrum is composed of single counts exclusively. For the spectrum at the end of the mission, the same pessimistic case as in § 5.2.1 was considered, i.e. ENC $= 18\,\mathrm{e}^-_{\mathrm{rms}}$ and $E_{\mathrm{thr}} = 200\,\mathrm{eV}$. It

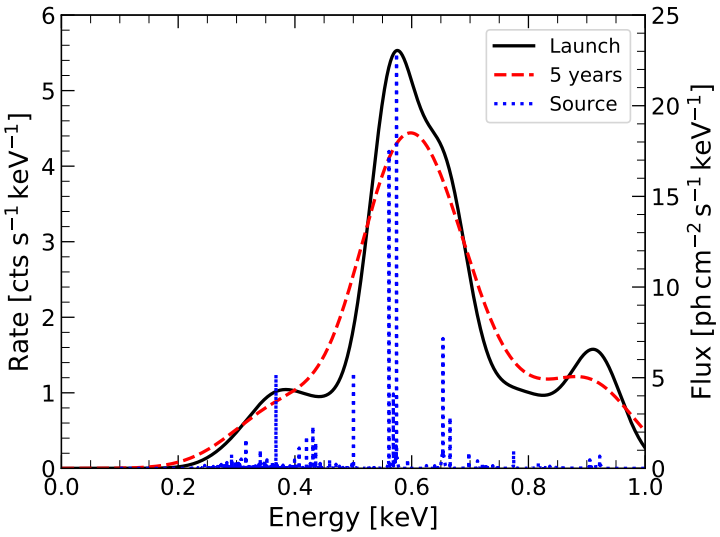

Figure 5.11 – Simulated spectrum of 1E 0102.2-7219 as seen by MXT at the beginning and end of the mission, compared to the model of the source flux. The 5 year scenario is based on the pessimistic case of ENC = 18 e^-_{rms} and E_{thr} = 200 eV.

is evident that, despite the fifty-two spectral lines included in the model, at most only three structures are really usable for calibration in the measured spectrum at the mission start, and two at most at the end in the pessimistic scenario. Furthermore, each line arises as a combination of many spectral features, implying that the reference energies are not easily determined either. Those facts imply that the use of this astrophysical source is somewhat limited and also dependent on the mission lifetime.

In order to assess the time required for a successful calibration, the same procedure described in § 5.2.1.3 was followed once more: N_γ photons were drawn from the spectrum at the start of the mission (Fig. 5.11) and the centers of the fitted spectral lines were studied as functions of N_γ itself; the procedure was repeated N_{rep} times for uncertainty estimation. Once again, one should be reminded that only the source was considered in the simulation, as no background (astrophysical or otherwise) was included. As for the validity of the chosen spectrum during the mission lifetime, § 4.4.1 suggests that a large degradation should not be expected, as far as low-level threshold and energy resolution are concerned, and as long as the detector is kept at sufficiently low temperature. The pessimistic scenario of Fig. 5.11 shall be dealt with at the end of the section. A final point to be stressed is the fact that CTI was not

included in the calculations.

Fig. 5.12 shows the relative deviation from the expected center of each line as a function of the total number of simulated events. One can see that after accumulating $\approx 10^4$ counts, the centers of two out of the three available lines can be identified with an accuracy better than 20 eV for about 99 % of the cases, which satisfies the calibration requirement.

Unlike the scenario with the ^{55}Fe calibration source, in this case photons are focused by the optics and therefore the pixel-by-pixel rate changes across the detector, meaning that the minimum required number of counts is achieved at different times in different locations. To address this point, the PSF given in Fig. 1.20b is used. Although it is only proper to 1.49 keV, this is the only one available for calculations and it will therefore be used for all photons in the $0.2 - 1$ keV range. With this caveat, the resulting pixel-by-pixel rate is shown in Fig. 5.13a.

Since the calibration algorithm requires the gathering of pixels according to their column and row (§ 3.1), one can consider the integral of Fig. 5.13a along each axis, represented in Fig. 5.13b. The focusing effect by the optics causes the rate to vary by a factor of 20 between the peak and the wings of the distribution, implying that more than 6×10^6 s are needed for the even the columns and rows lying the farthest from the central spot of the PSF to accumulate enough counts to ensure a successful calibration. This is particularly troubling if one takes into account that the calculation of the CTI (§ 3.1.2.2) is most effectively determined by the top and bottom rows.

This issue can be alleviated by multiple observations, with the image of the target placed at each time in different locations of the focal plane instead of the center. In a scenario such as the one represented in Fig. 5.14a, the source is focused at the centers of two opposite quadrants, one consequence being that photons are concentrated at the top and bottom of the CCD, which, as stated earlier, helps with the CTI fit. If the rate per column/row is considered (Fig. 5.14b), this configuration requires a total exposure time of ≈ 1800 ks, or two ≈ 900 ks observations. Of course, a larger number of observations of various lengths may be envisaged to achieve a more uniform photon distribution across the matrix.

It is worth mentioning that the previous discussion retains its value even in the pessimistic scenario at the end of the mission (ENC $= 18\,\mathrm{e}^-_{\mathrm{rms}}$ and $E_{\mathrm{thr}} = 200$ eV), although in that case calibration will be more difficult due to

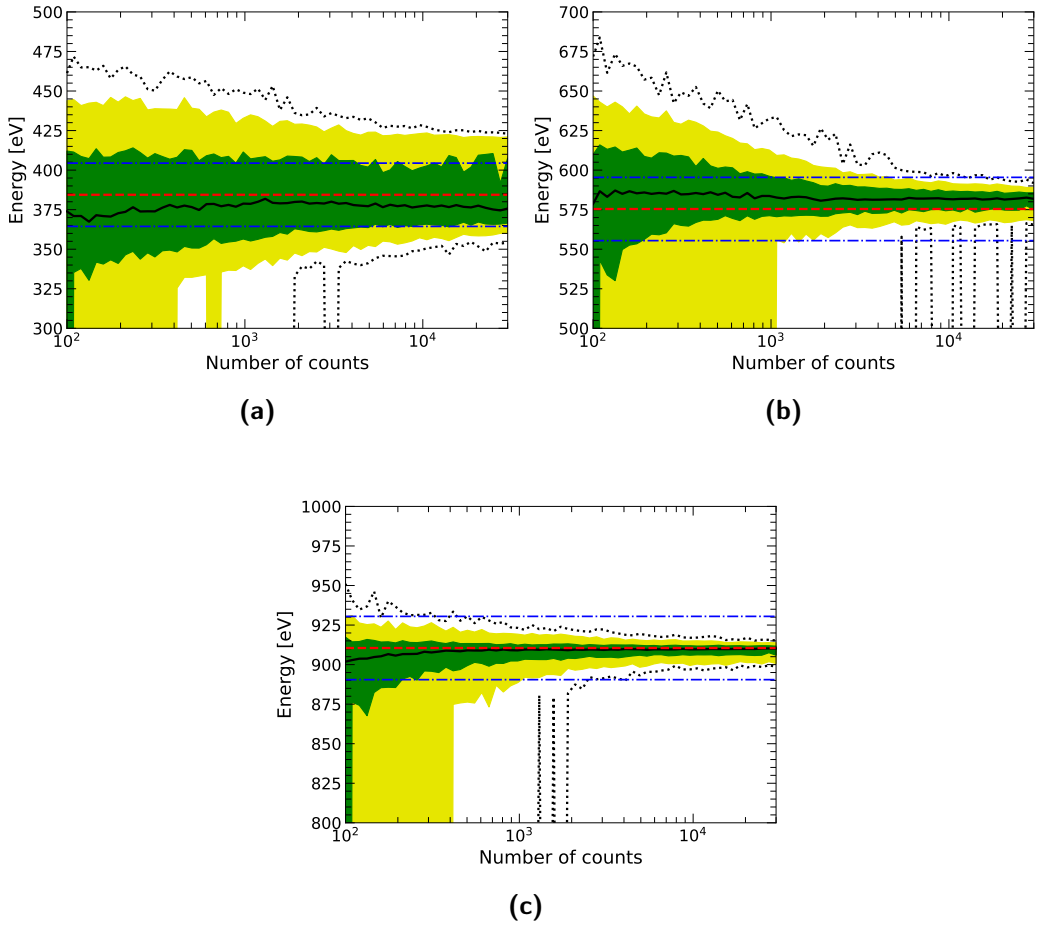

Figure 5.12 – Calibration error as a function of the number of simulated single counts from the spectrum of 1E 0102.2-7219 at the beginning of the mission. a) 384 eV. b) 575 eV. c) 910 eV. In all the cases, the solid black curve represents the median, while the inner green (outer yellow) region indicates where 68 % (95 %) of the results lie. The black dotted curves identify the 99 % interval. The ±20 eV requirement is marked by the blue dash-dotted lines. The red dashed line corresponds to the true line energy.

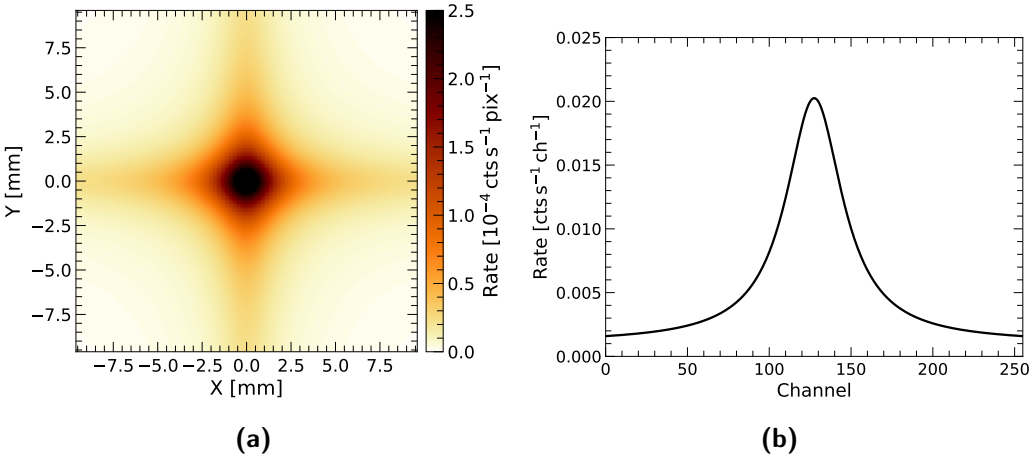

Figure 5.13 – Rate distribution across the detector during an observation of 1E 0102.2-7219. a) Pixel-by-pixel rate. b) Column-by-column or row-by-row rate, i.e. the integral along one CCD dimension.

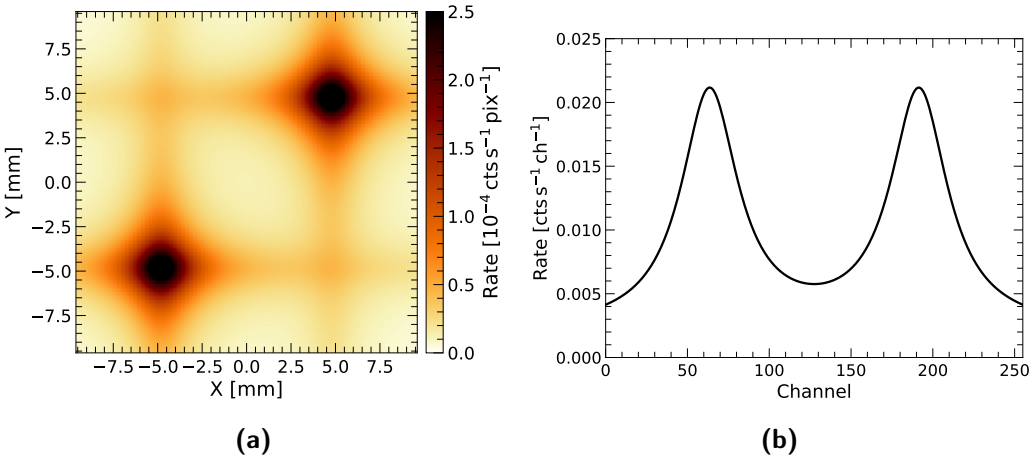

Figure 5.14 – Rate distribution across the detector for two observations of 1E 0102.2-7219 in which the image of the source is placed in opposite quadrants of the CCD. a) Pixel-by-pixel rate. b) Column-by-column or row-by-row rate, i.e. the integral along one CCD dimension.

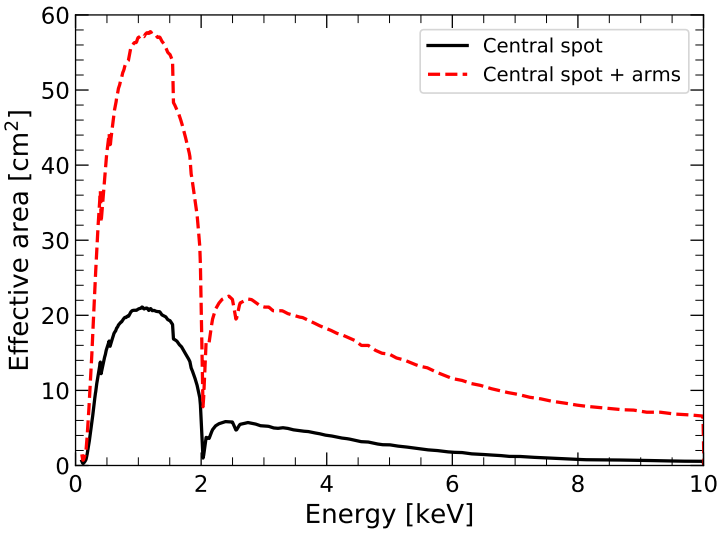

Figure 5.15 – Simulated effective area of the MXT optics. The two curves correspond to the case in which only the central spot is considered or the spot along with the cross-arms. This is the same plot as Fig. 1.24.

the further degradation of the available spectral lines.

5.3 Flux calibration

The effective area of MXT as a function of energy (visible in its simulated form in Fig. 5.15) is a fundamental piece of information for the measurement of the flux of astrophysical sources during observations. It is defined by two contributions: the energy-dependent collecting area of the optics and the quantum efficiency of the detector at the focal plane. When positioned along the optical axis, the UV filter (§ 1.3.3.3) also contributes to the overall effective area. A successful calibration demands measurements to be performed with a source with known flux, so that the total response can be inferred from the output.

In the following sections, the planned approaches to the flux calibration of MXT shall be reviewed and also some more suggested for both before the start of the mission (§ 5.3.1) and during in-orbit operation (§ 5.3.2).

5.3.1 On-ground flux calibration

Within the scope of the ground tests before the delivery of the telescope, MXT will undergo full characterization of its energy-dependent efficiency at PANTER (§ 5.3.1.1). However, such a campaign involves some serious drawbacks, which will be discussed in the following sections along with some possible solutions (§ 5.3.1.2).

5.3.1.1 PANTER

According to the mission plan, MXT will be subject to an on-ground calibration campaign at the PANTER X-ray test facility in Neuried (south-west of Munich), Germany. Part of the Max Planck Institute for Extraterrestrial Physics, PANTER (Freyberg et al., 2005; PANTER, 2019) is primarily involved in the characterization of X-ray telescopes, notable examples being ROSAT, EXOSAT, BeppoSAX, XMM-Newton, Swift, Suzaku and eROSITA. With its 1 m-diameter vacuum tube stretching for 130 m between its X-ray source at one end and the 12 m-long 3.5 m-diameter main test chamber at the other, this structure is superseded in size only by NASA's X-ray test facility in Huntsville, (AL, USA).

The facility At PANTER X-rays are generated by a 1 mm-wide filament, whose apparent size is 1 arcsec at the end of the tube. In combination with fluorescence targets, the source can produce 19 separate spectral lines between 0.18 keV (B-K) and 22.16 keV (Ag-K) as well as Bremsstrahlung continuum. Filters can be used to suppress selected portions of the spectra, e.g. continuum and/or K_β lines. The resulting beam is uniform across a 1 m-diameter, although corrections have to be taken into account due to the finite distance between the source and the test chamber. The detector available for measurements at the focal plane of any telescope under measurement is an eROSITA-like pnCCD named TRoPIC (Freyberg et al., 2008).

Planned tests and related issues As anticipated, MXT's optical system will undergo X-ray characterization at PANTER, which will allow to measure its energy-dependent collecting area. Moreover, a second campaign with the full telescope will be performed for alignment purposes. However, due to technical reasons, it will not be possible to carry out X-ray reference measurements

with the TRoPIC camera to measure the absolute incident flux. This implies that the complete effective area of the telescope will not be readily available: instead, relative measurements taken in the two campaigns will have to be combined into the final effective area of the telescope.

5.3.1.2 SOLEX and SOLEIL

Since the knowledge of the Quantum Efficiency of the MXT detector depends mostly on the characterization of its various absorption edges (Fig. 2.24), a facility such as PANTER is not fully adapted for the task, as its emission is mainly composed of isolated spectral lines. On the contrary, a continuous emission is preferred, such as that provided by SOLEX and SOLEIL.

SOLEX Thanks to an X-ray tube coupled with one of many different anodes, the *Source Of Low-Energy X-rays* or SOLEX (Ménesguen & Lépy, 2012) generates an X-ray continuum along with the characteristic spectral lines of the anode being used. A crystal may be inserted in the system to act as a Bragg diffractor, thus selecting a portion of the emitted spectrum via Bragg's rule

$$n\lambda = 2d\,(1 - T)\sin\theta, \tag{5.4}$$

where n and θ are the order and angle of reflection, λ the wavelength of the reflected photons, d the lattice spacing of the diffractor and T a correction due to the refractive index of the material. Various materials with different lattice parameters may be chosen to select different spectral regions. The λ-θ relation is calibrated based on the characteristic fluorescence spectral lines of the X-ray tube anodes. Before reaching the detector under test, the incoming photon beam is split so that a portion of it reaches a gaseous proportional counter which ensures flux monitoring and calibration at all times.

The system is able to provide a calibrated monochromatic X-ray beam in the $0.6 - 28\,\mathrm{keV}$ range[3] with an energy dispersion of $1 - 10\,\mathrm{eV}$. Typical photon rates are $\sim 10^3\,\mathrm{cts\,s^{-1}}$ over a spot stretching from 6 mm to 10 mm in diameter depending on the distance between source and detector.

[3]The efficiency of the reference detector drops sharply at $\lesssim 2\,\mathrm{keV}$ and decreases below 10 % above $\approx 10\,\mathrm{keV}$.

SOLEIL SOLEIL, acronym for *Source Optimisée de Lumière d'Énergie Intermédiaire du LURE* (SOLEIL, 2019), is an electron-synchrotron capable of generating high-luminosity polarized photon beams with energies spanning from infrared light ($\sim$ µeV) to hard X-rays ($\sim$ 100 keV). Among the many available lines, the interesting one for the purpose of testing the QE of the MXT detector is the UV/soft X-ray line.

This line delivers photons whose energy can be chosen continuously between 40 eV and 1.8 keV, with < 1 eV precision. A $10^8 - 10^{11}$ ph s^{-1} nominal rate is projected over a spot measuring 100 µm $\times$ 200 µm (FWHM) with a 1 mrad-divergence. The possibility of de-focusing the beam along one direction and the use of additional attenuators between source and detector allow to reduce the incoming flux in order to limit pile-up.

Discussion Of the two facilities discussed above, SOLEIL is certainly the better one for measuring the low-energy QE of the MXT pnCCD, which is predicted to present most of its structures in the energy range of the UV/soft X-ray line at the synchrotron (Fig. 2.24). Indeed, the characterization of the UV filter to be mounted on the Calibration Wheel Assembly (§ 1.3.3.3) was already carried out there.

Due to the timescales of a proposal, however, a calibration campaign at SOLEIL might not be compatible with the mission schedule. In a scenario like that, the more accessible SOLEX would represent a viable solution, aided by the fact that the low photon flux limits pile-up.

It is worth noting that, whichever the case, tests conducted in any of those facilities would require to scan the detector across both its axes, because of the limited size of the light spot. This was indeed the reason behind the inclusion of the two orthogonal micrometric sliding tables inside the cryostat designed for MXT FPA testing (§ 3.3.1).

5.3.2 In-orbit flux calibration

Because of the impossibility to carry out a flux calibration of the complete detection system (optics and detector together), it will be mandatory to perform in-orbit measurements on astrophysical sources of known flux.

This will be the object of the next sections, where the selection of suitable targets for the task will be carried out (§ 5.3.2.1), along with the quantification

of the expected performances (§ 5.3.2.2) and, most importantly, the evaluation of the observation time necessary to achieve accurate results (§ 5.3.2.3).

5.3.2.1 Target selection

Contrary to the optical band, the X-ray sky lacks proper *standard candles* that can be used for calibration purposes, because the X-ray emission of astrophysical sources is usually much more variable than in the optical regime. For this reason, as previously discussed in § 5.2.2.1, suitable targets are usually drawn from among Supernova Remnants (and also clusters of galaxies) which are supposed not to vary on human timescales.

This analysis is limited to two strong X-ray sources, i.e. the Active Galactic Nucleus 3C273 and the Crab Nebula. Both of them are known to have time-variable emissions, but also possess several important advantages: they are strong X-ray emitters, meaning that they can ensure good accuracy even after relative short observations; they feature broadband spectra that cover the entire operating range of MXT; they have been (and continue to be) the object of many multi-mission cross-calibration studies, implying that up-to-date information relative to their flux and spectral properties are always available. To further support the target choice, both sources are featured in the documentation of the routine calibration of ESA's XMM-Newton (Smith, M. J. S., 2017).

It is worth noting that flux measurements are also relevant for the inter-calibration between MXT and ECLAIRs. According to the performance specifications, the accuracy of flux estimates between the two instruments shall be accurate at a level better than 10 % (to be confirmed) at the end of the Performance Verification phase. Over the same energy range the spectral slope of sources described by a single power law model (such as the ones under consideration here) shall be in agreement among the two instruments to better than 5 %.

3C273 3C273 (Courvoisier, 1998) is the brightest Active Galactic Nucleus (AGN) in the sky and, at $z = 0.158$, also the nearest. It is classified as a radio-loud quasar and presents a jet moving away from the center at apparently superluminal velocities. Due to its proximity and ease of observation (it is close to the celestial equator and therefore accessible to any location on

Earth, depending on the time) it has been studied extensively across the entire electromagnetic spectrum. Its X-ray emission ($2\,\mathrm{keV} - 1\,\mathrm{MeV}$) is well described by a power law and features both flux and spectral variations (the same its true at other wavelengths), the spectral index changing from $\Gamma \sim 1.5$ in the 1980s to $\Gamma \sim 1.82$ in 2003. Since then, a value of $\Gamma \sim 1.6 - 1.7$ has been measured. Like other AGNs, 3C273 may present a soft X-ray excess below $\sim 2\,\mathrm{keV}$.

Crab Nebula The Crab Nebula was first optically discovered by Chinese astronomers in 1054 and identified as one of the strongest X-ray sources in the sky since the birth of X-ray astronomy. Being the remnant of a supernova explosion, it is composed of a pulsar surrounded by a nebula extending across approximately four light years in diameter. This implies that flux and spectral variations, initiated for instance by electron injection by the central pulsar, should occur on relative long timescales, since most of the emission comes from the diffused nebula. Indeed, such variations have been observed in hard X-rays and γ-rays (for a short review, see Wilson-Hodge et al., 2011). In the (soft) X-ray regime, the Crab spectrum is well modeled by an absorbed power law.

5.3.2.2 Simulation

This study is based on the multi-mission cross-calibration carried out by Madsen et al. (2017) for 3C273 and by Kirsch et al. (2005) for the Crab Nebula. In both cases, the models representing the source emission were the best fits on XMM/EPIC-pn data, which were chosen due to the similarity between EPIC-pn's and MXT's detectors. Both papers carried out their analyses through XSPEC, but their results were here translated into Python, the proper fitting routine being based on the `sherpa` package. Except for the different implementation, the spectral models of the two sources retained their original expressions, i.e. `cflux` $\times$ `tbabs` $\times$ `pow` for 3C273 and `phabs` $\times$ `pow` for the Crab Nebula[4]. In both cases, Wilms abundances (Wilms et al., 2000) and Verner cross-sections (Verner et al., 1996) were chosen. For 3C273, the $1 - 5\,\mathrm{keV}$ energy range was used, whereas the $0.3 - 10\,\mathrm{keV}$ interval was chosen for the Crab Nebula. The sources models are presented in Fig. 5.16 and Tab. 5.2.

The best fit spectra from the papers were combined with the (simulated)

[4]XSPEC models are described at `https://heasarc.gsfc.nasa.gov/xanadu/xspec/manual/Models.html`.

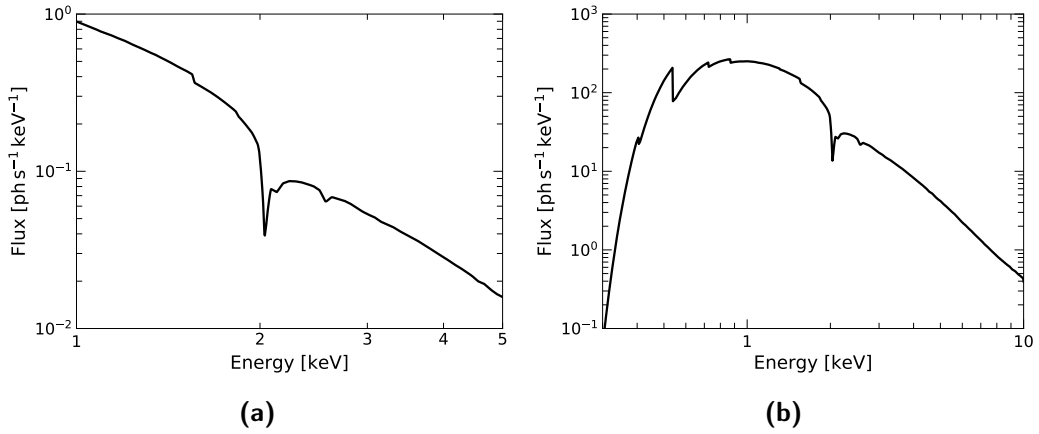

Figure 5.16 – Primary source spectra as measured by MXT. a) 3C273. b) The Crab Nebula.

Table 5.2 – Parameters of the primary source spectra. Values for 3C273 are taken from Madsen et al. (2017), while those for the Crab Nebula from Kirsch et al. (2005).

Source	Paramter	Value
3C273	Energy flux	$(53.90 \pm 0.34) \times 10^{-12}\,\mathrm{erg\,cm^{-2}\,s^{-1}}$
	Spectral index	1.69 ± 0.01
	Column density	$1.79 \times 10^{22}\,\mathrm{cm^{-2}}$ (fixed)
Crab	Normalization	$(8.80 \pm 0.04)\,\mathrm{ph\,cm^{-2}\,s^{-1}\,keV^{-1}}$
	Spectral index	2.130 ± 0.003
	Column density	$(0.408 \pm 0.020) \times 10^{22}\,\mathrm{cm^{-2}}$

effective area of MXT of Fig. 5.15 (central spot and cross arms) and used to generate photon lists corresponding to several observation time lengths, the number of photons drawn in each time interval following a Poisson distribution. The photons were binned (hereafter referred to as *experimental spectra*) and fitted with their respective reference model. The sought parameters were the integral flux and the spectral index in case of 3C273 (the column density $n_{\mathrm{H}} = 1.79 \times 10^{20}\,\mathrm{cm^{-2}}$ was fixed as in Madsen et al. (2017)), and the normalization, the spectral index and the column density in the case of the Crab.

It is worth noting that the analysis was not restricted to single counts (contrary to § 5.2.2), so the full intensity of the spectrum was used each time and not a fraction of it. However, since energy resolution was not factored in the instrument response, which was limited to the effective area of the telescope, a coarse enough energy binning of the experimental spectra was

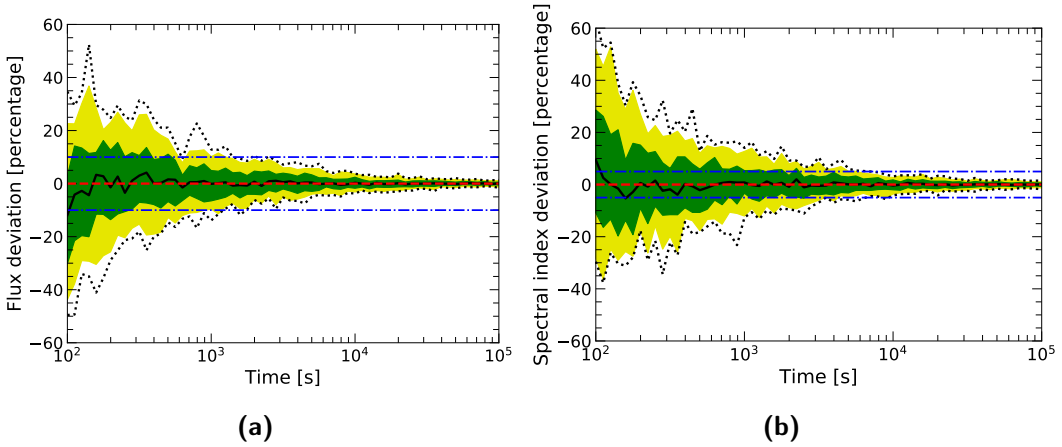

Figure 5.17 – Relative deviation from the spectral parameters for 3C273. a Energy flux. b) Spectral index. In both cases, the solid black curve represents the median, while the inner green (outer yellow) region indicates where 68 % (95 %) of the results lie. The black dotted curves identify the 99 % interval. The blue dash-dotted lines mark the ±10 % interval around the expected flux and the ±5 % interval around the expected spectral index. The red dashed line corresponds to no deviation.

chosen in order to smear out all the visible features (mainly absorption edges) of the source emissions. Furthermore, only the photons from the target sources were simulated: no background (astrophysical or otherwise) was included.

For each time step, several runs were carried out to assess the uncertainty. The results were compared to the reference values with the goal of identifying the smallest possible exposure to obtain reliable results. Since the performance requirements are based on the flux, the latter was added to the results for the Crab Nebula, although it was not used a a fit parameter.

5.3.2.3 Estimated performances

Fig. 5.17 and 5.18 show, for each estimated parameter P_{est}, the relative deviation from the reference value P_{ref}, calculated as $(P_{\mathrm{est}} - P_{\mathrm{ref}})/P_{\mathrm{ref}}$. The deviation is represented as a function of the observation time. The performance specifications require the calculated flux to be within 10 % of the reference models as well as of the corresponding value obtained by ECLAIRs. In addition, the estimates of the spectral index ought to agree within 5 % for sources modeled by simple power-law, e.g. the two targets under study.

For 3C273, the fitted flux is within 10 % from the input value at least 95 % of the times for $t > 2$ ks. The spectral index instead deviates < 5 % of the

times by less than 5 % from the reference if $t > 10$ ks. For the Crab Nebula, both the flux and the spectral index are always within 3 % for observations longer than 100 s.

The previous results give some timescales for the case in which the instrument response is known while the spectral parameters are to be calculated. In an in-orbit flux calibration scenario, the reverse can be considered, with the effective area being adjusted to improve the match between the measured source parameters and the expected values. Observations of similar duration to the ones simulated are supposed provide similar accuracy even in this reversed scenario. As already stated, the practice of estimating the total effective area of the optical system by astrophysical observations is helped by the fact that both sources examined here are routinely objects of cross-calibration studies by missions like XMM, Swift/XRT, Chandra and Suzaku. Such studies constituted indeed the basis of this analysis.

5.4 Multi-energy instrument response

In § 3.3 were reported the links between the spectral response of the Performance Model of the MXT detector and several experimental parameters, such as temperature and operating voltages. However, since the tests were based on radioactive ^{55}Fe spectroscopy, it was impossible to truly assess the dependence of the performances on the photon energy, since only ≈ 6 keV photons were available.

In the following sections, how the detector response varies with the energy shall be assessed by means of a new experimental setup based on an X-ray tube system (§ 5.4.1). Thanks to the new available data, the topic of energy calibration shall be expanded upon, delving into the problem of the linearity of the response and in-orbit calibration (§ 5.4.2). Finally, the dependence of the Charge Transfer Inefficiency on the photon energy will be evaluated (§ 5.4.3).

5.4.1 Experimental setup, data acquisition and analysis

The multi-energy response of the Performance Model of MXT was investigated using the same setup as described in § 3.3.1, the only difference being the X-ray source. For the occasion, the ^{55}Fe radioisotope was substituted with an X-ray generator, whose outline is provided in Fig. 5.19.

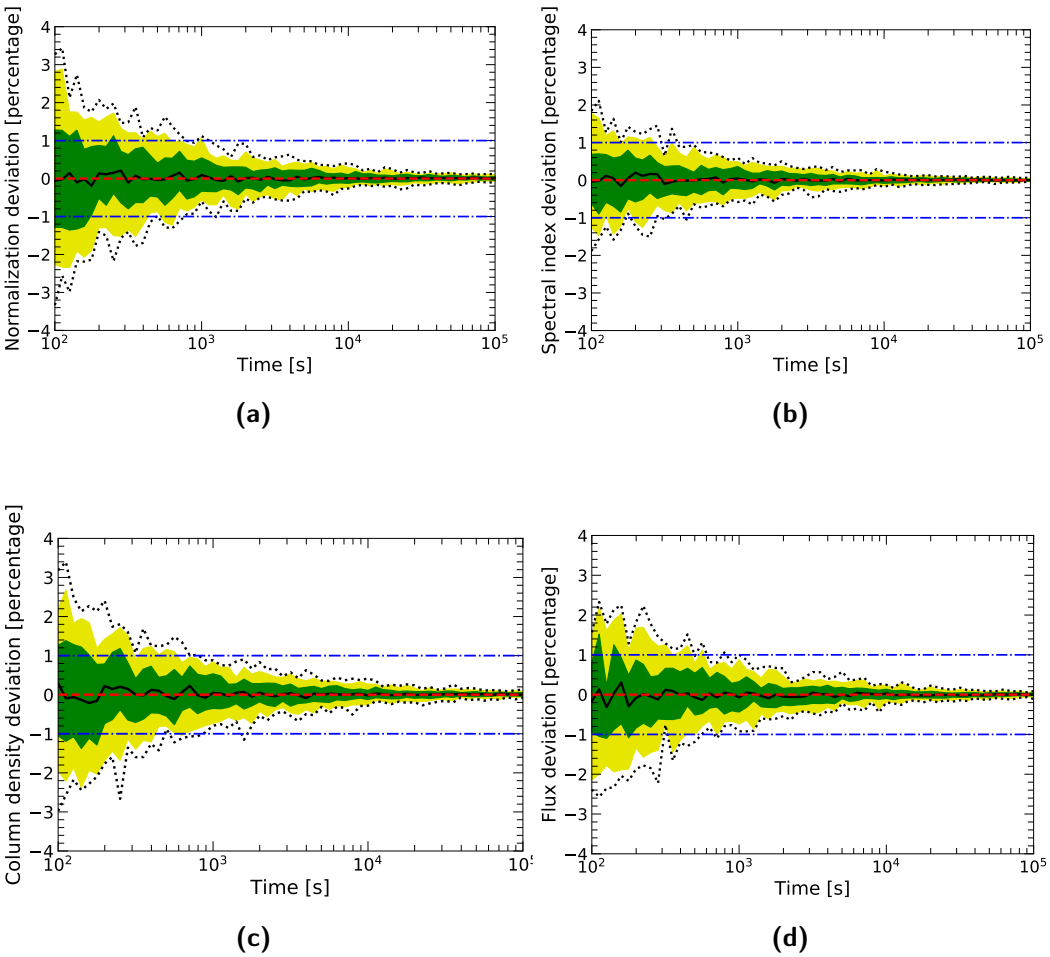

Figure 5.18 – Relative deviation from the spectral parameters for the Crab Nebula. a) Normalization. b) Spectral index. c) Column density. c) Energy flux in the $0.3 - 10\,\mathrm{keV}$. In all the cases, the solid black curve represents the median, while the inner green (outer yellow) region indicates where 68 % (95 %) of the results lie. The black dotted curves identify the 99 % interval. The blue dash-dotted lines mark the $\pm 1\,\%$ interval around the expected value. The red dashed line corresponds to no deviation.

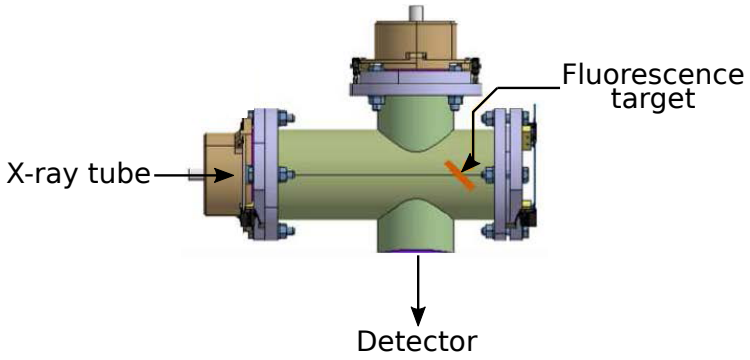

Figure 5.19 – Schematic view of the system based on the X-ray generator.

Table 5.3 – Composition of the fluorescence target. The relevant spectral lines are marked as well.

Element	Spectral line eV	
Al	1486	
Sn	3443	3772
Ti	4509	4932
Cr	5412	5947
Fe	6395	7058
Ni	7472	
Cu	8040	8905

The primary source of the system is a transmission X-ray tube which produces a Bremsstrahlung continuum when electrons emitted by a filament and accelerated by an electric field hit a silver anode. The photons are then directed to a composite target where they are partially reflected and scattered, and they also excite fluorescence emission in the materials making up the target itself. The latter was optimized for line production in the operating energy range of the MXT detector. The final configuration is summarized in Tab. 5.3, where both the elements and the relevant associated spectral lines are reported. Fig. 5.20 shows the resulting spectrum measured by the MXT PM.

Data were acquired under nominal conditions (`VRK` $= -230\,\mathrm{V}$, `VBST` $= -1.8\,\mathrm{V}$) and at different temperatures varying in a range relevant to MXT, i.e. between $-100\,^{\circ}\mathrm{C}$ and $-55\,^{\circ}\mathrm{C}$ with $5\,^{\circ}\mathrm{C}$-steps. The high voltage and the filament current of the X-ray tube were respectively regulated in order to maximize the yield of the fluorescence target and the count rate, while at the

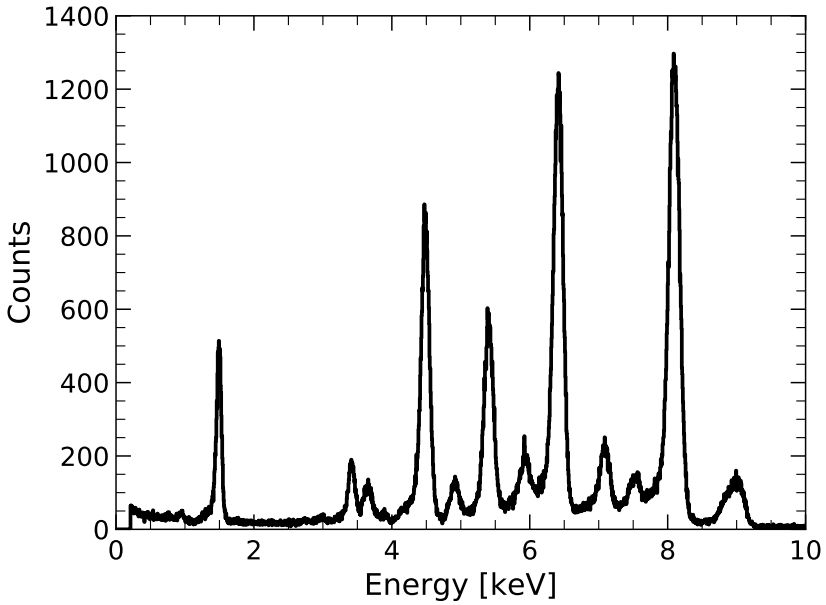

Figure 5.20 – X-ray tube spectrum measured by the MXT Performance Model. The plot was taken at −60 °C and realized by using only single counts.

same time limiting pile-up and CTI underestimation in high flux conditions (Fig. 2.18b).

Measurements were analyzed with the same pipeline already employed for the Performance Model, that is, frame reduction (§ 3.1.1), multiplexing trailing correction (§ 3.3.2.2) and spectral analysis (§ 3.1.2). For the energy calibration, the five most prominent lines were used as references: Al-K_α (1486 eV), Ti-K_α (4509 eV), Cr-K_α (5412 eV), Fe-K_α (6395 eV) and Cu-K_α (8040 eV). It is worth noting that in order to improve the reliability of the results, the residual Bremsstrahlung continuum was also fitted during both energy calibration and CTI determination.

5.4.2 Calibration

In the following, the topic of energy calibration shall be examined more closely by taking advantage of the multi-energy measurements available thanks to the X-ray tube system. Starting from a discussion about detected non-linear behavior (§ 5.4.2.1), the impact of the latter will be evaluated for in-orbit scenarios involving energy calibration at temperatures different than those of the scientific measurements. Also, the effect of a limited number of reference energies on the calibration itself will be investigated (§ 5.4.2.2). Finally, the

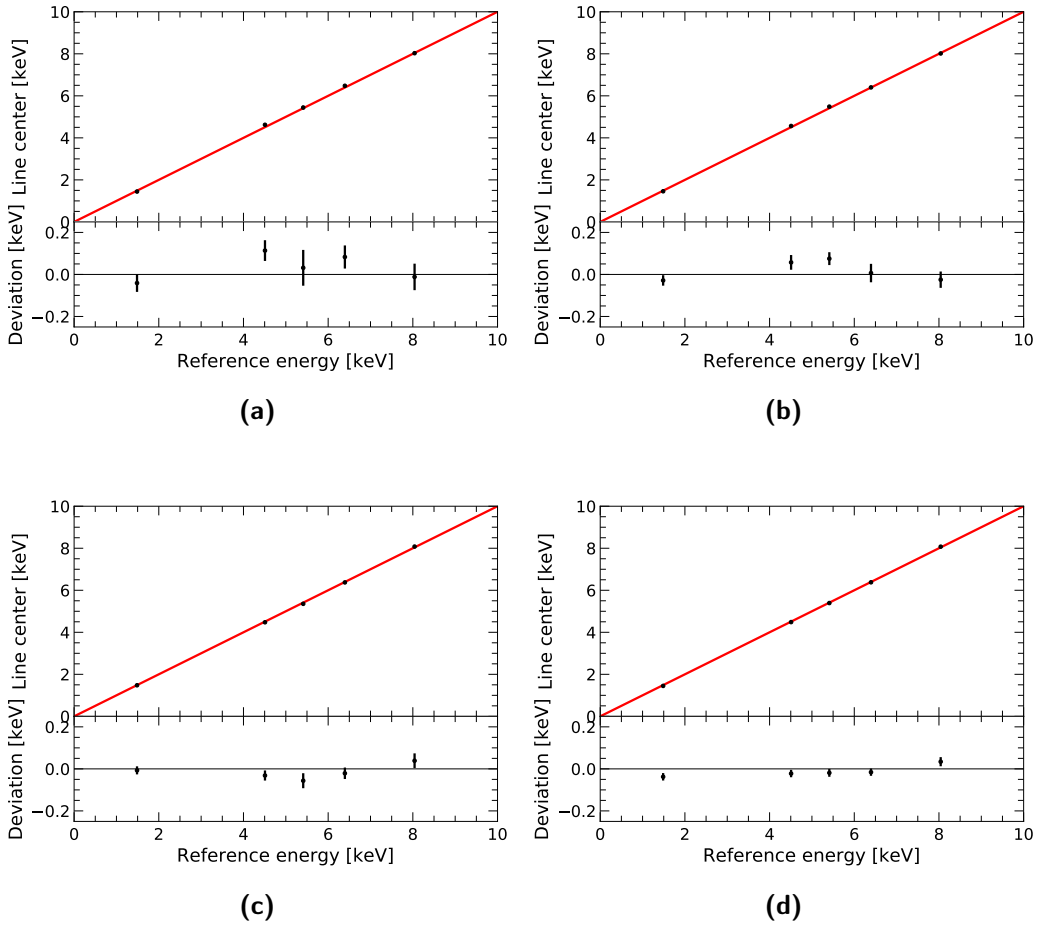

Figure 5.21 – Calibrated fitted line centers versus their respective reference energies at −65 °C. a) Column 50. b) Column 100. c) Column 150. d) Column 200. In all the graphs, the red solid lines represent the identity and the smaller plots below each one show the deviation from that relation.

calibration of events of higher multiplicity will be addressed (§ 5.4.2.3).

5.4.2.1 Linearity

With regard to Fig. 3.27b, the presence of a small non-linearity was detected in § 3.3.2.3, although it could not be further investigated at the time due to the lack of spectral references to be used for calibration. Acquisitions via the X-ray spectrum solved that limitation.

Fig. 5.21 shows the centers (in keV) of the five reference spectral lines plotted against their respective *true* energies for a few columns. Although the relation appears to be fairly linear, residuals are sometimes far from being randomly distributed around zero, with deviations of up to ≈ 100 eV,

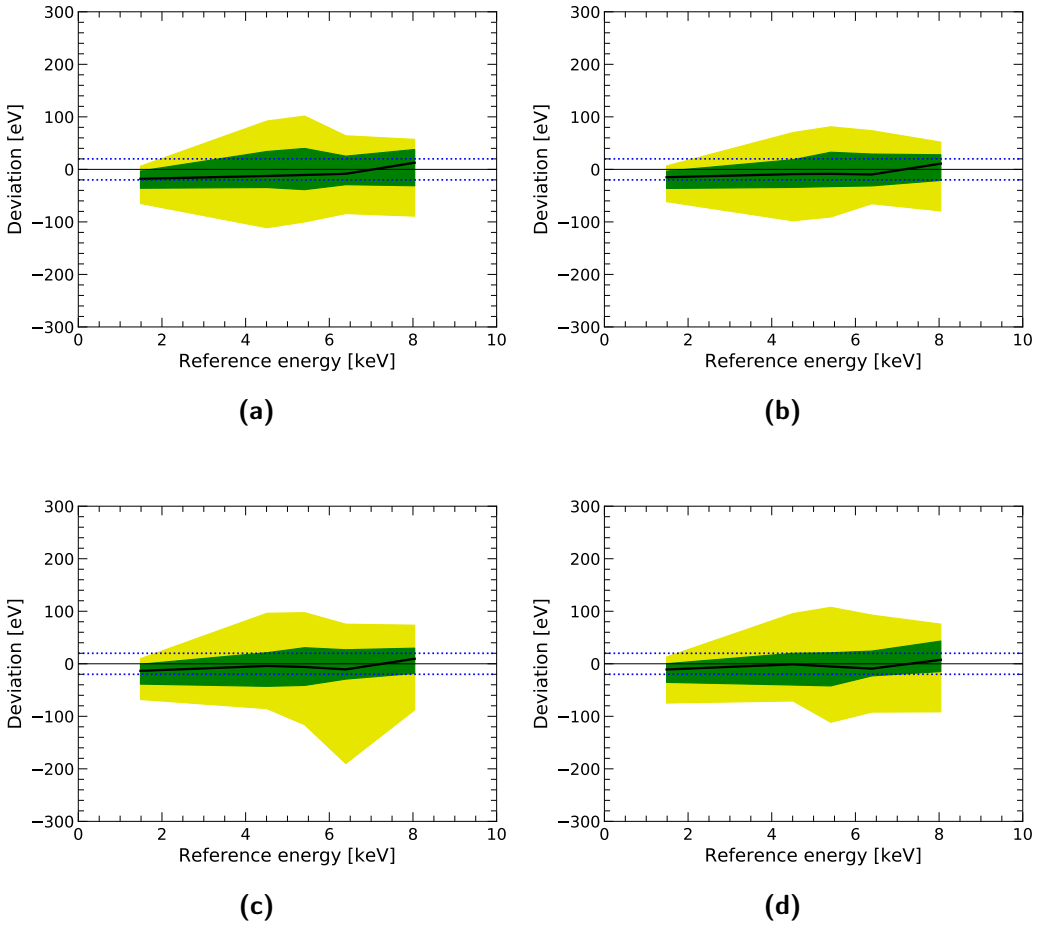

Figure 5.22 – Distribution of the energy shifts across the columns at each reference energy. a) $T = -60\,°\mathrm{C}$. b) $T = -70\,°\mathrm{C}$. c) $T = -80\,°\mathrm{C}$. d) $T = -90\,°\mathrm{C}$. In all the cases, the solid black curve represents the median, while the inner green (outer yellow) region indicates where 68 % (95 %) of the results lie. The dotted blue lines mark the $\pm 20\,\mathrm{eV}$ interval.

especially near the middle of the energy range. For some columns, points follow concave or convex relations, while in other cases the behavior is actually linear. Nonetheless, the trend appear not to be influenced by temperature, with the concavity always having the same sign given a column.

To study this effect one may calculate, for a given temperature, the dispersion across all columns of the distance of every fitted line center from the corresponding reference energy. The result is shown in Fig. 5.22, from which several observations can be made.

The median deviation as a function of the reference energy generally has an upward concavity. This corresponds to linear fits linking ADU line centers to their respective energies having generally positive offsets and therefore explains

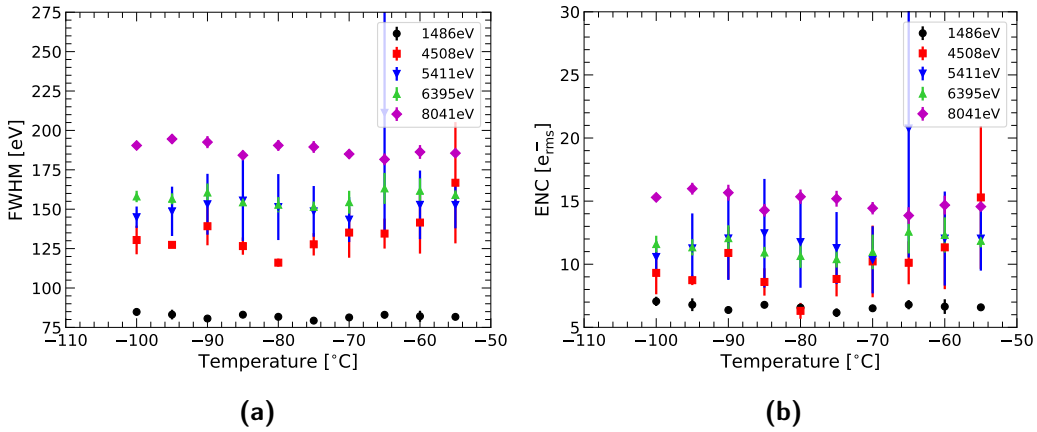

Figure 5.23 – Energy resolution at the five reference lines of the X-ray tube spectrum as a function of temperature. a) Full Width at Half Maximum. b) Equivalent Noise Charge.

the feature that was detected in § 3.3.2.3 (Fig. 3.24a), where a mainly-positive residual offset was measured: it is not a leftover of incomplete image correction, but a direct consequence of trying to fit a straight line through points actually following a concave curve.

Median values are always within ±20 eV from zero, with 68 % of cases within about ±40 eV. However, the dispersion across the detector can exceed 200 eV. This dispersion also appears to be dependent on the energy itself and it is at its tightest at the Al-K_α line. More importantly, the distribution is less wide than at ≈ 6 keV. This helps interpret both why the resolution of the detector-wide spectrum appear to be energy-dependent on a level incompatible to a model simply involving Fano noise and a constant Equivalent Noise Charge (Fig. 5.23), and why the resulting resolution at the Al-K_α line (FWHM (1486 eV) ≈ 80 eV) is so much smaller than the expected value calculated from ^{55}Fe measurements (FWHM (1486 eV) ≈ 100 eV from § 3.3.2.3). It is worth mentioning that this newly-found value is more in agreement with the instrument specifications than the one previously estimated.

As far as the global spectrum is concerned, the generally asymmetric distribution of the column-by-column energy deviation has the effect of not only increasing the width of the spectral lines, but also generally shifting their centers with the same sign as the associated median deviation, although by a different magnitude (Tab. 5.4 and Tab. 5.5).

Several attempts at fitting non-linear functions, most notably polynomials, were carried out on column-wise spectra, but they never yielded satisfactory

Table 5.4 – Fitted centers of the five reference lines under different calibration conditions: data calibrated from X-ray tube measurements at −70 °C (original), from ^{55}Fe measurements at −70 °C and from ^{55}Fe measurements at −60 °C. In all cases, the fits were performed on detector-wide spectra of single counts. Uncertainties are 1-σ intervals.

Reference eV	X-ray tube (−70 °C) eV	^{55}Fe (−70 °C) eV	^{55}Fe (−60 °C) eV
1486	-7 ± 4	-17 ± 4	-105 ± 3
4509	-33 ± 7	37 ± 7	-54 ± 1
5412	-18 ± 19	81 ± 13	6 ± 30
6395	5 ± 6	130 ± 8	166 ± 7
8040	41 ± 7	224 ± 16	156 ± 12

Table 5.5 – Fitted Full Width at Half Maximum of the five reference lines under different calibration conditions: data calibrated from X-ray tube measurements at −70 °C (original), from ^{55}Fe measurements at −70 °C and from ^{55}Fe measurements at −60 °C. In all cases, the fits were performed on detector-wide spectra of single counts. Uncertainties are 1-σ intervals.

Reference eV	X-ray tube (−70 °C) eV	^{55}Fe (−70 °C) eV	^{55}Fe (−60 °C) eV
1486	77 ± 1	81 ± 1	79 ± 2
4509	115 ± 4	124 ± 10	157 ± 41
5412	144 ± 22	124 ± 9	150 ± 32
6395	152 ± 2	140 ± 3	166 ± 2
8040	182 ± 3	197 ± 8	206 ± 4

results. The main issue with such approach is the presence of a limited number of data points (five at most) and a comparatively large number of parameters (three at least), which causes the fitting procedure to fail in a large percentage of detector channels, thus degrading the final result. Furthermore, since no non-linear behavior is documented for the CAMEX ASIC, this effect may be caused by the Front-End Electronics and therefore bound to be change after the coupling of the MXT PM to the next FEE model. For all those reasons, it was decided to maintain a linear calibration.

5.4.2.2 In-orbit energy calibration

When describing the active cooling of the MXT Focal Plane Assembly (§ 1.3.3.2), it was pointed out that, although the system is designed to keep the detector at a single temperature between $-80\,^{\circ}\mathrm{C}$ and $-60\,^{\circ}\mathrm{C}$ throughout the mission (namely at $\approx -65\,^{\circ}\mathrm{C}$), it is difficult to know beforehand what the temperature will be precisely, due to the large variations in heat flux the instrument will incur in, especially during satellite slews. Furthermore, in general it will not be possible to calibrate the detector whenever a significant temperature change is detected on the focal plane, as calibration will be performed according to a schedule. Finally, according to what was concluded at the end of § 5.2.1, the detector will be calibrated only thanks to the two Mn lines produced by the on board (direct) ^{55}Fe source.

It thus becomes clear the necessity to investigate what the spectral performances may be if an observation is carried out in temperature conditions different from the ones valid during the corresponding calibration run, and also how using only two relatively high-energy reference points will affect the response at other energies.

Fig. 5.24 shows an analogous plot to Fig. 5.22, except for the fact that the calibration is provided by ^{55}Fe measurements taken at the same temperature. It is obvious the presence of a trend, likely to be caused by the different number and energy distribution of the references used in the calibration process, which caused an overall overestimation of the gain and underestimation of the offset in the case of ^{55}Fe. Indeed, Fig. 5.25 shows, as a function of column number and temperature, the difference between the gain (and offset) calculated respectively from X-ray tube and ^{55}Fe data. Whenever possible, measurements taken at the same temperature were considered together; for $-95\,^{\circ}\mathrm{C}$, $-85\,^{\circ}\mathrm{C}$, $-75\,^{\circ}\mathrm{C}$ and

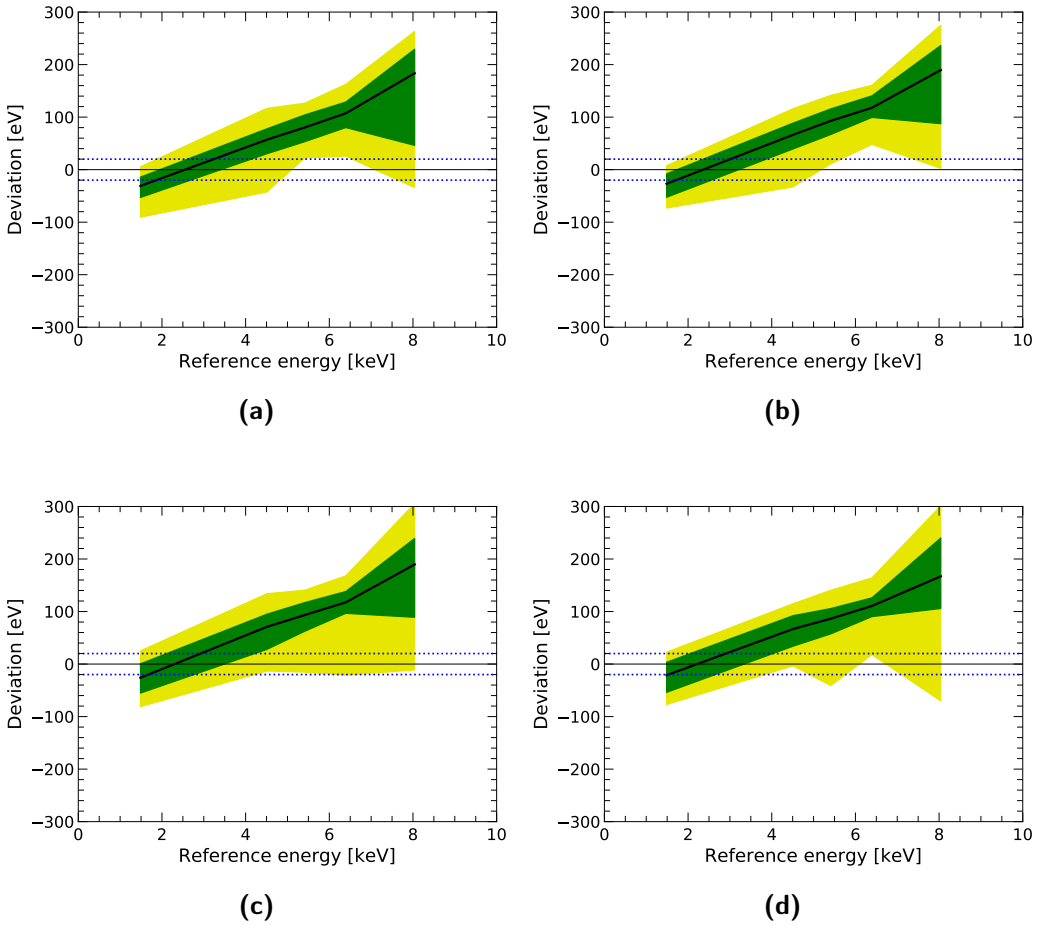

Figure 5.24 – Distribution of the energy shifts across the columns at each reference energy if the X-ray tube data are calibrated via ^{55}Fe measurements at the same temperature. a) $T = -60\,°\mathrm{C}$. b) $T = -70\,°\mathrm{C}$. c) $T = -80\,°\mathrm{C}$. d) $T = -90\,°\mathrm{C}$. In all the cases, the solid black curve represents the median, while the inner green (outer yellow) region indicates where 68 % (95 %) of the results lie. The dotted blue lines mark the $\pm 20\,\mathrm{eV}$ interval.

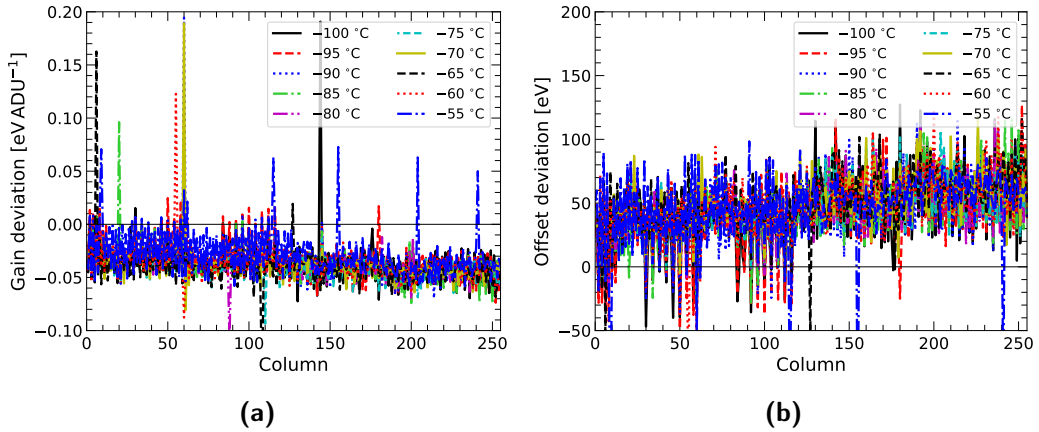

Figure 5.25 – Deviation between the spectral parameters calculated via the X-ray tube and the ^{55}Fe data. a) Difference between the X-ray tube and the ^{55}Fe gain. b) Difference between the X-ray tube and the ^{55}Fe offset. When available, measurements at the same temperature are used (the reader is referred to the text for further details).

−65 °C, radionuclide data gathered at +5 °C with respect to each temperature were used, i.e. −90 °C, −80 °C, −70 °C and −60 °C; ^{55}Fe gain and offset at −90 °C and −60 °C were employed for $T = -100$ °C and −55 °C respectively. It can be seen that both for the gain and the offset the trend depends on the column and apparently not on the temperature itself. Being the dependence approximately linear in both cases, it may be envisaged to derive a relation between the gain and offset calculated from ^{55}Fe data alone and those same parameters extracted by using other energies, in order to fall back to a situation such as the one depicted in § 5.4.2.1.

It is worth pointing out that, although the energies are shifted all across the range, the dispersion is little affected with the consequence that the lines of the detector-wide X-ray tube spectrum calibrated via ^{55}Fe have their centers displaced, despite maintaining their resolution mostly unchanged, the same being true in case gain and offset come from ^{55}Fe measurements at different temperatures (Tab. 5.4 and Tab. 5.5).

Finally, one should be aware that the findings reported above are to be considered a first approach to the application of ^{55}Fe calibration to multi-energy measurements. The results may in fact be affected by some bias, especially linked to the complexity of the X-ray tube spectrum, i.e. the proximity of many spectral lines to each other and the presence of the Bremsstrahlung continuum. However preliminary, those results suggest that it will be necessary

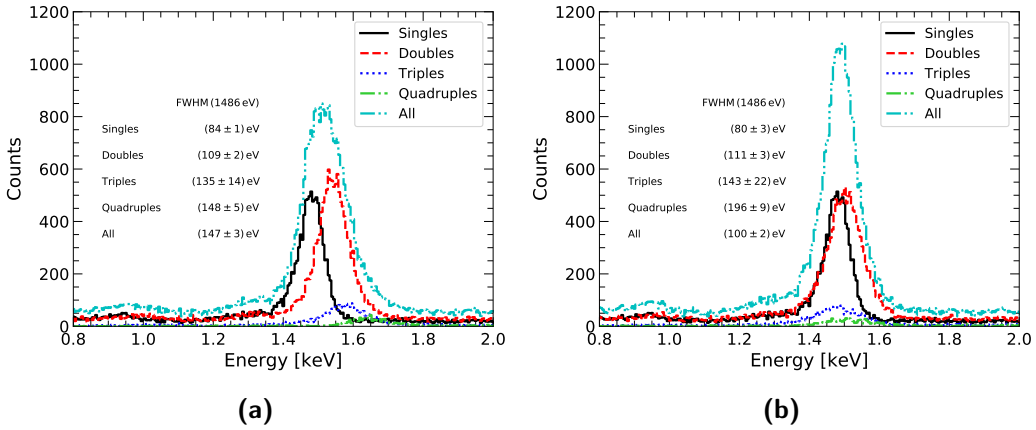

Figure 5.26 – The Al-K$_\alpha$ line of the X-ray tube spectrum made out of all valid patterns, divided according to their multiplicity. a) Patterns calibrated via gain and offset from single counts. b) Patterns calibrated via gain and offset from single counts, the other multiplicities being shifted with respect to the spectrum of single counts.

to combine in-orbit ^{55}Fe calibration measurements with a detailed model of the detector, supported by on-ground measurements. For this reason, other multi-energy studies must be carried out. Indeed, the Performance Model will undergo a test campaign in PANTER (§ 5.3.1.1), where the MXT team will take advantage of the possibility to have a single spectral line at a time, thus solving many of the issues of the current system.

5.4.2.3 Multiplicity

So far the analysis has always been limited to single counts, i.e. photon events where no charge splitting between neighboring pixels is detected. However, during in-orbit operation multiple events are not ignored, which leads to the question of whether events of different multiplicities can be straightforwardly combined after calibration with parameters derived from single counts or some further manipulations are required.

Fig. 5.26a shows the Al-K$_\alpha$ of the X-ray tube spectrum made out of all the allowed photon events, grouped according to their multiplicity, all the data being calibrated via the spectrum of single counts. Along with the expected degradation of the energy resolution with the number of split events, as in eq. (2.86), it can also be observed that the line centers are shifted towards higher energies the larger the multiplicity (the same is true for the other lines).

The explanation behind this effect lies in the same phenomenon investigated

in § 3.4.2.3 that causes the resolution loss: the charge in a photon event is usually shared among neighboring pixels, with some of it being under threshold for some of the pixels, thus affecting the reconstructed photon energy and introducing an additional noise source to the system, dependent on the size of the original charge cloud with respect to the dimensions of the pixel. A corollary of this effect is that, since only part of the photon energy is actually detected, the center of the resulting spectral line will be shifted towards lower energies. This was in fact already visible in Fig. 3.41, where the Mn-K_α line is centered around 5820 eV instead of 5898 eV.

Like in the case of the spectral resolution, this effect is mitigated as the ratio between the cross-section of the charge cloud the pixel area decreases. In practice, this also corresponds to the case of multiple events, since the *effective* pixel size becomes several times that of a single pixel (from two to four according to the multiplicity) while the charge cloud stays the same. If a data set is calibrated via a gain (and offset) calculated for events with lower multiplicity, the result will cause the spectral line centers to be shifted to the right, which is exactly what is observed in this instance. As a consequence, when all events are considered regardless of their multiplicity, spectral lines get artificially broadened.

Instead of determining the calibration parameters separately for each multiplicity, which might be computation-intensive and also not solve the issue completely due to the uncertainties arising from limited statistics or non-linearity effects, I propose to calibrate all events thanks to the gain and offset obtained from the analysis of the single counts and then simply apply a multiplicity-dependent energy offset calculated on the basis of the detector-wide spectrum. The result of the application of such algorithm, in which the offset is simply taken as the median difference between each line center and the corresponding energy difference, is presented in Fig. 5.26b.

It is worth noting that an analogous multiplicity-dependent shift is observed on the calibration documentation of XMM/EPIC-pn (Valtchanov, I. and Smith, M. and Schartel, N., 2019), for which the same explanation is given (although in much more concise terms) and a similar operation is applied.

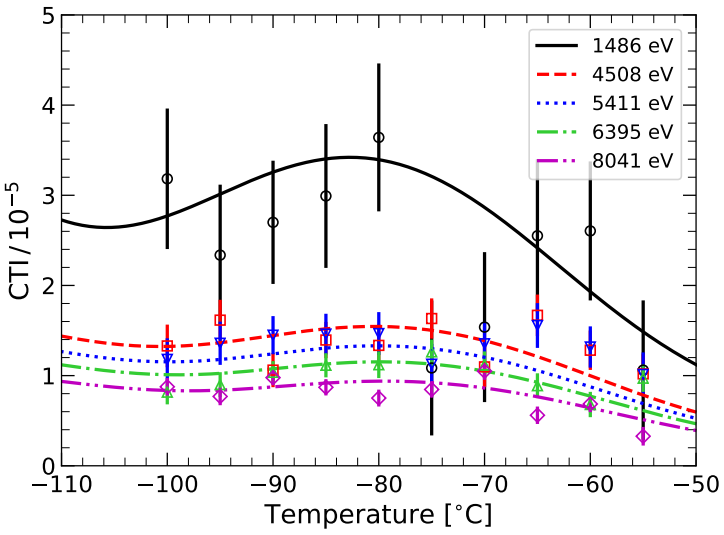

Figure 5.27 – Charge Transfer Inefficiency as a function of temperature at the five reference energies of the X-ray tube system. The points are the experimental data, whereas the curves come from eq. (5.5).

5.4.3 Charge Transfer Efficiency

As extensively discussed on several occasions (e.g. § 2.3.2.3 and § 4.4.1.1) the Charge Transfer Efficiency of a CCD is influenced by a multitude of parameters, including physical characteristics of the detector itself (e.g. material and internal structure), its operation (e.g. temperature, integration time, transfer rate) and the nature and properties of the defects actually trapping the charges. Once an experimental configuration is fixed, the CTE is still a function of the energy and flux of the incoming photons.

The results obtained after the parametric studies on the MXT Performance Model (§ 3.3.2.4), especially Fig. 3.35 and Fig. 3.36, could not provide any information about the behavior at energies other than the Mn fluorescence lines. By taking advantage of the many spectral lines available with the X-ray generator setup, this aspect could be investigated.

Fig. 5.27 shows the results of the multi-energy analysis performed on the new data set. The Charge Transfer Inefficiency is plotted as a function of the temperature for the five chosen reference energies, i.e. the same lines used for calibration. Superimposed to the experimental points are the curves that describe how the CTI varies with temperature and primary photon energy. The curves were obtained through the application of eq. (2.70) in the case of the MXT detector, therefore taking into account the presence of both fast and

Table 5.6 – List of defects used for the calculation of the curves in Fig. 5.27. Enthalpy difference ΔH and cross-section σ for the Ti traps are from Roth et al. (2008), while the existence of the other two defects was invoked to better describe the data.

Trap type	N_t $10^8\,\mathrm{cm}^{-3}$	ΔH eV	σ $10^{-14}\,\mathrm{cm}^2$
Ti	3	0.27	1.3
	3	0.08	3.5
	3	0.49	1
Unknown	1	0.31	1
Unknown	4	0.20	1

slow transfer, as well as the image and the frame-store regions:

$$\mathrm{CTI} = 1 - \frac{\mathrm{CTE}_{\mathrm{im,fast}}\mathrm{CTE}_{\mathrm{fs,slow}}}{\mathrm{CTE}_{\mathrm{fs,fast}}}, \tag{5.5}$$

where the subscripts retain the same meaning as in eq. (3.9).

Compatibly with the uncertainties, one can see that lower-energy photons generally suffer from higher CTI than the more energetic ones, which is in line with what is expected from the theoretical discussion of § 2.3.2.3. The fact that the CTI seems to increase around $-90\,^\circ\mathrm{C}/-80\,^\circ\mathrm{C}$, especially for Al photons, is particularly interesting since titanium impurities, which may occur during the fabrication of the detector, produce charge traps resulting in a CTI peak near that same temperature.

On the hypothesis that Ti traps are present in the detector, the curves were thereby calculated. Adopted energy levels and capture cross sections were taken from the literature and are reported in Tab. 5.6. Due to the large relative uncertainties of the experimental points, especially in the case of Al data which provide the strongest constraints to the results, along with the complex functional form of eq. (2.70), it was opted not to perform a fit. Instead, the analysis was limited to a visual comparison with the data points in Fig. 5.27, thanks to which defect concentrations could be estimated (also presented in Tab. 5.6).

If one accepts those results about the nature and concentration of charge traps, a parametrization of the CTI as a function of both energy and temperature can be provided (Fig. 5.28). It is worth pointing out that, within

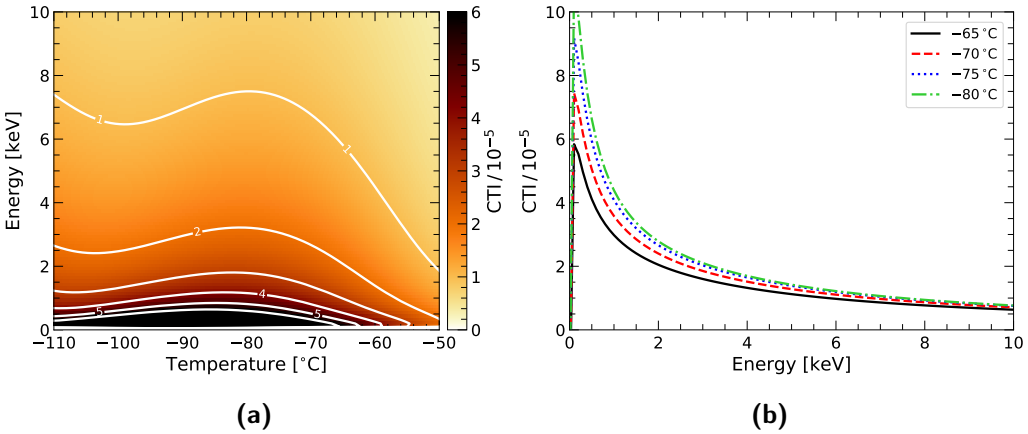

Figure 5.28 – Charge Transfer Inefficiency as a function of temperature and energy, based on Fig. 5.27 and Tab. 5.6. a) Multi-parameter view. b) CTI as a function of energy at selected temperatures.

the wider scope of the MXT experiment, the use of a CTI model such as this one is limited to the first stages of the mission. Indeed, as radiation damage accumulates in the detector, it results in the onset of other defects that cannot be predicted from the measurements and analysis described here. This thus supports the necessity of carrying out radiation tests on a MXT-like detector, which would also provide a detailed CTI model for the correction of in-orbit scientific data.

Chapter 6

Summary and conclusions

The Micro-channel X-ray Telescope or MXT is part of the French-Chinese mission SVOM, to be launched at the end of 2021 for the study of Gamma-Ray Bursts and other transient phenomena. In this thesis I have been interested in the capabilities of the detector at the focal plane of MXT, especially from a spectroscopic point of view. Experimental investigations and simulations, along with a purely theoretical approach on occasions, enabled to investigate its response in detail, which in turn allowed to quantify its compliance with the mission requirements, as well as propose strategies to improve the results.

Beginning-of-life spectral performances

In § 3, I described the first tests ever to be carried out on the first available models of the Detector Assembly of MXT. Although the Engineering Model unfortunately yielded some disappointing results that were far from the instrument specifications, it provided a first test bench for both the data analysis codes, developed specifically on that occasion, and the experimental equipment. By learning from the limited performances of the device and its eventual structural failure, new procedures and a whole new laboratory setup were devised specifically in preparation for the arrival of the next model.

With the Performance Model (§ 3), the first successful measurement of the detector performances was carried out. Earlier tests based on ^{55}Fe spectroscopy demonstrated the excellent capabilities of the system, featuring low noise (ENC $= 3\,\mathrm{e}^-_{\mathrm{rms}}$ from electronic contributions and leakage current), a 40 eV low-level threshold, a high energy resolution of FWHM (5898 eV) = 146 eV and a limited Charge Transfer Inefficiency of CTI (5898 eV) $= 1.8 \times 10^{-5}$ for

temperatures below $-60\,^{\circ}\mathrm{C}$.

In addition to the quality of the results themselves, the Performance Model proved the compliance of the system with the beginning-of-life mission specifications of low-level threshold below 200 eV and ≈ 80 eV energy resolution at 1.5 keV. Although the latter requirement was partially missed according to the extrapolation obtained from those first ^{55}Fe measurements, later multi-energy tests, carried out thanks to an X-ray tube system (§ 5.4), actually confirmed the full agreement with the 80 eV performance requirement at 1.5 keV. Furthermore, preliminary results from the new setup taking advantage of the next model of the Front-End Electronics, representative of the Flight Model, suggest similar capabilities and compliance with the instrument specifications.

The aforementioned X-ray tube measurements also highlighted some more subtle features in the detector response, such as non-linearity and multiplicity-dependent calibration, that certainly require further investigation, especially in the context of the new readout electronics and the next detector models.

Predicted degradation of the spectral performances

During its operation on board the SVOM satellite, the MXT detector will be exposed to the harsh space radiation environment, especially during its passages across the South Atlantic Anomaly. A consequence of this is that the performances of the device are predicted to degrade as the mission progresses.

In § 4, I proceeded to address this point by modeling the particle environment along the orbit of the satellite, thanks to the use of specialized software such as SPENVIS and OMERE. By carrying out simulations based on the Geant4 toolkit, I was able to evaluate how much space radiation the detector will be exposed to once a realistic model of its surroundings is taken into account, most notably in the form of the focal plane shielding and the spacecraft itself. The prediction consisted of a 10 MeV-proton equivalent fluence of $\approx 10^{9}\,\mathrm{cm}^{-2}\,\mathrm{yr}^{-1}$, which stands out for being more than one order of magnitude larger than the corresponding values for missions such as XXM/EPIC-pn and eROSITA, an interesting comparison as they mount similar detectors to MXT's at their focal planes.

By combining those findings with some previous tests by the teams of both the aforementioned missions (reported in the literature), and the experimental results obtained from the Performance Model of the MXT Detector Assembly,

I attempted to predict how much and how fast the spectroscopic capabilities of the MXT detector will degrade during its permanence in orbit and how they will compare to the mission specifications of $< 200\,\mathrm{eV}$ low-energy threshold throughout the mission, and FWHM $(1.5\,\mathrm{keV}) < 160\,\mathrm{eV}$ after 3 years and $< 280\,\mathrm{eV}$ after 5 years.

If one supposes that the nominal $-65\,^{\circ}\mathrm{C}$ operating temperature of MXT is attained and maintained throughout the mission, it may be expected to detect an increase of the low-level threshold from the value of $\approx 40\,\mathrm{eV}$ measured in laboratory to 90 eV after 1 year spent in orbit, 125 eV after 3 years and 155 eV after 5 years, those values being well below the 200 eV requirement. As far as the energy resolution at 1.5 keV is concerned, a similar agreement with the performance specifications is found, with a value reaching 110 eV after the first year, 120 eV at the end of the nominal three-year nominal mission and 130 eV at the end of the five-year extended mission. Finally, the total Charge Transfer Inefficiency at the same energy is predicted to rise from the current measured value of 2.5×10^{-5} to $1 - 1.4 \times 10^{-4}$ in the first year and then stay approximately constant for the rest of the mission. In all those instances, estimates are always clearly well within the allowed limits.

In-orbit performance estimation

From those results, one may notice that the biggest changes are predicted to occur in the first year of in-orbit operation, with the low-energy threshold more than doubling and the CTI increasing by a factor of five with respect to its pre-launch value in that same time frame. This will require accurate monitoring of the performances in order to always employ the most up-to-date calibration parameters to ensure the best scientific results.

The use of the ^{55}Fe calibration source mounted inside the MXT camera itself (§ 5.2.1) will be essential to attain this goal. A reasonable suggestion might be to perform at least one calibration via the internal radioactive source per month, although the fact that this period of relatively fast performance evolution happens to coincide with the time when the source activity is at its highest opens the possibility for even more frequent calibration runs, up to almost one per orbit in the very early stages of the mission.

Calibration via the internal ^{55}Fe source has the problematic feature of providing only two relatively high-energy spectral lines for reference, which

may negatively effect the estimation of the response as was explored during multi-energy laboratory tests on the MXT Performance Model (§ 5.4). A solution might be represented by observations of line-rich astrophysical sources such as Supernova Remnants (§ 5.2.2), although current simulations suggests the necessity to accumulate at least ≈ 2000 ks of total exposure time over the entire CCD matrix to achieve channel-by-channel calibration. The feasibility of such an approach, especially as far as the frequency of measurement is concerned should be evaluated in relation to the scientific schedule of the mission.

The quality of the scientific results of MXT will also depend on the knowledge of its total effective area, composed of both the energy-dependent collecting area of its optical system and the quantum efficiency of its detector. Since measurements of both the contributions at the same time is not possible on ground (§ 5.3.1), observations of selected astrophysical sources are needed after launch. The calculations suggest that, after at least 2 ks observing a source such as the AGN 3C273, the accuracy of the flux estimate can be as high as 10 % (5 % for a > 10 ks exposure) *for a given model of the effective area.* Likewise, after 1 ks, the parameters of the Crab Nebula can be derived with an accuracy better than 1 %.

Perspectives

The investigation of the response of the MXT detector is certainly not over yet. As already anticipated, extensive tests are required to confirm the compliance with the beginning-of-life specifications of the next available models of both the detector itself and its Front-End Electronics, while at the same time the selection of the Flight Model of the detector itself has to take place.

An especially important point concerns the performance degradation during in-orbit operation. The predictions contained in this manuscript are based on extrapolations of laboratory measurements taken with the MXT Performance Model detector as well as from tests of similar devices described in literature. This implies that they are affected by some level of uncertainty that only direct testing can solve. Moreover, as already stated, the pace of the evolution is predicted to be the highest in the first year of operation, its details being not easily deducible from the current available information. This is especially true for a figure of merit such as the Charge Transfer Inefficiency, for which

I developed a theoretical model that can quantify its dependence on various parameters. Nonetheless, it is itself highly dependent on the concentration and physical properties of the (radiation-induced) defects. This justifies the need to carry out an irradiation campaign of a model of the MXT detector (§ 4.4.2), even after the delivery of the instrument itself.

Finally, this thesis work may constitute a basis for the development of the codes necessary to the exploitation of in-orbit data, notably regarding calibration. As just mentioned, the CTI model may help with the correction of this effect under many conditions even though only selected measurements are available. Furthermore, the analysis software developed for the treatment of laboratory data might be expanded to include a more user-friendly interface as well as compliance with the scientific data format of MXT. New fitting routines may be implemented that are better adapted to low-flux in-orbit conditions. An especially interesting approach would be the inclusion of Bayesian methods in the calibration, therefore allowing to base the process on the previously established knowledge of the detector response. This will likely result, among other advantages, in the decrease of the necessary integration time to reach a satisfactory precision, a particularly important point if one considers the central role astrophysical observations are predicted to be playing in the evaluation of the instrument response.

Résumé en français

Le *Télescope X à Microcanaux* (*Micro-channel X-ray Telescope* ou MXT en anglais) fait partie de la mission Franco-Chinoise SVOM, dont le lancement est prévu fin 2021 pour l'étude des sursauts gamma. Dans mon travail de thèse, je me suis chargé de l'étude de la réponse du détecteur au plan focal de MXT, en particulier ses performances spectrales. À travers des expériences en laboratoire, des simulations et parfois une approche théorique, j'ai pu investiguer ses capacités en détail, ce qui a permis de quantifier la conformité avec les spécifications de mission, ainsi que de proposer des stratégies pour améliorer les performances.

Contexte scientifique, SVOM et MXT

Les sursauts gamma (Gamma-Ray Bursts ou GRBs en anglais) sont les phénomènes les plus violents de l'Univers. Ils apparaissent aléatoirement et uniformément sur le ciel, et ils montrent des courbes de lumière (flux en fonction du temps) avec des formes et durées très variées. Sur la base de la durée de son émission *prompte*, c'est-à-dire la première émission à être détectée, forte en rayons gamma, les GRBs sont divisés en deux classes : les sursauts courts (durée inférieure à 2 s, en moyenne 0.3 s), avec des spectres plus durs et concentrés à un redshift (distance) de $z = 0.5$, et les sursauts longs (durée supérieure à 2 s, en moyenne de 20 s), plus doux et concentrés à $z = 1 - 2$. Grâce aux mesures de redshift, on peut calculer l'énergie émise par les sursauts, atteignant $10^{48} - 10^{55}$ erg en cas d'émission isotrope. Faisant suite à l'émission prompte, l'émission rémanente (*afterglow*) est plus étendue dans le temps (jusqu'à plusieurs minutes, heures ou jours après l'émission prompte) et elle est constituée de photons de plus basse énergie, principalement des rayons X, mais aussi des longueurs d'onde dans les domaines visible, infra-rouge et radio.

Le modèle le plus accepté de l'origine des GRBs consiste en un objet

compact (trou noir ou magnetar) en accrétion qui éjecte de la matière dont l'interaction avec l'environnement proche cause l'émission des photons des GRBs. Bien que le mécanisme soit commun aux deux classes de sursauts, la distinction se fait au niveau du progéniteur : une explosion de supernova dans le cas d'un GRB long et la coalescence entre deux étoiles à neutrons pour un GRB court. Toutefois, beaucoup de questions restent ouvertes autour de la physique à la base de ces phénomènes.

La mission Franco-Chinoise SVOM (*Space-based multi-wavelength astronomical Variable Object Monitor*) se situe dans ce cadre et vise à réaliser des observations de sursauts gamma dans un large domaine d'énergie, allant du MeV au µm. Pour atteindre ces objectifs, SVOM sera composé de deux segments, un satellite et un réseau de télescopes au sol, qui permettront un suivi continu et multi longeur d'onde des sursauts ainsi que leur localisation rapide et précise.

À bord du satellite, le Télescope X à Microcanaux (Micro-channel X-ray Telescope ou MXT), travaillant dans la bande $0.2 - 10\,\mathrm{keV}$, sera chargé de la localisation des sursauts avec une précision $< 2\,\mathrm{arcmin}$, ainsi que de l'étude de l'émission de rémanence. Il montera au plan focal d'un système optique à *œil de langouste* (*lobster-eye*) un Charge Coupled Device basé entièrement sur des jonctions pn (pnCCD), hérité des missions XMM-Newton et eROSITA.

Performances spectrales en début de vie

Dans le cadre des expériences en laboratoire, deux modèles du détecteur de MXT ont été testés, le but étant l'évaluation de leurs performances et la comparaison avec les exigences de la mission. Pour pouvoir interpréter les données mesurées, j'ai développé et codé entièrement les algorithmes pour le traitement d'images des CCD et l'analyse spectrale. Précédemment, aucun code n'était disponible pour cette tâche.

Le Modèle d'Ingénierie (Engineering Model) a fourni des résultats insatisfaisants qui étaient loin des spécifications de l'instrument, avant de subir une casse mécanique qui a empêché des études ultérieures. Néanmoins, il a permis de valider le banc de test dans son intégralité ainsi que les codes pour l'analyse des données, développés pour l'occasion. De plus, l'investigation des causes de son fonctionnement anormal a conduit l'équipe MXT au développement de nouvelles procédures et d'un setup expérimental complètement nouveau en

préparation de la livraison du modèle suivant.

Les premières mesures fructueuses ont été réalisées avec le Modèle de Performance (Performance Model). Grâce à l'éclairage par une source radioactive de ^{55}Fe, j'ai pu démontrer ses excellentes capacités spectroscopiques : bruit de $3\,e^-_{rms}$ (à partir du courant de fuite), seuil bas de 200 eV, haute résolution spectrale (FWHM (5898 eV) = 146 eV) et grande efficacité de transfert de charge (CTI (5898 eV) = 1.8×10^{-5}) pour des températures inférieures à $-60\,°C$.

En plus de la qualité des résultats, le Modèle de Performance a prouvé la conformité de la chaîne de détection avec les spécifications de début de vie de la mission, c'est-à-dire le seuil bas de 200 eV et la résolution spectrale de ≈ 80 eV à 1.5 keV. En particulier, le développement d'une source basée sur un générateur X et une cible métallique composite, émettant des nombreuses raies de fluorescence dans le domaine d'opération de MXT ($0.2 - 10$ keV), nous a permis de vérifier directement que l'exigence sur la résolution spectrale est bien respectée, en allant au-delà de l'extrapolation à partir des données du ^{55}Fe.

La même source multi-énergie a aussi révélé des particularités moins évidentes de la réponse du détecteur, notamment des effets de non-linearité et de calibration énergétique dépendante de la multiplicité des événements, ce qui nécessite une investigation plus profonde, en préparation des prochains modèles de détecteurs et d'électronique de lecture.

Effets des radiations sur les performances spectrales

Pendant son fonctionnement, le satellite SVOM, embarquant l'instrument MXT, sera exposé au rayonnement spatial de l'orbite basse terrestre, notamment pendant les passages dans l'Anomalie de l'Atlantique Sud (South Atlantic Anomaly ou SAA), région à haute concentration de particules piégées dans le champ magnétique terrestre. L'interaction avec ces particules, en particulier les protons, causera une dégradation des performances du détecteur de MXT.

À travers des logiciels spécialisés comme SPENVIS et OMERE, j'ai modélisé l'environnement de l'orbite terrestre basse le long de l'orbite de SVOM. En combinant les résultats avec des simulations Monte Carlo que j'ai réalisées grâce à l'outil Geant4 en incluant une géométrie simplifiée de la caméra de MXT et du satellite, j'ai pu estimer le niveau de rayonnement auquel le détecteur de MXT sera exposé pendant son opération en orbite. La prédiction est une fluence de $\approx 10^9\,\mathrm{cm^{-2}\,yr^{-1}}$, exprimée en équivalent de protons de 10 MeV.

Cette valeur est de plus d'un ordre de grandeur supérieure à celles évaluées pour XMM/EPIC-pn et eROSITA, tous les deux ayant des détecteurs similaires à celui de MXT.

La combinaison de ces simulations et des résultats expérimentaux obtenus avec le Modèle de Performance et disponibles en littérature (tests pour XMM/EPIC-pn et eROSITA) a permis d'estimer le niveau et la vitesse de dégradation des performances spectrales du détecteur de MXT, pour les comparer avec les exigences de la mission, c'est-à-dire un seuil bas $< 200\,\mathrm{eV}$ et une résolution à $1.5\,\mathrm{keV}$ inférieure à $160\,\mathrm{eV}$ après 3 années en orbite et $< 280\,\mathrm{eV}$ après 5 années. En supposant que la température du plan focal se mantienne à $-65\,^{\circ}\mathrm{C}$ pendant toute la durée de la mission, j'ai estimé une augmentation du seuil bas à partir des $40\,\mathrm{eV}$ mesurés au laboratoire à $90\,\mathrm{eV}$ après une année en orbite, $125\,\mathrm{eV}$ après 3 années et $155\,\mathrm{eV}$ après 5 années. En ce qui concerne la résolution spectrale à $1.5\,\mathrm{keV}$, je l'ai estimée à $110\,\mathrm{eV}$ après la première année, $120\,\mathrm{eV}$ à la fin de la mission ordinaire de 3 ans et $130\,\mathrm{eV}$ à la fin de la mission étendue de 5 ans. Enfin, je prévois que l'inefficacité de transfert de charge du CCD passera de la valeur actuelle de $\approx 2.5 \times 10^{-5}$ à $\approx 10^{-4}$ dans la première année et restera approximativement constante par la suite. Dans tous les cas analysés, les prédictions sont en conformité avec les spécifications de l'instrument.

Cependant, les incertitudes liées aux simulations et à l'extrapolation nécessitent une validation expérimentale à travers des essais d'irradiation du détecteur de MXT. Pour cette raison, une campagne de tests de protons dans un accélérateur de particules a été mise en place, bien que n'étant pas réalisée dans le cadre de cette thèse en raison du manque de modèles de détecteur disponibles.

Estimation des performances en orbite

Les prédictions suggèrent que les changements les plus importants des performances auront lieu pendant la première année en orbite, ce qui exige une surveillance constante et la mise à jour des paramètres de calibration pour assurer les meilleurs résultats scientifiques. L'utilisation d'une source radioactive de $^{55}\mathrm{Fe}$ à bord sera donc nécessaire pour garantir l'étalonnage. Deux designs ont été étudiés à travers des simulations Geant4 et ont permis de sélectionner une configuration dans laquelle la source, montée sur la roue de calibration de la caméra MXT, est placée en face du détecteur (illumination

directe). L'activité de la source étant à son plus haut juste après le lancement, on peut envisager au moins une calibration par mois, jusqu'à presque une par orbite tout au début de la mission.

La source de ^{55}Fe ne possède que deux raies autour de 6 keV, ce qui peut causer une mauvaise calibration, surtout à plus basse énergie. Une solution possible est l'étalonnage par des sources astrophysiques comme des restes de supernova. Cependant, les estimations suggèrent la nécessité de temps d'exposition supérieurs à 2000 ks pour permettre une calibration complète du CCD, ce qui représente une contrainte à considérer par rapport au planning des observations.

La qualité des résultats scientifiques de MXT sera aussi basée sur la connaissance de sa surface efficace, qui dépend de l'énergie. Elle est composée de la surface de collection des optiques du télescope ainsi que de l'efficacité quantique du détecteur. En raison de contraintes expérimentales, les deux ne pourront pas être mesurées au même moment au sol, ce qui implique la nécessité d'observer des sources astrophysiques. Les calculs suggèrent que, après 2 ks d'observation de l'AGN 3C273, le flux peut être estimé à mieux que 10 %. Également, 1 ks d'exposition permet de mesurer le flux de la Crabe avec une précision de 1 %.

Bibliography

Abbott, B. P., LIGO Scientific Collaboration, & Virgo Collaboration. 2017, Physical Review Letters, 119, 161101

Abdo, A. A., Ackermann, M., Arimoto, M., et al. 2009, Science, 323, 1688

Adams, J. H., J., Silberberg, R., & Tsao, C. H. 1981, Cosmic ray effects on microelectronics. Part 1: The near-Earth particle environment, Tech. rep., NASA

Adrián-Martínez, S., Ageron, M., Aharonian, F., et al. 2016, Journal of Physics G Nuclear Physics, 43, 084001

Agostinelli, S., Allison, J., Amako, K., et al. 2003, Nucl. Instrum. Methods Phys. Res. A, 506, 250

Alig, R. C., Bloom, S., & Struck, C. W. 1980, Phys. Rev. B, 22, 5565

Allison, J., Amako, K., Apostolakis, J., et al. 2006, IEEE T. Nucl. Sci., 53, 270

Allison, J., Amako, K., Apostolakis, J., et al. 2016, Nucl. Instrum. Methods Phys. Res. A, 835, 186

Als-Nielsen, J. & McMorrow, D. 2011, Elements of Modern X-ray Physics (Wiley)

Andritschke, R., Hartner, G., Hartmann, R., Meidinger, N., & Struder, L. 2008, in 2008 IEEE Nuclear Science Symposium Conference Record, 2166–2172

Angel, J. R. P. 1979, The Astrophysical Journal, 233, 364

ASTM International. 2014, ASTM E722-14 Standard Practice for Characterizing Neutron Fluence Spectra in Terms of an Equivalent Monoenergetic

Neutron Fluence for Radiation-Hardness Testing of Electronics., West Conshohocken, PA, doi: https://doi.org/10.1520/E0722-14

Band, D., Matteson, J., Ford, L., et al. 1993, ApJ, 413, 281

Barth, J. 2009, RADECS 2009 Short Course Session I: The Evolution of the Radiation Environments, https://www.ntrs.nasa.gov/search.jsp?R=20180001142&qs=N%3D4294949044%2B4294964268

Barthelmy, S. D., Barbier, L. M., Cummings, J. R., et al. 2005, Space Sci. Rev., 120, 143

Berger, E. 2014, ARA&A, 52, 43

Boschini, M. J., Rancoita, P. G., & Tacconi, M. 2014, SR-NIEL Calculator: Screened Relativistic (SR) Treatment for Calculating the Displacement Damage and Nuclear Stopping Powers for Electrons, Protons, Light- and Heavy- Ions in Materials (version 5.5.1), [Online] available at INFN sez. Milano-Bicocca, Italy [2019, May]: http://www.sr-niel.org/

Boyle, W. S. & Smith, G. E. 1970, Bell Syst. Tech. Jour., 49, 587

Braun, R., Bourke, T., Green, J. A., Keane, E., & Wagg, J. 2015, in Advancing Astrophysics with the Square Kilometre Array (AASKA14), 174

Brotherton, S. D. & Bradley, P. 1982, J. Appl. Phys., 53, 5720

Burrows, D. N., Hill, J. E., Nousek, J. A., et al. 2004, in Society of Photo-Optical Instrumentation Engineers (SPIE) Conference Series, Vol. 5165, Proc. SPIE, ed. K. A. Flanagan & O. H. W. Siegmund, 201–216

Buttler, W., Hosticka, B. J., & Lutz, G. 1990, Nucl. Instrum. Methods Phys. Res. A, 288, 187

Cain, J. C., Daniels, W. E., Hendricks, S. J., & Jensen, D. C. 1965, J. Geophys. Res., 70, 3647

Campana, S., Lodato, G., D'Avanzo, P., et al. 2011, Nature, 480, 69

Cano, Z., Wang, S.-Q., Dai, Z.-G., & Wu, X.-F. 2017, Advances in Astronomy, 2017, 8929054

Cherenkov Telescope Array Consortium, Acharya, B. S., Agudo, I., et al. 2019, Science with the Cherenkov Telescope Array (World Scientific Publishing Co. Pte. Ltd.)

Courvoisier, T. J. L. 1998, A&A Rev., 9, 1

Dado, S., Dar, A., & De Rújula, A. 2009, ApJ, 696, 994

Dennerl, K., Burkert, W., Burwitz, V., et al. 2012, in Proc. SPIE, Vol. 8443, Space Telescopes and Instrumentation 2012: Ultraviolet to Gamma Ray, 844350

Esser, L. 1974, in 1974 IEEE International Solid-State Circuits Conference, Vol. XVII, 28–29

European Cooperation for Space Standardization, ECSS Secretariat, ESA Requirements and Standards Division, ESTEC. 2008a, Space engineering — Methods for the calculation of radiation received and its effects, and a policy for design margins, `https://ecss.nl/standards/ecss-standards-on-line/active-standards/engineering/`

European Cooperation for Space Standardization, ECSS Secretariat, ESA Requirements and Standards Division, ESTEC. 2008b, Space engineering — Space environment, `https://ecss.nl/standards/ecss-standards-on-line/active-standards/engineering/`

European Cooperation for Space Standardization, ECSS Secretariat, ESA Requirements and Standards Division, ESTEC. 2010, Space engineering — Calculation of radiation and its effects and margin policy handbook, `https://ecss.nl/hbs/published-hbs-on-line/active-engineering-handbooks/`

European Space Agency and Belgian Institute for Space Aeronomy. 2019, SPace ENVironment Information System, `https://www.spenvis.oma.be/`

Fano, U. 1946, Physical Review, 70, 44

Fano, U. 1947, Physical Review, 72, 26

Fiorini, C. & Lechner, P. 1999, IEEE T. Nucl. Sci., 46, 761

Fraser, G. W., Abbey, A. F., Holland, A., et al. 1994, Nucl. Instrum. Methods Phys. Res. A, 350, 368

Freyberg, M. J., Bräuninger, H., Burkert, W., et al. 2005, Exp. Astron., 20, 405

Freyberg, M. J., Budau, B., Burkert, W., et al. 2008, in Society of Photo-Optical Instrumentation Engineers (SPIE) Conference Series, Vol. 7011, Proc. SPIE, 701117

Garmire, G. P., Bautz, M. W., Ford, P. G., Nousek, J. A., & Ricker, Jr., G. R. 2003, in Proc. SPIE, Vol. 4851, X-Ray and Gamma-Ray Telescopes and Instruments for Astronomy., ed. J. E. Truemper & H. D. Tananbaum, 28–44

Gatti, E. & Manfredi, P. F. 1986, Nuovo Cimento Rivista Serie, 9, 1

Gatti, E. & Rehak, P. 1984, Nucl. Instrum. Methods Phys. Res., 225, 608

Gehrels, N., Chincarini, G., Giommi, P., et al. 2004, ApJ, 611, 1005

Gehrels, N., Norris, J. P., Barthelmy, S. D., et al. 2006, Nature, 444, 1044

Gendre, B., Stratta, G., Atteia, J. L., et al. 2013, ApJ, 766, 30

Ghirlanda, G., Bernardini, M. G., Calderone, G., & D'Avanzo, P. 2015, Journal of High Energy Astrophysics, 7, 81

Grum-Grzhimailo, A. N., Pikuz, T., Faenov, A., et al. 2017, European Physical Journal D, 71, 69

Hall, R. N. 1952, Physical Review, 87, 387

Herrmann, S., Buttler, W., Hartmann, R., et al. 2007, in 2007 IEEE Nuclear Science Symposium Conference Record, Vol. 3, 2398–2403

Herrmann, S., Buttler, W., Hartmann, R., et al. 2008, in 2008 IEEE Nuclear Science Symposium Conference Record, 2952–2957

Holland, A. D. 1993, Nucl. Instrum. Methods Phys. Res. A, 326, 335

Hu, Y.-D., Liang, E.-W., Xi, S.-Q., et al. 2014, ApJ, 789, 145

Huston, S. L., Kuck, G. A., & Pfitzer, K. A. 1996, in Washington DC American Geophysical Union Geophysical Monograph Series, Vol. 97, 119

IceCube-Gen2 Collaboration, :, Aartsen, M. G., et al. 2014, arXiv e-prints, arXiv:1412.5106

IEEE. 2011, IEEE Std 1241-2010 (Revision of IEEE Std 1241-2000), 1

Ivezić, Ž., Kahn, S. M., Tyson, J. A., et al. 2019, ApJ, 873, 111

Jackson, K. A. & Schröter, W. 2000, Handbook of Semiconductor Technology, 2 Volume Set (Wiley-VCH), 1556

Japan Atomic Energy Agency, Nuclear Data Center. 2007, Japanese Evaluated Nuclear Data Library (JENDL), High Energy File, 2-4 Shirakata, Tokaimura, Nakagun, Ibaraki 319-1195, Japan: `https://wwwndc.jaea.go.jp/ftpnd/jendl/jendl-he-2007.html`

Jensen, D. C. & Cain, J. C. 1962, J. Geophys. Res., 67, 3568

Kim, C. 1979, in Charge-coupled devices and systems, ed. M. Howes & D. Morgan, Wiley series in solid state devices and circuits (Wiley), 1–80

Kinchin, G. H. & Pease, R. S. 1955, Rep. Prog. Phys., 18, 1

Kirsch, M. G., Briel, U. G., Burrows, D., et al. 2005, in Society of Photo-Optical Instrumentation Engineers (SPIE) Conference Series, Vol. 5898, Proc. SPIE, ed. O. H. W. Siegmund, 22–33

Klein, C. A. 1967, Phys. Lett. A, 24, 513

Klein, C. A. 1968, J. Appl. Phys., 39, 2029

Kotov, I. V., Neal, H., & O'Connor, P. 2018, Nucl. Instrum. Methods Phys. Res. A, 901, 126

Kouveliotou, C., Meegan, C. A., Fishman, G. J., et al. 1993, ApJ, 413, L101

Kulkarni, S. R., Frail, D. A., Sari, R., et al. 1999, ApJ, 522, L97

Kumar, P. & Zhang, B. 2015, Phys. Rep., 561, 1

Law, C., Gaensler, B., Metzger, B., Ofek, E., & Sironi, L. 2019, in American Astronomical Society Meeting Abstracts, Vol. 233, American Astronomical Society Meeting Abstracts #233, 424.05

Lebrun, F., Leray, J. P., Lavocat, P., et al. 2003, A&A, 411, L141

Lechner, P., Hartmann, R., Soltau, H., & Strüder, L. 1996, Nucl. Instrum. Methods Phys. Res. A, 377A, 206

Leo, W. R. 1994, Techniques for Nuclear and Particle Physics Experiments: A How-to Approach (Springer)

Leroy, C. & Rancoita, P. G. 2009, Principles of Radiation Interaction in Matter and Detection (World Scientific)

Lowe, B. G. 1997, Nucl. Instrum. Methods Phys. Res. A, 399, 354

Lowe, B. G. & Sareen, R. A. 2007, Nucl. Instrum. Methods Phys. Res. A, 576, 367

Lutz, G. 2007, Semiconductor Radiation Detectors: Device Physics (Springer Berlin Heidelberg)

Madsen, K. K., Beardmore, A. P., Forster, K., et al. 2017, AJ, 153, 2

Maier, D. & Limousin, O. 2016, Nuclear Instruments and Methods in Physics Research A, 812, 43

Marshall, C. J. & Marshall, P. W. 1999, Proton Effects and Test Issues for Satellite Designers, Tech. Rep. 19990099117, NASA Goddard Space Flight Center, Greenbelt, MD United States

Mazziotta, M. N. 2008, Nuclear Instruments and Methods in Physics Research A, 584, 436

Meidinger, N., Andritschke, R., Assmann, W., et al. 2010a, in IEEE Nuclear Science Symposuim Medical Imaging Conference, 24–31

Meidinger, N., Andritschke, R., Ebermayer, S., et al. 2010b, Nucl. Instrum. Methods Phys. Res. A, 624, 321

Meidinger, N., Andritschke, R., Hälker, O., et al. 2006a, Nucl. Instrum. Methods Phys. Res. A, 568, 141

Meidinger, N., Andritschke, R., Hartmann, R., et al. 2006b, Nucl. Instrum. Methods Phys. Res. A, 565, 251

Meidinger, N., Bonerz, S., Englhauser, J., et al. 2004, in Proc. SPIE, Vol. 5501, High-Energy Detectors in Astronomy, ed. A. D. Holland, 66–77

Meidinger, N., Schmalhofer, B., & Struder, L. 1998, IEEE T. Nucl. Sci., 45, 2849

Meidinger, N., Schmalhofer, B., & Strüder, L. 2000, Nucl. Instrum. Methods Phys. Res. A, 439, 319

Meidinger, N., Strüder, L., Holl, P., Soltau, H., & Zanthier, C. v. 1996, Nucl. Instrum. Methods Phys. Res. A, 377A, 298

Ménesguen, Y. & Lépy, M. C. 2012, Nucl. Instrum. Methods Phys. Res. A, 695, 193

Mercier, K., Gonzalez, F., Götz, D., et al. 2018, in Society of Photo-Optical Instrumentation Engineers (SPIE) Conference Series, Vol. 10699, Space Telescopes and Instrumentation 2018: Ultraviolet to Gamma Ray, 1069921

Messenger, S. R., Burke, E. A., Xapsos, M. A., Summers, G. P., & Walters, R. J. 2004, IEEE T. Nucl. Sci., 51, 2846

Moll, M., Fretwurst, E., Lindström, G., & ROSE/CERN-RD48 Collaboration. 1999, Nucl. Instrum. Methods Phys. Res. A, 426, 87

Ofek, E. O., Cenko, S. B., Gal-Yam, A., et al. 2007, ApJ, 662, 1129

PANTER. 2019, PANTER X-ray test facility, `http://www.mpe.mpg.de/heg/panter`

Parker, E. N. 1958a, ApJ, 128, 664

Parker, E. N. 1958b, ApJ, 128, 677

Paul Scherrer Institute (PSI). 2019, Proton Irradiation Facility (PIF), `http://pif.web.psi.ch/pif.htm`

Piran, T. 1999, Phys. Rep., 314, 575

Plucinsky, P. P., Beardmore, A. P., Foster, A., et al. 2017, A&A, 597, A35

Porro, M., Herrmann, S., & Hornel, N. 2007, in 2007 IEEE Nuclear Science Symposium Conference Record, Vol. 1, 291–298

Pullia, A. 1998, Nucl. Instrum. Methods Phys. Res. A, 405, 121

Roth, T., Rudiger, M., Trupke, T., & Glunz, S. W. 2008, in 2008 33rd IEEE Photovoltaic Specialists Conference, 1–4

Sawyer, D. M. & Vette, J. I. 1976, AP-8 trapped proton environment for solar maximum and solar minimum, Tech. rep., NASA STI

Schanz, T. 2017, X-ray CCD Lab Operators Manual

Schmaler, G. 2012, Ph. d. thesis, Technische Universität München

Schmidt, J., Hartmann, R., Holl, P., et al. 2014, Journal of Instrumentation, 9, P10008

Scholze, F., Rabus, H., & Ulm, G. 1998, Journal of Applied Physics, 84, 2926

Shea, M. A. & Smart, D. F. 2004, Adv. Space. Res., 34, 420 , solar Variability and Climate Change

Shockley, W. & Read, W. T. 1952, Physical Review, 87, 835

Siegbahn, K. 2012, Alpha-, Beta- and Gamma-Ray Spectroscopy (Elsevier Science)

Smith, M. J. S. 2017, XMM-SOC-CAL-PL-0001, XMM-Newton: Routine Calibration Plan, `https://www.cosmos.esa.int/web/xmm-newton/calibration-documentation`

SOLEIL. 2019, SOLEIL synchrotron, `https://www.synchrotron-soleil.fr/fr`

Soppera, N., Bossant, M., & Dupont, E. 2014, Nuclear Data Sheets, 120, 294

Spieler, H. 2005, Semiconductor Detector Systems, Series on Semiconductor Science and Technology (OUP Oxford)

Strüder, L., Bräuninger, H., Meier, M., et al. 1990, Nucl. Instrum. Methods Phys. Res. A, 288, 227

Strüder, L., Briel, U., Dennerl, K., et al. 2001, A&A, 365, L18

Strüder, L., Englhauser, J., Hartmann, R., et al. 2003, Nucl. Instrum. Methods Phys. Res. A, 512, 386

Strüder, L., Holl, P., Lutz, G., & Kemmer, J. 1987a, Nucl. Instrum. Methods Phys. Res. A, 257, 594

Strüder, L., Holl, P., Lutz, G., & Kemmer, J. 1987b, Nucl. Instrum. Methods Phys. Res. A, 253, 386

Sun, H., Zhang, B., & Li, Z. 2015, The Astrophysical Journal, 812, 33

Sze, S. M. & Ng, K. K. 2006, Physics of Semiconductor Devices, 3rd edn. (Wiley-Interscience)

Technical Committee ISO/TC 20, Aircraft and space vehicles, Subcommittee SC 14, Space systems and operations. 2004, Space environment (natural and artificial) – Galactic cosmic ray model, `https://www.iso.org/standards.html`

The LIGO Scientific collaboration. 2019, arXiv e-prints, arXiv:1904.03187

TRAD. 2019, OMERE, `http://www.trad.fr/en/space/omere-software/`

Turner, M. J. L., Abbey, A., Arnaud, M., et al. 2001, A&A, 365, L27

Valkealahti, S., Schou, J., & Nieminen, R. M. 1989, Journal of Applied Physics, 65, 2258

Valtchanov, I. and Smith, M. and Schartel, N. 2019, XMM-SOC-CAL-SRN-0367, EPIC-pn Energy Scale for Large Window Mode: long-term CTI and pattern corrections, `https://www.cosmos.esa.int/web/xmm-newton/calibration-documentation`

van Ginneken, A. 1989, Non ionizing energy deposition in silicon for radiation damage studies, Tech. Rep. FN-522, Fermi Nat. Accelerator Lab.

Varshni, Y. P. 1967, Physica, 34, 149

Verner, D. A., Ferland, G. J., Korista, K. T., & Yakovlev, D. G. 1996, ApJ, 465, 487

Vette, J. I. 1991, The AE-8 trapped electron model environment, Tech. rep., NASA STI

Virgili, F. J., Mundell, C. G., Pal'shin, V., et al. 2013, ApJ, 778, 54

Walden, R. H., Krambeck, R. H., Strain, R. J., et al. 1972, Bell Syst. Tech. Jour., 51, 1635

Wei, J., Cordier, B., Antier, S., et al. 2016, arXiv e-prints, arXiv:1610.06892

Wilms, J., Allen, A., & McCray, R. 2000, ApJ, 542, 914

Wilson-Hodge, C. A., Cherry, M. L., Case, G. L., et al. 2011, ApJ, 727, L40

Wolter, H. 1952, Ann. Phys., 445, 286

Wood, S., Doyle, N. J., Spitznagel, J. A., et al. 1981, IEEE T. Nucl. Sci., 28, 4107

Xapsos, M. 2006, 2006 IEEE NSREC Short Course Section I: Modeling the Space Radiation Environment, https://ntrs.nasa.gov/search.jsp?R=20060027781

Xapsos, M. A., Barth, J. L., Stassinopoulos, E. G., Burke, E. A., & Gee, G. B. 1999, Space environment effects: model for emission of solar protons (ESP) - cumulative and worst-case event fluences, Tech. Rep. NASA/TP–1999-209763, NASA

Xapsos, M. A., Summers, G. P., Barth, J. L., Stassinopoulos, E. G., & Burke, E. A. 2000, IEEE T. Nucl. Sci., 47, 486

Zhang, B. 2006, Nature, 444, 1010

Zhang, B., Fan, Y. Z., Dyks, J., et al. 2006, ApJ, 642, 354

Zhang, B.-B., Zhang, B., Murase, K., Connaughton, V., & Briggs, M. S. 2014, ApJ, 787, 66

Ziegler, J. F., Biersack, J. P., & Ziegler, M. D. 2008, SRIM, the Stopping and Range of Ions in Matter (SRIM Company)

université PARIS-SACLAY

ÉCOLE DOCTORALE
Astronomie et Astrophysique d'île-de-France

Titre : Caractérisation et optimisation des performances du plan focal du télescope X de la mission d'astronomie spatiale SVOM

Mots clés : Astronomie Spatiale, Astronomie en rayons X, Instrumentation Spatiale, SVOM, MXT

Résumé : SVOM est une mission Franco-Chinoise prévue pour fin 2021, pour l'étude des sursauts gamma (GRBs). SVOM sera composée d'un réseau de télescopes au sol, ainsi que d'un satellite. À bord de celui-ci, le Télescope X à Micro-canaux (MXT) étudiera l'émission rémanente des GRBs dans la bande 0.2-10 keV et localisera les sources avec une précision de 2 arcmin. Au plan focal d'optiques à œil de langouste, MXT montera un Charge Coupled Device en silicium complètement déplété et basé sur jonctions pn (pnCCD), hérité de XMM-Newton et eROSITA. Dans ce travail, les premiers essais de laboratoire sur le détecteur de MXT sont présentés. Une attention particulière est portée à l'étalonnage spectral par des méthodes instrumentales et d'analyse permettant une caractérisation rapide et fiable du détecteur, au sol et en vol. L'évolution des performances est critique en raison de l'environnement radiatif sévère de l'orbite terrestre basse auquel le détecteur sera exposé. Ceci fait l'objet de simulations Monte Carlo approfondies, amenant aux prédictions des performances à la fin de la mission, ainsi qu'à la planification d'une campagne d'essais d'irradiation de protons dans un accélérateur de particules pour une validation expérimentale des prédictions.

Title: Characterization and performance optimization of the focal plane of the Micro-channel X-ray Telescope on-board the space astronomy mission SVOM

Keywords: Space Astronomy, X-ray Astronomy, Space Instrumentation, SVOM, MXT

Abstract: SVOM is a Chinese-French astronomy mission due to launch at the end of 2021 for the study of Gamma-Ray Bursts (GRBs). SVOM will be composed of a network of ground telescopes along with a satellite. On board, the Micro-channel X-ray Telescope (MXT) will study the afterglow emission of GRBs in the 0.2-10 keV range and provide source localization within a 2 arcmin precision. At the focal plane of lobster-eye optics, MXT will mount a back-illuminated fully-depleted frame-store Charge Coupled Device based on silicon pn-junctions (pnCCD), heritage of XMM-Newton and eROSITA. In this work, the first laboratory tests on the MXT detector are presented. Special attention is dedicated to energy calibration, in terms of algorithms and setups for fast and reliable characterization of the detector, both on ground and in orbit. The evolution of the performance is of critical concern because of the harsh radiation environment of the low Earth orbit to which the detector will be exposed. This is the object of extensive Monte Carlo simulations, leading to predictions of the end-of-life performances as well as the planning of a proton irradiation campaign at a particle accelerator for the experimental validation of the predictions.

Université Paris-Saclay
Espace Technologique / Immeuble Discovery
Route de l'Orme aux Merisiers RD 128 / 91190 Saint-Aubin, France